Network Morphologies in Monodisperse and Polydisperse Multiblock Terpolymers

A DISSERTATION
SUBMITTED TO THE FACULTY OF THE GRADUATE SCHOOL
OF THE UNIVERSITY OF MINNESOTA
BY

Adam James Meuler

IN PARTIAL FULFILLMENT OF THE REQUIREMENTS
FOR THE DEGREE OF
DOCTOR OF PHILOSOPHY

Frank S. Bates and Marc A. Hillmyer, Advisors

January 2009

Acknowledgements

I feel very privileged to have had the opportunity to attend graduate school at the University of Minnesota. My time here has been full of intellectual and personal growth, and plenty of fun as well. These experiences were only possible because of my interactions with a number of terrific individuals. First and foremost, I would like to thank my advisors Frank Bates and Marc Hillmyer. They exhibited a great deal of patience and provided just the right amount of guidance to help me find my research path. I learned a great deal about fostering a productive, collaborative environment by observing their management firsthand and I am a much better scientist, and person, because of their influence. Tim Lodge and Dave Morse also played crucial roles in my development, and I learned a great deal from them through formal teaching and informal discussions.

Many other members of the Polymer Group aided my intellectual growth. Eric Cochran and Thomas Epps taught me a lot about block copolymers as I was getting started, and I still enjoy beating Thomas at fantasy football. Mahesh Mahanthappa offered invaluable synthetic chemistry and writing guidance, and I continue to learn a great deal about polymer science from him. Guillaume Fleury works with a patience I do not have and was a great collaborator for studying the OSISO materials. Team Polydispersity- Nate Lynd, Chris Ellison, Jian Qin, and Chris Evans- all played key roles in my research. Nate Lynd encouraged me to initially pursue polydispersity studies, and my understanding of polydispersity effects greatly benefited from our discussions. I could not have found a better partner-in-crime for polydispersity studies than Chris Ellison. He has incredible focus and drive, taught me a lot about how to

frame scientific problems, and was instrumental in convincing Frank to join a game of pickup basketball. Without his persistence, I would not have seen the work of art that is Frank's jump shot. None of my theoretical studies would have gotten off the ground without Jian Qin. He patiently taught me both the concepts of SCFT and the mechanics of performing the calculations, and I have lost count of the number of fruitful conversations we have had. Chris Evans contributed significantly to the synthetic and characterization efforts in the polydispersity studies, and his hard work is greatly appreciated. I have benefited from scholarly conversations with a number of other individuals, including Kevin P. Davis, Sumeet Jain, Aaron Brannan, Alhad Phatak, Joon Chatterjee, Javid Rzayev, Mike Bluemle, Zach Thompson, Adam Buckalew, John Zupancich, Bryan Boudouris, Sangwoo Lee, Will Edmonds, Peter Simone, Bill Phillip, Ning Zhou, Kathleen Schreck, and Louis Pitet.

My graduate experience would not have been nearly as enjoyable without the support of my family and friends. The members of the Bad News Beers softball juggernaut (back-to-back champs!) and College Football Saturday crew were particularly adept at providing ways to escape from work. My parents, brother, and sister, have been very supportive of my quest to avoid a "real job," and I am grateful for their encouragement. Finally, I owe Nicole and Dane many thanks for their love and support that kept me sane during the pressure-filled past few months.

To My Family

Abstract

Multiply continuous network morphologies were previously identified in "monodisperse" (polydispersity index (PDI) < ~1.1 in all blocks) poly(isoprene-*b*-styrene-*b*-ethylene oxide) (ISO) triblock terpolymers. This work extends the investigation of multiply continuous network structures to two other classes of multiblock terpolymers: i) "monodisperse" OSISO pentablocks and ii) polydisperse ISO triblocks. The OSISO pentablocks are synthesized using a protected initiation strategy that required the development of the functional organolithium 3-triisopropylsilyloxy-1-propyllithium (TIPSOPrLi). TIPSOPrLi may be used to prepare α-hydroxypolystyrene with narrower molecular weight distributions (PDI ~ 1.1) than are attainable using the commercially available 3-*tert*-butyldimethylsilyloxy-1-propyllithium. A telechelic triblock terpolymer (HO-SIS-OH) with narrow molecular weight distributions in all blocks is prepared using TIPSOPrLi. A series of OSISO pentablocks is synthesized from this parent triblock, and a stable region of O^{70} (the orthorhombic *Fddd* network) is identified between two-domain lamellae (LAM_2) and three-domain lamellae (LAM_3) in OSISO materials. This sequence of morphologies was previously reported in ISO triblocks with comparable compositions. Mechanical tensile testing reveals that an OSISO sample with a lamellar mesostructure fractures in a brittle fashion at a strain of 0.06. An OSISO containing the O^{70} network, in contrast, has a strain at failure of 1.3, even though the crystallinity of the terminal blocks is above the brittle threshold established in other multiblock materials. This improved toughness is attributed to the combined effects of a triply continuous morphology and an intrinsically tough SIS core.

The ISO triblock studies probe the stability of network morphologies with respect to polydispersity in the polystyrene and poly(ethylene oxide) chains. Three series of ISO triblocks with polydisperse (PS PDI = 1.16, 1.31, 1.44) polystyrene blocks are prepared by anionic polymerization. While the network "window" in the PS PDI = 1.16 series is comparable in width and location to the window reported in the "monodisperse" ISO materials, it apparently shrinks for the higher PS PDI values. Only lamellar mesostructures are reported in the PS PDI = 1.31 materials, and network morphologies are identified over only a narrow range of compositions in the PS PDI = 1.44 samples. Polydispersity does not always destabilize network morphologies, however, as broadening the molecular weight distribution of the terminal poly(ethylene oxide) block drives a morphological transition from lamellae to the core-shell gyroid network. This result demonstrates that polydispersity can be used to tune block terpolymer phase behavior and stabilize technologically useful network mesostructures. Self-consistent field theory calculations augment the experimental analysis and offer insight into the physics underlying the polydispersity-driven morphological changes.

Table of Contents

List of Tables

List of Figures

1

Introduction

1.1 Why Block Copolymers?

The material properties of metals, including tensile strength and electrical conductivity, are often tailored by mixing multiple elements. These composite materials are called metal alloys, and some common examples include steel (mostly iron with ~1-2% carbon) and brass (copper and zinc).[1] In principle the properties of polymeric materials can be tuned in a similar fashion. For instance, mechanical properties could be controlled by judiciously mixing glassy and rubbery polymers. In order for blending to yield the desired synergistic effects, the polymers must not macrophase separate. The miscibility criteria for polymer blends can be discussed within the context of the well-known Flory-Huggins framework. This theory yields the following expression for the Gibbs' free energy of mixing (ΔG_m) for A and B homopolymers:

$$\frac{\Delta G_m}{\mathrm{k_B}T} = \frac{\phi_A}{N_A}\ln(\phi_A) + \frac{\phi_B}{N_B}\ln(\phi_B) + \phi_A\phi_B\chi_{AB} \qquad (1\text{-}1)$$

where k_B is the Boltzmann constant, T is the temperature, χ_{AB} is the segment-segment interaction parameter (commonly called the Flory-Huggins interaction parameter), N_A and N_B are the degrees of polymerization of the A and B homopolymers, and ϕ_A and ϕ_B are the volume fractions of the A and B homopolymers.[2] (Note that in this theory N_i is

not the number of monomers, as this number depends on an arbitrary choice of chemical repeat unit. Rather, the N_i here refers to the number of segments of a defined reference volume. χ_{AB} is also defined with respect to this same reference volume.) Negative terms in Equation 1-1 favor mixing while positive terms favor macrophase separation. The entropy terms $\frac{\phi_A}{N_A}\ln(\phi_A)$ and $\frac{\phi_B}{N_B}\ln(\phi_B)$ are always negative and promote miscibility. In typical polymers, however, N_A and N_B are greater than 50, and the entropic terms are largely negligible. The enthalpy term $\phi_A\phi_B\chi_{AB}$ thus becomes the dominant contribution to the Gibbs' free energy. Since there are usually weak repulsions between chemically distinct polymers (i.e., $\chi_{AB} > 0$), ΔG_m is positive and polymer blends, like mixtures of oil and water, tend to macrophase separate. (Note that in a limited number of systems there is a negative χ_{AB} due to specific interactions between the A and B chains (e.g., hydrogen bonding).[3])

Macrophase separation makes the preparation of stable polymer blends difficult and limits their utility in technological applications. An alternative approach for the fabrication of composite polymeric materials is provided by block copolymers. Block copolymers are formed by the covalent end-to-end union of two or more chemically distinct polymer chains. These hybrid macromolecules can be prepared by a variety of techniques, including living anionic polymerizations,[4] controlled radical polymerizations,[5] and ring-opening metathesis polymerizations.[6] The disparate blocks in block copolymers, like the homopolymers discussed above, typically will phase separate into domains rich in one component. The covalent linkages on block copolymers constrain the phase separation of chemically incompatible blocks to the

length scale of the polymer chains (typically ~5 – 100 nm) and inhibit macrophase separation.[7] These microphase separated block copolymers retain features of both constituent homopolymers, unlike macrophase separated blends, and it is the suppression of macrophase separation that is largely responsible for the current success of block copolymers in materials applications.[8] For example, poly(styrene-*b*-isoprene-*b*-styrene) and poly(styrene-*b*-butadiene-*b*-styrene) triblock copolymers microphase separate into glassy polystyrene and rubbery polyisoprene or polybutadiene domains. The presence of nanometer sized domains of both blocks leads to robust elastomeric behavior that is unlike the behavior of either constituent homopolymer and has resulted in the widespread use of these triblock copolymers as thermoplastic elastomers.[9]

Block copolymers may find utility in advanced materials applications for reasons other than the suppression of macrophase separation. Namely, when block copolymers microphase separate, they adopt ordered mesostructures with features on the ~5 – 100 nm length scale. The symmetry of the ordered morphology depends on a number of variables, including the number of chemically distinct blocks, the component volume fractions, and the interactions between the blocks.[7, 10] It is anticipated that future applications will take advantage of the spatial extent, connectivity, and orientations of the block copolymer domains in these ordered mesostructures.[8] The research described in this Thesis focuses on one particular class of ordered morphologies formed by block copolymers: multiply continuous network structures. The spatial ordering of these fascinating structures could make them useful in technologies such as catalysis,[11] photonic materials,[12, 13] and separations,[14] as will be discussed in Chapter 2.

1.2 Thesis Outline

All of the Chapters in this Thesis are designed to both stand alone and serve as portions of a longer narrative. Chapter 2 contains an extensive review of the structures and properties of multiply continuous network morphologies formed by both AB diblock copolymers and ABC triblock terpolymers. This discussion provides the reader with the requisite background information and motivates the research that is described in the remaining Chapters. General information about the experimental techniques that were widely used in this research is provided in Chapter 3. The focus here is largely conceptual, and specific experimental details are provided in Chapters 4-7. The development of the functional organolithium 3-triisopropylsilyloxy-1-propyllithium (TIPSOPrLi) is summarized in Chapter 4. This protected initiator was used to prepare some of the polymers that are described in Chapters 5 and 6. Chapter 5 focuses on the structures and properties of poly(ethylene oxide-*b*-styrene-*b*-isoprene-*b*-styrene-*b*-ethylene oxide) (OSISO) pentablock terpolymers, and a mechanically robust network-forming OSISO sample is described in detail. An investigation of polydispersity effects in poly(isoprene-*b*-styrene-*b*-ethylene oxide) (ISO) triblock terpolymers is described in Chapter 6. This discussion focuses on the stability of multiply continuous network morphologies with respect to polydispersity in either the terminal poly(ethylene oxide) or middle polystyrene blocks. Chapter 7 includes a brief summary of the advances described in Chapters 4-6 as well as some preliminary experimental data from possible future research directions.

1.3 References

(1) Callister, W. D., Jr. *Materials Science and Engineering: An Introduction*, 7th ed.; John Wiley & Sons, Inc.: New York, NY, 2007.

(2) Hiemenz, P. C.; Lodge, T. P. *Polymer Chemistry*, 2nd ed.; CRC Press: Boca Raton, FL, 2004.

(3) Kuo, S.; Huang, W.; Huang, C.; Chan, S.; Chang, F. *Macromolecules* **2004**, *37*, 4164-4173.

(4) Hong, K.; Uhrig, D.; Mays, J. W. *Curr. Opin. Solid State Mater. Sci.* **2000**, *4*, 531-538.

(5) Braunecker, W. A.; Matyjaszewski, K. *Prog. Polym. Sci.* **2007**, *32*, 93-146.

(6) Bielawski, C. W.; Grubbs, R. H. *Prog. Polym. Sci.* **2007**, *32*, 1-29.

(7) Leibler, L. *Macromolecules* **1980**, *13*, 1602-1617.

(8) Lodge, T. P. *Macromol. Chem. Phys.* **2003**, *204*, 265-273.

(9) Holden, G., Legge, N. R., Quirk, R. P., Schroeder, H. E. *Thermoplastic Elastomers*, 2nd ed.; Hansen Publishers: New York, NY, 1996.

(10) Bates, F. S.; Fredrickson, G. H. *Phys. Today* **1999**, *52*, 32-38.

(11) Hashimoto, T.; Tsutsumi, K.; Funaki, Y. *Langmuir* **1997**, *13*, 6869-6872.

(12) Campbell, M.; Sharp, D. N.; Harrison, M. T.; Denning, R. G.; Turberfield, A. J. *Nature* **2000**, *404*, 53-56.

(13) Urbas, A. M.; Maldovan, M.; DeRege, P.; Thomas, E. L. *Adv. Mater* **2002**, *14*, 1850-1853.

(14) Chan, V. Z. -H.; Hoffman, J.; Lee, V. Y.; Latrou, H.; Avgeropoulos, A.; Hadjichristidis, N.; Miller, R. D; Thomas, E. L. *Science* **1999**, *286*, 1716-1719.

2

Ordered Network Mesostructures in Block Copolymer Materials

2.1 Introduction

Block copolymers are hybrid macromolecules formed by coupling together two or more chemically distinct homopolymers. They have been the focus of extensive research efforts since Szwarc's development of living anionic polymerization as a relatively facile means of block copolymer synthesis in 1956.[1] There are a number of block copolymer architectures, the simplest of which is the linear AB diblock copolymer. Early experimental research revealed that these materials self-assemble primarily into three periodically ordered mesostructures: lamellae (LAM), hexagonally packed cylinders (HEX), and body-centered cubic spheres (BCC).[2-4] Real space representations of these morphologies are provided in Figure 2.1. Theoretical studies followed these experimental reports and delineated the statistical mechanical phenomena governing mesostructure formation in block copolymers.[5-7]

AB diblock copolymers are generally characterized by the overall degree of polymerization N, the volume fraction of each block f_i, and the segment-segment (Flory-Huggins) interaction parameter χ_{AB}, where the product $\chi_{AB}N$ scales with the segregation

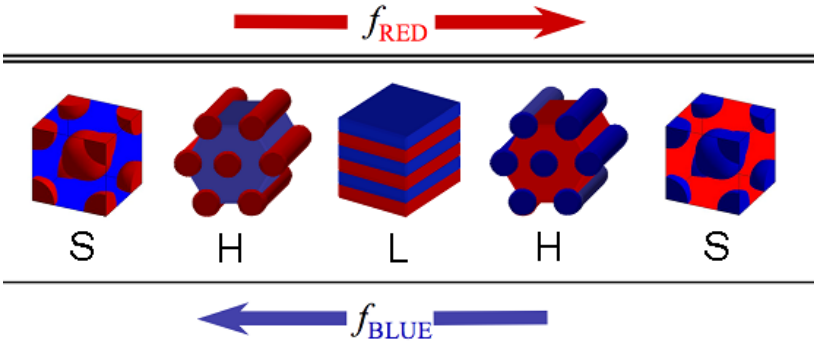

Figure 2.1. Real space representations of the (S) BCC, (H) HEX, and (L) LAM morphologies that are accepted as equilibrium mesostructures for AB diblock copolymers. Morphologies are presented, from left to right, in the order of increasing volume fraction of the red block. Figure reproduced from Reference 8.

strength of the system (note that both χ_{AB} and N must be defined with respect to the same segment reference volume).[9, 10] Above a minimum value of $\chi_{AB}N$, the constituent blocks are thermodynamically incompatible and, like oil and water, segregate to minimize the overall free energy. Unlike oil and water, the covalent linkages between blocks prevent macrophase separation and constrain block separation to a length scale commensurate with the size of the polymer chains (typically ~5 – 100 nm). Free energy minimization drives block copolymers to adopt periodically ordered morphologies, and a balance of interfacial tension and entropic stretching energy considerations governs selection of the equilibrium state.[9, 10] In AB diblock copolymers, the identity of the equilibrium morphology depends largely on f_i and $\chi_{AB}N$.[7, 11-13]

BCC, HEX, and LAM have been identified as the equilibrium morphologies for the majority (> 80% at $\chi_{AB}N$ = 100) of AB diblock copolymer compositions.[13] None of

these mesostructures have multiple domains that continuously percolate across the specimen. A multiply continuous, percolating domain structure would provide physical attributes that could be useful in many technological applications. From a mechanical property standpoint, a multiply continuous network structure permits each domain to contribute directly to the modulus of the material[14] and may allow for synergistic improvements in toughness, stress at failure, and creep resistance.[15] Multiply continuous block copolymer morphologies are characterized by a high interfacial area per specimen volume, an attribute that could facilitate gas separation[16] and the separation and extraction of free charges (and improve efficiency) in solar cells.[17-19] Percolating domain structures could be useful in membranes for water purification; HEX-forming diblock copolymers have been employed, following the degradation and removal of the minority components, as water filtration membranes.[20, 21] Anisotropic structures such as HEX often require costly and/or time-consuming alignment procedures to minimize pore dead ends and maximize flux through the membrane. The percolating domains of network mesostructures are not likely to terminate at grain boundaries, rendering these alignment procedures unnecessary. Three-dimensional (3-D) domain connectivity may also enhance ionic transport in, for example, battery or fuel cell membranes, when the mesostructure contains a conducting domain.[22] Triply periodic order is also important in 3-D photonic crystals,[23-27] and block copolymer network mesostructures may find application in this emerging technology.[28]

Scriven first suggested, in 1976, that morphologies with multiple continuous, percolating domains could arise in complex fluids (e.g., melt-phase block copolymers).[29] Numerous types of multiply continuous structures have since been

identified in polymeric materials, including co-continuous blends,[14, 15] bicontinuous microemulsions,[30, 31] a distorted bicontinuous structure,[32] and network morphologies with long-range translational order.[33-35] Ordered network morphologies are arguably the most versatile of these multiply continuous structures, as only they contain the translational order that may be important in photonic crystal[23-27] or solar cell applications.[36] This Chapter focuses on theoretical and experimental investigations of ordered network morphologies containing two or more percolating, continuous domains in block copolymer materials. It includes a discussion of the symmetries and microdomains structures of all known network morphologies and a discussion of network stability with respect to solvent or homopolymer addition, block polydispersity, ionic groups, salts, and confinement in thin films.

2.2 Network Morphologies formed by Block Copolymers

Ordered Bicontinuous Double Diamond (OBDD)

Scriven first hypothesized that bicontinuous structures could arise in complex fluids in 1976.[29] In that prescient publication, he described a bicontinuous structure as "a bicontinuous partitioning in which each subvolume is filled with a distinct, not necessarily uniform composition or state of matter." When a structure contains more than two continuous, percolating domains, it can, in a generalization of Scriven's notation, be referred to as a "multiply continuous network structure." Scriven noted that, for certain subvolume ratios, bicontinuous geometries have less interfacial area than structures comprised of discrete spheres of one component packed in a continuum

of the other component. Thermodynamic considerations that favor a minimization of interfacial area could thus drive formation of a bicontinuous structure, and Scriven pointed out that the dividing surfaces that minimize interfacial area are periodic minimal surfaces;[29] Schoen had mathematically described 17 such surfaces.[37]

The phrase "ordered bicontinuous structure" was first used to describe a block copolymer morphology by Alward et al. in 1986.[38] These researchers characterized starblock copolymers comprised of poly(styrene-*b*-isoprene) (PS-PI) arms. (Note that a list of abbreviations for all of the polymers dicussed in Chapter 2 is provided in Table 2.4 at the end of the Chapter.) They obtained, from materials with 8, 12, and 18 branches and 30 wt% PS, transmission electron microscopy (TEM) images with both "wagon-wheel" and square arrangements; representative micrographs are provided in Figure 2.2.[38] Aggarwal had published a similar wagon-wheel micrograph ten years prior (acquired from a 15-arm PS-PI starblock copolymer with 30 wt % PS), but, unlike Alward et al., did not comment on the nature of the underlying mesostructure.[39] Alward and coworkers suggested that both of the projections provided in Figure 2.2 were the product of a single ordered bicontinuous morphology, as tilting a specimen in the TEM led to a transformation of one projection into the other. They probed the bicontinuity of the materials using gas sorption and dynamic mechanical spectroscopy measurements; the high rates of gas diffusion and the large elastic moduli (*G'*) indicated continuity of the PI and PS domains, respectively, in the specimens forming the mesostructure depicted in Figure 2.2.[38] Ordered bicontinuous mesostructures were subsequently reported in various other PS-PI starblock copolymers.[40, 41]

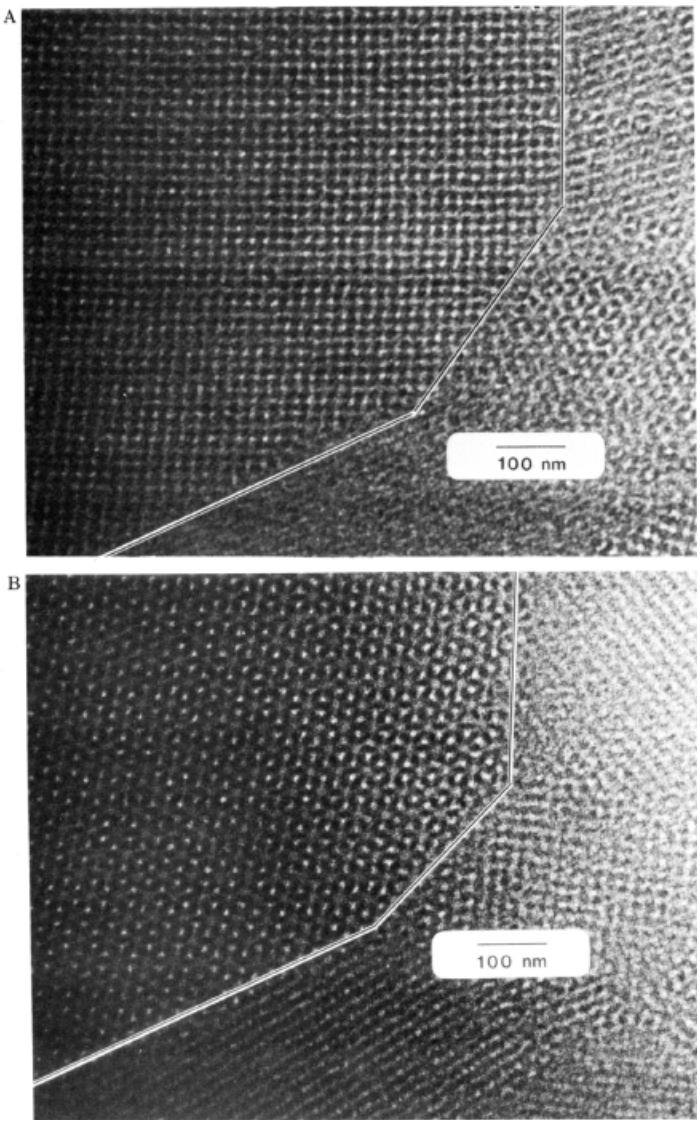

Figure 2.2. TEM micrographs obtained from a starblock copolymer material comprised of PS-PI arms with 30 wt % PS. The majority PI appears black because it was stained with OsO_4. Tilting the specimen in the TEM converted the square projection in 2A into the wagon-wheel arrangement in 2B; Alward et al. suggested these projections are the product of an ordered bicontinuous mesostructure and the micrographs are reproduced from their original publication.[38] Aggarwal had published a similar wagon-wheel micrograph without comment ten years earlier.[39]

Thomas and colleagues next attempted to elucidate the detailed microdomain structure of the ordered bicontinuous morphology depicted in Figure 2.2.[33] They noted that the micrographs provided in Figure 2.2 contain both fourfold (2a) and threefold (2b) axes of symmetry and concluded that the space group must be cubic, as only cubic space groups contain both of these symmetry elements. Small-angle X-ray scattering (SAXS) measurements were used to probe the space group symmetry, but the Bragg patterns contained features that were artifacts of the data desmearing process and were thus not reflective of the underlying mesostructure.[42] TEM images obtained from particularly thin (~30 nm thick) polymer slices revealed threefold connected PS rods separated by 120° in the two-dimensional projection. Thomas et al. suggested these rods were part of a fourfold connector, with the fourth rod being perpendicular to the plane of the image, and proposed a 3-D model for the ordered bicontinuous structure based upon *Pn3m* symmetry.[33] The model unit cell contained eight tetrahedral elements that formed two independent, peroclating networks within a continuous matrix. Simulated TEM images were generated using this model and they generally resembled the experimental micrographs. Thomas et al. cited this agreement as evidence in support of their model, and called the bicontinuous mesostructure the ordered bicontinuous double diamond (OBDD).[33] Solvent casting and thermal annealing experiments provided some evidence that the bicontinuous structure was the equilibrium phase. Films cast from toluene adopted OBDD that persisted upon thermal annealing, while those cast from cyclohexane initially formed HEX and subsequently transitioned to OBDD following thermal treatment.[33]

At roughly the same time, an ordered bicontinuous mesostructure was independently reported in solvent cast films of linear PS-PI diblock copolymers by Hasegawa et al.[43] TEM micrographs comparable to those provided in Figure 2.2 (but with opposite contrast) were acquired from specimens with PS volume fractions ranging from 0.62 to 0.66.[43] Like Thomas et. al,[33] Hasegawa and coworkers suggested the TEM images were consistent with interpenetrating networks connected by fourfold elements. They considered models of all three of the possible fourfold-connected network structures and reported that simulated TEM images generated from the OBDD lattice model with *Pn3m* symmetry were the most consistent with the experimental micrographs.[43] The bicontinuous mesostructure in the PS-PI specimens was further interrogated using SAXS. The acquired Bragg patterns did not contain all of the allowed reflections[44] for the *Pn3m* space group of OBDD, but appeared to be consistent with a Bravais lattice with hexagonal symmetry. Hasegawa et al. suggested that some peaks were not visible in SAXS patterns due to either detector resolution issues or form factor extinctions and, largely on the basis of TEM analysis, they identified the bicontinuous mesostructure as OBDD.[43]

Thomas et al. attempted to understand the molecular factors driving the selection of the OBDD mesostructure.[45] They noted that the interfacial width in strongly segregated diblock copolymers is small relative to the domain periodicity and suggested that, in this limit, the minimization of interfacial tension becomes more significant than the minimization of the entropic free energies associated with chain stretching. It was reasoned that block copolymers adopt morphologies with minimal-surface area interfaces separating the chemically distinct domains to minimize segment-segment

contacts and interfacial tension.[45] The surfaces that mathematically minimize their area are known as constant mean curvature (CMC) surfaces and Anderson and colleagues calculated that it is possible to have CMC surfaces with OBDD symmetry provided the volume fraction of the minority component is at least 0.262%.[46] Thomas et al. pointed out that this CMC volume fraction limit agreed remarkably well with block copolymer experiments,[45] as OBDD had been identified only in block copolymer materials with minority volume fractions above 0.26 (ranging from 0.27-0.38).[33, 41, 43] Thomas et al. generated simulated TEM projections using the CMC OBDD model and compared them to experimental TEM micrographs; both the simulated and experimental images are provided in Figure 2.3.[45] The agreement between the experimental and simulated images was cited as evidence that block copolymers form mesostructures with CMC, although Thomas et al. pointed out the visual similarities did not provide definitive proof.[45]

A number of additional experimental reports[47-50] of the OBDD mesostructure appeared in the literature following the seminal publications by Thomas et al.[33, 38, 40, 41, 45] and Hasegawa et al.[43] These investigations focused on binary blends of block copolymers and homopolymers. Winey et al. noted[47] that the OBDD morphology was only reported over narrow ranges of composition (a volume fraction range of ~0.05) in both diblock[43] and starblock[33, 38, 40, 41] copolymers. Targeting this narrow composition window can be synthetically challenging, and these reports illustrated that blending could be used to overcome the stringent synthetic requirements.[47-50] Winey et al. studied blends of PS-PI or PS-PB diblock copolymers and a constituent homopolymer (either PS, PI, or PB).[47] Most of the blends formed a

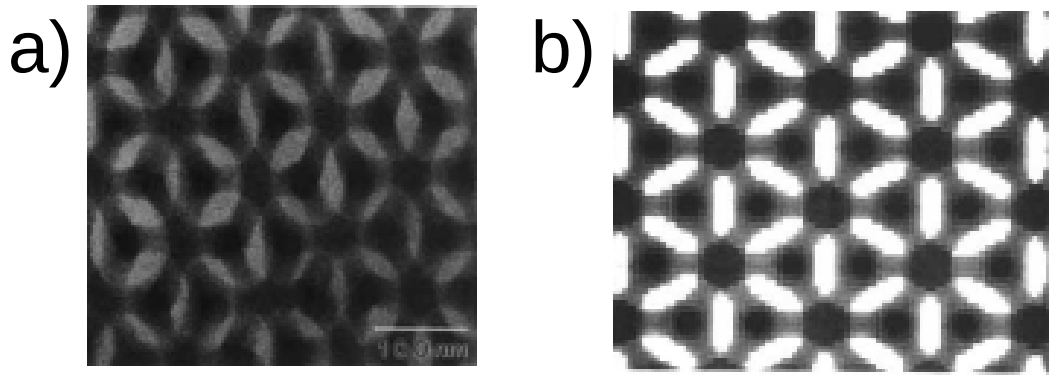

Figure 2.3. (a) TEM micrograph obtained from a PS-PI diblock copolymer with a PS volume fraction of 0.62 (PS appears light in the image because the PI is stained). (b) Simulated [111] projection from a model OBDD structure with CMC interfaces and the same composition as the experimental material probed in (a). Figure reproduced from Reference 45.

single morphology with long-range order than was qualitatively comparable to the long-range order in mesostructures formed by neat diblock copolymers (e.g., a similar number of Bragg peaks in the SAXS data). The blends formed the OBDD network in the appropriate coposition range and generally behaved like neat diblocks with the same overall composition, provided (i) the homopolymer weight fraction in the blend was below 0.40 and (ii) the homopolymer molecular weight was roughly equal to or less than the appropriate block molecular weight. Higher homopolymer fractions and/or higher molecular weight homopolymers usually triggered macrophase separation.[47] Spontak et al. extended Winey et al.'s investigations[47] of blends of PS-PI diblocks and PS or PI homopolymers to additional absolute and relative molecular weights.[48, 49]

Generally the reported results were consistent with Winey et al.'s study,[47] although some higher molecular weight blends formed poorly ordered mesostructures with both cylindrical and network features, and not well-ordered bicontinuous morphologies, possibly due to kinetic limitations.[48] Xie and coworkers examined blends of symmetric PS-PB-PS triblock copolymers (28 wt % PS, overall PDI = 1.35) and PVME homopolymers (PDI = 1.70).[50] The HEX mesostructure was identified using TEM in the neat PS-PB-PS triblock and the OBDD mesostructure was reported from binary blends containing 10, 12, and 15 wt % PVME (a total volume fraction of 0.33 – 0.37 for the mixed PS/PVME domains). The authors reported that there was no evidence of macrophase separation, and this work demonstrated that monodisperse materials are not required to form an ordered bicontinuous network mesostructure.[50]

A number of theoretical investigations also followed the Thomas et al.[33, 38, 40, 41, 45] and Hasegawa et al.[43] publications. These studies largely focused on the stability of the OBDD network mesostructure.[51-55] Wang and Safran studied model ternary blends comprised of an AB diblock copolymer and the constituent A and B homopolymers.[51] They calculated the curvature free energy of the block copolymer interface and suggested that the OBDD morphology was stable for systems with certain compositions and molecular weights, although the analysis was not valid for neat block copolymer materials.[51] Anderson and Thomas used a mean-field theory to calculate the free energies of the LAM, HEX, BCC, and OBDD morphologies for AB diblock and starblock copolymers in the strong-segregation limit (SSL).[52] The lowest free energy OBDD configuration (microdomains separated by CMC interfaces) never was predicted to be the equilibrium morphology; at least one of the BCC, HEX,

and LAM morphologies always had a computed free energiy that was more than 1% lower than that of OBDD. Anderson and Thomas suggested that non-Gaussian behavior of core chains that was not accounted for by the theory prevented OBDD from being identified as the equilibrium mesostructure.[52] Two other groups employed alternative strong-segregation theory (SST) calculations to re-examine Anderson and Thomas' conclusion regarding the stability of the OBDD morphology in AB diblock copolymers in the SSL.[53-55] Likhtman and Semenov used a more accurate mean-field approach to compute the free energies of competing morphologies in linear AB diblock copolymers with a minority block volume fraction ranging from 0.27-0.37.[53] They calculated that the OBDD morphology has a free energy at least 4% higher than either the LAM or HEX mesostructure over this composition range and suggested that free energy differences of this magnitude could not be accounted for by errors associated with either model assumptions or numerical approximations. Likhtman and Semenov hypothesized that the reported[43] OBDD morphologies in AB diblock copolymers were metastable structures.[53] Olmsted and Milner modified the SST approach by relaxing the assumption of CMC interfaces.[54, 55] This methodology allegedly improved the realism of the unit cells used in the calculations and, unlike studies based on Semenov's original SST approach,[56] enabled differentiation of the free energies associated with different packing arrangements (e.g., it could distinguish between BCC and FCC packing of spheres). Olmsted and Milner calculated that the free energy of the OBDD mesostructure was always at least ~3% higher than the competing LAM and HEX morphologies, a result in good agreement with Likhtman and Semenov's report.[53] (Note that Olmsted and Milner corrected[55] a numerical mistake in their initial publication[54] that had led to an initial

erroneous identification of ODBB as an equilibrium morphology.) None of these studies provided a theoretical basis for considering the OBDD an equilibrium mesostructure in strongly segregated AB diblock copolymers.

Gyroid (Q^{230})

While the OBDD morphology was the only bicontinuous mesostructure described in the block copolymer literature prior to 1994, additional interpenetrating phases were well-known in lipid-water systems. An ordered structure with $Ia\bar{3}d$ symmetry was first identified by Luzzati and Spegt in 1967 in strontium saturated soaps.[57] Schoen mathematically described a minimal surface with $Ia\bar{3}d$ symmetry in 1970 and called it the gyroid,[37] and the name "gyroid" has been widely used in literature to describe structures with $Ia\bar{3}d$ symmetry (and will be used in this review). The gyroid structure was reported in a number of water-lipid systems by 1991,[57-60] but was not known in block copolymer materials until 1994 when two experimental groups[34, 35] and one theoretical team[61] independently identified the gyroid morphology in weakly segregated diblock copolymer materials. These seminal publications are discussed in the following paragraphs.

Hajduk and coworkers synthesized a 27.4 kg/mol PS-PI diblock copolymer containing 37 wt% PS.[34] This diblock was annealed at least one hour in the melt to allow the material to approach equilibrium and improve the long-range order of the resulting morphology. SAXS data acquired following a 150 °C heat treatment contained two peaks at relative reciprocal space positions of $\sqrt{3}:\sqrt{4}$, with the second peak

having approximately 10% of the intensity of the primary peak. Hajduk et al. noted that although these relative peaks positions did not definitively eliminate HEX, BCC spheres, or OBDD as morphological candidates, the absence of peaks at relative *q* positions of 1 (for HEX and BCC) and $\sqrt{2}$ (for OBDD) were strongly suggestive of a new mesostructure.[34] Several complementary characterization techniques were employed in an attempt to determine the identity of this morphology. A representative TEM micrograph from this specimen is provided in Figure 2.4a. Both the PS and PI domains appear to be continuous in the image, eliminating HEX and BCC as mesostructural candidates.[34] This PS-PI sample had a measured birefringence of zero and, consequently, an optically isotropic structure, consistent with cubic symmetry.[34] Since neither the TEM nor the birefringence experiments eliminated OBDD as a mesostructural candidate, Hajduk et al. returned to SAXS analysis and modified their procedure to maximize the number of higher order Bragg peaks obtained from the experiment; the sample was now annealed for 8 hours and then exposed to X-rays for 8 hours. The one-dimensional profile obtained from this SAXS experiment is provided in Figure 2.4b; Bragg reflections are present at relative *q* positions of $\sqrt{3}$, $\sqrt{4}$, $\sqrt{10}$, $\sqrt{11}$, $\sqrt{16}$, and $\sqrt{19}$. Hajduk et al. noted that the $\sqrt{10}$, $\sqrt{11}$, and $\sqrt{19}$ reflections are inconsistent with noncubic space groups, a result in accord with the birefringence experiment.[34] Only three of the 17 possible cubic extinction symbols (*P*..., *P4*$_2$.., and *Pn*..) have allowed reflections at the relative $\sqrt{3}$, $\sqrt{4}$, $\sqrt{10}$, $\sqrt{11}$, $\sqrt{16}$, and $\sqrt{19}$ Bragg locations. However, each of these symbols also have at least eight allowed reflections that are not present in the SAXS data. Hajduk et al. noted that while a couple

of these absences can be rationalized as minima in the structure factor, such reasoning is unlikely to account for the large number of peaks absent in the SAXS data. They argued that these data suggest the new morphology does not belong to either the *P*..., *P4₂*.., or *Pn*.. space groups.[34]

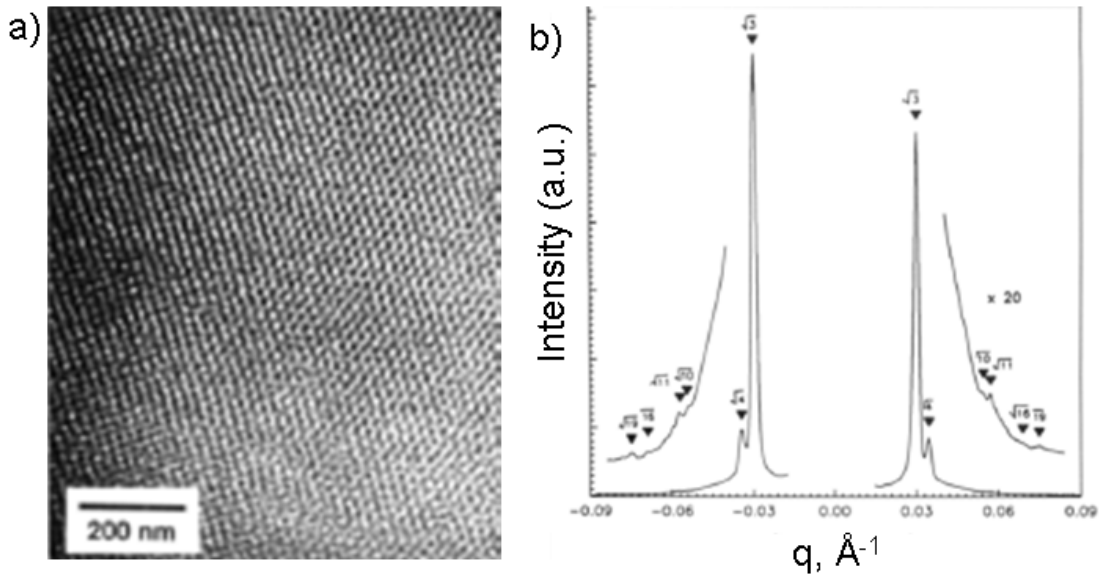

Figure 2.4. (a) TEM micrograph acquired from a PS-PI diblock copolymer with 37 wt% PS. Prior to TEM analysis, the sample was annealed for 22 h at 160 °C and then quenched in liquid nitrogen to preserve the high-temperature morphology. (b) One-dimensional SAXS profile acquired from the SI diblock that formed the morphology imaged in (a). Reproduced from Reference 34.

Hajduk et al. pointed out that these peak locations can be rescaled, as the $\sqrt{3}$, $\sqrt{4}$, $\sqrt{10}$, $\sqrt{11}$, $\sqrt{16}$, and $\sqrt{19}$ values simply represent the lowest quantities consistent with the relative positions.[34] Additional possibilities for the space group arise

when all of these values are multiplied by $\sqrt{2}$, an operation that leaves the peak ratios unchanged. The reinterpretation of the peak positions as $\sqrt{6}$, $\sqrt{8}$, $\sqrt{20}$, $\sqrt{22}$, $\sqrt{32}$, and $\sqrt{38}$ reflections is supported by the fact that this renormalization yields better agreement between the unit cell dimensions measured by SAXS and those measured using TEM than the previous $\sqrt{3}$, $\sqrt{4}$, $\sqrt{10}$, $\sqrt{11}$, $\sqrt{16}$, and $\sqrt{19}$ assignments. Twelve cubic space groups (all of those with *P* or *I* symmetry) allow Bragg reflections at the rescaled peaks positions. However, all of these space groups have at least seven allowed reflections that are not present in the experimental Bragg pattern, except for $Ia\bar{3}d$, which is only missing five allowed reflections. Hajduk et al. suggested the gyroid (i.e., the morphology with $Ia\bar{3}d$ symmetry) was the mesostructure that was the most consistent with their data.[34]

This analysis of the relative peak positions helped establish the space group symmetry of the gyroid morphology, but did not lead to an understanding of the detailed microdomain structure. Hajduk et al. generated a microdomain space-filling model based on Schoen's G surface[37] that is reproduced in Figure 2.5. They used this model to predict both the relative intensities of the SAXS peaks and the projections that should be obtained using TEM.[34] Analysis of the model depicted in Figure 2.5 suggests that the $\sqrt{6}$ and $\sqrt{8}$ reflections in the SAXS data should be strong and all other peaks should have low intensities; this prediction agrees with the experimental SAXS data reproduced in Figure 2.4. The simulated TEM images obtained using the model contained both 3-fold and 4-fold symmetry elements, as is characteristic of cubic morphologies. Hajduk et al. obtained TEM micrographs from the sample that agreed

with both the [111] and [100] simulated projections. The good general agreement between the predicted and experimental SAXS and TEM data suggests the model displayed in Figure 2.5 is a valid representation of the microdomain structure of the gyroid.[34]

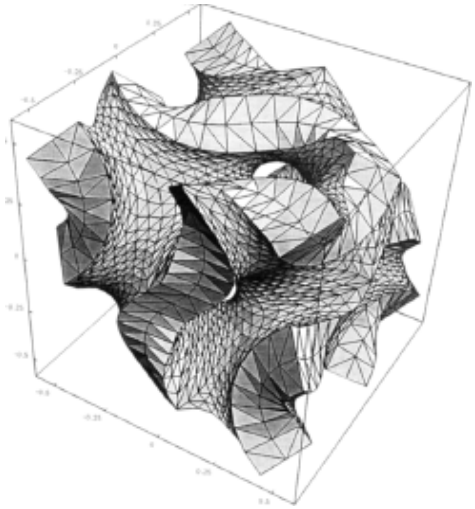

Figure 2.5. Space-filling model of the gyroid morphology proposed by Hajduk et al.[34] The model is based on Schoen's minimal gyroid surface and contains a minority volume fraction of 0.33. Reproduced from Reference 34.

Hajduk et al. noted that the gyroid mesostructure resembles the previously proposed OBDD morphology[33, 52] in a number of ways.[34] Namely, both are bicontinuous mesostructures with infinite triply periodic minimal surfaces underlying their topology. As a result, the TEM images obtained from the gyroid closely mirror those expected from the OBDD mesostructure. Hajduk et al. warned that differentiating the two morphologies on the basis of only TEM was very difficult and noted that SAXS

was integral in their identification of the gyroid.[34] One key difference between OBDD and the gyroid is the valency of the connecting elements; the OBDD mesostructure contains fourfold connectors while the gyroid contains threefold connectors.

Schulz et al. independently identified the bicontinuous gyroid mesostructure in a weakly segregated blend of PS-P2VP diblock copolymers that had an overall PS volume fraction of 0.37.[35] The PS blocks were deuterated to provide contrast for small-angle neutron scattering (SANS), an integral characterization technique employed in the study. The sample was aligned using a dynamic shearing device[62] and then quenched to room temperature to preserve the high temperature structure prior to exposure to neutrons. Rheological measurements revealed that the blend underwent an order-order transition (OOT) upon heating, with *G'* increasing by about an order of magnitude as the temperature was increased from 150 to 170 °C.[35] SANS experiments were employed to probe the morphology of the blend above and below the OOT. Data consistent with a HEX morphology were obtained from the sample sheared at 140 °C and a Bragg pattern consistent with the gyroid was acquired from the material aligned at 175 °C. Schulz et al. were able to identify epitaxial relationships between the HEX and gyroid morphologies because they investigated aligned mesostructures. (Note, the (10) ↔ (211) correspondence between the HEX and gyroid phases was mistakenly rotated by 90° in this initial paper.)[35]

These experimental investigations[34, 35] stimulated self-consistent mean field theory (SCFT) calculations reported by Matsen and Schick.[61] With this method, the free energies of various mesostructural candidates are computed for a model block copolymer with a given composition and segregation strength, ignoring fluctuation

effects. The morphology with the lowest free energy is accepted as the equilibrium phase. Matsen and Schick considered a number of mesostructural candidates, including LAM, HEX, BCC, OBDD, gyroid, and various stackings of perforated lamellae. They noted that the consideration of these morphologies was largely guided by experimental reports, and their work illustrates the benefits that arise when theoreticians and experimentalists work in concert on a problem. The initial study focused on conformationally symmetric diblock copolymers with $\chi_{AB}N$ values below 20, and the predicted SCFT phase portrait generated by Matsen and Schick is reproduced in Figure 2.6.[61] The BCC, HEX, gyroid, and LAM morphologies were predicted to be equilibrium mesostructures in this weak segregation regime, and the predicted stability range for the gyroid generally agreed with the experimental reports of Hajduk et al.[34] and Schulz et al.[35] The OBDD and perforated lamellar morphologies never produced the lowest computed free energy, although they closely competed with the equilibrium HEX, gyroid, and LAM mesostructures at some compositions and segregation strengths.[61]

Matsen and Schick subsequently utilized the same general SCFT methodology to investigate conformationally asymmetric linear diblock,[63] linear multiblock,[63] and starblock[64] copolymers. Asymmetry in the statistical segment lengths (i.e., conformational asymmetry) drives a shift in the boundaries of the phase portrait depicted in Figure 2.6 and changes the sizes of the various stability windows, but does not destabilize the gyroid or stabilize either the OBDD or perforated lamellar morphologies when the ratio of statistical segment lengths is equal to 1.5 or 2.[63] Changing the molecular architecture to linear multiblock (e.g., ABA, ABABA, etc.) or

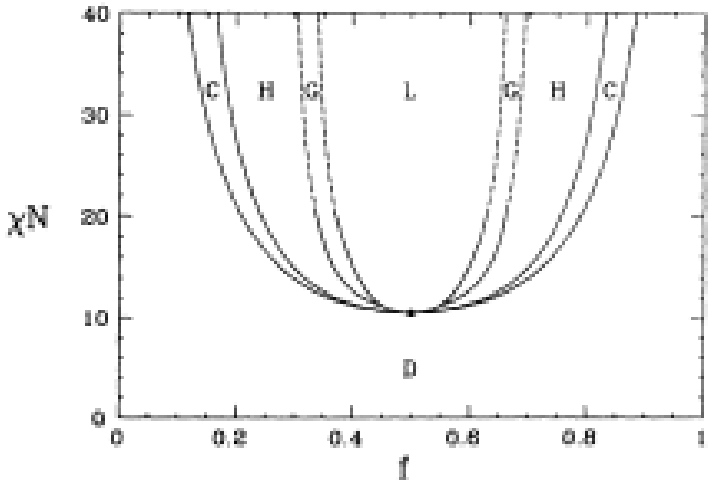

Figure 2.6. SCFT phase portrait depicting the predicted stable regions for various morphologies in conformationally symmetric linear AB diblock copolymers: (D) disordered, (L) LAM, (G) gyroid, (H) HEX, and (C) BCC. Dashed lines represent extrapolated mesostructural boundaries and the critical point is marked by a dot. The gyroid stability region does not reach the critical point, but terminates at a HEX/gyroid/LAM triple point. OBDD is not predicted to be an equilibrium phase. Reproduced from Reference 61.

starblock ($(AB)_n$ with the number of arms n = 3, 5, or 9) configurations also does not significantly alter the topology of the phase portrait; only the positions of the boundaries change, and the gyroid remains the only bicontinuous morphology predicted to be stable.[63, 64] Interestingly, Matsen and Schick predicted that the "gyroid windows" (i.e., the range of compositions at which gyroid is stable) widen as the number of arms increases, intimating that the starblock architecture could provide a means of stabilizing the bicontinuous network mesostructure.[64]

Re-examining the OBDD Morphology

The gyroid appears to be quite stable, as it is predicted to be the equilibrium bicontinuous morphology in both conformationally symmetric[61] and asymmetric[63] linear diblock, linear multiblock,[63] and starblock[64] copolymers. The calculated free energies of the OBDD and perforated lamellar morphologies are close to, but never lower than, the computed free energy of the gyroid for these weakly segregated materials.[64] Rigorous experimental analysis[34, 35] also identified the gyroid, and not OBDD, as a bicontinuous network structure in linear diblock copolymers. These results, coupled with the fact that the OBDD morphology was not predicted to be the equilibrium mesostructure for strongly segregated block copolymer materials,[52, 54] led to a reexamination of the morphological assignments of the OBDD network in the previously discussed 6-arm and 18-arm PS-PI starblock copolymers.[42] The 6-arm and 18-arm materials were annealed at 120 °C for three and eleven days, respectively, to improve long-range order, cooled to ambient temperatures, and probed using SAXS. The resulting Bragg patterns contained peaks at relative *q* positions of $\sqrt{3}$, $\sqrt{4}$, $\sqrt{10}$, and $\sqrt{11}$; Hajduk et al. suggested that, while not definitive, these relative positions were most consistent with $Ia\bar{3}d$ space group symmetry (i.e., the gyroid), and good general agreement between the experimental peak intensities and computed intensities based upon a mesostructural model supported this claim. A reversible, thermally-induced OOT from gyroid to HEX in the 6-arm material provided compelling evidence that gyroid was in fact the equilibrium morphology.[42]

Hajduk et al.'s reclassification of the OBDD mesostructure as gyroid in the starblock samples[42] led some to wonder if OBDD was ever the stable morphology for block copolymer materials. As mentioned earlier, several groups had reported the OBDD network in binary blends comprised of AB diblock copolymer and a constituent homopolymer.[47-49] Matsen theoretically interrogated this system in the weak segregation regime using SCFT and presented phase portraits for several ratios of homopolymer chain length to diblock chain length ($\alpha = N_{homo}/N_{AB}$).[65, 66] The broad features of the phase diagrams could be understood by viewing the addition of homopolymer as equivalent to an increase in the volume fraction of the constituent block,[65, 66] and the gyroid windows were comparable in size to those for the neat AB diblock copolymers that were shown in Figure 2.6.[61] Matsen did, however, predict that OBDD would be stable over very narrow ranges of composition for systems with certain values of α.[65, 66] However, since these predicted OBDD windows were so narrow, Matsen believed that previous experimental studies[47-49] had actually produced gyroid, and not OBDD. He implied that at least some[47] of these experimental materials had been reexamined and the bicontinuous structure reclassified as the gyroid.[65] Martínez-Veracoechea and Escobedo recently investigated blends of AB diblock and A homopolymer ($\alpha = 0.8$) using lattice Monte Carlo (MC) simulations and predicted that the OBDD network would be stable for some blend compositions,[67] a result in qualitative agreement with Matsen's SCFT calculations.[65, 66] Although these theoretical studies have predicted OBDD to be stable in blend systems, we are not aware of any reports definitively identifying the OBDD network mesostructure in experimental materials.

Matsen and Bates attempted to elucidate why gyroid is more stable than OBDD in nearly all block copolymer materials.[68, 69] Thomas et al. had previously proposed that interfacial tension dominated block copolymer self-assembly, with the materials adopting constant mean curvature (CMC) mesostructures to minimize interfacial area.[45] Matsen and Bates used SCFT to demonstrate that a second factor, termed "packing frustration,"[70] played an equally important role in block copolymer phase behavior.[68, 69] Packing frustration is minimized when block copolymers adopt morphologies with uniform domain thicknesses because polymer chains do not have to excessively stretch (compress) to fill space. SCFT provided Matsen and Bates with a theoretical tool to investigate the relative importance of packing frustration. Critically, unlike some other theoretical calculations,[52-55] SCFT does not require *a priori* assumptions about the shapes of domain interfaces. Rather, the chains in each mesostructural candidate adjusted their conformations (and thus the shape of the interface) to minimize free energy.[68, 69] Matsen and Bates noted that while the classical LAM, HEX, and BCC mesostructures simultaneously minimize both interfacial area (with nearly CMC interfaces) and packing frustration (with nearly uniform domain thicknesses), the complex gyroid, OBDD, and perforated lamellar phases do not. If these latter structures were to have domain interfaces described by CMC surfaces, significant variations in domain thicknesses and large degrees of packing frustration would result. The actual free energy-minimizing domain interfaces computed using SCFT deviated from these complex CMC surfaces to alleviate the packing frustration associated with nonuniform domain thicknesses. Matsen and Bates found that, of the complex mesostructural candidates, the gyroid had a calculated interfacial shape that varied the least from a

CMC surface (i.e., it had the lowest standard deviation of the mean curvature distribution) and they therefore reasoned that packing frustration considerations stabilized gyroid relative to OBDD and perforated lamellae.[68, 69] Additional support for this deduction came from SCFT calculations of AB diblock/A homopolymer blends.[65, 66] These SCFT analyses predicted that the homopolymer that was added to the minority domains in the blend preferentially filled space in the center of the domains, relieving packing frustration and stabilizing OBDD because the minority blocks no longer had to excessively stretch to fill the centers of the domains.[68] Martínez-Veracoechea and Escobedo presented a similar rationale for OBDD stabilization in their recent lattice MC investigation of AB diblock/A homopolymer blends.[67] Jinnai et al. directly measured the interfacial curvature distributions in gyroid-forming PS-PI-PS triblock copolymer materials using 3-D image reconstruction of TEM micrographs to test the SCFT prediction that gyroid mesostructures would not contain CMC interfaces.[71] They reported that the domain interfaces in the PS-PI-PS specimen did not possess CMC,[71] in support of the SCFT predictions.[68, 69]

Gyroid: an Accepted Equilibrium Bicontinuous Morphology in Block Copolymer Systems

The gyroid morphology became widely accepted as an equilibrium block copolymer mesostructure following the extensive experimental[34, 35, 42] and theoretical[61, 68, 69] publications described in the previous sections. The gyroid network has been reported in many AB diblock, AB starblock, and ABA triblock copolymer

systems, including those listed in Table 2.1. A bevy of theoretical investigations have augmented these experimental reports and concluded that the bicontinuous gyroid is a stable block copolymer mesostructure.[12, 61, 63-69, 120-129]

Table 2.1: Block copolymer systems in which the gyroid (Q^{230}) has been identified.

Block Copolymer	**Reference(s)**
starblock PS-PI	42, 119
PS-PI	11, 28, 34, 72-84
PS-P2VP	35, 85
PS-P4VP	86
PI-P2VP	79, 87
PEO-PBO	88, 89
PS-PDMS	90
PS-PLA	91
PS-PEO	91
PI-PEO	92-95
PI-PDMS	96
PEP-PEE	97, 98
PEP-PLA	99
PEP-PDMS	96, 100
PEE-PEO	98, 101-103
PEE-PE	104, 105
PE-PCHE	98
P4FS-PLA	18, 19
difluorocarbene-modified PI-PEE	106, 132
PSS-PMB	107
PFCDMS-PMMA	108
PS-PI-PS	71, 109-113
PI-PS-PI	110, 114
PS-PB-PS	115
PI-PPMDS-PI	116, 117
PS-PNIPAM-PS	118
PEO-PEE-PEO	98
PCHE-PE-PCHE	98

One aspect of the equilibrium nature of the gyroid morphology has only recently been resolved. Typically the gyroid has been identified in block copolymers with weak

to intermediate segregation strengths ($\chi_{AB}N$ < ~40),[11, 34, 35, 72, 97, 100] although a few groups[28, 33, 43, 48, 49] reported a bicontinuous mesostructure in strongly segregated block copolymer films prepared by solvent casting. It was uncertain whether the gyroid represented the equilibrium state in these materials[28, 33, 43, 48, 49] given the slow chain dynamics that are common in high molecular weight polymers. SST analyses predicted that gyroid was not an equilibrium structure,[130, 131] and SCFT calculations were not performed for the gyroid phase when $\chi_{AB}N$ > ~ 40 due to the prohibitively large number of basis functions (i.e., computational time) required to accurately evaluate the free energy of triply periodic network structures.[12, 61] Matsen and Bates posited that increased packing frustration at higher segregation strengths would destabilize the gyroid in favor of LAM or HEX when $\chi_{AB}N$ > ~60.[68, 69] They suggested that the bicontinuous mesostructures reported in the slowly solvent cast strongly segregated block copolymers[28, 33, 43, 48, 49] were metastable.[12] Davidock and colleagues tested Matsen and Bates' hypothesis[68, 69] by examining the phase behavior of difluorocarbene-modified PI-PEE diblock copolymers.[106, 132] These samples, unlike the previously investigated[28, 33, 43, 48, 49] strongly segregated block copolymers, were designed to have relatively low molecular weights and thus relatively fast chain dynamics.[106, 132] Davidock et al. reported that materials with $\chi_{AB}N$ as high as ~120 formed the gyroid, and two types of experiments provided evidence that this network was the equilibrium phase. First, the gyroid persisted following four weeks of melt-phase thermal annealing.[106] Second, metastable samples containing LAM or HEX were prepared by solvent casting from preferential solvents, and these specimens always transitioned to gyroid following thermal annealing.[132] While these reports provided convincing

experimental evidence that the gyroid is an equilibrium morphology in the limit of strong segregation,[106, 132] drawing such conclusions must be done with caution due to the difficulties associated with achieving thermodynamic equilibrium even in intermediately segregated experimental systems.[133] Cochran et al. used an improved SCFT methodology that overcame the numerical hurdles encountered by Matsen et al.[12, 61] to theoretically re-examine the stability of the gyroid in the strong segregation regime.[13] They found that the gyroid had the lowest free energy over a narrow range of compositions ($\Delta f_A \approx 0.015$) for $\chi_{AB}N$ values up to 100. Theory[13] and experiment[28, 33, 43, 48, 49, 106] are now in agreement that gyroid persists as an equilibrium morphology into the strong segregation regime, and possibly all the way to the $\chi_{AB}N = \infty$ limit.[13]

Gyroid Epitaxial Relationships

Epitaxial relationships between the gyroid and other phases had been proposed in lyotropic liquid crystals[59] prior to the identification of the gyroid in block copolymer materials.[34, 35] Schulz and colleagues were the first to discuss epitaxial relationships between the gyroid and other mesostructures in block copolymer materials.[35] They investigated shear-aligned HEX mesostructures that directly transformed to gyroid upon heating and identified epitaxial relationships between the HEX and gyroid morphologies using SANS data.[35] The correspondence between the (10) lattice plane in the HEX morphology and the $(1\,\bar{2}\,1)$ cubic plane controlled the orientation of the gyroid that was grown from the aligned HEX mesostructure.[72]

A number of subsequent investigations have focused on the transition mechanisms and epitaxial relationships between gyroid and the LAM and HEX morphologies.[72, 77, 81, 85, 92, 93, 100, 103, 134-139] Förster et al. identified epitaxial relationships between the equilibrium gyroid and the metastable hexagonally perforated lamellar (HPL) mesostructure.[72] HPL may appear as an intermediate state during the ordering of gyroid from a disordered melt[137] or in morphological transitions between the gyroid and LAM morphologies[103] Matsen used SCFT to examine the Landau free energy surface of a diblock copolymer melt.[134] A low-energy pathway connecting the gyroid and HEX mesostructures was reported, and the calculated evolution between two morphologies is provided in Figure 2.7. The computed energy barriers and stability limits implied that the gyroid-to-HEX morphological transition proceeds by a nucleation and growth mechanism,[134] a prediction validated by subsequent experiments.[93, 100, 135] Gyroid does not always grow directly from the HEX morphology, however; the HPL mesostructure may appear as an intermediate state during this morphological transition.[135, 136]

2.3 Network Morphologies formed by Multiblock Terpolymers

The phase behavior of AB diblock copolymers was generally understood by about 1995. Both experimentalists[11] and theoreticians[61] presented the equilibrium

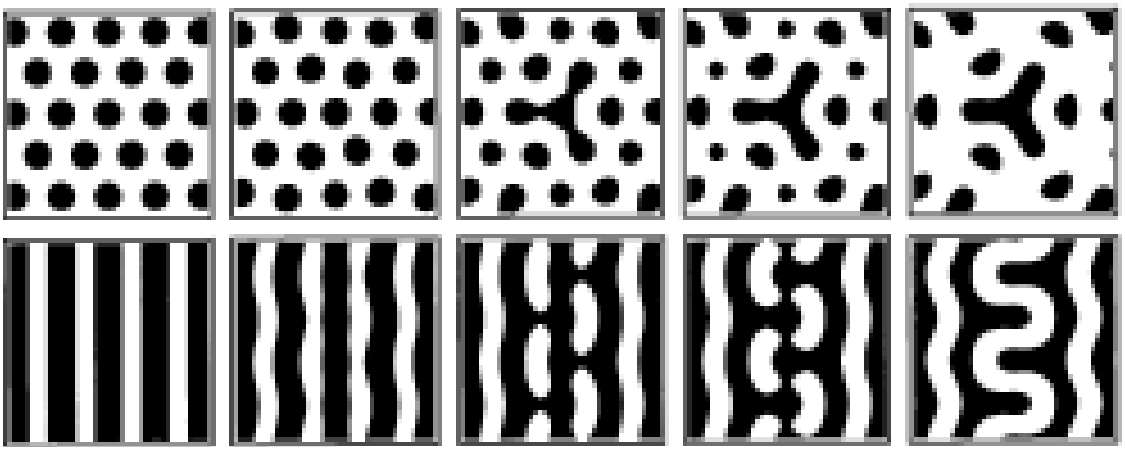

Figure 2.7. Calculated pathway for the evolution of HEX into the gyroid. Here black represents the minority A domain (f_A = 0.35). The horizontal axes are oriented in the $[1\bar{1}0]$ direction and the vertical axes are oriented in the [111] (bottom panel) and $[11\bar{2}]$ (top panel) directions. Figure reproduced from Reference 134.

morphologies formed by block copolymers on a "universal" phase portrait with the composition (f_A) as the abscissa and the segregation strength ($\chi_{AB}N$) of the material as the ordinate, and generally good agreement existed between theoretical predictions and experimental results. In contrast, no such "universal" understanding exists for linear ABC triblock terpolymers. (Note that "triblock" describes the number of blocks in the polymer chain while "terpolymer" means the material contains three chemically distinct repeat units.) There are more molecular variables in ABC triblock systems than in AB diblock sytems, including two independent composition variables, three χ_{ij}'s (χ_{AB}, χ_{BC}, χ_{AC}), three statistical segment lengths (b_A, b_B, b_C), and three distinct block sequences (ABC, ACB, BAC). This increased number of molecular variables results in more complex phase behavior, and more than 30 distinct mesostructures have been identified

in the ABC triblock terpolymer literature.[140] Included amongst these triblock morphologies are a number of multiply continuous network mesostructures that are the focus of this section.

Ordered Tricontinuous Double Diamond (OTDD)

Mogi and coworkers authored the first reports describing a multiply continuous network structure in ABC triblock terpolymers in 1992.[141-143] They prepared a series of PI-PS-P2VP triblock terpolymers with narrow molecular weight distributions (PDI $\leq$ 1.05) and roughly equivalent PI and P2VP volume fractions, but different lengths of middle PS chains.[141] PI-PS-P2VP triblock terpolymers have roughly symmetric interfacial tensions and a large enthalpic incompatibility between the terminal blocks (i.e., $\chi_{IV} > \chi_{IS} \approx \chi_{SV}$);[144] Bailey et al. described block terpolymers with this block sequence as "nonfrustrated,"[145] and we will use this terminology in this review. Mogi et al. characterized solvent cast and annealed films of PI-PS-P2VP triblock terpolymers using TEM. The polymers containing PS volume fractions of 0.48 to 0.66 formed the same mesostructure, and representative TEM micrographs of this morphology are provided in Figure 2.8.[142] Mogi et al. suggested, on the basis of the agreement between the experimental and simulated micrographs provided in Figure 2.8, that this mesostructure was an ordered tricontinuous double diamond (OTDD) morphology.[142] The model of this postulated OTDD network is a three domain analog of the OBDD morphology;[33, 38, 40, 43] it consisted of cylindrical struts connected by fourfold connectors and contained two chemically distinct interpenetrating networks,

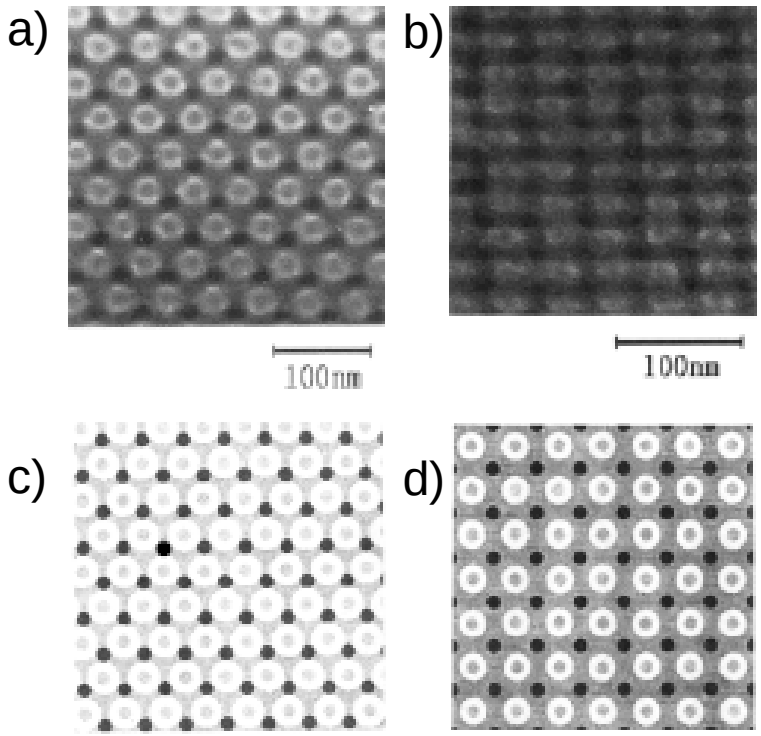

Figure 2.8. a, b) Representative TEM micrographs obtained from PI-PS-P2VP triblocks with PS volume fractions ranging from 0.48 to 0.66. The polymer samples were stained with OsO_4, and the black, white, and gray images correspond to domains rich in PI, PS, and P2VP, respectively. Mogi et al. suggested that these images were consistent with the a) [111] and b) [001] projections of an order tricontinuous double diamond (OTDD) network containing independent interpenetrating domains of PI and P2VP in a PS matrix. c, d) Simulated TEM images corresponding to the c) [111] and d) [001] projections. These simulated micrographs were obtained using a model comprised of cylindrical struts and fourfold connectors. Images reproduced from Reference 142.

one comprised of PI and the other of P2VP, in a PS matrix.[142] Mogi et al. noted a shortcoming of the proposed OTDD model. Namely, the OTDD model suggested that a 55° rotation of the sample should result in a transition between the [111] and [001] projections, and this transition was never identified in TEM experiments in which the sample was tilted 55°.[142] Mogi et al.'s study is particularly notable because it established that multiply continuous network morphologies could persist over much broader ranges of compositions in ABC triblock terpolymers than they do in AB diblock copolymers. The network mesostructure formed in the PI-PS-P2VP materials over a range of ~0.18 in the PS volume fraction,[142] while the gyroid only occurs over a volume fraction range of ~0.04 in AB diblock copolymers.[11]

Revisiting OTDD and the Alternating Gyroid (Q^{214})

Mogi et al.'s series of publications[141-143] catalyzed many investigations of multiply continuous network morphologies in block terpolymers. Several theoretical studies directly built upon Mogi et al.'s work and focused on "symmetric" (i.e., equal volumes of A and C domains) ABC triblock terpolymers.[144, 146-148] Both Matsen[144] and Phan and Fredrickson[146] suggested that, given the initial misidentification of the gyroid as OBDD in block copolymer systems,[42] the OTDD should be accepted as an equilibrium morphology with caution.[144, 146] Phan and Fredrickson extended the theoretical approaches of Likhtman and Semenov[53] and Milner et al.[54, 55, 149] from AB diblocks to ABC triblocks and investigated "symmetric" ABC triblock terpolymers in the SSL.[146] Two network morphologies were considered in this study: OTDD and an

alternating gyroid with $I4_132$ symmetry (Q^{214}, with "214" being the number of the space group[44]). Q^{214}, like OTDD, contains two chemically distinct, interpenetrating lattices. The valencies of the connectors in these lattices are different, however; OTDD contains fourfold connectors while Q^{230} has threefold connectors. Phan and Fredrickson constructed approximate representations of the OTDD and Q^{214} domain interfaces and computed the free energies of these networks and a number of other mesostructural candidates.[146] The equilibrium morphology was predicted to change from BCC to tetragonally packed cylinders to LAM as the combined volume fraction of the terminal A and C blocks was increased from 0 to 0.4. While Q^{214} always had a lower computed free energy than OTDD, neither of these networks was predicted to be the equilibrium mesostructure for any of the investigated compositions. Phan and Fredrickson suggested Q^{214} could become stable for intermediate segregation strengths and, since it was always stable relative to OTDD in their calculations, they suggested Mogi et al.'s assignment[141-143, 150] of OTDD should be revisited, with Q^{214} being considered as an alternative.[146]

Dotera and Hatano developed a diagonal bond method based on the Verdier-Stockmayer model[151] to perform MC simulations on block copolymer melts.[147, 148] This method has the benefit of not requiring the selection of mesostructural candidates (i.e., simulations progressed from a random initial configuration), although it does rely on the selection of unit cell dimensions. A series of "symmetric" ABC triblock terpolymers encompassing the OTDD "window" reported by Mogi et al.[141] were "annealed" in the MC simulations from random initial configurations.[147, 148] A twice-periodic strategy was utilized to minimize metastability effects related to the simulation box size, and Q^{214},

and not OTDD, was predicted to be the equilibrium morphology over the composition range $0.14 < f_A < 0.23$.[148]

Matsen used a spectral implementation of SCFT to interrogate the phase behavior of "symmetric" ($b_A = b_B = b_C$ and $\chi_{AB} = \chi_{BC} = \chi$) ABC triblock terpolymers in the intermediate segregation regime ($\chi N < 65$).[144] These ABC triblocks can be characterized by three parameters: the volume fraction of one of the terminal blocks (f), χN, and χ_{AC} / χ.[144] Matsen determined that, for compositions with $f \leq 0.3$, the morphology selection is not sensitive to either the χ_{AC} / χ ratio or χN, and the equilibrium mesostructure was largely selected based on the composition of the triblock terpolymer. BCC spheres, hexagonally and tetragonally packed cylinders, Q^{214}, OTDD, and LAM were considered as mesostructural candidates in the SCFT calculations. The sequence of equilibrium morphologies was predicted to be BCC spheres → tetragonally packed cylinders → Q^{214} (for $0.145 \leq f \leq 0.198$ when $\chi N = 50$) → LAM with increasing f. Matsen noted that this sequence was analogous to that predicted in AB diblock copolymers (see Figure 2.6), with a tetragonally packed cylinders replacing HEX due to packing frustration. This packing frustration also reduces the width of the cylinder window and, consequently, widens the network window in ABC triblocks relative to AB diblocks.[144]

OTDD, like OBDD in diblock copolymers, never had the lowest computed free energy in SCFT.[144] Matsen posited that a minimization of packing frustration drives ABC triblock terpolymers to form Q^{214}, and not OTDD, much like it drove ABA triblock copolymers to adopt the gyroid with $Ia\bar{3}d$ symmetry,[109, 110] and not OBDD.[144] The SCFT predictions were in excellent agreement with Dotera and Hatano's MC

simulations[147, 148] and contained many of the same features as Phan and Fredrickson's SST results.[146] Approximations in the SST involving chain trajectories and the shape of internal interfaces[146] may account for the fact that SCFT[144] and MC simulations[147, 148] identified Q^{214} as an equilibrium structure, but SST did not.[144] Matsen also re-examined some of Mogi et al.'s experimental data[142] obtained from the network-forming PI-PS-P2VP materials. He argued in detail that the simulated Q^{214} projections more closely matched the experimental micrographs, including those obtained by tilting the TEM specimen, than the simulatd OTDD images did.[144]

Matsushita et al., independent of Matsen,[144] reconsidered the OTDD assignment in the PI-PS-P2VP triblock terpolymer system.[152-155] They generated model unit cells in which the domain interfaces were parallel surfaces to the either the gyroid or diamond minimal surface. These constructions illustrated how blocks could fill space with a given space group symmetry, but, unlike SCFT results, did not have any connection to the statistical mechanics of the individual chains. Matsushita et al. used these space-filling models to simulate the TEM projections that would be obtained from samples with varying thicknesses. When film thickness was considered, the simulated images from the Q^{214} model matched the experimental TEM micrographs acquired from three PI-PS-P2VP specimens ($f_I = f_V = 0.26$,[152-154] $f_I = 0.20$, $f_V = 0.14$,[154] and $f_I = 0.22$, $f_V = 0.19$[155]), much better than did the predicted OTDD projections. Matsushita and colleagues also utilized the space-filling models to predict the intensities of SAXS peaks from the Q^{214} morphology.[153-155] The predicted intensities of the allowed reflections qualitatively agreed with experimental data obtained at three different compositions ($f_I = f_V = 0.26$,[153, 154] $f_I = 0.20$, $f_V = 0.14$,[154] and $f_I = 0.22$, $f_V = 0.19$[155]),

corroborating the TEM analysis and further supporting the change in the assignment of the tricontinuous mesostructure from OTDD to Q^{214}.[153, 154]

The OTDD network was also reported in a PS-PI-P2VP triblock terpolymer sample.[150] The mesostuctural assignment of OTDD in the PS-PI-P2VP system was made by finding good general agreement between simulated TEM images and experimental micrographs.[150] This PS-PI-P2VP specimen is similar to the network-forming PI-PS-P2VP samples[141, 142] in terms of the compositions of the middle and terminal blocks, but, as pointed out by Matsen,[144] the PS-PI-P2VP sequencing does not yield symmetry in the A/B and B/C interfacial tensions. Matsen questioned the OTDD assignment, and suggested that no indication of minority domain continuity was present in the experimental TEM micrographs. He speculated, based on Zheng and Wang's theoretical investigation[156] of triblock terpolymers with asymmetric interfacial tensions, that the reported OTDD morphology in the PS-PI-P2VP specimen[150] was in fact a BCC sphere mesostructure.[144] To our knowledge this OTDD assignment has not been revisited experimentally. Given the reclassification of the OTDD network in PS-PI-P2VP triblocks,[152-155] the reported identification[150] of OTDD in the PS-PI-P2VP sample should be accepted with caution.

The reassignment of the tricontinuous morphology formed by PI-PS-P2VP triblock terpolymers from OTDD to Q^{214} in many ways paralleled the change in the accepted identity of the bicontinuous network structure commonly formed by block copolymers from OBDD to gyroid. The initial OBDD[33] and OTDD[142] assignments were both made primarily using TEM micrographs and did not include definitive scattering data or theoretical support for the identification of the diamond mesostructures. While

TEM is a very powerful and useful characterization technique, interpreting the two-dimensional projections of an inherently three-dimensional structure is very difficult.[34] In both the OBDD and OTDD cases, scattering (either X-ray or neutron) data[34, 35, 153, 154] and SCFT calculations[61, 144] were crucial corroborative elements used to correctly interpret the experimental data and identify the gyroid (Q^{230}) and Q^{214} morphologies.

Several investigations of Q^{214} followed Matsushita et al.'s definitive identification[152-155] of Q^{214} in the PI-PS-P2VP materials. Suzuki and coworkers focused on the mechanism driving the Q^{214} morphology to preferentially oriented with [110] normal to the film surface in solvent cast films of PI-PS-P2VP.[157] A PI-PS-P2VP triblock sample ($f_I = f_V = 0.26$) was solvent cast from THF and the morphology of the polymer film was probed using a combination of TEM and synchrotron SAXS following various lengths of thermal annealing times at 150 °C. The as-cast PI-PS-P2VP specimen contained a lamellar mesostructure oriented with [110] normal to the film surface. Subsequent annealing at 150 °C drove a morphological transition, over a period of two days, to a Q^{214} network that was, according to the analysis of two-dimensional SAXS data, oriented in the same manner as the lamellae. Suzuki et al. suggested that the metastable lamellar morphology formed with [110] normal to the film surface as a result of the affinity between the P2VP block and the teflon substrate on which the film was cast. Since the stable Q^{214} retained this orientation, the process of solvent casting and subsequent thermal annealing could generally be used to prepare polymer films containing oriented network mesostructures.[157]

Epps and Cochran et al. investigated PI-PS-PEO triblock terpolymers over a wide range of compositions.[158, 159] PI-PS-PEO triblock terpolymers, like PI-PS-P2VP

samples,[144] have symmetric interfacial tensions and are "nonfrustrated" (i.e., $\chi_{IO} > \chi_{IS} \approx \chi_{SO}$).[160] The melt-phase morphologies of PI-PS-PEO materials were probed using a combination of synchrotron SAXS, TEM, dynamic mechanical spectroscopy (DMS), and static birefringence. This thorough characterization process identified Q^{214} in seven samples along two different isopleths: (i) $f_I / f_S = 0.64$, $0.14 < f_O < 0.18$ (ii) $f_I / f_S = 0.45$, $0.17 < f_O < 0.29$.[158, 159] This Q^{214} composition "window" is broadly consistent with Matsen's calculations[144] and Matsushita et al.'s PI-PS-P2VP investigations,[141-143, 152-155] although Q^{214} is stable in more asymmetric materials in the PI-PS-PEO system than in the PI-PS-P2VP materials, possibly due to differences in the statistical segment lengths of the PEO and P2VP chains.[158, 159] The PI-PS-PEO system will be discussed in more detail later in this review.

Core-Shell Gyroid (Q^{230})

Q^{214} topologically resembles the gyroid morphology identified in AB block copolymers in that it contains two independent, interpenetrating domains embedded in a matrix. The two morphologies have different space groups, however, because the two interpenetrating domains are chemically distinct in Q^{214} ($I4_132$) but chemically identical in the gyroid ($Ia\bar{3}d$). One could envision that a block terpolymer could also form a core-shell version of the gyroid structure with $Ia\bar{3}d$ symmetry, with two chemically identical interpenetrating networks that are comprised of cores of C encased in shells of B and embedded in a matrix of A blocks. Core-shell versions of the HEX and BCC morphologies had been reported in block terpolymer systems,[140] and there was no

reason an analogous version of the gyroid could not be formed. Two groups independently and almost simultaneously identified the core-shell gyroid (Q^{230}) morphology with $Ia\bar{3}d$ symmetry in block terpolymer systems in 1999.[16, 161]

Shefelbine et al. synthesized a PI-PS-PDMS triblock terpolymer (f_I = 0.40, f_S = 0.41) and interrogated its melt-phase morphology using a combination of SAXS, SANS, TEM, and static birefringence.[16] PI-PS-PDMS triblocks are "frustrated,"[145] as the PS and PDMS blocks have the largest χ parameter (χ_{SD} = 0.12, χ_{ID} = 0.09, and χ_{IS} = 0.033 at 150 °C)[16] and they are required by chain connectivity to form an interface. The PI-PS-PDMS polymer powder was heated to 200 °C and subjected to large amplitude oscillatory shear to reduce mesostructural defects and facilitate the formation of large grains. Both the sheared sample and unsheared powder were nonbirefringent, an indication that the morphology formed by the PI-PS-PDMS triblock had cubic symmetry. X-rays were passed, at ambient temperature, through the sheared material in all three directions orthogonal to the sample surfaces (see schematic in Figure 2.9). Discrete spots, and not continuous rings, were present in these Bragg patterns, indicating relatively large mesostructural grains were present in the sheared PI-PS-PDMS specimen. These 2-D SAXS data are provided in Figure 2.9. Shefelbine et al. considered all of the cubic space groups as candidates when fitting these data. Space groups with *F* symmetry were eliminated from consideration because those groups do not allow the 211 reflections present in the data in Figure 2.9, while all space groups with *P* symmetry and most with *I* symmetry were ruled out because a large number of reflections consistent with the space groups were not present in the SAXS data. Shefelbine et al. reported that, while both the radial positions and relative angular

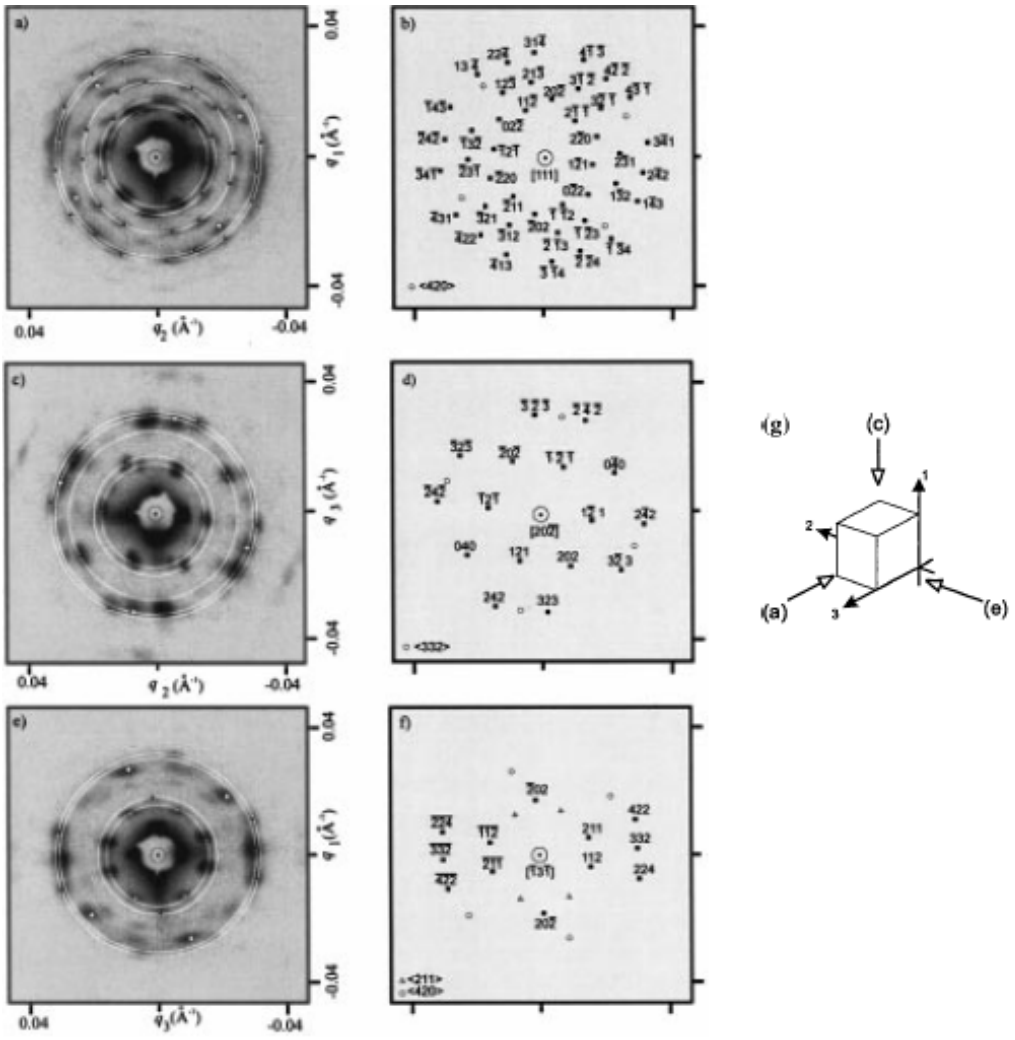

Figure 2.9. SAXS diffraction patterns obtained from a sheared sample of PI-PS-PDMS. SAXS data (a, c, e) are presented next to the indexing scheme (b, d, f) for each orientation. All peaks are indexed to Q^{230}. The black squares mark the expected peak positions in a "single-crystal" pattern while the open circles and triangles connote out-of-plane reflections that are consistent with twinning (i.e., the sample contains multiple grains of Q^{230} oriented in different directions). g) Schematic illustrating the orientations at which the SAXS data were obtained. Reproduced from Reference 16.

positions of all of these reflections are consistent with a Q^{230} mesostructure, a morphology with $I\bar{4}3d$ symmetry could not be ruled out solely on the basis of scattering data.[16]

TEM was used to examine how the PI-PS-PDMS microdomains filled space and to try to distinguish between the two possible space group symmetries.[16] Micrographs consistent with a Q^{230} mesostructure were acquired from PI-PS-PDMS samples in both their native state and following staining with OsO_4. Shefelbine et al. did not yet rule out a mesostructure with $I\bar{4}3d$ symmetry, however,[16] given the difficulties associated with interpretation of TEM images from multiply continuous morphologies.[34] Rather, they augmented their experimental analysis with SCFT calculations. The segment distributions for a Q^{230} network were computed and used to predict the intensities of SAXS and SANS peaks. The predicted scattering intensities generally matched the experimental SAXS and SANS data, with the predictions even capturing the extinctions of the first two peaks in the SANS data.[16] The computed segment distributions were also used to simulate the projections expected in TEM experiments. Excellent agreement was found between predicted projections and experimental micrographs for both the unstained and stained materials. Shefelbine et al. concluded, on the basis of all of these results, that their PI-PS-PDMS triblock terpolymer had formed a pentacontinuous Q^{230} morphology with two discrete domains of PDMS cores, two separate domains of PS shells, and a PI matrix. They noted that this mesostructure made intuitive physical sense, as the area of the enthalpically costly PS/PDMS interface was smaller than that of the less costly PI/PS interface because the PDMS occupied the

cores of the interpenetrating networks. It was intimated that the Q^{230} network persisted over a relatively narrow range of compositions in the PI-PS-PDMS system.[16]

At approximately the same time as Shefelbine et al.'s paper[16] appeared, Goldacker and Abetz detailed their morphological investigation of binary blends of PS-PB-PtBMA triblock terpolymers (f_S = 0.33, f_B = 0.37) and PB-PtBMA diblock copolymers (f_B = 0.58).[161] While these ABC/BC blends were initially targeted to produce non-centrosymmetric lamellae,[162] Goldacker and Abetz reported that PS-PB-PtBMA / PB-PtBMA blends with a PB-PtBMA volume fraction of 0.22 predominantly formed a Q^{230} morphology. This network assignment was made by comparing TEM micrographs to simulated [110] and [112] projections of a Q^{230} mesostructure comprised of two interpenetrating networks of PS that are encased in shells of PB and embedded in a matrix of PtBMA. Notably the microtomed slices used in the TEM analysis had a thickness less than that of a single Q^{230} unit cell. As a result, the experimental micrographs contained, due to variations in the film thickness, a near-continuum of projections that represented the same projection viewed through different fractions of the Q^{230} unit cell.[161] This experimental feature allowed for a more definitive morphology assignment than is typical of TEM analyses.[152] Goldacker and Abetz hypothesized that the increase in PB / PtBMA junction points resulting from the addition of the PB-PtBMA diblock to the PS-PB-PtBMA triblock increased the chain crowding at the PB / PtBMA interface and drove a morphological transition from lamellae to Q^{230}.[161]

Many reports[145, 158, 159, 163-168] of the pentacontinuous Q^{230} morphology followed the two initial publications[16, 161] identifying the network mesostructure. Hückstädt and

coworkers investigated the melt-phase morphologies of linear PS-PB-P2VP triblock and heteroarm PS-PB-P2VP starblock terpolymers using TEM.[163] The linear PS-PB-P2VP sample (PS wt% = 0.48, PB wt% = 0.31), like Shefelbine et al.'s PI-PS-PDMS material,[16] is frustrated ($\chi_{BV} > \chi_{BS} \approx \chi_{SV}$) and has a terminal block that comprises ~20% of the volume of the polymer.[163] Analysis of the experimental and simulated TEM micrographs led to the identification of a Q^{230} network containing P2VP cores, PB shells, and a PS matrix in the linear PS-PB-P2VP specimen. Hückstädt et al. intimated that Q^{230} persisted over a narrow range of compositions. The PS-PB-P2VP starblock sample (PS wt% = 0.14, PB wt% = 0.37), unlike the linear PS-PB-P2VP triblock, contained multiple morphologies. Hückstädt et al. compared experimental TEM micrographs obtained from samples that contained various fractions of a unit cell with simulated projections through various fractions of a unit cell and concluded that a minority of the PS-PB-P2VP starblock sample contained a Q^{230} network. The "shell" in this starblock Q^{230} morphology must, as a result of chain connectivity, be a mixed domain. Notably, the interpenetrating networks in this Q^{230} morphology were largely comprised of P2VP and had a volume fraction (> 0.45) larger than is typically obtained in gyroid mesostructures formed by materials with linear architectures. Hückstädt et al. offered several hypotheses to account for this feature of Q^{230} in the starblock sample.[163]

Bailey et al. investigated the melt-phase morphological behavior of another frustrated triblock terpolymer system, PS-PI-PEO triblock terpolymers ($\chi_{IO} > \chi_{IS} \approx \chi_{SO}$).[145] Ten neat PS-PI-PEO triblock samples with $0.03 < f_O < 0.33$ were synthesized from a parent PS-PI-OH diblock with $f_I \approx f_S$. In addition, thirteen PS-PI-PEO specimens with intermediate compositions were prepared by blending consecutive pairs (to

minimize polydispersity effects) of neat PS-PI-PEO triblocks. The mesostructures of these 24 intermediate and weakly segregated materials were probed using a combination of rheological measurements, SAXS, and TEM. This complement of experimental data allowed Bailey et al. to identify pentacontinuous Q^{230} in four PS-PI-PEO samples (a neat triblock and three blends) with $0.19 < f_O < 0.23$; representative SAXS and TEM data are provided in Figure 2.10.[145] The range of compositions over which Q^{230} persists in the PS-PI-PEO samples includes the composition of the Q^{230}-forming PI-PS-PDMS material reported by Shefelbine et al.;[16] these two frustrated ABC systems have a comparable sequence of χ parameters ($\chi_{BC} > \chi_{AB} \sim \chi_{AC}$).[145] All of the Q^{230}-forming PS-PI-PEO materials underwent an OOT from Q^{230} to core-shell cylinders upon heating. While this transition was reversible, the formation of Q^{230} upon cooling exhibited significant hysteresis. Bailey et al. investigated the hysteresis at a variety

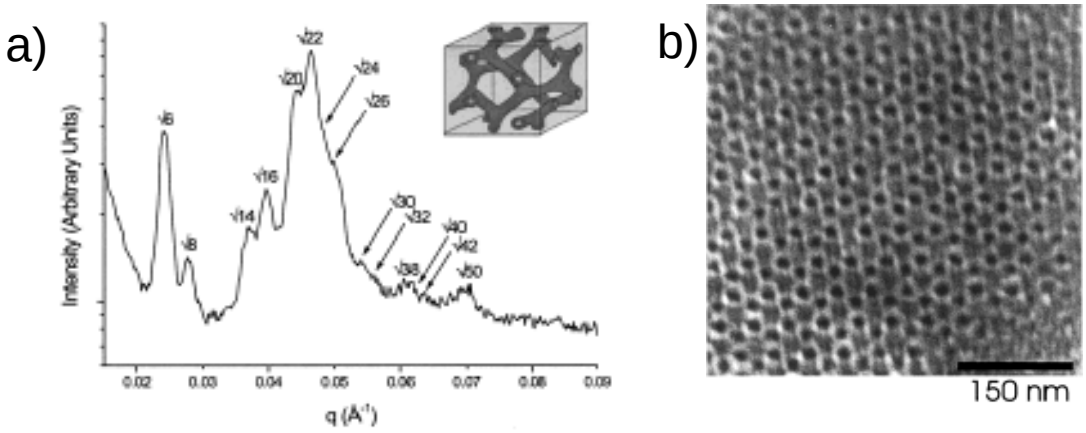

Figure 2.10. Data acquired from a PS-PI-PEO sample with $f_O = 0.21$. a) SAXS data obtained at 180 °C. The first 14 reflections allowed for Q^{230} are marked. b) TEM micrograph corresponding to the [111] projection of Q^{230}. Figure reproduced from Reference 145.

of cooling/quenching rates and reported a complex kinetic rate dependence, with some PS-PI-PEO materials requiring more than 12 hours of thermal annealing to reach an (presumably) equilibrium Q^{230} morphology. The core-shell cylinder-to-Q^{230} transition likely occurred through a rearrangement process that resulted in the formation of a metastable semiperforated lamellar intermediate.[145]

Sugiyama and colleagues studied a variation of the triblock terpolymer system investigated by Shefelbine et al;[16] the materials contained the same PI, PS, and PDMS components but the block architecture was changed from the frustrated PI-PS-PDMS sequence to the nonfrustrated PS-PI-PDMS arrangement.[164] Sugiyama et al. synthesized a PS-PI-PDMS triblock terpolymer (M_n = 42 kg/mol, f_S = 0.20, f_I = 0.59) and subsequently solution blended it in toluene with various equal volume fractions of PS (M_n = 2.4 kg/mol) and PDMS (M_n = 2.2 kg/mol) homopolymers. SAXS, SANS, and TEM measurements were used to interrogate the morphologies of the samples. Sugiyama et al. reported that the neat PS-PI-PDMS triblock specimen formed a complex mesostructure, but they were unable to ascertain its exact state of order;[164] Epps and Cochran et al. later suggested this morphology was actually O^{70} (see next section for a description of this multiply continuous network mesostructure).[159] Q^{230} was identified in blends containing an overall homopolymer volume fraction ranging from 0.15-0.45 ($0.25 < f_S$ (f_D) < 0.34). Sugiyama et al. suggested that the slight asymmetry in χ parameters ($\chi_{SI} < \chi_{ID}$) led to the formation of core-shell morphologies (Q^{230} and core-shell cylinders) in the PS-PI-PDMS system.[164] Hardy et al. expanded upon this work by investigating a variety of weakly segregated triblock terpolymer

materials with segment volume fractions near 0.33, including frustrated PI-PS-PDMS triblocks, nonfrustrated PS-PI-PDMS triblocks, and blends of PI-PS-PDMS and PS-PI-PDMS triblock terpolymers with varying intermediate amounts of frustration.[165] The morphologies of these materials were characterized using a combination of DMS, SAXS, and SANS measurements. While the neat triblock samples adopted cylindrical or LAM morphologies, several blends with intermediate levels of frustration adopted a Q^{230} mesostructure, as evidenced by SAXS reflections with a relative spacing of $\sqrt{6}\,q^*$ to $\sqrt{8}\,q^*$ and an intensity ratio of 10:1. Hardy et al. suggested, based on the 10:1 intensity ratio, that the PI and PS chains formed a mostly mixed domain in this gyroid morphology. They noted that the composition near the PDMS interface (i.e., a thin "shell") must, due to chain connectivity, depend on the relative amounts of the PI-PS-PDMS and PS-PI-PDMS chains in the blend. It was hypothesized that changing this interfacial composition altered the interfacial tension and drove the morphological transition to the Q^{230} mesostructure. These results demonstrated that frustration effects can be used to manipulate the state of order of triblock terpolymer materials with the same overall chemical composition and molecular weight.[165]

Epps and Cochran et al. identified Q^{230} during their aforementioned thorough investigation of the nonfrustrated PI-PS-PEO system.[158, 159] Definitive SAXS data, complemented by TEM, DMS, and static birefringence measurements, led to the identification of Q^{230} in six samples along two different isopleths: (i) $f_I / f_S = 1.38$, $0.14 < f_O < 0.20$ (ii) $f_I / f_S = 1.27$, $0.11 < f_O < 0.20$.[158, 159] Chatterjee et al. expanded the investigation of the PI-PS-PEO system to PEO-rich specimens and identified Q^{230} in six

PEO-rich samples.[166] The PI-PS-PEO system will be discussed in more detail in the following sections.

The pentacontinuous Q^{230} with the familiar $Ia\bar{3}d$ space group symmetry has been reported in both frustrated[16, 145, 163] and nonfrustrated[158, 159, 161, 164, 166-168] triblock terpolymer systems. In addition, the Q^{230} mesostructure was reported in blends containing both frustrated PI-PS-PDMS and nonfrustrated PS-PI-PDMS components.[165] Clearly, many block copolymer and block terpolymer materials can minimize the overall free energy by forming a structure with $Ia\bar{3}d$ symmetry. This fact renders the gyroid something of a universal network mesostructure, albeit one whose precise phase boundaries are sensitive to the block sequence, χ values, and block statistical segment lengths.

O^{70}, the Orthorhombic *Fddd* Network

The previous two sections demonstrated that a number of groups[16, 141-143, 145, 152-155, 161, 163-165] had, by 2002, identified multiply continuous network morphologies in block terpolymer systems. The associated publications did not, however, establish a systematic framework for preparing network-forming materials.[169] Bailey set out to establish this sort of systematic approach, and first noted that symmetric diblock copolymers form LAM with flat interfaces. He surmised that an ABC triblock with equivalent block volume fractions (prepared by adding a similarly sized third block to a symmetric AB diblock) and roughly symmetric interfacial tensions ($\chi_{AB} \approx \chi_{BC}$) would form a LAM morphology with two flat interfaces (A/B and

B/C), provided there was no thermodynamic driving force for the formation of an A/C interface (i.e., provided $\chi_{AC} \gg \chi_{AB}, \chi_{BC}$). He suggested that ABC triblocks with intermediate, asymmetric compositions, would have packing frustrations that would best be accommodated by the hyperbolic interfacial surfaces (i.e., saddle surfaces) of network morphologies.[169] A cartoon illustrating this strategy is provided in Figure 2.11.

Bailey and colleagues selected PI-PS-PEO triblock terpolymers as the model system to test this hypothesis.[170] This system was chosen for several reasons. First, PI-PS-PEO triblock terpolymers are nonfrustrated ($\chi_{IO} > \chi_{IS} \approx \chi_{SO}$) and formation of PI/PEO interfaces is not enthalpically preferred. Thus, only the PI/PS and PS/PEO interfaces required by chain connectivity should form, and Bailey et al. hoped to use these competing interfaces to drive network formation. Second, the magnitudes of the

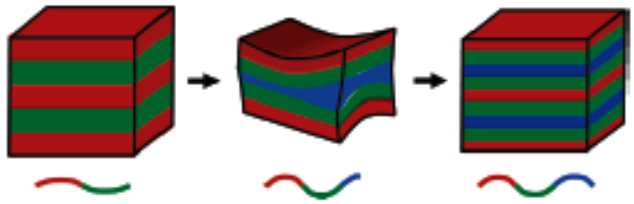

Figure 2.11. A cartoon illustration of Bailey et al.'s strategy for inducing network formation in nonfrustrated ABC triblock terpolymers with symmetric interfacial tensions. The left and right structures depict the flat interfaces preferred by samples with symmetric compositions. The middle polymer contains an intermediate length of the terminal C chains. It was hypothesized that this intermediate chain length would destabilize the flat interfaces, leading the saddle surfaces and network morphologies.[159] Reproduced from Reference 159.

χ parameters placed the order-disorder transition temperatures (T_{ODT}'s) at experimentally tractable temperatures when the molecular weight ranged from ~15 – 25 kg/mol. These chain lengths were convenient for experimental characterization while also being long enough to permit comparison with SCFT. Finally, the PI-PS-PEO system was synthetically tractable, as many PI-PS-PEO triblock samples could be prepared from a single parent PI-PS-OH diblock. This synthetic methodology minimized variation across triblock specimens, with only the length of the O blocks being altered. Thirteen PI-PS-PEO samples with $0 < f_O < 0.34$ were synthesized from a parent PI-PS-OH diblock (M_n = 13.6 kg/mol, $f_I \approx f_S$).[170] The melt-phase morphologies of these materials were probed using DMS, SAXS, TEM, static birefringence, and differential scanning calorimetry (DSC). As expected, lamellar mesostructures were reported for samples in two different regimes: (i) short terminal PEO chains ($f_O < 0.10$) or (ii) approximately equal volume fractions in each of the three domains ($0.27 < f_O < 0.34$). Bailey et al. classified the mesostructures formed by the low PEO-content (i) materials as two-domain lamellae (LAM_2), with the short PEO chains mixing with the segment in the PS domain. The morphologies adopted by the PEO-rich materials were called three-domain lamellae (LAM_3), as striped domains rich in each of the three components were identified.[170]

Characterization data that were not consistent with LAM mesostructures were acquired from six samples with intermediate compositions ($0.13 < f_O < 0.24$). The non-lamellar symmetry of this mesostructure is readily apparent upon inspection of the TEM micrographs provided in Figure 2.12. Bailey et al. reported that both of these images were frequently observed during their TEM analysis and concluded that these

micrographs represent different directional orientations of the same structural element.[170] These micrographs resemble those acquired from gyroid-forming materials, but do not contain any regions with true threefold or fourfold symmetries.[159] Additionally, lab-source SAXS data were not consistent with either Q^{230} or Q^{214}.[170]

Bailey et al. utilized a systematic approach to elucidate the symmetry of this unknown mesostructure. DSC measurements were deployed to probe the percent crystallinity of the PEO block. The crystallinity was negligible for short PEO chains,

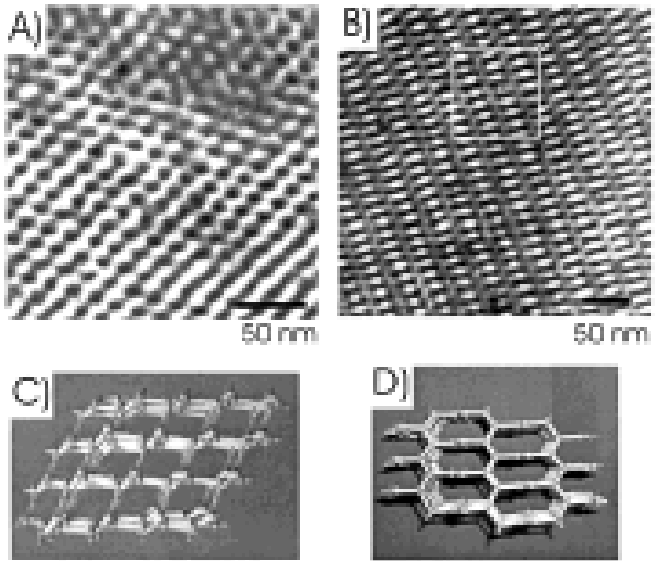

Figure 2.12. a, b) Representative TEM images of the two predominate projections obtained by Bailey et al. from a PI-PS-PEO specimen with f_O = 0.18. The black and white regions correspond to OsO_4-stained PI and unstained PS and/or PEO domains. c, d) Two orientations of a lattice model of the O^{70} network morphology. The open channels in this model correspond to the black (PI) regions of the TEM micrographs, while the model struts represent the white (PS and PEO) portions of the images. Figure reproduced from Reference 170.

which Bailey et al. attributed to mixing of the PEO and PS chains. The fractional crystallinity sharply increased to ~0.5 as f_O changed from 0.10 to 0.13, and remained roughly constant as f_O was further increased to 0.34. Bailey et al. suggested the increase in crystallinity corresponded to the formation of relatively pure PEO domains.[170] Rheological measurements were used to probe the viscoelastic response of the materials. The unknown mesostructure was highly elastic, with a nearly frequency-independent elastic modulus (*G'*) that was orders of magnitude larger than the loss modulus (*G"*).[170] This viscoelastic pattern was known to be associated with cubic mesostructures such as gyroid or BCC.[98] Bailey et al. employed static birefringence measurements to definitively establish if the unknown mesostructure had a cubic symmetry. Optically isotropic phases, such as those with cubic symmetry, are nonbirefringent. This unknown mesostructure, in contrast, was strongly birefringent, leading Bailey et al. to deduce that it was noncubic.[170] Bailey et al. reasoned that, since it was noncubic, the unknown mesostructure had to be a triply periodic morphology; other phases were not consistent with both the birefringence and rheological measurements.[170]

Bailey and colleagues next turned to TEM analysis to try and develop a microdomain model of the unknown mesostructure. They pointed out that the TEM micrograph provided in Figure 2.12 contains an array of bright white, stain deficient spots that are indicative of continuous channels comprised of PS and/or PEO chains and they posited that these continuous PS/PEO channels percolated through a continuous PI matrix.[170] Using these TEM images as a guide, Bailey et al. built a simple network

model consisting of tubes connected by threefold connectors. This model contained elements of both the gyroid and perforated lamellar morphologies, as shown in Figure 2.13, and had *Fddd* symmetry.[170] (This morphology was subsequently called O^{70},[158] with "O" indicating an orthorhombic unit cell and "70" referring to the number of the space group in the crystallographic tables.[44] The O^{70} notation will be used in this review.) The two projections of this lattice model that most closely match the experimental micrographs are provided in Figure 2.12; the model captures the qualitative features present in the TEM images and is also consistent with the rheological and birefringence measurements.[170] (Tyler et al.[171] later noted that Bailey et al.'s simplistic geometrical model could not account for the lattice parameter ratios obtained from SAXS experiments, and should not be considered quantitatively accurate.) Bailey et al. then reconsidered their SAXS data in the context of the O^{70} morphology. (Note that the allowed reflections for the orthorhombic lattice of O^{70} are not simple multiples of the primary peak q^*, as they are for a cubic lattice such as Q^{230}. Rather, orthorhombic peak positions change with the lattice dimensions *a*, *b*, and *c* according to $q_{hkl} = 2\pi [h^2/a^2 + k^2/b^2 + l^2/c^2]^{1/2}$, where *h*, *k*, and *l* are the associated Miller indices. Specific orthorhombic space groups are associated with different sets of allowed reflections, as identified in the crystallographic tables.[44] The *a*, *b*, and *c* parameters must be varied to obtain optimal least–squares fits of the allowed reflections for O^{70} to the recorded SAXS peaks.) The peaks in the experimental 1-D data were nicely accommodated by the allowed reflections for the O^{70} structure, although there were many more allowed reflections than there were experimental Bragg peaks. In addition, four spots on a 2-D SAXS pattern were found to be consistent with O^{70} Bragg

scattering. Bailey et al. tentatively concluded that the PI-PS-PEO specimens had formed the O^{70} network morphology, but noted that higher resolution scattering data with an improved signal-to-noise ratio would be required to make the claim definitive. Regardless of the network structure's symmetry, this report validated the strategy for producing multiply continuous network morphologies that was highlighted in Figure 2.11.[170]

Epps and Cochran et al. augmented Bailey et al.'s[170] investigation of PI-PS-PEO materials along the $f_I \approx f_S$ isopleth by probing the specimens with synchrotron X-ray radiation; the resulting data had a higher resolution and higher signal-to-noise ratio[158, 159] than the lab-source data previously reported by Bailey et al.[170] SAXS data acquired

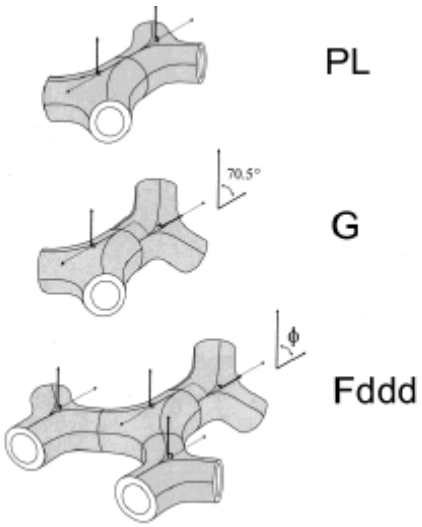

Figure 2.13. Local configurations of threefold connectors in the perforated lamellar (PL), gyroid (G), and O^{70} (Fddd) morphologies. The O^{70} lattice was constructed using two parts PL and one part G (with some distortion in Φ). Reproduced from Reference 170.

from eight PI-PS-PEO samples (not all along the $f_I \approx f_S$ isopleth) are provided in Figure 2.14. Epps and Cochran et al. indexed all of these Bragg patterns to the O^{70} mesostructure, as shown in Figure 2.14.[159] Interestingly, in all cases, the 111, 022, and 004 peaks are nearly coincident. The reflections absent from these data match the extinction rules for O^{70} and, remarkably, none of the allowed peaks are missing in the low-*q* regime. These data definitively affirm Bailey et al.'s tentative O^{70} assignment. In addition to the six samples prepared by Bailey and coworkers,[170] Epps and Cochran et al. identified the O^{70} network in nine other samples along four different isopleths: (i) $f_I / f_S = 1.1$, $0.15 < f_O < 0.22$ (ii) $f_I / f_S = 0.8$, $f_O = 0.21$ (iii) $f_I / f_S = 0.6$, $0.16 < f_O < 0.25$ (iv) $f_I / f_S = 0.4$, $0.22 < f_O < 0.29$. Clearly, O^{70} persisted over a substantial range of compositions in the PI-PS-PEO system. Note that four of those samples were also listed as forming Q^{214}; they underwent an OOT from Q^{214} to O^{70} upon heating. These OOT's were always reversible, as were O^{70} to disorder transitions in materials with experimentally accessible T_{ODT}'s; these reversibilities provide compelling support for the notion that O^{70} is an equilibrium morphology.[158, 159]

The microdomain topology of the O^{70} morphology, and those of the more familiar Q^{214} and Q^{230} mesostructures, were further interrogated by Epps and Cochran et al. using a combination of TEM and level set modeling.[159] This effort was aimed at bridging the gap between the symmetry information present in the reciprocal space SAXS data and the actual domain structure in real space. Level set models are space filling constructs generated using arbitrarily chosen structure factors that have the experimentally determined space group symmetry and divide space into the appropriate volume fractions. These models do not contain any information about individual chain

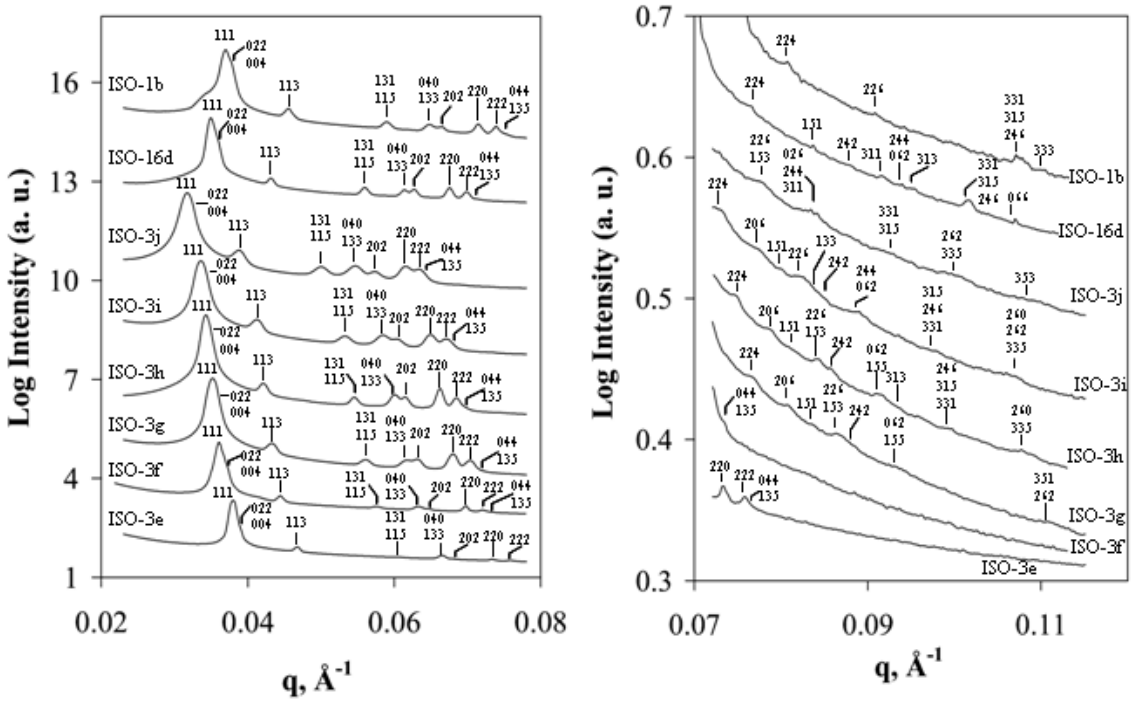

Figure 2.14. Synchrotron SAXS data acquired from eight PI-PS-PEO specimens in the O^{70} regime. All of the curves are indexed with the allowed reflection for *Fddd* symmetry. Figure reproduced from Reference 159.

conformations (i.e., polymer statistical mechanics is not considered), but they can be used to simulate TEM projections. Epps and Cochran et al. adjusted the structure factors in their level sets until the simulated TEM projections contained features that closely matched the experimental micrographs. The excellent agreement that was obtained for all three network mesostructures indicated that somewhat plausible microdomainmodels had been proposed and further supported the space group assignments.[159] Level set models of the three network morphologies are provided in Figure 2.15. Epps and Cochran et al. pointed out that these models do contain some obvious chain packing deficiencies. Namely, there are relatively wide variations in the thickness of individual

domains, while SCFT has demonstrated that relatively uniform domains minimize packing frustration and thus overall free energy.[68] Epps and Cochran et al. suggested that SCFT would provide more realistic composition profiles than the level set models, although the latter were useful spatial representations.[159]

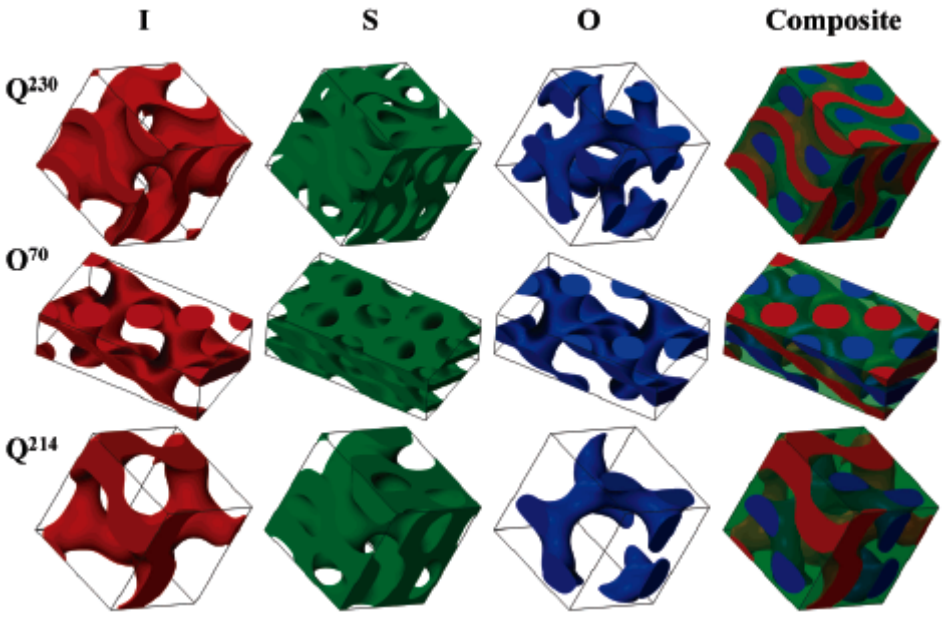

Figure 2.15. Top row: single unit cell level set models of the Q^{230}, O^{70}, and Q^{214} network morphologies. Bottom row: cross sections of the level set models and sketches of PI-PS-PEO chains demonstrating how each morphology could be assembled. Reproduced from Reference 159.

The O^{70} network morphology was the first noncubic network structure identified in soft materials[159] and it was a featured topic in numerous subsequent publications.[166-168, 172-176] Chatterjee et al. extended the investigations of Bailey, Epps, and Cochran et al.[158, 159, 170] to PEO-rich PI-PS-PEO triblock terpolymers and identified O^{70} in three different specimens, all of which underwent an OOT from lamellae to O^{70}

upon heating.[166] Again, the 111, 022, and 004 peaks in the SAXS data were essentially coincident for O^{70}. Chatterjee et al. incorporated both their own and previously published[158, 159, 170] results into a comprehensive ternary phase map for PI-PS-PEO triblock terpolymers; this portrait is provided in Figure 2.16. Chatterjee et al. pointed out that a ternary phase map of perfectly symmetric ABC triblock terpolymers would be symmetric about the $f_I = f_O$ isopleth; the asymmetry in Figure 2.16 was attributed to asymmetries in the block statistical segment lengths and χ parameters.[166] The expansive network windows on this phase portrait validate the strategy of using nonfrustrated ABC triblock terpolymers with symmetric interfacial tensions ($\chi_{AB} \approx \chi_{BC}$) to prepare multiply continuous network morphologies.

Epps and Bates examined the effects of segregation strength on O^{70} network formation.[172] They prepared four series of PI-PS-PEO triblocks along the $f_I \approx f_S$ isopleth with overall molecular weights ~30 – 130% higher than the previously investigated[158, 159, 170] O^{70}-forming materials. The melt-phase morphologies of these specimens were probed using a combination of SAXS, TEM, and DMS, and well-ordered O^{70} mesostructures were reported in the network windows for PI-PS-PEO materials with 30 and 75% higher molecular weights, although the precise location of the phase boundaries may have shifted slightly. In contrast, the 80 and 130% higher molecular weight materials with compositions in the network window did not form well-ordered grains of the O^{70} mesostructure. SAXS data acquired from these specimens contained just two broad peaks, not the rich assortment of reflections associated with O^{70}. The degree of translational order was sensitive to the symmetry of

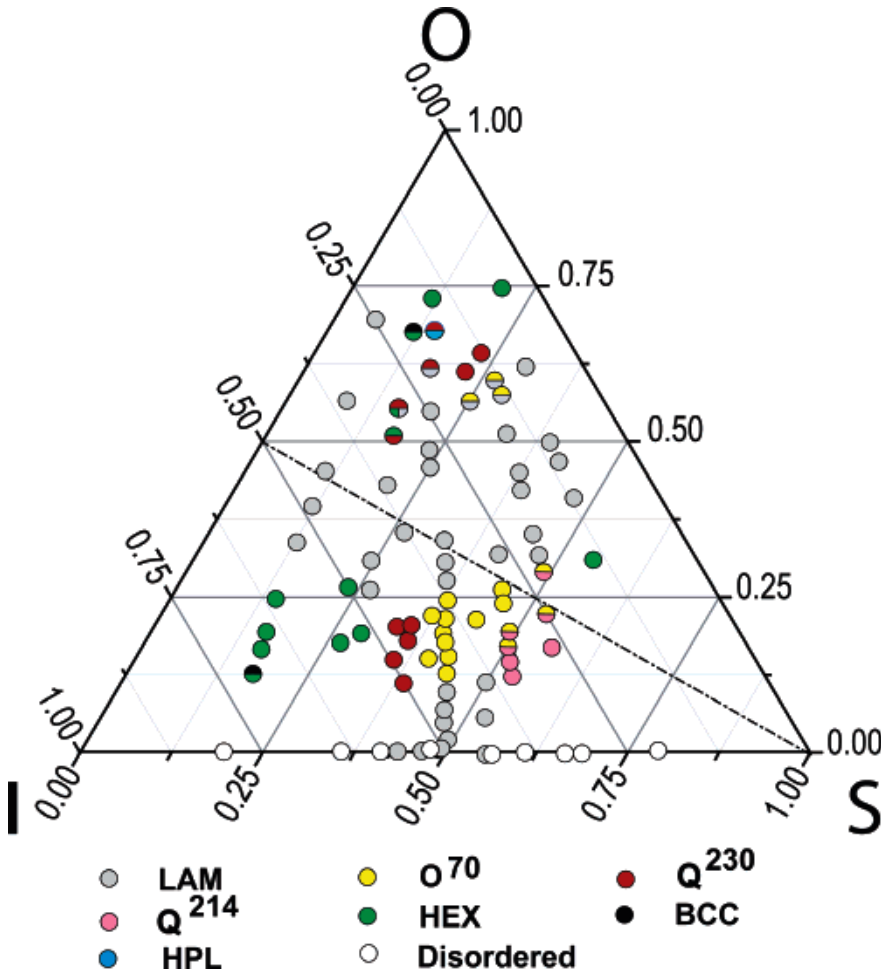

Figure 2.16. Ternary phase portrait for PI-PS-PEO triblock terpolymers. The axes represent volume fractions of each component, and an imaginary axis normal to the page would represent the segregation strength (all of these samples had comparable molecular weights). Six stable ordered morphologies (LAM, HEX, BCC, O^{70}, Q^{214}, Q^{230}), the metastable hexagonally-perforated lamellae (HPL), and a disordered phase are denoted by the colored circles. Symbols containing two colors indicate specimens that underwent OOT's and the dashed line corresponds to the $f_I = f_O$ isopleth. Figure reproduced from Reference 166.

the underlying morphology, as the 80 and 130% higher molecular weight PI-PS-PEO materials in the LAM regimes did adopt mesostructures with significant long-range order. Several sample preparation strategies were pursued in an effort to improve the translational order of the mesostructures formed by the high molecular weight PI-PS-PEO materials with compositions in the network window. Neither solvent casting from three different solvents nor annealing at 130 °C for 30 days appreciably altered the state of order of these materials, however. TEM analysis revealed a poorly ordered morphology that appeared to consist of interpenetrating domains of the constituent blocks. Rheological measurements yielded a *G'* that was relatively invariant with frequency,[172] consistent with a triply periodic morphology.[98] Epps and Bates generically labeled this poorly ordered, triply periodic mesostructure a "network" morphology.[172]

These high molecular weight PI-PS-PEO results appeared to contrast reports detailing network morphologies in AB diblock copolymers. As was discussed earlier, it is now generally agreed that the gyroid is an equilibrium morphology for AB diblock copolymers in the SSL,[13, 28, 106, 132] and Urbas et al. published TEM images of strongly segregated PS-PI diblocks that indicated gyroid "crystals" that spanned many microns were present in the material.[28] The high molecular weight PI-PS-PEO materials did not behave like the diblock counterparts, as they did not adopt a network mesostructure with significant translational order. Epps and Bates suggested the different behaviors derived from differences in molecular diffusion between the PS-PI and PI-PS-PEO systems.[172] In strongly segregated block copolymers, chains do not readily diffuse across domain interfaces.[177, 178] Chains can, however, diffuse parallel to the domain interfaces. Epps and Bates noted that, due to the large magnitude of χ_{IO}, the PS chains

almost exclusively adopt conformations that bridge the domain.[172] As a result the PI/PS and PS/PEO block junctions would have to move in concert in order for the PI-PS-PEO chains to diffuse parallel to the domain interface. Junction coordination is never present in AB diblock copolymers because no chains are forced to bridge across a domain, and chains are able to freely diffuse parallel to domain interfaces (subject to entanglement effects). The junction coordination in the PI-PS-PEO system apparently does not prevent diffusion that results in the coarsening of lamellae, as well ordered LAM_2 and LAM_3 mesostructures were reported.[172] Epps and Bates posited that the coordination does inhibit parallel diffusion in network morphologies provided diffusion across domain interfaces is sufficiently suppressed by high segregation strengths. They argued that, since domains in network structures do not have constant thicknesses, PI-PS-PEO chains are not able to freely diffuse parallel to domain interfaces without stretching (compressing) the middle PS block. These stretching requirements are alleviated when the chains can diffuse normal to the domain interface, as they can for lower molecular weight materials. Presumably these entropic stretching considerations inhibit molecular diffusion in the higher molecular weight PI-PS-PEO materials and thus minimize the coarsening network mesostructures into coherent ordered grains. Epps and Bates noted that the preservation of the triply periodic morphology at higher molecular weights could potentially be very beneficial from a practical applications point of view.[172]

Epps and Bates pointed out that ordered network structures could be the equilibrium state for these generic “network”-forming materials, but the kinetic limitations prevented them from making a definitive determination.[172] Meuler and colleagues subsequently provided evidence that O^{70} was in fact the equilibrium

configuration for these "network"-forming samples.[174] They annealed several of the higher molecular weight specimens at 250 °C, above the 200 °C level investigated by Epps and Bates,[172] and probed the morphologies with synchrotron SAXS. While this heat treatment did not alter the state of order of most of the PI-PS-PEO materials, one of the samples did transition from the "network" structure to a (presumably equilibrium) O^{70} morphology at the elevated temperatures.[174] This result supported Epps and Bates' hypothesis that, absent kinetic limitations, the higher molecular weight PI-PS-PEO materials could form order network mesostructures.

Meuler et al. extended the investigation of block terpolymers comprised of PI, PS, and PEO chains to PEO-PS-PI-PS-PEO pentablock terpolymers.[174] Previous experimental[109, 110] and theoretical[122] reports had identified the familiar gyroid in higher order ABA triblocks; Meuler et al. prepared a series of PEO-PS-PI-PS-PEO pentablocks along the $f_I \approx f_S$ isopleth to determine if, like in the block copolymer materials, the PI-PS-PEO network morphologies persisted in the higher order PEO-PS-PI-PS-PEO pentablocks.[174] A combination of synchrotron SAXS, TEM, and DMS were used to identify O^{70} in an PEO-PS-PI-PS-PEO specimen ($f_O = 0.13$) with approximately the same segregation strength as some previously investigated[158, 159, 170] PEO-PS-PI-PS-PEO materials (i.e., the PEO-PS-PI-PS-PEO sample had about twice as high an overall molecular weight as a homologous PI-PS-PEO specimen), proving that the PI-PS-PEO network morphologies are formed by materials with the higher order PEO-PS-PI-PS-PEO architecture.[174] Numerous other investigations focused on the stability of O^{70} in PI-PS-PEO materials with respect to increased PS and PEO block

polydispersities,[167, 168, 173] constituent homopolymer addition,[176] and lithium perchlorate doping;[175] these investigations are described in more detail later in this review.

The O^{70} network structure was reported in two nonfrustrated ABC triblock systems besides PI-PS-PEO. Both other systems, like PI-PS-PEO, have symmetrically balanced interfacial tensions ($\chi_{AC} \gg \chi_{AB} \approx \chi_{BC}$) and all of the O^{70}-forming samples were in the weak segregation regime. Epps and Cochran et al. reported that a reexamination of the SAXS and TEM data obtained from a PS-PI-PDMS triblock terpolymer ($f_S = 0.20$, $f_I = 0.59$)[164] led them to conclude that the specimen had formed O^{70}.[159] Cochran and Bates probed the morphology of a PCHE-PEE-PE triblock terpolymer sample ($f_C = 0.29$, $f_{EE} = 0.49$) using synchrotron SAXS and reported that it had adopted O^{70}. Once again the first three peaks in the Bragg pattern were nearly coincident.[179] These results indicate that O^{70} may be common to many block copolymer systems.

O^{52}, the Orthorhombic *Pnna* Network

The report of the first known orthorhombic network structure in soft materials (O^{70})[170] was closely followed by a publication identifying a second network morphology with an orthorhombic lattice.[179] This latter research focused on the processing behavior of O^{70}-forming materials; Cochran and Bates subjected a melt of the O^{70}-forming PCHE-PEE-PE triblock sample to reciprocating shear (rate of 5 s^{-1}, 600% strain amplitude) and probed the morphology using SANS (the beam was situated along the shear gradient direction). The 2-D SANS pattern did not change after six minutes, indicating a steady state structure had formed. The peaks in this SANS pattern

satisfied the extinction rules for multiple space groups, and additional experiments were required to definitively establish the symmetry of the mesostructure. The sheared sample was cooled to room temperature, sectioned, and exposed to X-rays that were coincident with the three orthogonal axes; these SAXS data are provided in Figure 2.17. Cochran and Bates reported that the multiple orders of reflections and systematic extinctions in these three Bragg patterns conformed uniquely to an orthorhombic (O) space group with *Pnna* symmetry (O^{52}, space group number 52^{44}) and lattice constant ratios of a = 2.00c, b = 1.73c.[179] The O^{52} structure locally resembles O^{70}, but fills space in a lower symmetry manner than the latter network; Cochran and Bates presented a level set model of the O^{52} network that contained continuous, triply periodic domains of all three constituent blocks. This reciprocating shear-induced transition from O^{70} to O^{52} was the first known field-induced network-to-network transition in soft materials. The O^{52} morphology persisted following cessation of the shear and several days of thermal annealing above the glass transition temperatures (T_g) of the constituent blocks. Cochran and Bates suggested that O^{52} was a long-lived metastable state, as the (presumably equilibrium) O^{70} always formed upon cooling below T_{ODT} under quiescent conditions. The O^{70} and O^{52} network morphologies apparently had nearly degenerate free energies, and some sort of kinetic barrier prevented a reversal of the shear-induced O^{70} to O^{52} transition.[179]

A morphology with *Pnna* symmetry was recently reported in another nonfrustrated system: PCHE-PE-PCHE-PDMS tetrablock terpolymers ($\chi_{ED} > \chi_{EC} \approx \chi_{CD}$).[180] Bluemle et al. prepared a series of PCHE-PE-PCHE-PDMS

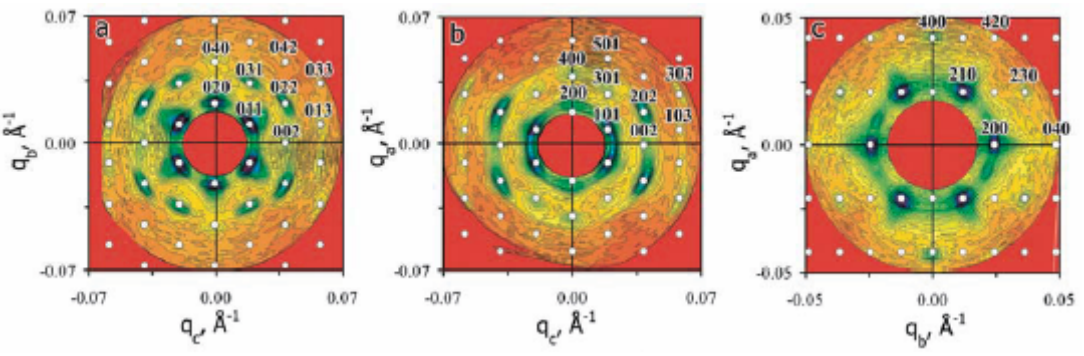

Figure 2.17. 2-D SAXS patterns from annealed, macroscopically aligned PCHE-PEE-PE. The circles mark the allowed reflection for the O^{52} morphology. The beam is parallel to a) the shear direction b) the shear gradient direction c) the vorticity direction. Figure reproduced from Reference 179.

specimens (f_E / f_C = 7/3) with varying lengths of terminal PDMS chains ($0 < f_D < 0.20$), subjected them to reciprocating shear in the melt, and interrogated the resulting sample morphologies (following vitrification of the PCHE domains) using SAXS, TEM, and DMS. All of these materials contained hexagonally packed cylinders, except for the specimen with f_D = 0.09. DMS experiments conducted on this sample revealed a frequency independent *G'* that is suggestive of a triply periodic morphology. SAXS data were acquired with the x-ray beam oriented along each of the orthogonal axes; Bluemle et al. were able to fit nearly all of the spots in these patterns with the allowed reflections of a *Pnna* space group with lattice ratios of a = 1.75c and b = 0.61c. TEM analysis of this specimen provided micrographs Bleumle et al. suggested were indicative of discrete spheres of PDMS embedded within the trivalent nodes of the interpenetrating PCHE domains. Although they share *Pnna* symmetry, this O^{52} network and the O^{52} structure reported by Cochran and Bates[179] clearly contain different

microdomain structures. The lattice parameter ratios are system dependent and the PCHE-PE-PCHE-PDMS version of O^{52} does not contain continuous domains of all of its components,[180] unlike the modeled PCHE-PEE-PE version.[179] It was unclear if O^{52} represented the equilibrium state of the PCHE-PE-PCHE-PDMS sample,[180] or if it was a long-lived metastable state like the O^{52} in the PCHE-PEE-PE specimen.[179]

Theoretical Approaches

In the preceding sections, we discussed selected theoretical publications[144, 146-148] that played a role in establishing the $I4_132$ symmetry of the triply continuous Q^{214} mesostructure. Several other[171, 181-183] groups have systematically examined triblock terpolymer phase behavior and discussed the network mesostructures adopted by these materials. Erukhimovich et al. developed a weak-segregation theory for ABC triblock terpolymers[184] that, like Leibler's analogous theory for diblock copolymer melts,[7] is rigorously valid only near a critical point. Erukhimovich used this theory to compute the free energies of numerous mesostructural candidates, including the Q^{214} and Q^{230} network morphologies, in various weakly segregated, nonfrustrated ABC triblock terpolymer systems.[181] (Tyler et al. suggested[171] that the phase relations among plane waves used by Erukhimovich to compute the free energy of another network structure were inconsistent with that morphology's reported $I\bar{4}3d$ symmetry. We will therefore omit this phase from our discussion here.) Detailed phase portraits for systems with symmetric χ parameters ($\chi_{AB} = \chi_{BC}$) that satisfy the Hildebrand (i.e., solubility

parameter) approximation were provided by Erukhimovich. Both Q^{214} and Q^{230} were predicted to be equilibrium morphologies over nontrivial composition ranges.[181]

Tyler and colleagues used SCFT to interrogate the phase behavior of nonfrustrated ABC triblock terpolymers with $\chi_{AC} \gg \chi_{BC} \approx \chi_{AC}$;[171, 182] both the PI-PS-P2VP[141-143, 152-155, 157] and PI-PS-PEO[158, 159, 166, 170] materials discussed earlier have this sequence of χ parameters. The free energies of 13 ordered morphologies, including Q^{214}, Q^{230}, O^{70}, O^{52}, OTDD (Q^{227}), and core-shell OBDD networks (Q^{228}), were computed and ternary phase portraits for several model systems were presented.[171] An idealized ABC system, like those studied by Matsen[144] and Erukhimovich,[181] had symmetric interfacial tensions ($\chi_{AB} = \chi_{BC}$) and blocks with equal statistical segment lengths. The Q^{230}, Q^{214}, and O^{70} networks were identified as equilibrium mesostructures for various ranges of compositions in these model materials.[171] While these same three network morphologies were reported in the PI-PS-PEO system,[158, 159, 166, 170] the sizes and positions of the network windows in the model triblocks differed significantly from those in the PI-PS-PEO materials. Tyler et al. aimed to reconcile these differences by incorporating experimentally measured χ and block statistical segment length values into their SCFT calculations. (Note that these values, along with the degree of polymerization, must be computed with respect to a common reference volume for use in SCFT; Tyler and colleagues selected 118 $Å^3$.) The phase triangle that was computed using these realistic parameters contained stable regions of Q^{230}, Q^{214}, and O^{70} and is provided in Figure 2.18. It differed significantly from the idealized version, illustrating the sensitivity of ABC triblock phase behavior to the χ and statistical segment length

values, and provided a much better qualitative, albeit not quantitative, match to the experimental data shown in Figure 2.16.[171]

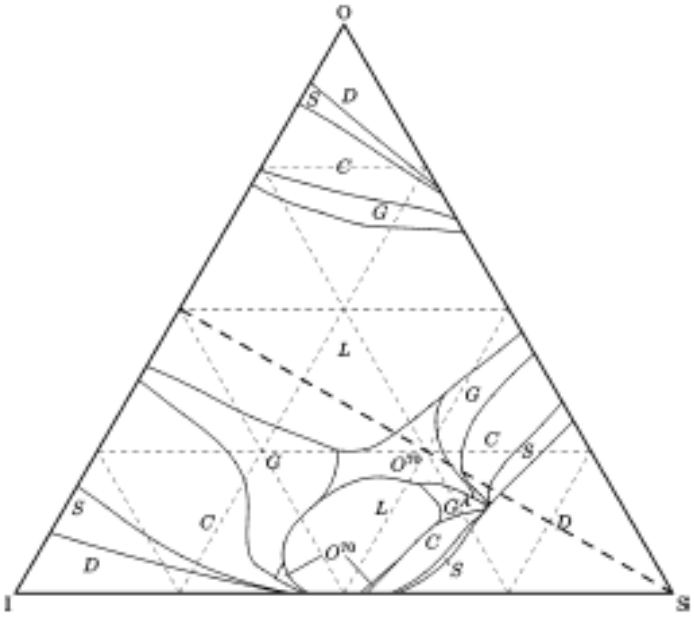

Figure 2.18. Ternary phase portrait for a model PI-PS-PEO triblock terpolymer. Experimentally measured χ and statistical segment length values were used in the SCFT calculations, and the molecular weights were comparable to those studied by Bailey, Epps, Cochran, and coworkers (here $\chi_{IS}N$ = 11.0, $\chi_{SO}N$ = 14.2, $\chi_{IO}N$ = 45.8).[158, 159, 166, 170] The predicted equilibrium states are: (D) disorder, (S) BCC, (C) HEX, LAM, (G) Q^{230}, (G^A) Q^{214}, and O^{70}. Figure reproduced from Reference 171.

Tyler et al. commented on several other features of the ABC triblock terpolymer phase behavior. They noted that the predicted microdomain structures typically contained diffuse domain interfaces due to the modest segregation strengths considered. Additionally, the predicted microdomain structures in the network morphologies were

not always continuous in all three domains, as short terminal chains could either mix with or form discrete domains within the continuous matrix.[171] The overall free energies of competing morphologies were decomposed into individual entropic and enthalpic contributions to provide some physical insight into the thermodynamic phenomena driving network formation. Tyler et al. provided comparisons of these contributions at a number of phase boundaries.[171] Notably, O^{70} was only predicted to be stable for unit cell parameter ratios that would result in a near coincidence of the 111, 004, and 022 peaks in a Bragg pattern, a prediction in agreement with the experimental ISO reports discussed earlier.[158, 159, 166, 170] Additional analysis focused on the sensitivity of the stability of the O^{70} network with respect to variations in the χ parameters; the size and location of the predicted O^{70} window depended strongly on the quantity $\chi_{AB} - \chi_{BC}$ (i.e., the asymmetry of the interfacial tensions).[171]

The spectral or pseudo-spectral SCFT implementation strategies utilized by researchers such as Matsen[144] and Tyler and colleagues[171, 182] suffer from at least one important limitation: they require the selection of mesostructural candidates. This requirement severely hinders the utility of SCFT as a predictive tool for identifying new equilibrium morphologies, as including every possible space group symmetry in calculations is not practically feasible. Numerical methods that do not require the selection of mesostructural candidates were developed to solve the SCFT equations and overcome this limiting feature beginning in 1999-2000.[185, 186] Guo and colleagues recently extended this type of SCFT analysis to ABC triblock terpolymers in three dimensions by using a generic Fourier-space approach.[183] They complemented Tyler et

al.'s investigations of nonfrustrated ABC systems[171, 182] by focusing on model frustrated ABC triblock terpolymers with equal block statistical segment lengths and $\chi_{AB}N = \chi_{BC}N = 35$ and $\chi_{AC}N = 15$. A ternary phase portrait containing 20 different morphologies was generated using this methodology; representations of these mesostructures and the resulting phase triangle are provided in Figure 2.19. Included amongst these morphologies are the traditional Q^{230} (here labeled "G") and Q^{214} (here labeled "G^A") network structures, as well as two decorated variations of gyroid that contain embedded, noncontinuous domains: gyroid with spheres at the interfaces (here labeled "G + S(I)") and gyroid with spheres inside a domain (here labeled "G + S(II)"). The absence of orthorhombic network mesostructures such as O^{52} and O^{70} in these model frustrated ABC triblocks is not surprising, given that these morhologies have only been identified experimentally in nonfrustrated block terpolymer systems.[158, 159, 166, 172, 174-176, 179, 180] Guo et al. examined the validity of their methodology by comparing the phase triangle provided in Figure 2.19 to the reported phase behavior of frustrated PS-PB-PMMA triblock terpolymers.[187] Notably, the SCFT phase portrait contains a $L_3 \rightarrow L + C(I) \rightarrow L + S(I) \rightarrow L_2$ sequence along the $f_A = f_C$ isopleth;[183] this same mesostructural procession was reported in the PS-PB-PMMA system,[187] an agreement that Guo et al. suggested validated their generic Fourier-space approach.[183] This general approach may prove to be a very powerful tool for investigating ABC triblock terpolymer phase behavior because of its predictive component and the resulting potential to serve as an effective guide for experimentalists preparing designer block copolymer materials.

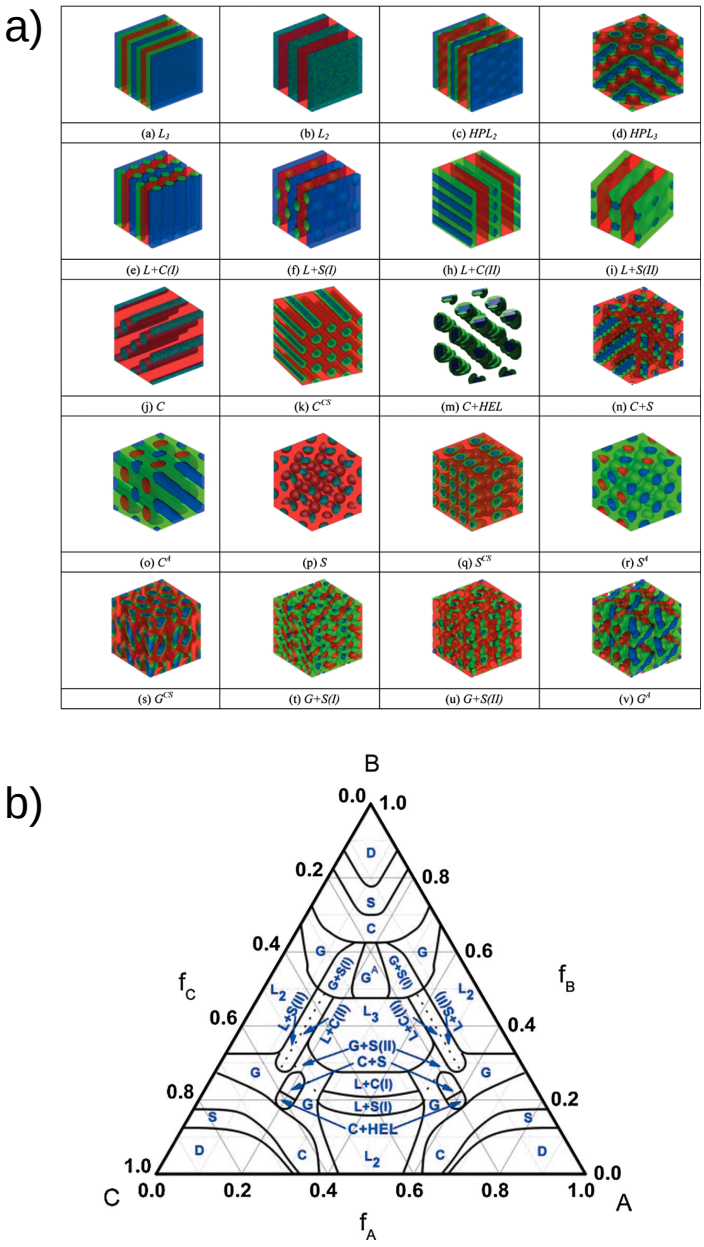

Figure 2.19. a) Ordered morphologies obtained by Guo et al. using the generic Fourier-space approach for a model ABC triblock terpolymer with equal block statistical segment lengths and $\chi_{AB}N = \chi_{BC}N = 35$ and $\chi_{AC}N = 15$. b) Ternary phase map of the equilibrium mesostructures in this model system. Figure reproduced from Reference 183.

2.4 Revisiting AB Diblock Copolymers: O^{70}

The reports of O^{70} in various triblock terpolymer systems[158, 159, 170, 174, 179] led Tyler and Morse to evaluate the stability of this orthorhombic network phase in AB diblock copolymers using SCFT.[182] Their SCFT approach that, like Matsen and Schick's method,[61] involved selecting mesostructural candidates and computing their free energies.[182] Tyler and Morse initially investigated O^{70} in ABC triblock terpolymers, but, upon finding that O^{70} was predicted to be an equilibrium morphology at certain compositions in the diblock limit (i.e., as the length of the C chain approached zero), decided to recalculate the entire phase portrait for conformationally symmetric AB diblock copolymers. Tyler and Morse included O^{70} as a mesostructural candidate, along with the familiar BCC, HEX, gyroid, and LAM morphologies identified as equilibrium mesostructures by Matsen and Schick,[61] and found that O^{70} has the lowest computed free energy for a narrow range of compositions and segregation strengths.[182] The portion of the phase diagram updated by Tyler and Morse is presented in Figure 2.20;[182] entropic considerations changed a portion of the LAM window to O^{70}, while enthalpic contributions stabilized O^{70} at the expense of Q^{230}.[171] Guo et al. recently calculated the AB diblock phase diagram using their new, generic Fourier-space SCFT approach that did not rely on *a priori* assumptions about the symmetry of the structure (i.e., it did not require the selection of mesostructural candidates)[183] and confirmed Tyler and Morse's predictions.[171, 182]

As mentioned earlier, orthorhombic unit cells have three independent lattice parameters, while the cubic counterparts are characterized by only one. Tyler and Morse concluded that O^{70} is only stable when the ratios of the cell parameters are

approximately $1:2:2\sqrt{3}$; the first three scattering peaks (004, 111, and 022) from unit cells with these exact ratios of lattice parameters are coincident.[182] This near coincidence of the first three reflections was reported in all of the experimental O^{70}-forming block terpolymer systems.[158, 159, 170, 174, 179] Tyler and Morse suggested that, since O^{70} was predicted to be stable in weakly segregated materials, the rationale for the near coincidence of the scattering peaks and the network structure's stability could be understood in the context of the Landau expansion of the SCFT free energy.[182] Ranjan and Morse subsequently extended Leibler's Landau theory[7] and analyzed the stability of O^{70} in diblock copolymers.[188] They assumed that the ratio of unit cell parameters was

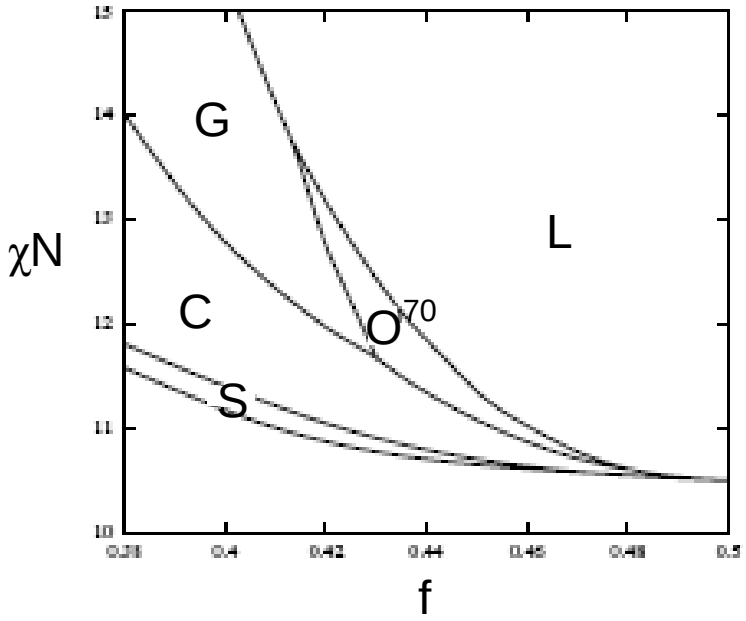

Figure 2.20. SCFT phase portrait of a conformationally symmetric diblock copolymer. (D) Disorder, (L) LAM, (G) gyroid, O^{70}, (C) HEX, (S) BCC. Reproduced from Reference 182.

$1:2:2\sqrt{3}$ and found excellent agreement between the Landau results and the SCFT calculations for weakly segregated ($\chi_{AB}N < 10.55$) materials. They speculated that, since it was predicted to be an equilibrium morphology in the context of the Landau theory, the stability of the O^{70} network may be related to geometric considerations, and not any specific features of block copolymers.[188] An additional theoretical investigation of the stability of O^{70} was undertaken by Yamada et al,[189] who calculated the phase diagram of weakly segregated diblock copolymers using two methods: (i) evaluating the free energy of morphological candidates using a Landau expansion in a manner similar to Ranjan and Morse[188] and (ii) direct numerical simulations of the time-evolution free energy equations from starting conditions that include random noise. Both methods led Yamada et al. to conclude that O^{70} was the equilibrium morphology over a small portion of the phase diagram.[189] Curiously the O^{70} unit cell considered by Yamada et al. did not have lattice parameter ratios of $1:2:2\sqrt{3}$, but was a deformed version of this O^{70} unit cell considered by other groups.[171]

These theoretical reports[182, 188, 189] have predicted that O^{70} should be the equilibrium structure over narrow ranges of composition. Some considered this prediction unlikely,[190] given that many experimental reports in the literature had focused on network structures in AB diblock copolymers, and none of them had identified O^{70}. Takenaka and coworkers provided decisive confirmation of the O^{70} predictions with a 2007 report that a PS-PI diblock with $f_I = 0.638$, $M_n = 26.4$ kg/mol, and a PDI of 1.02 formed O^{70} at temperatures ranging from 145 – 160 °C.[82] The diblock material was first annealed in the disordered state at 230 °C for 30 minutes to eliminate effects associated with thermal history and then annealed at the target temperatures for

8 hours prior to being quenched in liquid nitrogen (for TEM analysis) or exposed to synchrotron X-rays. The resulting SAXS data and TEM micrographs were used to identify O^{70} between LAM (at lower temperatures) and the gyroid (at higher temperatures),[82] a sequence of transitions consistent with Tyler and Morse's SCFT prediction.[182] The first three peaks in the SAXS data were essentially coincident,[82] consistent with the findings in block terpolymer systems,[158, 159, 170, 174, 179] and in agreement with most of the predictions[182, 188] for diblock copolymers.

Miao and Wickham were skeptical that the O^{70} morphology reported by Takenaka et al.[82] represented the equilibrium state of the PS-PI diblock sample.[190] They noted that O^{70} was not identified in experimental diblock copolymer reports in the literature prior to 2007, even though a large number of investigations focused on network morphologies in those systems. Miao and Wickham also noted that meastability can be an issue with network mesostructures, as the transition from the metastable HPL to the equilibrium gyroid network reportedly required thermal anneals as long as 31 days, depending on the specific characteristics of the diblock material.[102] Furthermore, composition fluctuations were known to significantly modify the predicted mean-field phase diagram in the weak segregation regime[191] in which O^{70} was identified by Takenaka et al.[82] Miao and Wickham hypothesized that composition fluctuations could suppress the O^{70} network in diblock copolymers,[190] a possibility initially mentioned by Tyler and Morse.[182] They utilized a Hartree-level treatment of a generic Landau-Brazovskii model[192] to theoretically examine whether or not O^{70} was an equilibrium morphology in diblock materials with composition fluctuations.[190] They assumed that the O^{70} unit cell had lattice dimensions in the ratio $1:2:2\sqrt{3}$ (and thus a

coincidence of the first three peaks in the predicted Bragg pattern), following experimental[82] and theoretical[182, 188] precedent. This theoretical treatment led Miao and Wickham to predict that composition fluctuations render O^{70} metastable with respect to the LAM and disordered states for experimentally relevant molecular weights ($N < 10^4$), and they suggested Takenaka et al.[82] had identified a metastable O^{70} morphology in their PS-PI diblock sample.[190]

Miao and Wickham's report[190] led the Takenaka group to revisit their claim that O^{70} represented the equilibrium state in their PS-PI diblock material.[84] The PS-PI diblock copolymer ($f_I = 0.638$, $M_n = 26.4$ kg/mol) was previously reported[82] to undergo order-order transitions from LAM to O^{70} to gyroid upon heating; these transitions are summarized diagrammatically in Figure 2.21. Kim et al. interrogated the stability of O^{70} by studying the thermoreversibility of the order-order transitions summarized in Figure 2.21.[84] Two protocols were employed to investigate the respective LAM to O^{70} (i) and O^{70} to gyroid (ii) transitions: (i) anneal at 130 °C for 24 hours, anneal at 150 °C for 48 hours, and anneal at 130 °C for 48 hours, and (ii) anneal at 170 °C for 24 hours, anneal at 150 °C for 48 hours, and anneal at 170 °C for 48 hours. The morphology of the PS-PI diblock sample was probed at each temperature using both synchrotron SAXS and TEM. These data conclusively established that protocol (i) yielded transitions from LAM to O^{70} to LAM while protocol (ii) resulted in transitions from gyroid to O^{70} to gyroid. The thermoreversibility of these transitions, coupled with the long annealing times, provided compelling evidence that O^{70} is in fact an equilibrium network morphology in PS-PI diblock copolymers.[84] It is currently unclear why Miao and

Wickham's theoretical investigation[190] found that the formation of O^{70} is completely suppressed in diblock copolymers with composition fluctuations.

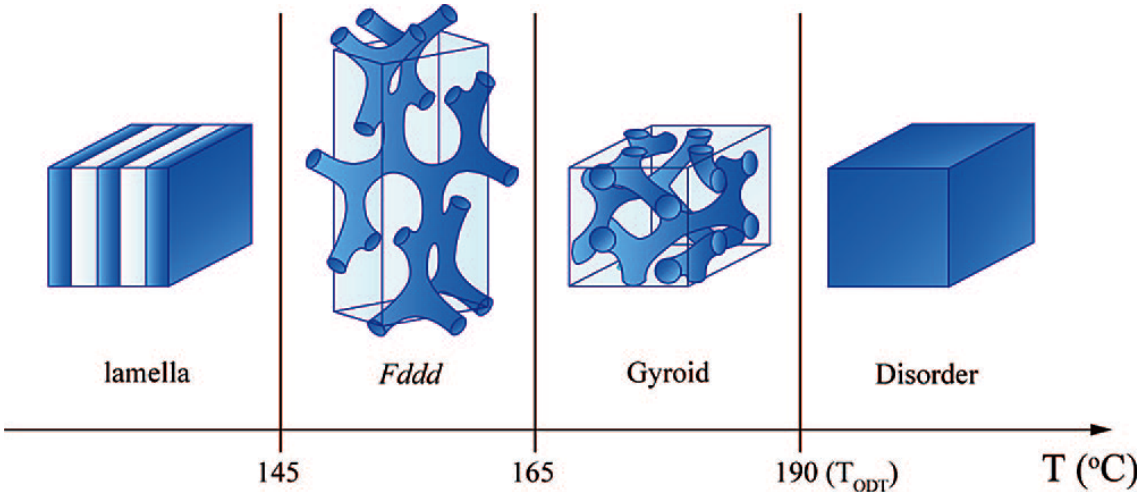

Figure 2.21. Thermally-driven order-order transitions of a PS-PI diblock copolymer with f_I = 0.638 and M_n = 26.4 kg/mol. Transitions to and from the O^{70} network are reportedly reversible. Reproduced from Reference 84.

2.5 Network Topologies

Two important characteristics of a network lattice are the connectivity of each node (p) and the smallest number of such nodes that form a closed loop in the lattice (n); Wells proposed a (n, p) labeling scheme to characterize these structures.[193] Cubic network lattices with threefold (n,3), fourfold (n,4), and sixfold (n,6) connectivity have been reported in low molecular weight surfactant systems.[57-60] The four block copolymer network morphologies described in the previous sections, in contrast, all contained threefold connectors and, to the best of our knowledge, the existence of

network mesostructures with fourfold or sixfold connectors has not been demonstrated in single component block copolymer materials. (An OBDD network would contain fourfold connectors.) Wells identified 30 different network lattices containing threefold connectors: one (12,3) net, seven (10,3) nets, three (9,3) nets, fifteen (8,3) nets, and four (7,3) nets.[193] Linear block copolymer materials have formed only three of these (10,3) nets: (10,3)a (Q^{230} and Q^{214}), (10,3)c (O^{70}), and (10,3)d (O^{52}).[169] An open and fascinating question is whether additional network lattices will be identified in block copolymer materials in the coming years, particularly those with complicated architectures (e.g., an ABCD tetrablock).

Bates and colleagues have postulated that chain stretching (entropic) considerations, which play only a minor role in surfactant systems, are primarily responsible for the different network morphologies, and threefold connectors in particular, found in block copolymers.[159, 169] Threefold connectors (also called "Y-junctions") have a larger angle between struts (120°) than either the fourfold (109.5°) or sixfold (90°) connectors. This relatively expansive opening presumably minimizes chain crowding and thus conformational restrictions at the domain interface near the connector.[159, 169] Threefold connectors also have less variation in both interfacial curvature and domain thickness than the higher order connectors;[169] these factors presumably alleviate packing frustration.[68] A thermodynamic preference for threefold connectors would limit the number of possible cubic network mesostructures and may be responsible for the formation of the orthorhombic network morphologies in block copolymers.[159] These geometric arguments, while not accounting for detailed molecular factors, are intuitively appealing and suggest that threefold connectors may be common

structural elements in other polymer systems. The fact that threefold connectors have been identified as a component of the disorganized network structures formed in aqueous block copolymer surfactant systems[194, 195] supports this reasoning.

2.6 Network Mesostructure Stability

Solvents

Numerous theoretical[67, 125] and experimental[103, 135-137, 196-205] investigations have focused on the phase behavior of block copolymers in the presence of solvent. Generally these samples adopt the ordered morphologies found in neat diblocks when the volume fraction of AB material exceeds 0.2. The broad features of the phase behavior can generally be understood by viewing the changes in domain volume fractions that result from the partitioning of the solvent as equivalent to changes in block volume fractions of melt-phase AB diblocks although the addition of solvent typically lowers the segregation strength of the system.[135, 136, 196-198] The gyroid morphology has been identified in a number of block copolymer/solvent mixtures, including those listed in Table 2.2.

Table 2.2: Block copolymer/solvent mixtures in which the gyroid (Q^{230}) has been identified.

Block Copolymer	Solvent(s)	Reference(s)
PS-PI	dioctyl phthalate	196, 198
PS-PI	di-*n*-butyl phthalate	196, 197
PS-PI	diethyl phthalate	197
PS-PI	dimethyl phthalate	197
PEO-PPO-PEO	water / *p*-xylene	200-203
PEO-PBO-PEO	water / *p*-xylene	204
PEO-PPO-PEO	formamide	205
PS-P4VP	toluene / ethanol	199

Homopolymers

The phase behavior of blends of block copolymers and constituent homopolymers generally resembles that of neat block copolymers with the same composition, provided the homopolymer is a minority component in the blend and the homopolymer molecular weight is roughly equal to or less than the appropriate block molecular weight; macrophase separation can occur when these two conditions are not met.[65, 66] Winey et al. first suggested that homopolymer blending could be used to adjust the compositions of block copolymer materials and place them within the narrow network window.[47] Multiply continuous network morphologies have since been reported in a number of blends, some of which are listed in Table 2.3. Theoretical analyses broadly agree with the reported experimental behavior, but also suggest that the addition of homopolymer can relieve packing frustration and stabilize morphologies not yet identified in experiments.[65-67, 130, 148]

Table 2.3: Block copolymer/homopolymer mixtures in which multiply continuous network morphologies have been identified.

Block Copolymer	Homopolymer(s)	Network(s)	Reference(s)
PS-PI	PS	Q^{230} *	47-49, 78, 206
PS-PI	PI	Q^{230} *	47-49, 207
PS-PB	PS	Q^{230} *	47
PS-PB	PB	Q^{230} *	47
PS-PB-PS	PVME	Q^{230} *	50
PEO-PBO	PBO	Q^{230}	89
PFCDMS-PMMA	PFCDMS/ PMMA	Q^{230}	108
PI-PS-PEO	PS	Q^{214}, Q^{230}, O^{70}	176
PI-PS-PEO	PI	Q^{214}, Q^{230}, O^{70}	176
PI-PS-PEO	PI / PS	O^{70}	176

* indicates that the reported network in some of the references is OBDD. These network morphologies are likely the gyroid.

Salts

Epps and coworkers have examined the stability of network phases with respect to lithium perchlorate ($LiClO_4$) doping in both PS-PI-PEO and PI-PS-PEO triblock terpolymer systems.[175, 208] This research was motivated by the fact that PEO, when complexed with alkali metal salts, can be used as a polymer electrolyte.[209, 210] It was hoped that the nonconductive blocks in the block copolymers would lead to improved mechanical toughness of the polyelectrolyte membranes.[208] $LiClO_4$-doped network mesostructures were thought to be particularly attractive because the continuous, percolating PEO domains would not, in principle, require any sort of alignment to ensure that the conducting channels traversed the membrane.[208] (A recent report demonstrated that network morphologies are not, in fact, required for high ionic

conductivities.[211]) PS-PI-PEO and PI-PS-PEO triblocks with $f_I \approx f_S$ were doped with $LiClO_4$ at ether oxygen-to-lithium ratios ranging from 48:1 to 3:1. While neat PS-PI-PEO and PI-PS-PEO triblock terpolymers formed Q^{230} and O^{70}, respectively, at certain compositions along this isopleth, the doped materials adopted a core-shell cylindrical mesostructure. This $LiClO_4$-induced morphological transition from the network morphologies to core-shell cylinders was rationalized on the basis of increases in the effective χ parameters in the systems upon the addition of the $LiClO_4$ salt.[175, 208]

Ionic Groups

Park and Balsara et al. investigated symmetric PSS-PMB diblock copolymers with various levels of sulfonation in both the dry and hydrated states.[107, 212, 213] These materials could potentially find application as polymer electrolyte membranes for fuel cells, with the sulfonic acid-containing PSS domains serving as channels for proton conduction. Park and Balsara et al. hoped to develop an understanding of the relationship between morphology and proton conductivity.[212] PSS-PMB diblock copolymers with sufficient levels of sulfonation adopted ordered morphologies, even at very low molecular weights (~3 kg/mol), due to the relatively large χ between the ionic and nonionic blocks, and well-ordered network mesostructures were obtained even at relatively high ionic contents.[107] Somewhat surprisingly, the gyroid morphology was identified in dry polymers with certain levels of sulfonation, even though f_{SS} lay between 0.45 and 0.50. Park and Balsara suggested that the "universal phase portrait" for block copolymers[13] did not apply to the PSS-PMB system, and that new theories

would be required to understand this complex phase behavior.[107] The gyroid network structure persisted as the ambient humidity was increased to modest levels before transitioning to LAM at high humidities.[213] It is not yet clear if a gyroid morphology offers enhanced proton conduction relative to LAM.

Polydispersity

The effects of polydispersity on block copolymer phase behavior have recently been reviewed[8] and only some features related to network morphologies are discussed here. Experimental[99] and theoretical[214-216] investigations have demonstrated that polydisperse block copolymers generally adopt equilibrium mesostructures that are comparable to those formed by monodisperse materials (i.e., the topologies of the phase diagram are generally the same).[99, 214-216] Changes in the shape of the molecular weight distributions alter the entropic and enthalpic free energy balances and thus the locations of the phase boundaries, however,[99, 214-216] and macrophase separation may occur for certain polydispersities, particularly in the gyroid window for intermediately to strongly segregated materials.[216] Polydispersity affects the free energy balance because the longer chains in the molecular weight distribution do not have to stretch as much to fill space, effectively lowering the elastic contribution to the system free energy for the polydisperse ensemble below its monodisperse counterpart.[216] This increased domain elasticity leads to elevated domain periodicity and may drive morphological transitions in which the domain interfaces curve towards the polydisperse block.[99, 214-216]

Xie and coworkers first demonstrated that polydisperse block copolymer materials could form multiply continuous network morphologies in 1993.[50] They investigated polydisperse blends of PS-PB-PS triblock copolymers (overall PDI = 1.35) and PVME homopolymers (PDI = 1.70) and reported that the components did not macrophase separate, but adopted a network mesostructure (identified as OBDD but likely gyroid).[50] Several subsequent studies focused on blends of nearly monodisperse diblock copolymers.[73-75, 83] The blends contained bimodal molecular weight distributions in both blocks and typically did not macrophase separate, but formed a well-ordered gyroid mesostructure. These results further demonstrated that narrow molecular weight distributions are not required for network formation.[73-75, 83]

Some groups have postulated that polydispersity could be used to alter the enthalpic/entropic free energy balance and stabilize ordered network mesostructures. Hasegawa et al. speculated that a distribution of block lengths would alleviate packing frustration and stabilize bicontinuous AB block copolymer mesostructures.[217] Martínez-Veracoechea and Escobedo tested this hypothesis by employing lattice Monte Carlo (MC) simulations to interrogate bimodal blends of AB diblock copolymers.[127] They found that bidisperse materials form the gyroid over a broader temperature range in the simulations because the distribution of chain lengths relieves packing frustration, with the longer chains occupying domain centers. These MC results support the idea that bidispersity could be used to stabilize the gyroid mesostructure.[127] Schröder-Turk et al. suggested polydispersity could be used to relieve the packing frustration of complex multiply continuous morphologies in block terpolymer systems.[218] They used geometric arguments to speculate that a complex triply continuous phase (called I-WP) could be

stabilized in certain ABC triblock terpolymers that contain monodisperse A and B domains and C chains with varying lengths.

Several investigations have provided experimental data supporting the notion that polydispersity could stabilize network morphologies.[99, 167, 168] Lynd and Hillmyer identified polydispersity-driven morphological transitions to gyroid at two different compositions in PEP-PLA diblock copolymers with varying polydispersities in the PLA chains.[99] Meuler and colleagues effectively widened the network window in the PI-PS-PEO system using a multicomponent blending strategy.[167, 168] This blending process broadened the molecular weight distribution of the PEO chains and drove a morphological transition from lamellae to Q^{230} in which the domain interface curved towards polydisperse PEO blocks. Blending is a generic process whose only "cost" is the preparation of additional block terpolymers with different compositions and the blending strategy likely can be deployed as a tool to tune phase behavior in many block copolymer systems. Note that polydispersity does not always stabilize network mesostructures, however.[168, 173] Morphological transitions from networks to lamellae were driven by increases in the breadth of the PS molecular weight distribution in PI-PS-PEO triblock terpolymers,[173] although PS polydispersity did not totally eliminate formation of network morphologies.[168] These results demonstrate that the effects of increasing the polydispersity of blocks with dangling chain ends are fundamentally different than the effects brought about by increases in the polydispersity of middle blocks that, due to enthalpic incompatibilities of the adjacent blocks, are forced to bridge the domain.[168]

Thin Films

Thin films of block copolymers have received considerable research attention due to their potential techonological applications in, for example, lithographic processes.[219-221] Generally the phase behavior of block copolymer thin films differs from the bulk materials due to confinement effects related to the film thickness and interactions between the constituent blocks with both the surface and the substrate.[220] Relatively few investigations have focused on thin films of block copolymers that adopt network morphologies in the bulk.[18, 19, 117, 124, 139, 222-226] A few groups have used theoretical simulations to examine gyroid-forming AB diblock copolymers.[124, 222] These investigations suggested that thin film effects frequently, albeit not always, destabilize the gyroid morphology.[124, 222] In experimental investigations, the gyroid has been identified using TEM and/or grazing incident SAXS in relatively thin (~400-700 nm thick, > 5x the domain periodicity) films in a few block copolymer systems, including PI-PPMDS-PI triblock copolymers solvent cast onto silicon,[117] PS-PI diblock copolymers solvent cast onto silicon,[77, 139, 223-225] and P4FS-PLA diblock copolymers solvent cast onto fluorine-doped tin oxide glass substrates.[18, 19] The gyroid has not, to the best of our knowledge, been reported in diblock copolymer films with thicknesses of less than twice the bulk domain periodicity. Epps et al. examined films of PI-PS-PEO triblock terpolymers in this thickness range.[226] As was discussed earlier, multiply continuous network morphologies are stable in the bulk PI-PS-PEO system over wide ranges of compositions.[158, 159, 170] These PI-PS-PEO specimens interrogated by Epps et al. formed Q^{214} in the bulk, but, despite the stability of networks in the bulk, did not adopt a multiply continuous structure in thin films that were cast onto substrates with a

wide variety of surface energies.[226] These results illustrate the difficulties associated with preparing multiply continuous structures in this thickness range. At least one group has fabricated such films, however.[227] Daoulas and colleagues prepared blends of PS-PMMA diblock copolymers and PMMA homopolymers that adopted lamellae in the bulk. These blends were deposited onto a substrate with chemically patterned features with a length scale roughly commensurate with the lamellar domain periodicity. A complicated bicontinuous morphology was reported for certain film thicknesses, illustrating the potential utility of lithographic patterning as a strategy for preparing bicontinuous structures in thin films.[227]

2.7 Physical Properties of Network Morphologies

Viscoelastic Response

While the rheology of microphase-separated block copolymers has been widely studied over the past 30 years,[228] relatively few[35, 98] investigations focused on the viscoelastic response of network-forming materials. Schulz et al. reported in 1994 that a gyroid-forming block copolymer sample had an elastic modulus (G') that varied little over a wide range of frequencies (i.e., a plateau in G') above a crossover frequency ω_{xx} (at ω_{xx}, $G' = G''$). For frequencies below ω_{xx}, the specimen exhibited an inelastic response ($G' < G''$) that Schulz et al. suggested was a result of fluctuations driving the local breaking and reforming of the gyroid mesostructure.[35] In 1999, Kossuth and coworkers detailed the rheological behavior of eleven chemically or architecturally

distinct block copolymer samples that contained cubic mesostructures (gyroid or BCC spheres).[98] These materials were subjected to isochronal temperature ramps, isochronal strain sweeps, and isothermal frequency sweeps, and time-temperature superposition was successfully used to shift the rheological data. Kossuth et al. reported that block copolymer materials containing cubic morphologies exhibited a universal viscoelastic response that is summarized in Figure 2.22. This universality was attributed to the three-dimensional translational order in these mesostructures and demonstrates that rheological data should only be used in a complementary fashion, and not as a principal tool for morphological characterization. At frequencies above ω_{xx}, samples with cubic mesostructures typically had *G'* values that were about an order of magnitude higher than those exhibited by noncubic morphologies such as LAM and HEX. Furthermore, nearly all of the samples that contained a cubic mesostructure exhibited a plateau region in plots of *G'* versus the frequency of the oscillating strain (ω). While the magnitude of the plateau did not depend strongly on the applied strain amplitude, the width of the plateau was highly sensitive to the strain amplitude and degrees of entanglement of the constituent blocks. The materials entered the terminal regime at higher frequencies (i.e., a narrower plateau) for larger applied strain amplitudes and at lower frequencies (i.e., a wider plateau) when at least one of the blocks was well entangled.[98]

The universal viscoelastic response described by Kossuth et al.[98] has been largely confirmed by a number of subsequent publications. Plateaus in *G'* have been reported in block terpolymers containing cubic Q^{230} (core-shell gyroid)[159, 166] and Q^{214} (alternating gyroid)[159] mesostructures, as well as the orthorhombic O^{70} network.[159, 174] Note that it is the triply periodic nature of the symmetry, and not the "connectedness" of

the domains, that is responsible for the plateaus in *G'* exhibited by materials containing network morphologies. A few groups have also reported more detailed theoretical studies of the viscoelastic response of block copolymers containing multiply continuous morphologies.[229-231]

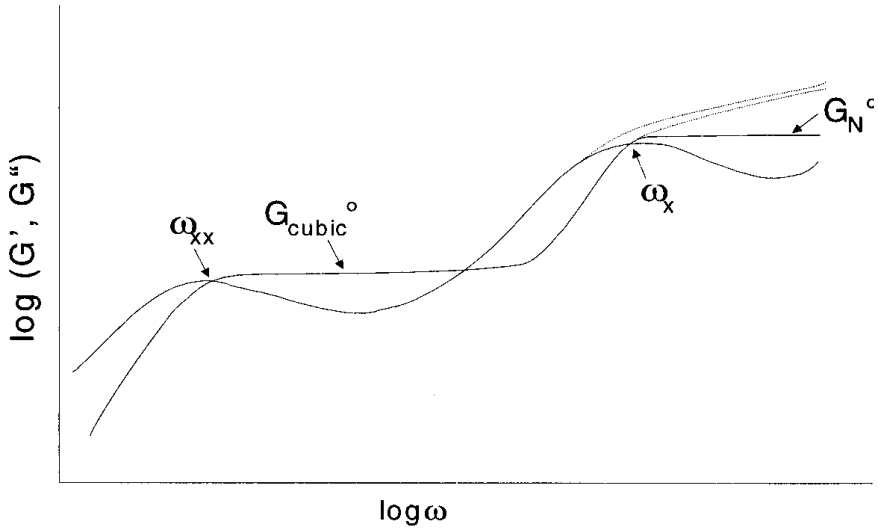

Figure 2.22. Universal viscoelastic response for block copolymers that contain cubic morphologies (including the gyroid) with respect to the entanglement plateau ($G_N°$, solid line) and the knee in the Rouse spectrum for unentangled systems (dashed line). Features that are commonly reported in block copolymer materials include the plateau in *G'* (labeled $G_{cubic}°$) and the crossover of *G'* and *G"* at low frequencies (denoted by ω_{xx}). Figure reproduced from Reference 98.

Mechanical Properties

It has long been recognized that network morphologies could enhance the mechanical properties of block copolymer materials because of the continuity of

multiple domains. Alward et al. did some small-strain mechanical testing in their seminal 1986 paper that first described a bicontinuous morphology in block copolymer materials.[38] They measured the Young's modulus (*E'*) of PS-PI starblock samples with the same composition (30 wt % PS) but different numbers of arms (and thus different mesostructures) over a range of temperatures below the T_g of the PS blocks. The samples that contained a bicontinuous mesostructure had *E'* values that were about an order of magnitude larger than those of the specimens containing a HEX morphology.[38] Additionally, the bicontinuous material, but not the HEX-containing sample, yielded when subjected to uniaxial extension.[40] Both of these phenomena were attributed to the enhanced continuity of the minority PS domains in the bicontinuous morphology.[38, 40]

Dair and coworkers completed the first thorough investigation of the large strain deformation behavior of the gyroid morphology in PS-PI-PS triblock copolymers.[112, 113] This research focused on materials in which glassy PS was the minority component, as triblock copolymers with those compositions had been widely used as thermoplastic elastomers.[232] The first study focused on solution cast polygranular materials.[113] Sample morphologies were changed by adjusting the composition of the PS-PI-PS triblocks (with comparable overall M_n). Each specimen was subjected to tensile testing and stress-strain curves were measured; representative curves for each morphology are provided in Figure 2.23. Dair et al. noted that the mechanical properties were sensitive to the underlying mesostructure. The yield stress was highest for the gyroid-containing sample, even though the LAM-forming specimen had a higher glassy block content. Additionally, only the gyroid curve contained a drop in stress at low strains (~0.2 in Figure 2.23) that was followed by a plateau and subsequent increase in stress with

increasing strain. Dair et al. suggested that this stress-strain behavior was consistent with the formation of a stable neck (confirmed with visual inspection) and eventual drawing. Both the higher yield stress and the necking were attributed to the three-dimensionally continuous glassy PS domains that were uniquely present in the gyroid-containing PS-PI-PS triblock material.[113] The evolution of the underlying (initially gyroid) mesostructure during these stress-strain experiments was also probed using SAXS. The Bragg pattern suddenly changed from rings to streaks at the onset of necking, which Dair et al. posited was the result of a disruption of the PS networks.[113] Sakurai et al. reported a similar sudden change in SAXS data while stretching a gyroid-containing PS-PB-PS triblock that was also attributed to the rupture of the glassy 3-D networks.[115]

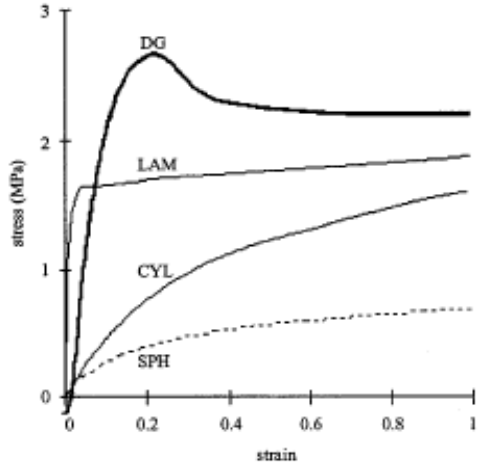

Figure 2.23. Stress-strain curves of polygranular PS-PI-PS samples containing gyroid (DG), LAM, HEX (CYL), and BCC (SPH) morphologies. Figure reproduced from Reference 113.

A second study of Dair et al. focused on the mechanical properties of a PS-PI-PS triblock copolymer film that contained oriented grains of gyroid.[112] This oriented film was prepared by roll casting and annealing a PS-PI-PS triblock. The roll casting process yielded a metastable, aligned HEX mesostructure, and subsequent annealing nucleated and epitaxially grew an equilibrium gyroid morphology with the [111] direction oriented along the cylinder axes.[111] This gyroid-containing film was subjected to tensile tests both along and transverse to the [111] direction.[112] The stress-strain curves obtained from these orthogonal directions were markedly different, as shown in Figure 2.24, indicating that the gyroid exhibits an anisotropic mechanical response. *E'* had a magnitude of 50 MPa along the [111] direction, but only 10 MPa in the transverse direction. Additionally, the sample necked and exhibited a strong Mullins effect when deformed in the [111] direction, but did not neck and only had a weak Mullins effect when stretched in the transverse direction. Dair et al. examined skeletal models of the PS struts and concluded that these mechanical responses were consistent with the PS carrying more of the deformation in the [111] direction and the PI doing so in the transverse direction. The polygranular sample exhibited a mechanical response between those of the [111] and transverse deformations because it contained grains with both extreme, as well as many intermediate, orientations.[112]

Several other groups[114, 233, 234] have published papers that confirmed one of Dair et al.'s[113] findings and disputed another. Sakurai et al. studied the mechanical properties of PS-PB-PS triblock copolymers with $f_S < 0.35$ that formed HEX, gyroid, and LAM.[233, 234] Neither the failure stress nor the strain at break were sensitive to the underlying morphology, but *E'* was; samples containing the gyroid had values of *E'* ~3

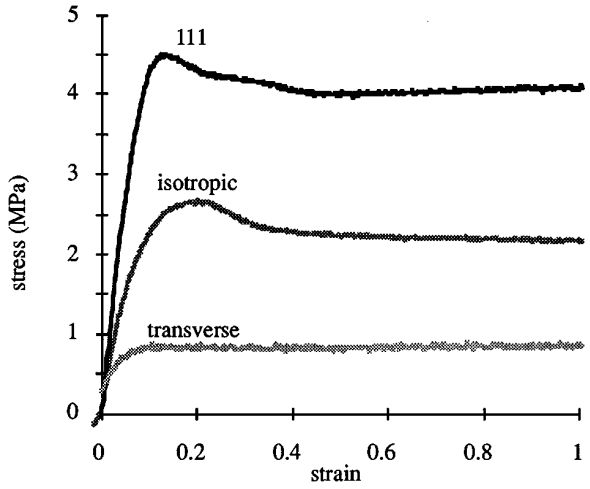

Figure 2.24. Overlaid stress-strain curves of a polygranular gyroid PS-PI-PS sample and of an oriented gyroid PS-PI-PS specimen deformed both along and tranverse to the [111] direction. Figure reproduced from Reference 112.

times as large as those containing HEX,[233, 234] a result in qualitative agreement with both Dair et al.'s[113] and Alward and coworkers'[38, 40] earlier reports. Qiao et al. measured the elastic moduli of PI-PS-PI triblock copolymers and were the first to truly isolate the effects of morphology from factors such as molecular weight and composition.[114] They produced HEX, LAM, and gyroid morphologies from the same PI-PS-PI specimen (M_n = 95 kg/mol, PS wt % = 0.38) by solvent casting the polymer from solvents of varying selectivity. The sample containing the gyroid had an *E'* that was ~3 higher than that containing HEX, in good agreement with previous reports.[38, 40, 113, 233, 234] The aspect of these reports that was not qualitatively consistent was the magnitude of *E'* of gyroid (E_G') relative to *E'* of LAM (E_L'). Dair et al. reported that E_L' was ~4 times *larger* than E_G',[113] Sakurai et al. measured essentially equivalent E_L' and E_G'

values,[233, 234] and Qiao et al. reported that E_L' was ~2 times *smaller* than E_G'.[114] It is not clear why these relative values differ, although the orientation of either LAM and/or gyroid grains may have played a role; both E_G'[112] and E_L'[235] can vary by a factor of ~5 depending on the orientation of the respective mesostructures.

Meuler et al. recently extended the investigation of the mechanical properties of network-containing materials from triblock copolymers to pentablock terpolymers.[174] They used tensile testing to probe the fracture properties of a number of PEO-PS-PI-PS-PEO pentablock samples, all of which were prepared from the same parent PS-PI-PS triblock. This PS-PI-PS core was designed to impart toughness, while the terminal PEO blocks could potentially provide functionality. Two PEO-PS-PI-PS-PEO specimens had terminal PEO block fractional crystallinities above 0.27; one contained three-domain lamellae (LAM_3), and the other the O^{70} network. Phatak and colleagues had previously studied LAM-forming multiblock copolymers that were comprised of a tough triblock core and semicrystalline termini; these materials failed in a brittle fashion for terminal block fractional crystallinities ranging from 0.21 – 0.27.[236] The PEO-PS-PI-PS-PEO materials had fractional crystallinities that exceeded this threshold established by Phatak et al., and the LAM_3-containing specimen failed in a brittle fashion at a strain of 0.06,[174] a result reminiscent of Phatak et al.'s earlier work.[236] The O^{70}-containing sample, in contrast, was quite tough, yielding and deforming prior to failing at a strain of 1.3 and a stress of 4.2 MPa. Meuler et al. attributed this toughness to the network morphology. Unlike LAM_3, O^{70} does not contain any fragile PEO bilayers, and a crack initiated in the PEO domain would have to break the tough PS-PI-PS subdomain at every unit cell in order to propagate through

the material. Meuler et al. suggested that materials with tough cores and fragile bilayers could be toughened by wrapping the bilayers into a 3-D network.[174]

2.8 Applications

A number of publications have focused on the potential applications of the multiply continuous network morphologies formed by block copolymers. Hashimoto et al. prepared the first nanoporous structure prepared from a gyroid precursor in 1997.[78] The PI domains in a gyroid-forming PS-PI diblock copolymer were removed via ozonolysis; the polymer sample was exposed to an ozone atmosphere for 24 hours and then soaked in ethanol for 24 hours. An SEM micrograph of the resulting nanoporous structure is provided in Figure 2.25. The nanochannels in this structure were nonelectrolytically plated with nickel metal by following a detailed procedure and Hashimoto et al. suggested this nickel metal could act as a catalyst on the high surface area support.[78] Nanoporous mesostructures have subsequently been prepared from a variety of gyroid-forming block copolymers. PI chains were removed from PS-PI and P2VP-PI networks by ozonolysis[79] and from PS-PI diblocks via exposure to ultraviolet radiation,[28] PLA and PEO domains were removed from PS-PLA and PS-PEO network materials, respectively, via treatment with hydroiodic acid,[91] and PDMS chains were removed from PS-PDMS specimens by treatment with hydrofluoric acid.[90]

Urbas et al. examined the utility of gyroid-forming diblock copolymers in photonic band gap applications.[28] Calculations suggested that the gyroid is an effective morphology for making photonic crystals, provided the structural features are

commensurate with the wavelength of visible light.[25-27] Urbas et al. prepared a high molecular weight (M_n ~ 750 kg/mol, PS wt% = 0.38) PS-PI diblock copolymer to obtain features on this length scale.[28] A solvent-cast film of the PS-PI specimen contained the gyroid morphology, and the PI domains were degraded and removed by exposure to ultraviolet radiation to improve the dielectric properties. An SEM micrograph of these nanoporous, interpenetrating PS networks is presented in Figure 2.26. Both the intact PS-PI gyroid and the PS networks were tested as photonic crystals, and these specimens reflected visible light with different wavelengths. These results proved that network-forming block copolymers can act as photonic crystals.[28]

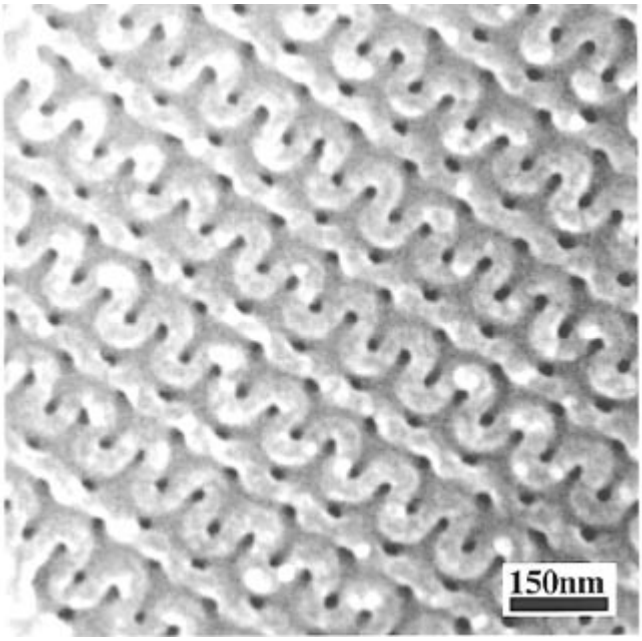

Figure 2.25. SEM micrograph of nanoporous PS following the degradation and removal of the PI chains from a gyroid-forming PS-PI diblock copolymer. Image reproduced from Reference 78.

Chan et al. used a block copolymer network as a precursor to triply periodic nanoporous ceramic films.[117] They synthesized PI-PPMDS-PI triblock copolymers that adopted the gyroid morphology and prepared gyroid films (~700 nm thick) by spin-coating polymer solutions in toluene onto a silicon wafer. These materials were converted into nanoporous ceramic networks following a two step procedure: (i) simultaneously exposing the polymers to a 2% ozone atmosphere and ultraviolet radiation for one hour and (ii) soaking the samples in deionized water overnight. This process degraded and removed the PI domains and transformed the PPMDS into silicon oxycarbide. These high surface area nanoporous ceramic films were solvent resistant and exhibited good high temperature chemical and dimensional stability, and could find

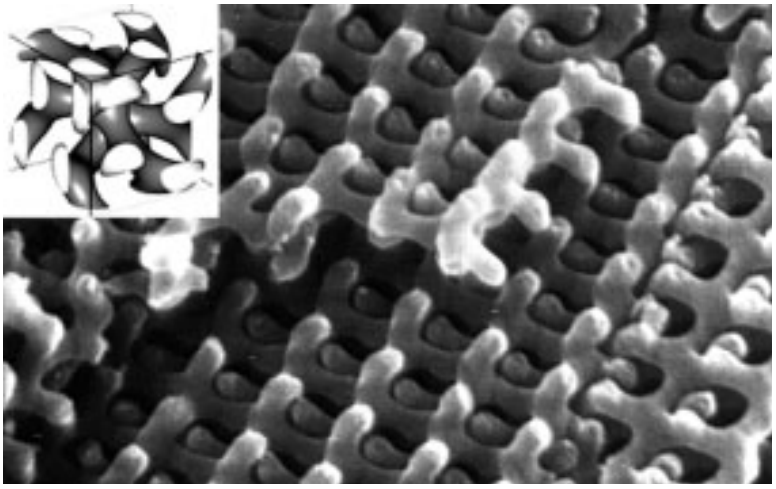

Figure 2.26. SEM image of the interpenetrating PS networks that remain following the removal of the majority PI chains in a gyroid-forming PS-PI diblock by exposure to ultraviolet radiation. The inset is a level set model of the gyroid mesostructure. Figure reproduced from Reference 28.

utility in separations, catalysis, or photonic crystal applications.[117] A variety of ceramic network structures have subsequently been prepared from block copolymer precursors.[95, 237, 238]

Crossland and colleagues incorporated a bicontinuous gyroid network structure into a hybrid bulk heterojunction solar cell.[18, 19] Network mesostructures are especially appealing for solar cell applications because they contain multiply continuous domains and such an interdigitation of continuous donor and acceptor layers is expected to facilitate the separation and extraction of free charges and maximize solar cell efficiency.[17] Crossland et al. used a gyroid-forming P4FS-PLA diblock copolymer as a sacrificial template in their hybrid solar cell fabrication procedure.[18] They solvent cast the diblock sample onto conductive fluorine-doped tin oxide glass substrates and degraded and removed the minority polylactide domains using a NaOH treatment to yield a nanoporous network. Titanium(IV) oxide (TiO_2) was deposited in the nanopores via anodic oxidative hydrolysis of aqueous $TiCl_3$, and the nanoporous P4FS template was removed, and the TiO_2 crystallized, during thermal annealing at 500 °C. The nanoporous TiO_2 was sensitized and converted into a dye-sensitized hybrid solar cell by imbibing dye into the nanopores and thermally evaporating an Ag counter electrode on top of the film. These non-optimized thin film devices had overall power conversion efficiencies of 0.7-1.7%,[18] a performance that is competitive with optimized, state-of-the-art nanoparticle-based dye sensitized solar cells.[36] Devices prepared from a gyroid precursor performed better than those prepared from a HEX template, and Crossland et al. attributed this excellent performance to the continuity of the donating and accepting

channels and the high surface area of the interfaces that were established by the gyroid template.[19]

Table 2.4: Abbreviations for all of the polymers discussed in Chapter 2.

Polymer	Abbreviation
polystyrene	PS
polyisoprene	PI
poly(vinyl methyl ether)	PVME
poly(2-vinylpyridine)	P2VP
poly(4-vinylpyridine)	P4VP
poly(ethylene oxide)	PEO
poly(butylene oxide)	PBO
polydimethylsiloxane	PDMS
polylactide	PLA
poly(ethylene-*alt*-propylene)	PEP
polyethylethylene	PEE
polyethylene	PE
polycyclohexylethylene	PCHE
poly(4-fluorostyrene)	P4FS
polystyrenesulfonate	PSS
polymethylbutylene	PMB
poly(1,1'-ferrocenyldimethylsilane)	PFCDMS
poly(methyl methacrylate)	PMMA
poly(pentamethyldisilylstyrene)	PPMDS
poly(N-isopropylacrylamide)	PNIPAM
poly(*tert*-butyl methacrylate)	PtBMA
poly(propylene oxide)	PPO

2.9 References

(1) Szwarc, M. *Nature* **1956**, *178*, 1168-1169.

(2) Inoue, T.; Soen, T.; Hashimoto, T.; Kawai, H. *J. Polym. Sci., Polym. Phys. Ed.* **1969**, *7*, 1283-1301.

(3) Gervais, M.; Gallot, B. *Makromol. Chem.* **1973**, *171*, 157-178.

(4) Hashimoto, T.; Nagatoshi, K.; Todo, A.; Hasegawa, H.; Kawai, H. *Macromolecules* **1974**, *7*, 364-373.

(5) Helfand, E. *Macromolecules* **1975**, *8*, 552-556.

(6) Helfand, E.; Wasserman, Z. R. *Macromolecules* **1976**, *9*, 879-888.

(7) Leibler, L. *Macromolecules* **1980**, *13*, 1602-1617.

(8) Lynd, N. A.; Meuler, A. J.; Hillmyer, M. A. *Prog. Polym. Sci.* **2008**, *33*, 875-893.

(9) Bates, F. S.; Fredrickson, G. H. *Annu. Rev. Phys. Chem.* **1990**, *41*, 525-557.

(10) Matsen, M. W. *J. Phys.: Condens. Matter* **2002**, *14*, R21-R47.

(11) Khandpur, A. K.; Förster, S.; Bates, F. S.; Hamley, I. W.; Ryan, A. J.; Bras, W.; Almdal, K.; Mortensen, K. *Macromolecules* **1995**, *28*, 8796-8806.

(12) Matsen, M. W.; Bates, F. S. *Macromolecules* **1996**, *29*, 1091-1098.

(13) Cochran, E. W.; Garcia-Cervera, C. J.; Fredrickson, G. H. *Macromolecules* **2006**, *39*, 2449-2451.

(14) Potschke, P.; Paul, D. R. *J. Macromol. Sci., Polym. Rev.* **2003**, *C43*, 87-141.

(15) Pernot, H.; Baumert, M.; Court, F.; Leibler, L. *Nat. Mater.* **2002**, *1*, 54-58.

(16) Shefelbine, T. A.; Vigild, M. E.; Matsen, M. W.; Hajduk, D. A.; Hillmyer, M. A.; Cussler, E. L.; Bates, F. S. *J. Am. Chem. Soc.* **1999**, *121*, 8457-8465.

(17) Yang, X.; Loos, J. *Macromolecules* **2007**, *40*, 1353-1362.

(18) Crossland, E. J. W.; Kamperman, M.; Nedelcu, M.; Ducati, C.; Wiesner, U.; Smilgies, D.; Toombes, G. E. S.; Hillmyer, M. A.; Ludwigs, S.; Steiner, U.; Snaith, H. J. *Nano Lett.* In Press.

(19) Crossland, E. J. W.; Nedelcu, M.; Ducati, C.; Ludwigs, S.; Hillmyer, M. A.; Steiner, U.; Snaith, H. J. *Nano Lett.* In Press.

(20) Yang, S. Y.; Ryu, I.; Kim, H. Y.; Kim, J. K.; Jang, S. K.; Russell, T. P. *Adv. Mater.* **2006**, *18*, 709-712.

(21) Phillip, W. A.; Rzayev, J.; Hillmyer, M. A.; Cussler, E. L. *J. Membr. Sci.* **2006**, *286*, 144-152.

(22) Cho, B. -K.; Jain, A.; Gruner, S. M.; Wiesner, U. *Science* **2004**, *305*, 1598-1601.

(23) Lin, S. Y.; Fleming, J. G.; Hetherington, D. L.; Smith, B. K.; Biswas, R.; Ho, K. M.; Sigalas, M. M.; Zubrzycki, W.; Kurtz, S. R.; Bur, J. *Nature* **1998**, *394*, 251-253.

(24) Campbell, M.; Sharp, D. N.; Harrison, M. T.; Denning, R. G.; Turberfield, A. J. *Nature* **2000**, *404*, 53-56.

(25) Maldovan, M.; Urbas, A. M.; Yufa, N.; Carter, W. C.; Thomas, E. L. *Phys. Rev. B: Condens. Matter* **2002**, *65*, 165123/1-165123/5.

(26) Maldovan, M.; Carter, W. C.; Thomas, E. L. *Appl. Phys. Lett.* **2003**, *83*, 5172-5174.

(27) Maldovan, M.; Ullal, C. K.; Carter, W. C.; Thomas, E. L. *Nat. Mater.* **2003**, *2*, 664-667.

(28) Urbas, A. M.; Maldovan, M.; DeRege, P.; Thomas, E. L. *Adv. Mater.* **2002**, *14*, 1850-1853.

(29) Scriven, L. E. *Nature* **1976**, *263*, 123-125.

(30) Bates, F. S.; Maurer, W. W.; Lipic, P. M.; Hillmyer, M. A.; Almdal, K.; Mortensen, K.; Fredrickson, G. H.; Lodge, T. P. *Phys. Rev. Lett.* **1997**, *79*, 849-852.

(31) Ellison, C. J.; Meuler, A. J.; Qin, J.; Evans, C. M.; Wolf, L. M.; Bates, F. S. *J. Phys. Chem. B* In Press.

(32) Court, F.; Yamaguchi, D.; Hashimoto, T. *Macromolecules* **2006**, *39*, 2596-2605.

(33) Thomas, E. L.; Alward, D. B.; Kinning, D. J.; Martin, D. C.; Handlin, D. L., Jr.; Fetters, L. J. *Macromolecules* **1986**, *19*, 2197-2202.

(34) Hajduk, D. A.; Harper, P. E.; Gruner, S. M.; Honeker, C. C.; Kim, G.; Thomas, E. L.; Fetters, L. J. *Macromolecules* **1994**, *27*, 4063-4075.

(35) Schulz, M. F.; Bates, F. S.; Almdal, K.; Mortensen, K. *Phys. Rev. Lett.* **1994**, *73*, 86-89.

(36) Snaith, H. J.; Schmidt-Mende, L. *Adv. Mater.* **2007**, *19*, 3187-3200.

(37) Schoen, A. H. *NASA TN D-5541* **1970**.

(38) Alward, D. B.; Kinning, D. J.; Thomas, E. L.; Fetters, L. J. *Macromolecules* **1986**, *19*, 215-224.

(39) Aggarwal, S. L. *Polymer* **1976**, *17*, 938-956.

(40) Kinning, D. J.; Thomas, E. L.; Alward, D. B.; Fetters, L. J.; Handlin, D. L.,Jr *Macromolecules* **1986**, *19*, 1288-1290.

(41) Herman, D. S.; Kinning, D. J.; Thomas, E. L.; Fetters, L. J. *Macromolecules* **1987**, *20*, 2940-2942.

(42) Hajduk, D. A.; Harper, P. E.; Gruner, S. M.; Honeker, C. C.; Thomas, E. L.; Fetters, L. J. *Macromolecules* **1995**, *28*, 2570-2573.

(43) Hasegawa, H.; Tanaka, H.; Yamasaki, K.; Hashimoto, T. *Macromolecules* **1987**, *20*, 1651-1662.

(44) Hahn, T., Ed. *International Tables for Crystallography*, 4th revised ed.; 1994; Vol. A.

(45) Thomas, E. L.; Anderson, D. M.; Henkee, C. S.; Hoffman, D. *Nature* **1988**, *334*, 598-601.

(46) Anderson, D. M.; Davis, H. T.; Scriven, L. E.; Nitsche, J. C. C. *Adv. Chem. Phys.* **1990**, *77*, 337-396.

(47) Winey, K. I.; Thomas, E. L.; Fetters, L. J. *Macromolecules* **1992**, *25*, 422-428.

(48) Spontak, R. J.; Smith, S. D.; Ashraf, A. *Macromolecules* **1993**, *26*, 956-962.

(49) Spontak, R. J.; Smith, S. D.; Ashraf, A. *Microsc. Res. Tech.* **1994**, *27*, 412-419.

(50) Xie, R.; Yang, B.; Jiang, B. *Macromolecules* **1993**, *26*, 7097-7099.

(51) Wang, Z. G.; Safran, S. A. *Europhys. Lett.* **1990**, *11*, 425-430.

(52) Anderson, D. M.; Thomas, E. L. *Macromolecules* **1988**, *21*, 3221-3230.

(53) Likhtman, A. E.; Semenov, A. N. *Macromolecules* **1994**, *27*, 3103-3106.

(54) Olmsted, P. D.; Milner, S. T. *Phys. Rev. Lett.* **1994**, *72*, 936-939.

(55) Olmsted, P. D.; Milner, S. T. *Phys. Rev. Lett.* **1995**, *74*, 829.

(56) Semenov, A. N. *Sov. Phys. JETP* **1985**, *61*, 733-742.

(57) Luzzati, V.; Spegt, P. A. *Nature* **1967**, *215*, 701-704.

(58) Mariani, P.; Luzzati, V.; Delacroix, H. *J. Mol. Biol.* **1988**, *204*, 165-189.

(59) Seddon, J. M. *Biochim. Biophys. Acta* **1990**, *1031*, 1-69.

(60) Fontell, K. *Colloid Polym. Sci.* **1990**, *268*, 264-285.

(61) Matsen, M. W.; Schick, M. *Phys. Rev. Lett.* **1994**, *72*, 2660-2663.

(62) Koppi, K. A.; Tirrell, M.; Bates, F. S. *Phys. Rev. Lett.* **1993**, *70*, 1449-1452.

(63) Matsen, M. W.; Schick, M. *Macromolecules* **1994**, *27*, 7157-7163.

(64) Matsen, M. W.; Schick, M. *Macromolecules* **1994**, *27*, 6761-6767.

(65) Matsen, M. W. *Phys. Rev. Lett.* **1995**, *74*, 4225-4228.

(66) Matsen, M. W. *Macromolecules* **1995**, *28*, 5765-5773.

(67) Martínez-Veracoechea, F. J.; Escobedo, F. A. *Macromolecules* **2007**, *40*, 7354-7365.

(68) Matsen, M. W.; Bates, F. S. *Macromolecules* **1996**, *29*, 7641-7644.

(69) Matsen, M. W.; Bates, F. S. *J. Chem. Phys.* **1997**, *106*, 2436-2448.

(70) Gruner, S. M. *J. Phys. Chem.* **1989**, *93*, 7562-7570.

(71) Jinnai, H.; Nishikawa, Y.; Spontak, R. J.; Smith, S. D.; Agard, D. A.; Hashimoto, T. *Phys. Rev. Lett.* **2000**, *84*, 518-521.

(72) Förster, S.; Khandpur, A. K.; Zhao, J.; Bates, F. S.; Hamley, I. W.; Ryan, A. J.; Bras, W. *Macromolecules* **1994**, *27*, 6922-6935.

(73) Spontak, R. J.; Fung, J. C.; Braunfeld, M. B.; Sedat, J. W.; Agard, D. A.; Kane, L.; Smith, S. D.; Satkowski, M. M.; Ashraf, A.; et al *Macromolecules* **1996**, *29*, 4494-4507.

(74) Sakurai, S.; Umeda, H.; Furukawa, C.; Irie, H.; Nomura, S.; Hyun Lee, H.; Kon Kim, J. *J. Chem. Phys.* **1998**, *108*, 4333-4339.

(75) Sakurai, S.; Irie, H.; Umeda, H.; Nomura, S.; Lee, H. H.; Kim, J. K. *Macromolecules* **1998**, *31*, 336-343.

(76) Park, S.; Cho, D.; Ryu, J.; Kwon, K.; Lee, W.; Chang, T. *Macromolecules* **2002**, *35*, 5974-5979.

(77) Park, I.; Lee, B.; Ryu, J.; Im, K.; Yoon, J.; Ree, M.; Chang, T. *Macromolecules* **2005**, *38*, 10532-10536.

(78) Hashimoto, T.; Tsutsumi, K.; Funaki, Y. *Langmuir* **1997**, *13*, 6869-6872.

(79) Hashimoto, T.; Nishikawa, Y.; Tsutsumi, K. *Macromolecules* **2007**, *40*, 1066-1072.

(80) Hwang, J.; Huh, J.; Jung, B.; Hong, J.; Park, M.; Park, C. *Polymer* **2005**, *46*, 9133-9143.

(81) Mareau, V. H.; Matsushita, T.; Nakamura, E.; Hasegawa, H. *Macromolecules* **2007**, *40*, 6916-6921.

(82) Takenaka, M.; Wakada, T.; Akasaka, S.; Nishitsuji, S.; Saijo, K.; Shimizu, H.; Kim, M. I.; Hasegawa, H. *Macromolecules* **2007**, *40*, 4399-4402.

(83) Chen, F.; Kondo, Y.; Hashimoto, T. *Macromolecules* **2007**, *40*, 3714-3723.

(84) Kim, M. I.; Wakada, T.; Akasaka, S.; Nishitsuji, S.; Saijo, K.; Hasegawa, H.; Ito, K.; Takenaka, M. *Macromolecules* **2008**, *41*, 7667-7670.

(85) Schulz, M. F.; Khandpur, A. K.; Bates, F. S.; Almdal, K.; Mortensen, K.; Hajduk, D. A.; Gruner, S. M. *Macromolecules* **1996**, *29*, 2857-2867.

(86) Valkama, S.; Ruotsalainen, T.; Nykaenen, A.; Laiho, A.; Kosonen, H.; ten Brinke, G.; Ikkala, O.; Ruokolainen, J. *Macromolecules* **2006**, *39*, 9327-9336.

(87) Okumura, A.; Nishikawa, Y.; Hashimoto, T. *Polymer* **2006**, *47*, 7805-7812.

(88) Hamley, I. W.; Fairclough, J. P. A.; Ryan, A. J.; Mai, S. -M.; Booth, C. *Phys. Chem. Chem. Phys.* **1999**, *1*, 2097-2101.

(89) Xu, J.; Turner, S. C.; Fairclough, J. P. A.; Mai, S.; Ryan, A. J.; Chaibundit, C.; Booth, C. *Macromolecules* **2002**, *35*, 3614-3621.

(90) Ndoni, S.; Vigild, M. E.; Berg, R. H. *J. Am. Chem. Soc.* **2003**, *125*, 13366-13367.

(91) Mao, H.; Hillmyer, M. A. *Soft Matter* **2006**, *2*, 57-59.

(92) Floudas, G.; Ulrich, R.; Wiesner, U. *J. Chem. Phys.* **1999**, *110*, 652-663.

(93) Floudas, G.; Ulrich, R.; Wiesner, U.; Chu, B. *Europhys. Lett.* **2000**, *50*, 182-188.

(94) Floudas, G.; Vazaiou, B.; Schipper, F.; Ulrich, R.; Wiesner, U.; Iatrou, H.; Hadjichristidis, N. *Macromolecules* **2001**, *34*, 2947-2957.

(95) Toombes, G. E. S.; Finnefrock, A. C.; Tate, M. W.; Ulrich, R.; Wiesner, U.; Gruner, S. M. *Macromolecules* **2007**, *40*, 8974-8982.

(96) Almdal, K.; Mortensen, K.; Ryan, A. J.; Bates, F. S. *Macromolecules* **1996**, *29*, 5940-5947.

(97) Bates, F. S.; Schulz, M. F.; Khandpur, A. K.; Förster, S.; Rosedale, J. H.; Almdal, K.; Mortensen, K. *Faraday Discuss.* **1994**, 7-18.

(98) Kossuth, M. B.; Morse, D. C.; Bates, F. S. *J. Rheol.* **1999**, *43*, 167-196.

(99) Lynd, N. A.; Hillmyer, M. A. *Macromolecules* **2005**, *38*, 8803-8810.

(100) Vigild, M. E.; Almdal, K.; Mortensen, K.; Hamley, I. W.; Fairclough, J. P. A.; Ryan, A. J. *Macromolecules* **1998**, *31*, 5702-5716.

(101) Hillmyer, M. A.; Bates, F. S.; Almdal, K.; Mortensen, K.; Ryan, A. J.; Fairclough, J. P. A. *Science* **1996**, *271*, 976-978.

(102) Hajduk, D. A.; Takenouchi, H.; Hillmyer, M. A.; Bates, F. S.; Vigild, M. E.; Almdal, K. *Macromolecules* **1997**, *30*, 3788-3795.

(103) Hajduk, D. A.; Kossuth, M. B.; Hillmyer, M. A.; Bates, F. S. *J. Phys. Chem. B* **1998**, *102*, 4269-4276.

(104) Bates, F. S.; Schulz, M. F.; Khandpur, A. K.; Förster, S.; Rosedale, J. H. *Faraday Discuss.* **1995**, *98*, 7-18.

(105) Zhao, J.; Majumdar, B.; Schulz, M. F.; Bates, F. S.; Almdal, K.; Mortensen, K.; Hajduk, D. A.; Gruner, S. M. *Macromolecules* **1996**, *29*, 1204-1215.

(106) Davidock, D. A.; Hillmyer, M. A.; Lodge, T. P. *Macromolecules* **2003**, *36*, 4682-4685.

(107) Park, M. J.; Balsara, N. P. *Macromolecules* **2008**, *41*, 3678-3687.

(108) Kloninger, C.; Rehahn, M. *Macromolecules* **2004**, *37*, 8319-8324.

(109) Laurer, J. H.; Hajduk, D. A.; Fung, J. C.; Sedat, J. W.; Smith, S. D.; Gruner, S. M.; Agard, D. A.; Spontak, R. J. *Macromolecules* **1997**, *30*, 3938-3941.

(110) Avgeropoulos, A.; Dair, B. J.; Hadjichristidis, N.; Thomas, E. L. *Macromolecules* **1997**, *30*, 5634-5642.

(111) Dair, B. J.; Avgeropoulos, A.; Hadjichristidis, N.; Capel, M.; Thomas, E. L. *Polymer* **2000**, *41*, 6231-6236.

(112) Dair, B. J.; Avgeropoulos, A.; Hadjichristidis, N.; Thomas, E. L. *J. Mater. Sci.* **2000**, *35*, 5207-5213.

(113) Dair, B. J.; Honeker, C. C.; Alward, D. B.; Avgeropoulos, A.; Hadjichristidis, N.; Fetters, L. J.; Capel, M.; Thomas, E. L. *Macromolecules* **1999**, *32*, 8145-8152.

(114) Qiao, L.; Leibig, C.; Hahn, S. F.; Winey, K. I. *Ind. Eng. Chem. Res.* **2006**, *45*, 5598-5602.

(115) Sakurai, S.; Isobe, D.; Okamoto, S.; Yao, T.; Nomura, S. *Phys. Rev. E: Stat., Nonlinear, Soft Matter Phys.* **2001**, *63*, 061803/1-061803/5.

(116) Avgeropoulos, A.; Chan, V. Z.; Lee, V. Y.; Ngo, D.; Miller, R. D.; Hadjichristidis, N.; Thomas, E. L. *Chem. Mater.* **1998**, *10*, 2109-2115.

(117) Chan, V. Z. -H.; Hoffman, J.; Lee, V. Y.; Latrou, H.; Avgeropoulos, A.; Hadjichristidis, N.; Miller, R. D; Thomas, E. L. *Science* **1999**, *286*, 1716-1719.

(118) Nykaenen, A.; Nuopponen, M.; Laukkanen, A.; Hirvonen, S.; Rytelae, M.; Turunen, O.; Tenhu, H.; Mezzenga, R.; Ikkala, O.; Ruokolainen, J. *Macromolecules* **2007**, *40*, 5827-5834.

(119) Tselikas, Y.; Hadjichristidis, N.; Lescanec, R. L.; Honeker, C. C.; Wohlgemuth, M.; Thomas, E. L. *Macromolecules* **1996**, *29*, 3390-3396.

(120) Matsen, M. W. *J. Chem. Phys.* **2000**, *113*, 5539-5544.

(121) Matsen, M. W.; Bates, F. S. *J. Polym. Sci. Part B* **1997**, *35*, 945-952.

(122) Matsen, M. W.; Thompson, R. B. *J. Chem. Phys.* **1999**, *111*, 7139-7146.

(123) Nonomura, M.; Yamada, K.; Ohta, T. *J. Phys.: Condens. Matter* **2003**, *15*, L423-L430.

(124) Podariu, I.; Chakrabarti, A. *J. Chem. Phys.* **2003**, *118*, 11249-11257.

(125) Sun, P.; Yin, Y.; Li, B.; Chen, T.; Jin, Q.; Ding, D.; Shi, A. *Phys. Rev. E: Stat., Nonlinear, Soft Matter Phys.* **2005**, *72*, 061408/1-061408/6.

(126) Abu-Sharkh, B.; AlSunaidi, A. *Macromol. Theory Simul.* **2006**, *15*, 507-515.

(127) Martínez-Veracoechea, F. J.; Escobedo, F. A. *Macromolecules* **2005**, *38*, 8522-8531.

(128) Martínez-Veracoechea, F. J.; Escobedo, F. A. *J. Chem. Phys.* **2006**, *125*, 104907/1-104907/12.

(129) Ranjan, A.; Qin, J.; Morse, D. C. *Macromolecules* **2008**, *41*, 942-954.

(130) Likhtman, A. E.; Semenov, A. N. *Macromolecules* **1997**, *30*, 7273-7278.

(131) Olmsted, P. D.; Milner, S. T. *Macromolecules* **1998**, *31*, 4011-4022.

(132) Davidock, D. A.; Hillmyer, M. A.; Lodge, T. P. *Macromolecules* **2004**, *37*, 397-407.

(133) Lipic, P. M.; Bates, F. S.; Matsen, M. W. *J. Polym. Sci. Part B* **1999**, *37*, 2229-2238.

(134) Matsen, M. W. *Phys. Rev. Lett.* **1998**, *80*, 4470-4473.

(135) Wang, C.; Lodge, T. P. *Macromol. Rapid Commun.* **2002**, *23*, 49-54.

(136) Wang, C.; Lodge, T. P. *Macromolecules* **2002**, *35*, 6997-7006.

(137) Chastek, T. Q.; Lodge, T. P. *Macromolecules* **2003**, *36*, 7672-7680.

(138) Ahn, J.; Zin, W. *Macromol. Res.* **2003**, *11*, 152-156.

(139) Park, H.; Jung, J.; Chang, T.; Matsunaga, K.; Jinnai, H. *J. Am. Chem. Soc.* **2009**, *131*, 46-47.

(140) Bates, F. S.; Fredrickson, G. H. *Phys. Today* **1999**, *52*, 32-38.

(141) Mogi, Y.; Kotsuji, H.; Kaneko, Y.; Mori, K.; Matsushita, Y.; Noda, I. *Macromolecules* **1992**, *25*, 5408-5411.

(142) Mogi, Y.; Mori, K.; Matsushita, Y.; Noda, I. *Macromolecules* **1992**, *25*, 5412-5415.

(143) Mogi, Y.; Nomura, M.; Kotsuji, H.; Ohnishi, K.; Matsushita, Y.; Noda, I. *Macromolecules* **1994**, *27*, 6755-6760.

(144) Matsen, M. W. *J. Chem. Phys.* **1998**, *108*, 785-796.

(145) Bailey, T. S.; Pham, H. D.; Bates, F. S. *Macromolecules* **2001**, *34*, 6994-7008.

(146) Phan, S.; Fredrickson, G. H. *Macromolecules* **1998**, *31*, 59-63.

(147) Dotera, T.; Hatano, A. *J. Chem. Phys.* **1996**, *105*, 8413-8427.

(148) Dotera, T. *Phys. Rev. Lett.* **2002**, *89*, 205502/1-205502/4.

(149) Xi, H.; Milner, S. T. *Macromolecules* **1996**, *29*, 2404-2411.

(150) Matsushita, Y.; Tamura, M.; Noda, I. *Macromolecules* **1994**, *27*, 3680-3682.

(151) Verdier, P. H.; Stockmayer, W. H. *J. Chem. Phys.* **1962**, *36*, 227-235.

(152) Matsushita, Y.; Suzuki, J.; Seki, M. *Physica B* **1998**, *248*, 238-242.

(153) Matsushita, Y.; Torikai, N.; Suzuki, J.; Seki, M. *J. Phys. Chem. Solids* **1999**, *60*, 1279-1284.

(154) Seki, M.; Suzuki, J.; Matsushita, Y. *J. Appl. Crystallogr.* **2000**, *33*, 285-290.

(155) Suzuki, J.; Seki, M.; Matsushita, Y. *J. Chem. Phys.* **2000**, *112*, 4862-4868.

(156) Zheng, W.; Wang, Z. *Macromolecules* **1995**, *28*, 7215-7223.

(157) Suzuki, J.; Nakane, K.; Takano, A.; Matsushita, Y. *Polymer* **2004**, *45*, 8989-8997.

(158) Epps, T. H., III; Cochran, E. W.; Hardy, C. M.; Bailey, T. S.; Waletzko, R. S.; Bates, F. S. *Macromolecules* **2004**, *37*, 7085-7088.

(159) Epps, T. H., III; Cochran, E. W.; Bailey, T. S.; Waletzko, R. S.; Hardy, C. M.; Bates, F. S. *Macromolecules* **2004**, *37*, 8325-8341.

(160) Frielinghaus, H.; Hermsdorf, N.; Almdal, K.; Mortensen, K.; Messe, L.; Corvazier, L.; Fairclough, J. P. A.; Ryan, A. J.; Olmsted, P. D.; Hamley, I. W. *Europhys. Lett.* **2001**, *53*, 680-686.

(161) Goldacker, T.; Abetz, V. *Macromolecules* **1999**, *32*, 5165-5167.

(162) Goldacker, T.; Abetz, V.; Stadler, R.; Erukhimovich, I.; Leibler, L. *Nature* **1999**, *398*, 137-139.

(163) Hückstädt, H.; Goldacker, T.; Goepfert, A.; Abetz, V. *Macromolecules* **2000**, *33*, 3757-3761.

(164) Sugiyama, M.; Shefelbine, T. A.; Vigild, M. E.; Bates, F. S. *J. Phys. Chem. B* **2001**, *105*, 12448-12460.

(165) Hardy, C. M.; Bates, F. S.; Kim, M.; Wignall, G. D. *Macromolecules* **2002**, *35*, 3189-3197.

(166) Chatterjee, J.; Jain, S.; Bates, F. S. *Macromolecules* **2007**, *40*, 2882-2896.

(167) Meuler, A. J.; Ellison, C. J.; Hillmyer, M. A.; Bates, F. S. *Macromolecules* **2008**, *41*, 6272-6275.

(168) Meuler, A. J.; Ellison, C. J.; Qin, J.; Evans, C. M.; Hillmyer, M. A.; Bates, F. S. *Manuscript in Preparation.*

(169) Bates, F. S. *MRS Bull.* **2005**, *30*, 525-532.

(170) Bailey, T. S.; Hardy, C. M.; Epps, T. H., III; Bates, F. S. *Macromolecules* **2002**, *35*, 7007-7017.

(171) Tyler, C. A.; Qin, J.; Bates, F. S.; Morse, D. C. *Macromolecules* **2007**, *40*, 4654-4668.

(172) Epps, T. H., III; Bates, F. S. *Macromolecules* **2006**, *39*, 2676-2682.

(173) Meuler, A. J.; Ellison, C. J.; Evans, C. M.; Hillmyer, M. A.; Bates, F. S. *Macromolecules* **2007**, *40*, 7072-7074.

(174) Meuler, A. J.; Fleury, G.; Hillmyer, M. A.; Bates, F. S. *Macromolecules* **2008**, *41*, 5809-5817.

(175) Epps, T. H., III; Bailey, T. S.; Waletzko, R.; Bates, F. S. *Macromolecules* **2003**, *36*, 2873-2881.

(176) Epps, T. H., III; Chatterjee, J.; Bates, F. S. *Macromolecules* **2005**, *38*, 8775-8784.

(177) Cavicchi, K. A.; Lodge, T. P. *Macromolecules* **2003**, *36*, 7158-7164.

(178) Cavicchi, K. A.; Lodge, T. P. *Macromolecules* **2004**, *37*, 6004-6012.

(179) Cochran, E. W.; Bates, F. S. *Phys. Rev. Lett.* **2004**, *93*, 087802-1.

(180) Bluemle, M. J.; Fleury, G; Lodge, T. P.; Bates, F. S. *Manuscript in Preparation*

(181) Erukhimovich, I. Y. *Eur. Phys. J. E Soft Matter* **2005**, *18*, 383-406.

(182) Tyler, C. A.; Morse, D. C. *Phys. Rev. Lett.* **2005**, *94*, 208302/1-208302/4.

(183) Guo, Z.; Zhang, G.; Qiu, F.; Zhang, H.; Yang, Y.; Shi, A. *Phys. Rev. Lett.* **2008**, *101*, 028301/1-028301/4.

(184) Erukhimovich, I.; Abetz, V.; Stadler, R. *Macromolecules* **1997**, *30*, 7435-7443.

(185) Drolet, F.; Fredrickson, G. H. *Phys. Rev. Lett.* **1999**, *83*, 4317-4320.

(186) Bohbot-Raviv, Y.; Wang, Z. *Phys. Rev. Lett.* **2000**, *85*, 3428-3431.

(187) Abetz, V.; Goldacker, T. *Macromol. Rapid Commun.* **2000**, *21*, 16-34.

(188) Ranjan, A.; Morse, D. C. *Phys. Rev. E: Stat., Nonlinear, and Soft Matter Phys.* **2006**, *74*, 011803/1-011803/6.

(189) Yamada, K.; Nonomura, M.; Ohta, T. *J. Phys: Condens. Matter* **2006**, *18*, L421-L427.

(190) Miao, B.; Wickham, R. A. *J. Chem. Phys.* **2008**, *128*, 054902/1-054902/5.

(191) Fredrickson, G. H.; Helfand, E. *J. Chem. Phys.* **1987**, *87*, 697-705.

(192) Brazovskii, S. A. *Sov. Phys. JETP* **1975**, *41*, 85.

(193) Wells, A. F. *Three-Dimensional Nets and Polyhedra;* John Wiley & Sons: New York, NY 1977.

(194) Jain, S.; Bates, F. S. *Science* **2003**, *300*, 460-464.

(195) Jain, S.; Gong, X.; Scriven, L. E.; Bates, F. S. *Phys. Rev. Lett.* **2006**, *96*, 138304/1-138304/4.

(196) Hanley, K. J.; Lodge, T. P.; Huang, C. *Macromolecules* **2000**, *33*, 5918-5931.

(197) Lodge, T. P.; Pudil, B.; Hanley, K. J. *Macromolecules* **2002**, *35*, 4707-4717.

(198) Lodge, T. P.; Hanley, K. J.; Pudil, B.; Alahapperuma, V. *Macromolecules* **2003**, *36*, 816-822.

(199) Park, S.; Sul, W. *Polymer* **2008**, *49*, 3327-3334.

(200) Alexandridis, P.; Olsson, U.; Lindman, B. *Macromolecules* **1995**, *28*, 7700-7710.

(201) Alexandridis, P.; Olsson, U.; Lindman, B. *J. Phys. Chem.* **1996**, *100*, 280-288.

(202) Alexandridis, P.; Olsson, U.; Lindman, B. *Langmuir* **1998**, *14*, 2627-2638.

(203) Svensson, B.; Alexandridis, P.; Olsson, U. *J. Phys. Chem. B* **1998**, *102*, 7541-7548.

(204) Alexandridis, P.; Olsson, U.; Lindman, B. *Langmuir* **1997**, *13*, 23-34.

(205) Alexandridis, P. *Macromolecules* **1998**, *31*, 6935-6942.

(206) Bodycomb, J.; Yamaguchi, D.; Hashimoto, T. *Macromolecules* **2000**, *33*, 5187-5197.

(207) Laurer, J. H.; Hajduk, D. A.; Dreckoetter, S.; Smith, S. D.; Spontak, R. J. *Macromolecules* **1998**, *31*, 7546-7549.

(208) Epps, T. H.,III; Bailey, T. S.; Pham, H. D.; Bates, F. S. *Chem. Mater.* **2002**, *14*, 1706-1714.

(209) Robitaille, C. D.; Fauteux, D. *J. Electrochem. Soc.* **1986**, *133*, 315-325.

(210) Chandrasekhar, V. *Adv. Polym. Sci.* **1998**, *135*, 139-205.

(211) Singh, M.; Odusanya, O.; Wilmes, G. M.; Eitouni, H. B.; Gomez, E. D.; Patel, A. J.; Chen, V. L.; Park, M. J.; Fragouli, P.; Iatrou, H.; Hadjichristidis, N.; Cookson, D.; Balsara, N. P. *Macromolecules* **2007**, *40*, 4578-4585.

(212) Park, M. J.; Downing, K. H.; Jackson, A.; Gomez, E. D.; Minor, A. M.; Cookson, D.; Weber, A. Z.; Balsara, N. P. *Nano Lett.* **2007**, *7*, 3547-3552.

(213) Park, M. J.; Nedoma, A. J.; Geissler, P. L.; Balsara, N. P.; Jackson, A.; Cookson, D. *Macromolecules* **2008**, *41*, 2271-2277.

(214) Lynd, N. A.; Hillmyer, M. A.; Matsen, M. W. *Macromolecules* **2008**, *41*, 4531-4533.

(215) Cooke, D. M.; Shi, A. *Macromolecules* **2006**, *39*, 6661-6671.

(216) Matsen, M. W. *Phys. Rev. Lett.* **2007**, *99*, 148304/1-148304/4.

(217) Hasegawa, H.; Hashimoto, T.; Hyde, S. T. *Polymer* **1996**, *37*, 3825-3833.

(218) Schröder-Turk, G. E.; Fogden, A.; Hyde, S. T. *Eur. Phys. J. B* **2007**, *59*, 115-126.

(219) Russell, T. P. *Curr. Opin. Colloid Interface Sci.* **1996**, *1*, 107.

(220) Fasolka, M. J.; Mayes, A. M. *Annu. Rev. Mater. Res.* **2001**, *31*, 323-355.

(221) Park, C.; Yoon, J.; Thomas, E. L. *Polymer* **2003**, *44*, 6725-6760.

(222) Yin, Y.; Sun, P.; Jiang, R.; Li, B.; Chen, T.; Jin, Q.; Ding, D.; Shi, A. *J. Chem. Phys.* **2006**, *124*, 184708/1-184708/8.

(223) Lee, B.; Park, I.; Yoon, J.; Park, S.; Kim, J.; Kim, K.; Chang, T.; Ree, M. *Macromolecules* **2005**, *38*, 4311-4323.

(224) Jin, S.; Yoon, J.; Heo, K.; Park, H. W.; Kim, J.; Kim, K. W.; Shin, T. J.; Chang, T.; Ree, M. *J. Appl. Crystallogr.* **2007**, *40*, 950-958.

(225) Park, H.; Im, K.; Chung, B.; Ree, M.; Chang, T.; Sawa, K.; Jinnai, H. *Macromolecules* **2007**, *40*, 2603-2605.

(226) Epps, T. H., III; DeLongchamp, D. M.; Fasolka, M. J.; Fischer, D. A.; Jablonski, E. L. *Langmuir* **2007**, *23*, 3355-3362.

(227) Daoulas, K. C.; Muller, M.; Stoykovich, M. P.; Park, S.; Papakonstantopoulos, Y. J.; de Pablo, J. J.; Nealey, P. F.; Solak, H. H. *Phys. Rev. Lett.* **2006**, *96*, 036104/1-036104/4.

(228) Fredrickson, G. H.; Bates, F. S. *Ann. Rev. Mater. Sci.* **1996**, *26*, 501-550.

(229) Tyler, C. A.; Morse, D. C. *Macromolecules* **2003**, *36*, 3764-3774.

(230) Yamada, K.; Ohta, T. *Europhys. Lett.* **2006**, *73*, 614-620.

(231) Tamate, R.; Yamada, K.; Vinals, J.; Ohta, T. *J. Phys. Soc. Jpn.* **2008**, *77*, 034802/1-034802/6.

(232) Holden, G.; Legge, N. R. In *Thermoplastic Elastomers*; 2nd ed.; Holden, G., Legge, N. R., Quirk, R. P., Schroeder, H. E., Eds.; Hansen Publishers: New York, NY, 1996; pp 48-69.

(233) Sakurai, S.; Isobe, D.; Okamoto, S.; Nomura, S. *Mater. Sci. Res. Int.* **2001**, *7*, 225-228.

(234) Sakurai, S.; Isobe, D.; Okamoto, S.; Nomura, S. *J. Macromol. Sci., Phys.* **2002**, *B41*, 387-395.

(235) Cohen, Y.; Albalak, R. J.; Dair, B. J.; Capel, M. S.; Thomas, E. L. *Macromolecules* **2000**, *33*, 6502-6516.

(236) Phatak, A.; Lim, L. S.; Reaves, C. K.; Bates, F. S. *Macromolecules* **2006**, *39*, 6221-6228.

(237) Finnefrock, A. C.; Ulrich, R.; Du Chesne, A.; Honeker, C. C.; Schumacher, K.; Unger, K. K.; Gruner, S. M.; Wiesner, U. *Angew. Chem., Int. Ed.* **2001**, *40*, 1208-1211.

(238) Finnefrock, A. C.; Ulrich, R.; Toombes, G. E. S.; Gruner, S. M.; Wiesner, U. *J. Am. Chem. Soc.* **2003**, *125*, 13084-13093.

3

General Experimental Techniques

This Chapter contains general information about the experimental techniques that were used in this research. The focus is generally on concepts, with detailed experimental procedures being provided within Chapters 4-6.

3.1 Living Anionic Polymerization

General Aspects. A living anionic polymerization was first described by Szwarc in a seminal 1956 publication.[1] Szwarc considered the polymerization "living" because, under the reaction conditions, the active anion did not terminate or participate in chain transfer reactions but persisted indefinitely upon depletion of the available monomer (provided no impurities entered the reaction vessel). Propagation could resume upon the addition of more monomer. This feature has made living anionic polymerization a mainstay of block copolymer synthesis, as chemically distinct monomers can be polymerized in succession, provided the living anion reacts with each additional monomer.[2] Typically block sizes are controlled by adding known amounts of monomer and allowing the reaction to proceed until all of the monomer has been incorporated into the polymer.

Molecular Weight Distributions. At least four kinetic events occur during living anionic polymerization. The initiator first dissociates (alkyllithium compounds tend to aggregate in nonpolar media) and then initiates the polymerization. The active center propagates and adds monomer before terminating, typically by reaction with a protic species (e.g., methanol) that was controllably added to the reactor. These general steps are shown below for an alkyllithium initiator. Here the charged species are shown as ion pairs although some may exist as free ions.[3]

$$\text{Dissociation: } \left(\text{I}-\text{Li}\right)_{\text{n}} \xrightarrow{k_d} \text{nI}^{-}\text{Li}^{+} \tag{3-1}$$

$$\text{Initiation: } \text{Li}^{+}\text{I}^{-} + \text{M} \xrightarrow{k_i} \text{Li}^{+}\left(\text{I}-\text{M}\right)^{-} \tag{3-2}$$

$$\text{Propagation: } \begin{array}{l} \text{Li}^{+}\left(\text{I}-\text{M}\right)^{-} + \text{M} \xrightarrow{k_p} \text{Li}^{+}\left(\text{I}-\text{M}_2\right)^{-} \\ \text{Li}^{+}\left(\text{I}-\text{M}_{\text{N}}\right)^{-} + \text{M} \xrightarrow{k_p} \text{Li}^{+}\left(\text{I}-\text{M}_{\text{N+1}}\right)^{-} \end{array} \tag{3-3}$$

$$\text{Termination: } \text{Li}^{+}\left(\text{I}-\text{M}_{\text{N}}\right)^{-} + \text{H}-\text{Y} \xrightarrow{k_f} \left(\text{I}-\text{M}_{\text{N}}-\text{H}\right) + \text{Li}^{+}\text{Y}^{-} \tag{3-4}$$

The shape and breadth of the resulting molecular weight distribution are largely governed by the relative rates of dissociation, initiation, and propagation, provided termination and chain transfer rates are negligible. When the rates of dissociation and initiation are much greater than the rate of propagation, all chains grow for essentially the same amount of time and the polymers are characterized by a Poisson distribution of molecular weights. The polydispersity index (PDI) of such a distribution is given by:

$$\text{PDI} = \frac{M_w}{M_n} \approx 1 + \frac{1}{N} \tag{3-5}$$

where N is the degree of polymerization, M_w the weight average molecular weight, and M_n the number average molecular weight. According to this expression, as N increases, the PDI asymptotically approaches 1. Although this Poisson expression does not

rigorously describe real systems (due to effects such as imperfect mixing), typically living anionic polymerizations yield narrow molecular weight distributions ($M_w/M_n < 1.1$)[4] because they are characterized by dissociation and initiation rates that exceed the rate of propagation. (A notable exception to this typical behavior will be discussed in Chapter 4.) Most investigations of block copolymers reported in the literature have focused on molecules prepared by living anionic polymerization that have narrow block molecular weight distributions.[5] Some researchers have even suggested that narrow molecular weight distributions are required in order for block copolymers to self-assemble into well-ordered morphologies.[6] This claim is incorrect,[7] as will be illustrated by the results presented in Chapter 6.

Monomers. Only a limited number of monomers are amenable to polymerizations by living anionic mechanisms. Monomers must have unsaturation from a double bond or a cyclic structure to undergo living anionic polymerization. While unsaturation is a necessary feature, it is not sufficient, as unsaturated monomers are not always amenable to living anionic polymerization. Thermodynamics does not typically limit the polymerization of these monomers, as breaking a double bond or relieving ring strain typically decreases free energy. It is the stability of the anion at the end of the propagating chain that limits the number of unsaturated monomers available for living anionic polymerization. The monomers added to the propagating chain must stabilize the propagating carbanion and prevent termination. Adequate carbanion stabilization can be provided by electron withdrawing groups such as phenyls, carbonyls, double bonds, or nitro groups.[3] Propagation does not always occur solely because the living carbanions are stable. The active chain ends also must exhibit nucleophilicity towards

the monomers remaining in solution or propagation will not occur. For example, ethylene oxide will not polymerize in a nonpolar medium when Li^+ is the counterion, even when the oxanion is stable.[8] Ethylene oxide will polymerize in polar tetrahydrofuran when K^+ is the counterion.[9] Successful block copolymer synthesis requires a crossover from the carbanion of one monomer to the carbanion of another. The stability of the second carbanion must be roughly equal to or greater than that of the first in order for this crossover to occur. The second block molecular weight distribution is sensitive to the rate of the crossover reaction, and a Poisson distribution will only be obtained when the crossover rate exceeds the propagation rate.

The research described in this Thesis focused on materials comprised of polystyrene (PS), polyisoprene (PI), and poly(ethylene oxide) (PEO) blocks. The corresponding styrene, isoprene, and ethylene oxide monomers were all polymerized using living anionic polymerization. The phenyl group stabilizes the propagating polystyryl anion and breaking the double bond provides the thermodynamic driving force. The second double bond in the isoprene provides resonance stabilization for the propagating polyisoprenyl carbanion and breaking the double bond provides the thermodynamic driving force. The electrophilic oxygen stabilizes the propagating ethylene oxide carbanion and strain relief from the opening of the three-membered ring provides the thermodynamic driving force.

Counterions and Reaction Media. Living anionic polymerization requires the use of aprotic solvents, as protons would terminate the propagating chains. Cyclohexane (CHX) and tetrahydrofuran (THF) are the aprotic solvents used in this research. THF is required for ethylene oxide polymerization while CHX is selected for isoprene and

styrene polymerization. Organolithium initiators do not facilitate ethylene oxide polymerization because of the oxophilicity of the Li^+ counterion.[10] Less tightly bound counterions, such as K^+, must be employed to allow the chain end to interact with ethylene oxide monomers and propagate. These counterions are typically larger than Li^+ and will not dissociate in nonpolar solvents such as CHX; polar media such as THF are required for successful polymerizations with these counterions. The organolithium initiators do promote isoprene and styrene polymerization and are active in nonpolar solvents even though the Li^+ counterions and carbanion chain ends tend to form aggregates in these media.[11] The chains ends in the aggregate react directly with the monomer, leading to chain propagation. Polar THF decreases the amount of aggregation and increases the propagation rate compared to CHX because more of the charged species are present as free ions. Despite the higher reaction rates obtained in THF, CHX is used for styrene and isoprene polymerization in this research because of the influence of the solvent on the isoprene regiochemistry. A living anionic polymerization of isoprene in CHX at 40 °C with Li^+ cations is expected to yield approximately 95% 1,4-addition, with the remainder adding 3,4.[12] The 1,4-microstructure has a lower T_g and more desirable elastomeric properties than its 3,4-counterpart.[13] These attributes are beneficial from a mechanical properties standpoint, as will be discussed in Chapter 5.

Solvent and Monomer Purifications. Eliminating chain transfer and termination reactions is essential for successful living anionic polymerizations and requires the absolute absence of any species that terminate the active carbanions. Oxygen, carbon dioxide, water, and other protic impurities must be removed from the solvents, monomers, and reaction vessels that are used during polymer synthesis. The

Schlenk vacuum line techniques used to manipulate the air and moisture sensitive compounds are described in the literature[14] (and commonly used in both the Bates and Hillmyer groups). In this research program all reactions were performed under an inert argon atmosphere. The CHX and THF reaction solvents were purified using column systems, as the operation of stills is very dangerous. Both solvents were initially sparged with Argon to remove oxygen and stored under 15 psi argon pressure. CHX was then purified by sequential passage through activated alumina followed by Q-5 (Englehard) to remove protic impurities and trace oxygen.[15] THF was purified using a similar procedure, except both columns contained activated alumina because of the reactivity of the Q-5 redox catalyst towards ether functional groups. The monomer purifications are described in detail in the following paragraph.

The styrene, isoprene, and ethylene oxide monomers were purified by (i) subjecting the monomers to a freeze-pump-thaw process to remove oxygen (ii) twice stirring the monomers for ~45 minutes over dibutylmagnesium for (styrene), *n*-butyllithium (isoprene), or butylmagnesiumchloride (ethylene oxide). Stirring the monomers over these purification agents removes inhibitors and other impurities. The choice of purification agent (*n*-butyllithium is the most reactive and butylmagnesiumchloride the least reactive) depends on the temperature of the purification and the reactivity of the monomer. Styrene has a low vapor pressure (boiling point of 145.2 °C) and purification can be performed at 40 °C without generating an overpressure that is unsuitable for glassware. This relatively high temperature allows for use of dibutylmagnesium; the more reactive *n*-butyllithium will initiate styrene polymerizations at this temperature. In contrast to styrene, the vapor

pressures of isoprene and ethylene oxide are quite high (boiling points of 34 °C and 10.7 °C, respectively). [*CAUTION: Ethylene oxide is a toxic gas at room temperature and must be handled with extreme care.*] The heat released during the purification reactions can lead a dangerous increase in vapor pressure; running these purification reactions in an ice bath removes heat and maintains the vapor pressure at safe levels (and, in the case of ethylene oxide, allows the monomer to be handled in the liquid state). A decrease in temperature lowers the activity of the purification agent. As a result, the highly reactive *n*-butyllithium can be used to purify isoprene. Despite the 0 °C temperature, the mild butylmagnesiumchloride is used to purify ethylene oxide. Reactive *n*-butyllithium is not used because it would open the ethylene oxide ring and produce alkoxides, depleting the monomer. Dibutylmagnesium is not used because some previous group members reported sporadic sparking when ethylene oxide was mixed with commercial dibutylmagnesium, possibly due to the presence of triethylaluminum added to the dibutylmagnesium by vendors to reduce viscosity. All monomers are vacuum distilled into an evacuated, flame treated burette prior to addition to the reaction vessel.

3.2 Size Exclusion Chromatography (SEC)

One of the fundamental characteristics of any polymer is its molecular weight distribution. This important property is typically measured using the liquid chromatography technique size exclusion chromatography (SEC) (sometimes referred to as gel permeation chromatography (GPC)). In SEC, a dilute (~1 mg/mL) solution of

the polymer (“mobile phase”) passes through a series of columns packed with various sizes of porous particles (“stationary phase”). Solutes, in this case the polymer chains, are retained in the columns to varying degrees depending on their hydrodynamic volume (V_h). The hydrodynamic volume is the volume pervaded by a molecule and can be considered proportional to the radius of gyration (R_g) cubed. Molecules with different V_h’s penetrate the pores of the stationary phase to varying degrees, providing the basis for separation.[16] Larger molecules enter fewer particle pores than smaller molecules and thus have a less tortuous path through the columns and elute before smaller molecules. A detector is used to monitor the concentration of the solute in the mobile phase eluting from the columns; the response of this detector as a function of time is sensitive to the distribution of V_h’s. It should be noted that this measured distribution would not be a delta function even for perfectly monodisperse samples, due to the random diffusion of the molecules into the pores of the stationary phase. This effect is called band broadening.[16] SEC detector readings are often presented in terms of retention volume (V_R), which is the product of elution time and the constant flow rate. Any detector whose output is linear with respect to concentration and independent of molecular weight suffices for SEC; refractive index detectors were used in this research program.

It is typically desirable to convert the detector signal into a statistical distribution of the number fraction of polymers with specific molecular weights. The relationship between V_R and the molecular weight of a single chain (M) varies across polymers and is typically unknown. This relationship is commonly determined empirically using a series of calibration standards (polymers with narrow molecular weight distributions

and known molecular weights). In this process, a polynomial function is fitted to the plot of M versus V_R for the standard samples. This smooth function assigns a specific molecular weight to each retention volume, and M_n and M_w can be determined using:

$$M_n = \frac{\sum_i c_i}{\sum_i c_i / M_i} \tag{3-6}$$

$$M_w = \frac{\sum_i c_i M_i}{\sum_i c_i} \tag{3-7}$$

The primary limitation of this approach is that V_h varies with M differently for different polymers or even different architectures of the same polymer. Consequently, an accurate measurement of M requires standards of the same polymer as the analyte.[16] While it is not practical to synthesize standards of every polymer, several polymer standards, including PI and PS, are commercially available. Thus it is practically feasible to quantitatively evaluate the molecular weights of PI and PS homopolymers using SEC. In this research program, the first block that was polymerized during a block copolymer synthesis was always either PI or PS. Small aliquots were extracted from the reactors and the molecular weight distributions of these PI and PS blocks were measured using SEC calibrated with the appropriate PI ($1000 < M_n < 27{,}000$ g/mol, Scientific Polymer Products) or PS ($580 < M_n < 377{,}400$ g/mol, Polymer Laboratories) standards. The overall M_n for each block copolymer was then computed using the M_n of the first block measured using SEC, the mole fractions obtained from ^{1}H NMR data, and the relative amounts of monomers added to the reactors; specific details are provided in Chapters 4-6. In keeping with common practice in the literature, all of the

block copolymer polydispersity indices (PDI = M_w/M_n) reported in this Thesis were determined with respect to PS standards. These reported values are almost universally higher than the actual PDI's, due to the effects of band broadening and any interactions between the analyte and the stationary phase. The shape of the molecular weight distribution can contain important information in addition to the values of M_n and M_w. For instance, the presence of multiple peaks could indicate that some chains had coupled or they could be the result of premature termination.

3.3 Nuclear Magnetic Resonance (NMR) Spectroscopy

Nuclear magnetic resonance (NMR) spectroscopy is a powerful and widely used characterization technique for organic molecules. The technique utilizes the magnetic properties of nuclei to provide structural information. Certain nuclei have non-zero spin quantum numbers analogous to the spin states of an electron. Nuclei with spin states of ±½ include isotopes of two atoms central to organic chemistry: ^{1}H (99.98% abundance) and ^{13}C (1.1% abundance). These spinning nuclei generate a magnetic moment vector $\underline{\mu}$; in the absence of an external magnetic field the magnetic moment vectors are randomly aligned. The application of a strong magnetic field induces the $\underline{\mu}$'s to adopt an orientation either parallel or antiparallel to the applied field. The parallel configuration possesses a lower energy than the antiparallel, although the difference is small enough that thermal energy nearly equilibrates the populations under NMR operating conditions (population excess is 1 part in 10,000 at room temperature for ^{1}H in a 1.4 T magnetic field).[17] These magnetic moments precess about the axis of the external magnetic field

at a frequency, known as the Larmor frequency, which depends on the energy difference between the two spin states. Application of an electromagnetic pulse at the Larmor frequency oriented normal to the applied magnetic field forces the μ's to precess in phase at the Larmor frequency. The magnetic moments relax to their equilibrium positions after pulsing and this decoherence process is measured in NMR spectroscopy. The summation of the individual μ's gives a net magnetic moment normal to the applied field for the system and the oscillating decay of this magnetic moment is measured as a function of time in NMR spectroscopy; the result is known as a Free Induction Decay (FID).[17]

NMR spectroscopy would not be a valuable tool if all protons (or other spinning nuclei such as ^{13}C) resonated at exactly the same frequency. All protons do not have the same Larmor frequency, however, because the exact magnetic field influencing protons depends on the local chemical environment. Nearby spinning protons generate local magnetic fields that either reinforce or oppose the applied external field. These local fields result in chemical environment-specific magnetic fields and the resonance frequency of each proton is shifted slightly to compensate for these effects. The ratio of this shift in frequency to the frequency of the pulse applied by the instrument is known as the chemical shift (δ). The chemical shift is a function of the chemical environment and is constant across instruments of different frequencies. The Fourier transform of the FID yields a plot of intensity as a function of δ, and the area under each peak is proportional to the number of protons in that chemical environment (this is not true for ^{13}C NMR due to relaxation effects).[17]

This research program only utilized ^{1}H NMR spectroscopy. In most of the ^{1}H NMR experiments, the specimens were dissolved in deuterated chloroform. Deuterated solvents are commonly employed in ^{1}H NMR experiments to limit the interference of the solvent signal with the signals from the protons of interest. However, a deuterated solvent is not a requirement,[18, 19] as is discussed in Section 8.1. ^{1}H NMR spectroscopy was used to probe the chemical structure of all of the polymers discussed in this Thesis. The molar compositions of the block copolymers were ascertained by comparing the relative areas under the ^{1}H NMR peaks associated with different blocks; the characteristic peaks of PI, PS, and PEO are marked in the representative ^{1}H NMR spectrum that is provided in Figure 3.1. The fractions of 1,4- and 3,4- microstructures in PI (representations of these two repeat units are provided in Figure 3.1) were also determined using the relative areas under the peaks associated these two regiochemistries.

The ^{1}H NMR data were used to compute the overall M_n values of all of the synthesized block copolymers. In the case of poly(styrene-*b*-isoprene-*b*-styrene) (SIS) triblock copolymers, the ^{1}H NMR data were typically used to affirm that complete conversion of the styrene and isoprene monomers had been achieved. The SIS M_n values were then calculated from the measured M_n of the first block and the masses of isoprene and styrene monomer subsequently added to the reactor. Alternatively, M_n of the SIS triblock could be determined solely by ^{1}H NMR end-group analysis. This method worked reasonably well for SIS triblock copolymers prepared using the 3-triisopropylsilyloxy-1-propyllithium (TIPSOPrLi) initiator described in Chapter 4, as the characteristic peak at ~0.9 ppm that is associated with the 21 isopropyl protons was

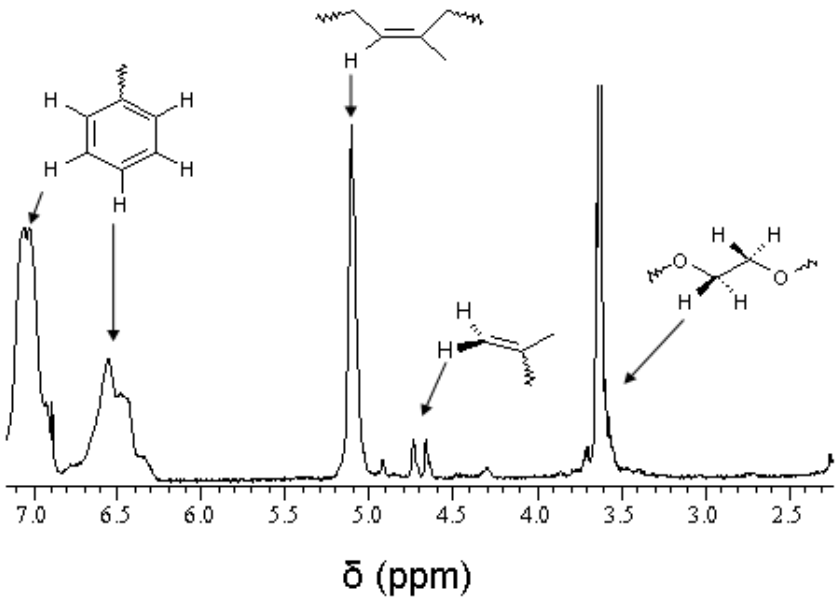

Figure 3.1. Representative ^{1}H NMR spectra obtained from a block terpolymer containing PS, PI, and PEO blocks. The specimen was dissolved in deuterated chloroform and the experiment was run at room temperature. The spectra was referenced to the residual hydrogenated solvent peak at 7.24 ppm. The peaks from 6.2-7.2 ppm are associated with the five phenyl protons of the PS segments. The peak at 5.1 ppm is associated with a single proton of the 1,4-microstructure of PI, while the two peaks from 4.6-4.8 ppm are associated with two protons on the 3,4-microstructure of PI. The peak at 3.6 ppm is associated with the four protons on a PEO segment.

typically prominent. (End-group analysis is subject to more uncertainty when the end-group peak is associated with only a few protons and has a low intensity.) The two alternative methods usually yielded M_n values that were equivalent within experimental uncertainty (± 10%). In the case of poly(ethylene oxide-*b*-styrene-*b*-isoprene-*b*-styrene-

b-ethylene oxide) (OSISO) pentablock terpolymers, the M_n values were computed from the M_n of the parent SIS triblock and the mole fractions obtained from the ^{1}H NMR data.

3.4 Differential Scanning Calorimetry (DSC)

Differential scanning calorimetry (DSC) is a thermal analysis technique that measures the constant pressure heat capacity (C_p) of a material as a function of temperature. A sample is placed in the instrument alongside a reference material with a known heat capacity and both are heated. The amount of heat flowing to each (in the form of electric current) is adjusted to keep both materials at the same temperature. The heat flow is plotted as a function of temperature and the slope of this curve is C_p. C_p changes whenever the sample undergoes a thermal transition and the DSC measures the magnitude and direction of the change in the heat flow associated with these transitions. A pseudo-step increase is suggestive of a glass transition, an exothermic peak below the curve is indicative of crystallization, and an endothermic peak above the curve is consistent with crystal melting. The integrations of the exothermic and endothermic peaks yield the latent heats of crystallization and melting, respectively. The endothermic peak integrations were used to determine the fractional crystallinity of the PEO chains in the ISO triblock and OSISO pentablock terpolymer materials described in Chapter 5.[16]

3.5 Dynamic Mechanical Spectroscopy (DMS)

The application of stress to a liquid induces flow during which inter-particle friction dissipates energy. The rate of energy dissipation depends on the viscosity, a quantity which is defined by Newton's relation as the ratio of stress to strain rate:

$$\sigma = \mu \dot{\gamma} \tag{3-8}$$

where σ is the stress, μ the viscosity , and $\dot{\gamma}$ the strain rate. Viscosity is a scalar quantity dependent on $\dot{\gamma}$ and temperature. In solid bodies, the application of stress results in deformation according to:

$$\sigma = G\gamma \tag{3-9}$$

where G is defined as the modulus and γ is the strain. Like viscosity, the modulus is a variable scalar quantity and can vary with γ, time, and temperature. The modulus acts as a spring constant that stores energy and favors restoration of the original pre-stress conformation. In general, viscosity and modulus become invariant with strain rate and strain as these latter quantities approach zero; responses in this regime are typically linear.[16]

Viscoelasticity is a signature characteristic of polymers that arises because motion of a small segment of the chain is coupled to the conformation of the rest of the chain. Viscoelastic materials exhibit rheological behavior intermediate between the elastic behavior of solids and the viscous behavior of small-molecule liquids. Polymers behave elastically because the intertwined chains possess many conformational degrees of freedom. When stress induces deformation, these chains adopt a non-equilibrium

distribution of conformations. Upon removal of stress, the chains will relax back to an equilibrium conformation to maximize entropy. Friction between chain segments leads to energy dissipation as the segments move past each other upon stretching and subsequent relaxation, adding a viscous component to polymer behavior.[16]

The viscoelastic response of polymers can be probed experimentally by applying an oscillating sinusoidal strain $\gamma^* = \gamma_o \exp(it\omega)$ to the samples and measuring the resultant time-varying stress; this technique is known as dynamic mechanical spectroscopy (DMS). The amplitude of the applied strain should be small enough to elicit a linear viscoelastic response because a linear response to a sinusoidal input is always a sinusoidal output at the same frequency. The linear viscoelastic response can be resolved into two components: one in-phase with strain and the other 90° out-of-phase with strain. The in-phase component corresponds to the elastic response and the out-of-phase component to the viscous response. The dynamic shear modulus (G^*) is given by:

$$G^*(\omega) = \frac{\sigma^*}{\gamma^*} = G' + iG'' \tag{3-10}$$

where σ^* is the complex stress ($\sigma^* = \sigma_o \exp[i(t\omega + \delta)]$) and δ is the phase shift. The elastic component *G'* is known as the storage modulus and the viscous component *G"* is the loss modulus:

$$G' = \frac{\sigma_o}{\gamma_o}\cos\delta \tag{3-11}$$

$$G'' = \frac{\sigma_o}{\gamma_o}\sin\delta \tag{3-12}$$

Typically both *G'* and *G"* are presented in DMS data to characterize both the viscous and elastic behavior of a polymer. The phase angle is sometimes presented in terms of the loss tangent (tan $\delta = G"/G'$).[16]

The frequency of the applied shear rate and the temperature dictate the length scale responsible for the viscoelastic response measured in a rheological experiment. The temperature and frequency dependencies are generally viewed as corresponding states; a measurement at a certain temperature and frequency is equivalent to a measurement at a lower (higher) temperature and a lower (higher) frequency.[16] At high frequencies (low temperatures), only relaxations on the shortest length scale, such as those of chain segments, contribute significantly to the modulus. The relaxation length scale that dominates the modulus becomes larger as the frequency is decreased (temperature increased) into the terminal regime. The ~5-50 nm length scale associated with ordered block copolymer morphologies dominates the relaxation dynamics below a critical frequency ω_c.

Two types of rheological experiments are commonly used to probe block copolymer materials. The first type consists of isochronal (constant ω, with $\omega \ll \omega_c$) measurements of *G'* and *G"* performed while heating or cooling a specimen. Experimental reports have consistently demonstrated that a sharp reduction in G' of several orders of magnitude upon sample heating is consistent with a transition from an ordered mesostructure to the disordered state.[20-22] Other discontinuous changes in *G'* are frequently associated with transitions between ordered morphologies (commonly called order-order transitions).[23] The second commonly employed DMS experiment consists of isothermal measurements of *G'* and *G"* as a function of ω. A typical experiment

involves applying shear at frequencies spanning several orders of magnitude at multiple temperatures. The data acquired at multiple temperatures are then superimposed onto a master curve using a time-temperature superposition (TTS) shift factor. The rationale for this shift relies on the principle of corresponding states discussed above.[16] Although TTS is not rigorously valid for block copolymers because the temperature dependences of relaxations in the different blocks are not identical,[24] it is commonly used in the literature to generate master curves. The relationship between G^* and ω below ω_c depends on the block copolymer mesostructure. Calculations[25] and experiments[20, 26, 27] have shown that polycrystalline lamellar phases often yield a scaling relationship of $G^*(\omega) \propto (i\omega)^{1/2}$. Ryu et al. demonstrated that hexagonal cylinders frequently exhibit scaling of $G^*(\omega) \propto (i\omega)^{1/3}$.[28] Kossuth and coworkers established that both the body-centered cubic and gyroid phases have a large elastic plateau modulus that persists to low frequency.[29] Kossuth et al. suggested that all triply periodic morphologies would exhibit this plateau in the modulus that is characteristic of an elastic response. Rheological data obtained by Epps and Cochran et al. from samples containing three types of multiply continuous network morphologies (called O^{70}, Q^{230}, and Q^{214}) support this conclusion.[30, 31] Although these rheological data are useful, it must be cautioned that definitive morphological assignments should not be made on the basis of DMS alone. Complementary characterization techniques, such as small angle X-ray scattering (SAXS) and transmission electron microscopy (TEM) that will be discussed in the following sections, should be used in conjunction with DMS.

Rheological analyses of the materials discussed in this Thesis were conducted on Rheometrics Scientific ARES strain-controlled rheometers equipped with either 25 mm or 8 mm parallel plates. Samples were prepared for DMS analyses in one of two ways: (i) compression molding the polymer powder into discs of the appropriate size (ii) loading the polymer powder directly onto the rheometer plates and melting it under a nitrogen gas purge. The specimens were always heated above the order-disorder transition temperature (T_{ODT}) (or to 250 °C) under the nitrogen purge prior to rheological measurements in an effort to erase effects associated with thermal history. The linear viscoelastic regime was then established at a temperature below T_{ODT} by measuring *G'* and *G"* for various strains (i.e., by conducting a strain sweep); the moduli were typically invariant with strain for displacements of 1-3%. Isochronal (ω = 1 rad/s) measurements of *G'* and *G"* as a function of temperature were used to characterize the T_{ODT}'s of all the block copolymers discussed in Chapters 5 and 6. (Note that temperatures above 250 °C were not accessed because polyisoprene and poly(ethylene oxide) may degrade at these elevated temperatures.) Isothermal frequency sweeps were employed to provide additional information about the morphologies of the OSISO pentablock terpolymers; the resulting master curves are provided in Figure 5.4.

3.6 Small Angle X-Ray Scattering (SAXS)

Small angle X-ray scattering (SAXS) is a powerful technique that can provide information about the dimensions and space group symmetry of a mesostructure. SAXS measurements are particularly useful because they probe a relatively large portion of a

sample and provide reciprocal space data that are three-dimensional in nature. The technique is particularly useful in the study of block copolymers because it can probe the ~5-50 nm length scale that is typically characteristic of block copolymer morphologies.[32] An extensive discussion of SAXS is provided in this section.

Oscillating electromagnetic waves interact with the electrons of materials they propagate through; this interaction results in scattering. In SAXS, the incident radiation is in the form of X-rays. The electrons in the material placed in the X-ray beam oscillate at the frequency of the incident X-rays. These oscillating electron clouds (scattering centers) emit spherical waves of radiation that propagate radially outward, effectively scattering the incident X-rays. When the energies of the incident and emitted waves are equal, the scattering is said to be elastic. Only elastic scattering is discussed in this section because this research program did not utilize any inelastic techniques. The basic scattering event is illustrated in Figure 3.2, along with some important scattering parameters. The wave vector of the incident radiation is denoted by $\mathbf{k_i}$ and that of the emitted radiation is connoted by $\mathbf{k_e}$. Note that there are emitted wave vectors pointing radially outward from the scattering center in all directions; $\mathbf{k_e}$ in Figure 3.2 is drawn arbitrarily. The frequencies and amplitudes ($\frac{2\pi}{\lambda}$, where λ is the wavelength) of these two waves are equal in elastic scattering events. The scattering vector **q** is defined as the difference between the incident and emitted wave vectors:

$$\mathbf{q} = \mathbf{k_e} - \mathbf{k_i} \tag{3-13}$$

The scattering vector represents the change in momentum incurred by the radiation as a result of the scattering event. It is useful to define because it takes into account both the

scattering angle and the wavelength used in a given experiment.[16] If the acute angle between $\mathbf{k_e}$ and $\mathbf{k_i}$ is defined as 2θ, trigonometry yields $|\mathbf{q}| = \frac{4\pi}{\lambda}\sin\theta$.

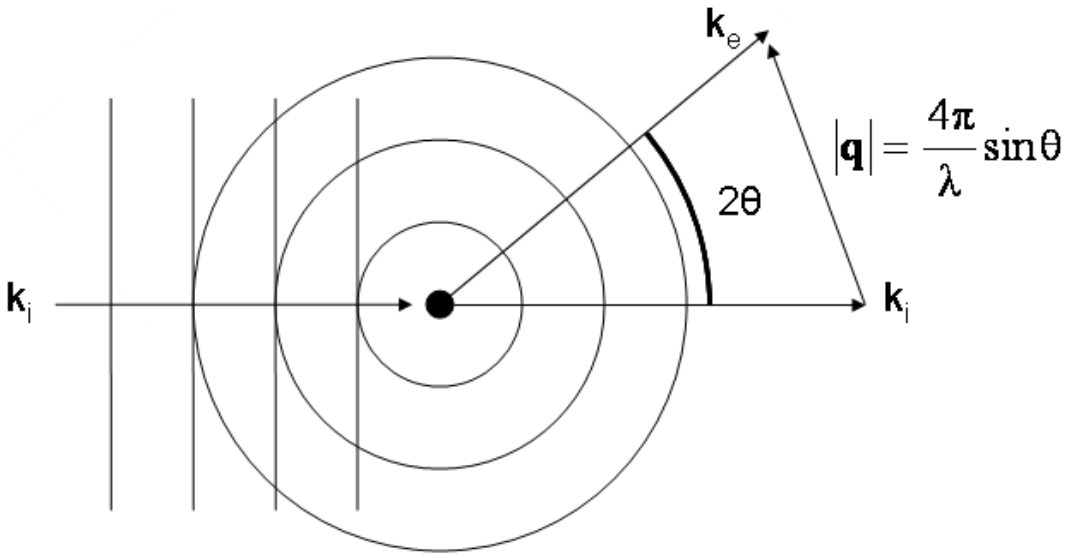

Figure 3.2. Schematic representation of the relationship between the incident plane wave $\mathbf{k_i}$ and the emitted spherical waves. The scattering vector **q** is defined as the difference between a scattered ray $\mathbf{k_e}$ and $\mathbf{k_i}$ ($\mathbf{q = k_e - k_i}$).

Scattering from an isolated center does not provide any useful structural information because the emitted wave is the same for every scattering vector. The superposition of scattered waves from the many centers in a material, however, yields an interference pattern that depends on the arrangement of the atoms in the material. The derivation of Bragg's law serves as a good starting point for understanding how scattering patterns provide structural information for ordered materials. Consider a plane wave incident upon an infinite series of semi-reflective planes with an interplanar

spacing d, as depicted in Figure 3.3. The reflection off the top plane can be considered the reference reflection. This reference reflection is interfered with by reflections from the other planes. These reflections must travel an additional distance $2dn\sin\theta$ to penetrate to layer n and reflect back to the reference plane, resulting in a shift in the

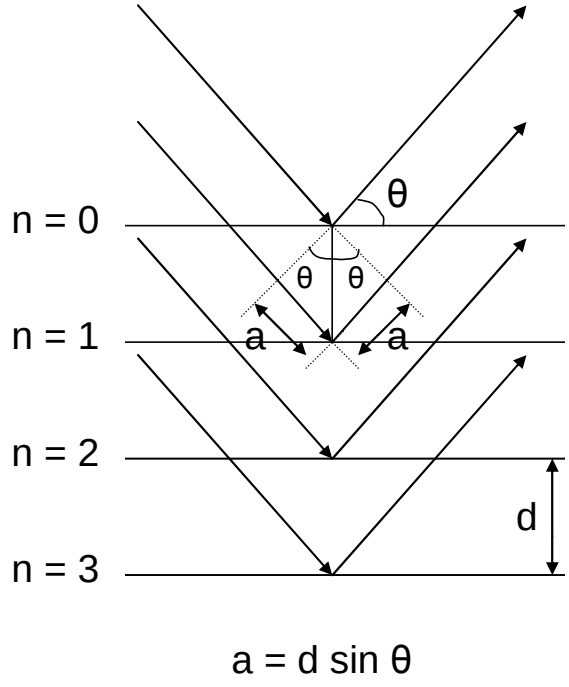

Figure 3.3. Schematic used to derive Bragg's Law. Waves travel an additional $2d\sin\theta$ for each n below the reference plane.

phase angle (ϕ) of $\phi = 2dn\sin\theta$. This phase shift leads to destructive interference unless δ is an integral multiple of the wavelength, a condition known as Bragg's Law:

$$2d\sin\theta = n\lambda \qquad (3\text{-}14)$$

Combining Bragg's Law with the magnitude of the scattering vector gives:

$$|\mathbf{q}| = \frac{2n\pi}{d} \tag{3-15}$$

Bragg's Law can be used to provide physical insight into the choice of SAXS as an analytical tool to investigate polymer morphologies. The domain spacings accessible in a scattering experiment depends upon both λ and θ. Cu-K_α X-rays generated in typical laboratory SAXS equipment have a wavelength of 1.54 Å; the angle of observation θ must be less than ~5° to access the 5-50 nm length scale that is typically characteristic of block copolymer mesostructures when X-rays with a 1.54 Å wavelength are used. In practice, the accessible q range for experimental equipment is adjusted by changing the sample-to-detector distance (and thus the accessible range of θ). The upper bound on θ accessibility is set by the detector size, while the lower bound is a function of the size of the beam stop and the amount of parasitic (background) scattering at low θ. Observation angles significantly above 5° (up to 90°) (i.e., wide angle X-ray scattering (WAXS)) can be used to probe domain spacings on the order of Angstroms, distances relevant in the study of molecular crystals.

Bragg's Law applies to scattering from planes of atoms in a unit cell and dictates the allowable reflections for a given morphology. The unit cell for a perfect crystal describes the location of the scattering centers and can be represented as:

$$\mathbf{R}_{hkl} = \mathbf{R}_o + u\mathbf{a} + v\mathbf{b} + w\mathbf{c} \tag{3-16}$$

where $\mathbf{R_o}$ is the coordinate of scattering center o, the integers *u*, *v*, and *w* are basis coefficients, and **a**, **b**, and **c** are the basis vectors describing the unit cell. The angles between the basis vectors can be denoted α (between **b** and **c**), β (between **a** and **c**), and γ (between **a** and **b**). The vector $\mathbf{R}_{hkl}$ describes the translational symmetry of a structure

and can be used to determine the conditions that satisfy Bragg's Law. Only specific distances between planes of atoms satisfy the Bragg criteria and allow scattering. To determine these specific distances, it is convenient to introduce the reciprocal lattice. Three vectors $\mathbf{a}^*$, $\mathbf{b}^*$, and $\mathbf{c}^*$ reciprocal to **a**, **b**, and **c** can be defined:

$$\mathbf{a}^* = \frac{\mathbf{b}\times\mathbf{c}}{\mathbf{a}\cdot[\mathbf{b}\times\mathbf{c}]} \qquad \mathbf{b}^* = \frac{\mathbf{c}\times\mathbf{a}}{\mathbf{b}\cdot[\mathbf{c}\times\mathbf{a}]} \qquad \mathbf{c}^* = \frac{\mathbf{a}\times\mathbf{b}}{\mathbf{c}\cdot[\mathbf{a}\times\mathbf{b}]} \tag{3-17}$$

According to these definitions, $\mathbf{a}^*$ is normal to the plane defined by **b** and **c** and has a magnitude of $\frac{1}{|\mathbf{a}|}$. These vectors can be used to define a reciprocal lattice vector $\mathbf{r}^*$:

$$\mathbf{r}^* = h\mathbf{a}^* + k\mathbf{b}^* + l\mathbf{c}^* \tag{3-18}$$

where *h*, *k*, and *l* are the Miller indices describing a plane in the real space lattice. This reciprocal lattice vector can be used to determine the distances d_{hkl} between real space planes of atoms defined by *h*, *k*, and *l* that satisfy Bragg's Law. Consider the plane ABC defined by Miller indices *h*, *k*, and *l* that is depicted in Figure 3.4. Two lines in this plane

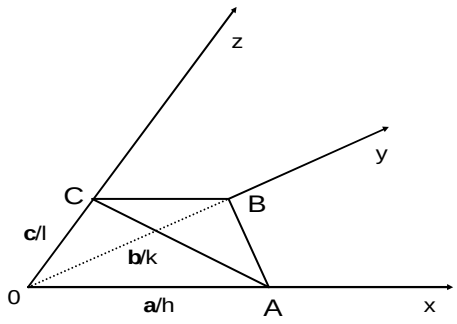

Figure 3.4. Real space plane ABC defined by Miller indices *h*, *k*, *l*.

can be represented using the basis vectors and Miller indices. The vector $\left(\frac{\mathbf{a}}{h}-\frac{\mathbf{b}}{k}\right)$ is the line BA and the vector $\left(\frac{\mathbf{a}}{h}-\frac{\mathbf{c}}{l}\right)$ the line CA. The reciprocal lattice vector must be normal to plane ABC if it is orthogonal to both BA and CA. The dot product of $\mathbf{r}^*$ with each of these vectors is zero, proving the normal relationship:

$$\begin{aligned}\mathbf{r}^*\cdot\left(\frac{\mathbf{a}}{h}-\frac{\mathbf{b}}{k}\right)&=\left(h\mathbf{a}^*+k\mathbf{b}^*+l\mathbf{c}^*\right)\cdot\left(\frac{\mathbf{a}}{h}-\frac{\mathbf{b}}{k}\right)=\frac{h}{h}\mathbf{a}\cdot\mathbf{a}^*-\frac{k}{k}\mathbf{b}\cdot\mathbf{b}^*=1-1=0\\ \mathbf{r}^*\cdot\left(\frac{\mathbf{a}}{h}-\frac{\mathbf{c}}{l}\right)&=\left(h\mathbf{a}^*+k\mathbf{b}^*+l\mathbf{c}^*\right)\cdot\left(\frac{\mathbf{a}}{h}-\frac{\mathbf{c}}{l}\right)=\frac{h}{h}\mathbf{a}\cdot\mathbf{a}^*-\frac{l}{l}\mathbf{c}\cdot\mathbf{c}^*=1-1=0\end{aligned} \tag{3-19}$$

Note that in the evaluation of the dot products in Equation 3-19, the dot product of any vector **i** with any $\mathbf{j}^*$ (i.e., the reciprocal vectors other than $\mathbf{i}^*$) must be zero because **i** and $\mathbf{j}^*$ are, by definition, orthogonal (see Equation 3-17). The unit vector normal to plane ABC can be obtained by dividing $\mathbf{r}^*$ by its magnitude. The distance between planes defined by h, k, and l can then be obtained by simply projecting any one of $\frac{\mathbf{a}}{h}$, $\frac{\mathbf{b}}{\mathrm{k}}$, or $\frac{\mathbf{c}}{\mathrm{l}}$ onto this unit normal vector. Using $\frac{\mathbf{a}}{h}$ as an example:

$$\mathrm{d}_{hkl}=\frac{\mathbf{a}}{h}\cdot\frac{\mathbf{r}^*}{\left|\mathbf{r}^*\right|}=\frac{h\mathbf{a}\cdot\mathbf{a}^*}{h\left|\mathbf{r}^*\right|}=\frac{1}{\left|\mathbf{r}^*\right|} \tag{3-20}$$

The magnitude of $\mathbf{r}^*$ can be calculated using:

$$\left|\mathbf{r}^*\right|=\sqrt{\left(h\mathbf{a}^*+k\mathbf{b}^*+l\mathbf{c}^*\right)\cdot\left(h\mathbf{a}^*+k\mathbf{b}^*+l\mathbf{c}^*\right)} \tag{3-21}$$

Expanding and recasting this expression in terms of the angles between the reciprocal basis vectors (α^*, β^*, and γ^*) gives:

$$\left|\mathbf{r}^*\right| = \sqrt{\left(h\mathrm{a}^*\right)^2 + \left(k\mathrm{b}^*\right)^2 + \left(l\mathrm{c}^*\right)^2 + 2hk\left(\mathrm{a}^*\mathrm{b}^*\right)\cos\left(\gamma^*\right) + 2hl\left(\mathrm{a}^*\mathrm{c}^*\right)\cos\left(\beta^*\right) + 2kl\left(\mathrm{b}^*\mathrm{c}^*\right)\cos\left(\alpha^*\right)} \quad (3\text{-}22)$$

where a^*, b^*, and c^* are the magnitudes of the vectors $\mathbf{a}^*$, $\mathbf{b}^*$, and $\mathbf{c}^*$, respectively. Combining this expression with Equations 3-20 and 3-14 yields an expression for all $\left|\mathbf{q}_{hkl}\right|$ that satisfy the Bragg criterion. In other words, these $\left|\mathbf{q}_{hkl}\right|$ values are the positions at which scattering peaks *may* appear:

$$\left|\mathbf{q}_{hkl}\right| = \mathrm{q}_{hkl} = \frac{2\pi}{\mathrm{d}_{hkl}} = 2\pi\left|\mathbf{r}^*\right| \quad (3\text{-}23)$$

Mathematically, these allowable q_{hkl} values can be expressed using a series of dirac delta functions that is known as the form factor ($F(q)$). The magnitude of $\mathbf{r}^*$ is presented in terms of reciprocal space parameters that can be related to real space values via a transformation to Cartesian coordinates. The relationships between real space and reciprocal space parameters are listed in Table 3.1.[33]

Table 3.1: Relationships between real space and reciprocal space parameters.

$\mathrm{a}^* = \frac{\mathrm{bc}}{\mathrm{V}}\sin\left(\alpha\right)$	$\cos\left(\alpha^*\right) = \frac{\cos\left(\beta\right)\cos\left(\gamma\right) - \cos\left(\alpha\right)}{\sin\left(\beta\right)\sin\left(\gamma\right)}$
$\mathrm{b}^* = \frac{\mathrm{ac}}{\mathrm{V}}\sin\left(\beta\right)$	$\cos\left(\beta^*\right) = \frac{\cos\left(\alpha\right)\cos\left(\gamma\right) - \cos\left(\beta\right)}{\sin\left(\alpha\right)\sin\left(\gamma\right)}$
$\mathrm{c}^* = \frac{\mathrm{ab}}{\mathrm{V}}\sin\left(\gamma\right)$	$\cos\left(\gamma^*\right) = \frac{\cos\left(\alpha\right)\cos\left(\beta\right) - \cos\left(\gamma\right)}{\sin\left(\alpha\right)\sin\left(\beta\right)}$
$\mathrm{V} = \frac{1}{\mathrm{V}^*} = \mathrm{abc}\sqrt{1 - \cos^2\left(\alpha\right) - \cos^2\left(\beta\right) - \cos^2\left(\gamma\right) + 2\cos\left(\alpha\right)\cos\left(\beta\right)\cos\left(\gamma\right)}$	

The form factor gives the q_{hkl} values that satisfy Bragg's Law for a given Bravais lattice; these are the q_{hkl} values at which scattering peaks *may* be present. The development of the expression for allowable q_{hkl} did not consider the positions of atoms within the unit cell, however. Specific arrangements of the atoms within the unit cell can result in systematic peak extinctions even when Bragg's Law is satisfied. Waves scattered from different atoms within a unit cell can destructively interfere if the scattering atoms are related by symmetry operations such as mirror planes, inversion centers, or screw axes. The structure factor S_{hkl} is the sum of the waves scattered by all of the individual atoms:

$$S_{hkl} = \sum_{1}^{N} f_n e^{2i\pi\left(h u_n + k v_n + l w_n\right)} \tag{3-24}$$

where f_n is the atomic scattering factor, i the imaginary number $\sqrt{-1}$, h, k, and l the Miller indices, and u_n, v_n, and w_n the coordinates of the atom within the unit cell. The structure factor describes how the arrangement of atoms within a unit cell affects the scattered wave. A structure factor of zero for specific h, k, and l values indicates scattering peaks will not be present for those Miller indices.[34] As an example, consider the C2 space group with unique positions of:

$$\begin{gathered} (u, v, w) \\ (-u, v, -w) \\ \left(u + \tfrac{1}{2}, v + \tfrac{1}{2}, w\right) \\ \left(-u + \tfrac{1}{2}, v + \tfrac{1}{2}, -w\right) \end{gathered} \tag{3-25}$$

Plugging these positions into the structure factor (Equation 3-24) yields:

$$S_{hkl} = f\left(e^{-2i\pi(hu+kv+lw)} + e^{-2i\pi(-hu+kv-lw)} + e^{-2i\pi(hu+kv+lw)}e^{-2i\pi\left(h/2+k/2\right)} + e^{-2i\pi(-hu+kv-lw)}e^{-2i\pi\left(h/2+k/2\right)} \right)$$

$$= f\left(\left(e^{-2i\pi(hu+kv+lw)} + e^{-2i\pi(-hu+kv-lw)}\right) + \left(e^{-2i\pi(hu+kv+lw)} + e^{-2i\pi(-hu+kv-lw)}\right)e^{-i\pi(h+l)}\right) \quad (3\text{-}26)$$

$= 0$ for $h + l$ = odd

This example illustrates how the interference of waves scattered from different atoms within a unit cell can lead to systematic extinctions even when the reflections satisfy the Bragg criteria.

The actual scattering from a sample depends on both the form and structure factors, as well as a third factor: the contrast within the material. In X-ray scattering, the contrast derives from differences in the electron densities (κ_i) between the different domains within a unit cell. Specifically, the contrast scales as the square of the difference in electron densities between domains. Block copolymers comprised of domains with equivalent electron densities would not scatter even if reflections were permitted by both the form and structure factors because there would be no scattering contrast. (For these materials, the alternative technique of small-angle neutron scattering (SANS) may be useful. The general features of SANS and SAXS are similar, except SANS involves neutrons, not X-rays, and the SANS contrast is derived from differences in scattering length densities of the nuclei within a material.) The dependence of the scattering intensity on the form and structure factors and the electron density difference can be summarized mathematically as:

$$\text{Intensity} \propto \left(\kappa_i - \kappa_j\right)^2 \mathrm{F}(q)\mathrm{S}(q) \quad (3\text{-}27)$$

The form factor dictates the allowed reflections while the structure factor and contrast govern the relative intensities of the allowed peaks.

The discussion of the physics of X-ray scattering thus far applies to a wide variety of materials regardless of length scale. In practice, however, significant differences exist between techniques applied to crystals with an Angstrom length scale and block copolymers with a ~5-50 nm length scale. The different scattering angles required to probe these length scales were already discussed above. There are also often differences in the numbers of grain present in crystals compared to block copolymer specimens. While many crystals contain only a few grains, block copolymer materials, absent some sort of alignment procedure, typically contain distributions of microscopic grains with random orientations.[35] These distributions make SAXS in block copolymers analogous to powder diffraction in crystals.[34] The presence of many grains effectively

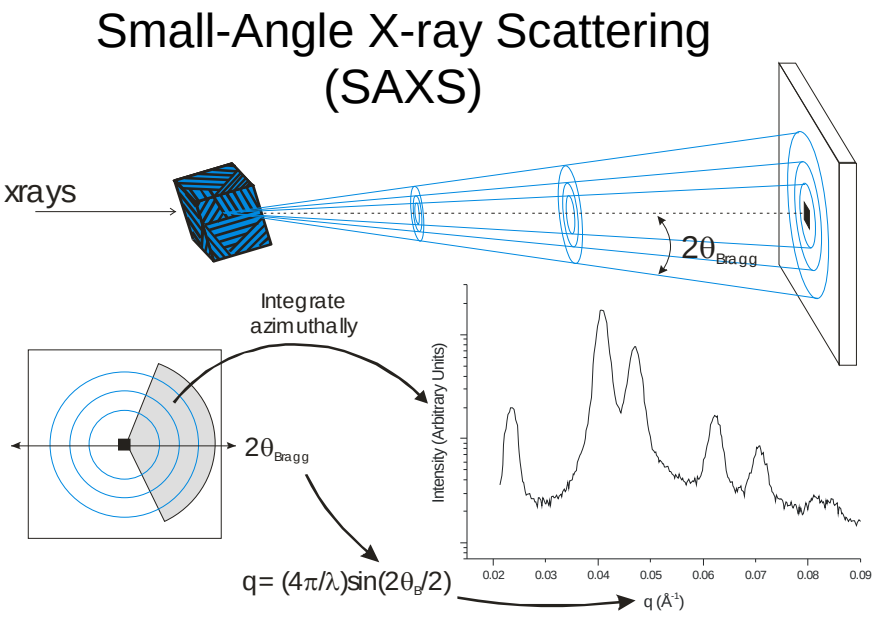

Figure 3.5. Diagram of a typical SAXS experiment and an example of resulting 2D and 1D data. Figure reproduced from Reference 36.

ensures that some grains are oriented to allow scattering from every lattice plane and the diffraction patterns obtained from these polygranular materials consist of a series of concentric rings with radius q_{hkl}. Azimuthal integration of these 2D patterns reduces the data to plots of scattered intensity versus q. Each peak in this 1D plot corresponds to a q_{hkl} allowed by the form factor, with the intensities of the reflections dictated by the structure factor, contrast, and long-range mesostructural order. A schematic illustration of a typical experimental SAXS setup and resulting data is presented in Figure 3.5. The positions of the peaks can be compared to allowed positions for various space group symmetries. The first step in this process is establishing the possible reflections for various unit cells; these positions are computed by inserting the unit cell parameters into Equation 3-22 and substituting the resulting $\left|\mathbf{r}^*\right|$ value into Equation 3-23. We can illustrate this for several types of unit cells commonly encountered in block copolymer materials. For a 1-D lamellar array, b = c = ∞ ($b^* = c^* = 0$), and the possible reflections are given by:

$$q_{hkl} = 2\pi\frac{h}{a} \tag{3-28}$$

For hexagonal unit cell (e.g., hexagonally packed cylinders), a = b, c = ∞, and $\gamma^* = 60°$, and the potential reflections are given by:

$$q_{hkl} = 2\pi\frac{\sqrt{h^2 + k^2 + hk}}{a} \tag{3-29}$$

For a cubic morphology (e.g., gyroid and body-centered cubic spheres), a = b = c and $\gamma^* = \beta^* = \alpha^* = 90°$ and the possible reflections are given by:

$$q_{hkl} = 2\pi \frac{\sqrt{h^2 + k^2 + l^2}}{a} \qquad (3\text{-}30)$$

Inspection of these Equations reveals that the relative peak locations (i.e., q_{hkl} / q_{001}) for these unit cells are independent of the single lattice parameter a. As a result, allowed Bragg reflections are commonly discussed in terms of the q_{hkl} / q_{001} ratios in the block copolymer literature.

Thus far we have only discussed the reflections that are possible for given unit cells, and have neglected the effects of symmetry within the various unit cells. It is these symmetry elements that modify the form factor according to the specific space group symmetry by eliminating some of the possible q_{hkl} values for a general unit cell type. These symmetry extinctions can be calculated, but they are already compiled in the *International Tables for Crystallography* and can be easily looked up in that reference.[37] The allowed q_{hkl} / q_{001} ratios for some commonly encountered block copolymer morphologies are provided in Table 3.2. The presence of a peak that is not allowed by the space group symmetry of a morphology indicates that morphology is not present in the sample. The absence of a peak, however, does not preclude a mesostructure from being present in a specimen, as structure factor extinctions are common in block copolymer systems. It should be noted that the absence of many allowed reflections strongly suggests a given morphology is not present, although these absences do not provide definitive proof. Some researchers have attempted to extract details of the microdomain structure, and not just the space group symmetry of a morphology, from SAXS data.[38, 39] In these studies, microdomain models for various morphologies were proposed and peak intensities were predicted on the basis of the

models. The intensity predictions were compared to the experimental data, with good agreement between the two being interpreted as evidence supporting the proposed microdomain structure. This sort of analysis was not pursued in the research described in this Thesis.

Table 3.2: Allowed peak reflections for some morphologies commonly encountered in block copolymer materials.

Polymer Morphology	**Allowed q_{hkl} / q_{001} Ratios**
Lamellae	1, 2, 3, 4, 5, 6……
Body-Centered Cubic Spheres	1, $\sqrt{2}$, $\sqrt{3}$, $\sqrt{4}$, $\sqrt{5}$, $\sqrt{6}$ ……
Hexagonally-Packed Cylinders	1, $\sqrt{3}$, $\sqrt{4}$, $\sqrt{7}$, $\sqrt{9}$, $\sqrt{12}$ ……
Gyroid (Core-Shell)	$\sqrt{6}$, $\sqrt{8}$, $\sqrt{14}$, $\sqrt{16}$, $\sqrt{20}$, $\sqrt{22}$ ……
Alternating Gyroid	$\sqrt{2}$, $\sqrt{6}$, $\sqrt{8}$, $\sqrt{10}$, $\sqrt{12}$, $\sqrt{14}$ ……

The allowed q_{hkl} / q_{001} ratios are not constant for unit cells that are characterized by multiple lattice parameters. Several such morphologies with orthorhombic unit cells have been reported in block copolymer materials.[30, 31, 40-42] These structures are called O^{70} and O^{52}, with the "O" indicating an orthorhombic unit cell and the 70 and 52 representing the numbers of the space groups in the crystallographic tables.[37] These unit cells are characterized by $\gamma^* = \beta^* = \alpha^* = 90°$ and $a \neq b \neq c$, and the possible peaks positions are given by:

$$q_{hkl} = 2\pi\sqrt{\frac{h^2}{a^2} + \frac{k^2}{b^2} + \frac{l^2}{c^2}} \qquad (3\text{-}31)$$

The allowed reflections for a specific space group can be computed by inserting the allowed Miller Indices found in the crystallographic tables. Indexing the peaks from Bragg patterns to these orthorhombic structures requires simultaneous fitting of lattice parameters and allowable reflections; a description of the process of indexing reflections to an O^{70} mesostructure is described in Section 8.2.

This discussion has largely focused on Bragg patterns comprised of isotropic rings. These patterns are characteristic of polygranular materials like those investigated in this research program. However, we do note that various types of alignment procedures (e.g., applying reciprocating shear) can reduce the number of grains present in a sample. The Bragg patterns acquired from specimens containing only a few grains typically contain spots at specific radial and angular positions. Both the radial location and the angles between spots provide information about the underlying sample morphology. Spot patterns can be used to establish mesostructural alignment[43] and they provide structural information that facilitates the identification of new, complex morphologies.[40-42]

3.7 Transmission Electron Microscopy (TEM)

As discussed in Section 3.6, SAXS data provide direct information about the symmetry and length scale of mesostructures in a material. Scattering does not provide any direct information about the microdomain structure, however. Transmission

electron microscopy (TEM) allows for the direct visualization of features on the nanometer length scale and these real space micrographs complement the reciprocal space images generated via SAXS. TEM is a crucial tool for establishing the arrangements of the domains within a morphology whose space group symmetry has been elucidated by scattering.

TEM is analogous to optical microscopy, except electrons, not visible light, are responsible for the image. In optical microscopy, the wavelength of visible light limits the resolution of the instrument to features of order 500 nm. The wavelengths of electrons are much lower (~6 pm) than those of visible light and transmission electron microscopes can be used to image features as small as a few angstroms in size (factors such as lens quality limit TEM resolution). In a TEM instrument, a high voltage electron beam is generated by an electron gun and focused onto the sample using electromagnetic lenses. The electrons in the beam either transmit through the sample or are deflected by electrons in the sample. The electrons passing through the sample register on a phosphor viewing screen, as the phosphors glow when struck by electrons. The resulting image is magnified 10,000-100,000 times and consists of a two-dimensional projection of the three-dimensional sample cross section. Sample specimens must be thin (~100 nm) to allow adequate transmission of the electrons. Samples must also have a relatively uniform thickness, as significant variations in thickness can lead to undesirable image contrast. Typically it is desirable to have contrast between domains with different chemical compositions, and additional contrast due to thickness variations could make domain assignment difficult.[44]

Regions with higher electron densities deflect a greater fraction of the incident electrons and appear darker on the phosphorescent viewing screen than regions with lower electron densities. Many polymers, including the polystyrene, polyisoprene, and poly(ethylene oxide) containing materials used in this research, contain carbon, hydrogen, and oxygen, none of which deflect a large fraction of the incident electrons. As a result, relatively little natural contrast between microdomains in block copolymers exists. The chemical modification of selective domains via osmium tetroxide (OsO_4) staining can provide contrast. The OsO_4 reacts with double bonds in polydiene chains and high electron density Os coordinates to the unsaturation in these domains. This staining makes the polydiene domains appear darker than other regions.

The polyisoprene chains in the OSISO pentablock materials that are discussed in Chapter 5 were stained with OsO_4 to enhance contrast. The preparation of these samples was as follows. OSISO powders were first compression molded between Teflon sheets into bars 0.5-1 mm thick using a pressure of 500-1000 psi at 100 °C for 5 min. The mold and polymer were then placed in a vacuum oven and the materials were annealed ~10 °C below T_{ODT} in the melt for ~4 hrs. The samples were subsequently cooled to 80 °C and annealed for ~1 hr to vitrify the glassy polystyrene before finally being cooled to room temperature. The 80 °C vitrification step was designed to reduce the deformation of the morphology that could result from the crystallization of the poly(ethylene oxide) segments at ~65 °C. The OSISO bars were removed from the over and sliced using a Reichart ultramicrotome fitted with a Microstar diamond knife operated at –120 °C (this temperature is below T_g for all three components). These polymer slices (~50-100 nm thick) were placed on copper grids and were exposed to the

vapor from a 4% aqueous solution of OsO_4 for 3-5 min. These slices were then probed using TEM, and representative micrographs obtained from four different polymers are provided in Figure 5.3.

Conclusive morphology assignments should never be made solely on the basis of TEM micrographs. Several shortcomings of TEM as an analytical tool provide the rationale for this statement. First, TEM images only contain projections of the local state of order over a small area (~1 μm^2). It is possible that this imaged area is not representative of the entire sample. The complementary DMS and SAXS techniques probe much larger specimen volumes. Second, TEM images are two-dimensional representations of three-dimensional structures, with the appearance of the micrograph depending on the sample's orientation with respect to the principal axes present in a specific morphology. The interpretation of these images, particularly for the network morphologies discussed in Chapters 2, 5, and 6, is not straightforward. Typically this interpretation has relied on the agreement between projections generated from proposed models of the microdomain structure and the experimental TEM micrographs.[45, 46] However, as pointed out by Hajduk et al.[47] and discussed in Chapter 2, similar TEM images can be obtained from morphologies with very different space group symmetries, making elucidation of the symmetry of a mesostructure solely from TEM micrographs nearly impossible. The danger of relying upon TEM as the primary characterization tool is illustrated by an example from the literature that was discussed in Chapter 2. A bicontinuous morphology formed by poly(styrene-*b*-isoprene) starblock copolymers was initially characterized as an ordered bicontinuous double diamond (OBDD) mesostructure largely on the basis of TEM micrographs.[48] A subsequent reexamination

of the materials using SAXS concluded that the network morphology was in fact the gyroid, a structure with different symmetry than OBDD.[47] Finally, it is important to note that consistency should be established between the TEM images of stained samples and characterization data from unstained samples that was acquired using other techniques. Inconsistencies between stained and unstained samples would suggest the staining alters the block copolymer morphology. TEM was only used in this research program to corroborate morphology assignments made using SAXS (see Chapter 5), and was never employed as the sole characterization technique.

3.8 Mechanical Tensile Testing

The mechanical properties of block copolymer materials are commonly probed using a tensile testing apparatus. In a uniaxial tensile test, a sample with initial dimensions L_o, W_o, and T_o is placed between two grips. In the MINIMAT tensile testing apparatus used in this research program, one of the grips is fixed while the other moves when a uniaxial tensile stain is imposed upon the sample, as is shown schematically in Figure 3.6. The applied strain deforms and stretches the sample, and the force exerted by the apparatus (f) is measured as a function of the sample length (L). These force and length values are commonly converted into engineering stresses (σ_E) and engineering strains (ε_E) using:

$$\sigma_E = \frac{f}{W_o T_o} \tag{3-32}$$

$$\varepsilon_E = \frac{L - L_o}{L_o} \tag{3-33}$$

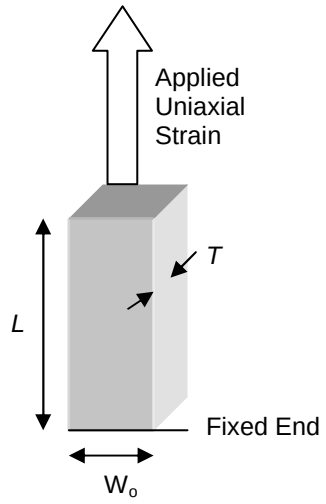

Figure 3.6 Schematic illustration of a uniaxial tensile test.

Tensile data are commonly presented as plots of engineering stress versus strain (stress-strain curves). Materials that are characterized by a linear stress-strain curve are considered elastic, and the slope of the curve is known as the Young's modulus (E). Most polymers, including those discussed in Chapter 5, exhibit elastic behavior in the low strain regime. The stress imposed upon ductile polymers (e.g., thermoplastic elastomers or other polymers that are sufficiently entangled) generally increases linearly with stain until the material yields and begins to draw (plastically deform). The yielding process may involve "necking," wherein the cross-sectional area of the sample decreases in a non-uniform fashion. Necking can be observed visually and may also be characterized by a decrease in the applied load (i.e., a drop in the stress-strain curve).[49,50] While necks in metallic materials can thin and lead to rupture, the necks in polymeric materials generally propagate across the entire sample with increasing strain.[51] The details of the plastic deformation process are material-dependent. For some

polymers, the engineering stress remains constant during plastic deformation until the sample fractures. For other polymers, the stress required to deform the material increases monotonically along with the applied strain; this phenomenon is known as strain hardening. Some polymers exhibit a plateau in the engineering stress immediately following the yield point before strain hardening at higher strains.

The mechanical response of a block copolymer sample is not simply the superposition of the responses of the constituent blocks. Rather, block copolymer mechanical properties depend on numerous factors, including the composition, the molecular weight, the chain architecture, the fractional crystallinities of the blocks, the identity of the morphology, and the alignment of the morphology.[49, 50, 52, 53] Tensile testing was used in this research program to probe the effects of chain architecture and morphology on the mechanical properties of the ISO triblock and OSISO pentablock materials discussed in Chapter 5; representative stress-strain curves are provided in Figure 5.5. Master tensile bars with dimensions of 17 mm x 13 mm x 0.5 mm were prepared by compression molding the polymer powders between Teflon sheets at 500-1000 psi and 100 °C for 5 min. These master bars were stored at –26 °C until, just prior to tensile testing, they were removed from the freezer, allowed to warm to room temperature, and cut into rectangular tensile bars measuring 13 mm x 2.5 mm x 0.5 mm using a fresh razor blade. Uniaxial tensile tests were then carried out at room temperature using a Rheometrics Scientific MINIMAT equipped with a 200 N load cell.

3.9 References

(1) Szwarc, M. *Nature* **1956**, *178*, 1168-1169.

(2) Hsieh, H. L.; Quirk, R. P. *Anionic Polymerization: Principles and Practical Applications*, 1997; Vol. 70.

(3) Odian, G. *Principles of Polymerization*, 4th ed.; John Wiley & Sons, Inc.: New York, NY, 2004.

(4) Lee, W.; Lee, H.; Cha, J.; Chang, T.; Hanley, K. J.; Lodge, T. P. *Macromolecules* **2000**, *33*, 5111-5115.

(5) Bates, F. S.; Fredrickson, G. H. *Phys. Today* **1999**, *52*, 32-38.

(6) Malenfant, P. R. L.; Wan, J.; Taylor, S. T.; Manoharan, M. *Nat. Nanotechnol.* **2007**, *2*, 43-46.

(7) Lynd, N. A.; Meuler, A. J.; Hillmyer, M. A. *Prog. Polym. Sci.* **2008**, *33*, 875-893.

(8) Quirk, R. P.; Ma, J. J. *J. Polym. Sci. Part A* **1988**, *26*, 2031-2037.

(9) Hillmyer, M. A.; Bates, F. S. *Macromolecules* **1996**, *29*, 6994-7002.

(10) Morton, M. *Anionic Polymerization: Principles and Practice*; Academic Press: New York, NY, 1983.

(11) Fetters, L. J.; Huang, J. S.; Young, R. N. *J. Polym. Sci. Part A* **1996**, *34*, 1517-1527.

(12) Rempp, P.; Merrill, E. W. *Polymer Synthesis*, 2nd ed.; Huethig & Wepf: New York, NY, 1991.

(13) Yu, Y. S.; Jerome, R.; Fayt, R.; Teyssie, P. *Macromolecules* **1994**, *27*, 5957-5963.

(14) Ndoni, S.; Papadakis, C. M.; Bates, F. S.; Almdal, K. *Rev. Sci. Instrum.* **1995**, *66*, 1090-1095.

(15) Pangborn, A. B.; Giardello, M. A.; Grubbs, R. H.; Rosen, R. K.; Timmers, F. J. *Organometallics* **1996**, *15*, 1518-1520.

(16) Hiemenz, P. C.; Lodge, T. P. *Polymer Chemistry*, 2nd ed.; CRC Press: Boca Raton, FL, 2004.

(17) Crews, P.; Rodríguez, J.; Jaspars, M. *Organic Structure Analysis*; Oxford University Press: New York, NY, 1998.

(18) Hoye, T. R.; Eklov, B. M.; Ryba, T. D.; Voloshin, M.; Yao, L. J. *Org. Lett.* **2004**, *6*, 953-956.

(19) Hoye, T. R.; Eklov, B. M.; Voloshin, M. *Org. Lett.* **2004**, *6*, 2567-2570.

(20) Rosedale, J. H.; Bates, F. S. *Macromolecules* **1990**, *23*, 2329-2338.

(21) Almdal, K.; Koppi, K. A.; Bates, F. S.; Mortensen, K. *Macromolecules* **1992**, *25*, 1743-1751.

(22) Förster, S.; Khandpur, A. K.; Zhao, J.; Bates, F. S.; Hamley, I. W.; Ryan, A. J.; Bras, W. *Macromolecules* **1994**, *27*, 6922-6935.

(23) Hillmyer, M. A.; Bates, F. S.; Almdal, K.; Mortensen, K.; Ryan, A. J.; Fairclough, J. P. A. *Science* **1996**, *271*, 976-978.

(24) Han, C. D.; Kim, J. K. *Polymer* **1993**, *34*, 2533-2539.

(25) Kawasaki, K.; Onuki, A. *Phys. Rev. A: At. Mol. Opt. Phys.* **1990**, *42*, 3664-3666.

(26) Bates, F. S. *Macromolecules* **1984**, *17*, 2607-2613.

(27) Koppi, K. A.; Tirrell, M.; Bates, F. S.; Almdal, K.; Colby, R. H. *J. Phys. II* **1992**, *2*, 1941-1959.

(28) Ryu, C. Y.; Lee, M. S.; Haiduk, D. A.; Lodge, T. P. *J. Polym. Sci. Part B* **1997**, *35*, 2811-2823.

(29) Kossuth, M. B.; Morse, D. C.; Bates, F. S. *J. Rheol.* **1999**, *43*, 167-196.

(30) Epps, T. H., III; Cochran, E. W.; Hardy, C. M.; Bailey, T. S.; Waletzko, R. S.; Bates, F. S. *Macromolecules* **2004**, *37*, 7085-7088.

(31) Epps, T. H., III; Cochran, E. W.; Bailey, T. S.; Waletzko, R. S.; Hardy, C. M.; Bates, F. S. *Macromolecules* **2004**, *37*, 8325-8341.

(32) Lodge, T. P. *Macromol. Chem. Phys.* **2003**, *204*, 265-273.

(33) Kelly, A.; Groves, G. W.; Kidd, P. *Crystallography and Crystal Defects*; Wiley: New York, NY 2000.

(34) Cullity, B. D. *Elements of X-ray Diffraction*; Addison-Wesley Pub. Co.: Reading, Mass., 1978.

(35) Bates, F. S. *Science* **1991**, *251*, 898-905.

(36) Epps, T. H., III; University of Minnesota: Doctoral Thesis, 2004.

(37) Hahn, T. *International Tables for Crystallography*, 4th ed., 1994; Vol. A.

(38) Hajduk, D. A.; Harper, P. E.; Gruner, S. M.; Honeker, C. C.; Kim, G.; Thomas, E. L.; Fetters, L. J. *Macromolecules* **1994**, *27*, 4063-4075.

(39) Chatterjee, J.; Jain, S.; Bates, F. S. *Macromolecules* **2007**, *40*, 2882-2896.

(40) Bailey, T. S.; Hardy, C. M.; Epps, T. H., III; Bates, F. S. *Macromolecules* **2002**, *35*, 7007-7017.

(41) Cochran, E. W.; Bates, F. S. *Phys. Rev. Lett.* **2004**, *93*, 087802.

(42) Bluemle, M. J.; Fleury, G.; Lodge, T. P.; Bates, F. S. *Manuscript in Preparation.*

(43) Mahanthappa, M. K.; Lim, L. S.; Hillmyer, M. A.; Bates, F. S. *Macromolecules* **2007**, *40*, 1585-1593.

(44) Williams, D. B.; Carter, C. B. *Transmission Electron Microscopy*; Plenum Press: New York, NY, 1996.

(45) Thomas, E. L.; Alward, D. B.; Kinning, D. J.; Martin, D. C.; Handlin, D. L., Jr.; Fetters, L. J. *Macromolecules* **1986**, *19*, 2197-2202.

(46) Hasegawa, H.; Tanaka, H.; Yamasaki, K.; Hashimoto, T. *Macromolecules* **1987**, *20*, 1651-1662.

(47) Hajduk, D. A.; Harper, P. E.; Gruner, S. M.; Honeker, C. C.; Thomas, E. L.; Fetters, L. J. *Macromolecules* **1995**, *28*, 2570-2573.

(48) Thomas, E. L.; Alward, D. B.; Kinning, D. J.; Martin, D. C.; Handlin, D. L., Jr.; Fetters, L. J. *Macromolecules* **1986**, *19*, 2197-2202.

(49) Dair, B. J.; Honeker, C. C.; Alward, D. B.; Avgeropoulos, A.; Hadjichristidis, N.; Fetters, L. J.; Capel, M.; Thomas, E. L. *Macromolecules* **1999**, *32*, 8145-8152.

(50) Dair, B. J.; Avgeropoulos, A.; Hadjichristidis, N.; Thomas, E. L. *J. Mater. Sci.* **2000**, *35*, 5207-5213.

(51) Young, R. J.; Lovell, P. A. *Introduction to Polymers*, 2nd ed.; Chapman & Hall: London, 1991.

(52) Phatak, A.; Lim, L. S.; Reaves, C. K.; Bates, F. S. *Macromolecules* **2006**, *39*, 6221-6228.

(53) Qiao, L.; Leibig, C.; Hahn, S. F.; Winey, K. I. *Ind. Eng. Chem. Res.* **2006**, *45*, 5598-5602.

4

Synthesis of Nearly Monodisperse α-Hydroxypolystyrene in Hydrocarbon Media

4.1 Introduction

Functional initiators for living anionic polymerizations of diene and styrenic monomers provide access to end-functionalized polymers and block copolymers that find widespread applications in coatings, adhesives, sealants, and asphalt modifiers.[1] In 1991, ω-(*tert*-butyldimethylsilyloxy)-1-alkyllithiums were introduced as "protected" anionic polymerization initiators and enabled the synthesis of α-functionalized semi-telechelic polymers.[2] Compounds of this type, particularly 3-*tert*-butyldimethylsilyloxy-1-propyllithium (*t*BDMSOPrLi), have been widely used to prepare functionalized polymers, as the silyl protecting group is readily removed by post-polymerization treatment with hydrochloric acid or fluoride sources (*e.g.*, tetra(*n*-butyl)ammonium fluoride (TBAF)) to unmask the latent hydroxyl group.[3-10] Nearly monodisperse hydroxy-functionalized 1,4-polybutadiene and 1,4-polyisoprene homopolymers have been synthesized with *t*BDMSOPrLi.[3,5] Functionalized polystyrene (PS) with a narrow molecular weight distribution is readily produced at low temperatures in

tetrahydrofuran,[9] but the use of cyclohexane as a reaction medium yields PS samples with relatively broad molecular weight distributions ($M_w/M_n > 1.3$).[3] The inability to produce nearly monodisperse PS in non-polar media limits access to model telechelic styrenic block copolymers containing 1,4-polydiene blocks. For example, the synthetic strategy used to prepare the poly(ethylene oxide-*b*-styrene-*b*-isoprene-*b*-styrene-*b*-ethylene oxide) (OSISO) pentablock terpolymers that will be described in Chapter 5 begins with the synthesis of α-hydroxypolystyrene in cyclohexane. Quirk and co-workers attributed these broad PS molecular weight distributions to slow initiation kinetics that result from intermolecular association of the *t*BDMSOPrLi with the propagating organolithium through coordination of the silyl ether oxygen to the electrophilic lithium cations.[8] In other words, the initiator dissociation was not fast relative to the rate of propagation and the Poisson expression (Equation 3.5) did not describe the molecular weight distributions of these polymers.

This Chapter describes the synthesis of a new functional organolithium, 3-triisopropylsilyloxy-1-propyllithium (TIPSOPrLi), and details its activity in anionic styrene polymerizations at 40 °C in cyclohexane. Our approach is predicated on the notion that the increased steric bulk of the triisopropylsilyl protecting group[11] will reduce the possibility of intermolecular aggregation and increase the rate of styrene initiation. The TIPSOPrLi initiator is used to prepare α-hydroxy polystyrene in cyclohexane with significantly narrower polydispersities than are possible with *t*BDMSOPrLi under comparable conditions. Since polar modifiers are not required to obtain nearly monodisperse polymers, the TIPSOPrLi initiator enables facile synthesis

of styrene/diene block copolymers with predominantly 1,4-diene regiochemistry and narrow molecular weight distributions in all blocks.

4.2 Experimental Section

Materials. Standard Schlenk techniques were used to manipulate all moisture and air-sensitive compounds under a high purity argon atmosphere. Imidazole, anhydrous *N*,*N*-dimethylformamide (DMF), tetrahydrofuran (THF), tetra(*n*-butyl)ammonium fluoride (TBAF), *tert*-butyldimethylchlorosilane, and lithium (3.2 mm dia. wire with 0.5-1% Na in mineral oil) were purchased from Aldrich and used as received. Triisopropylchlorosilane (Gelest) was used as received without further purification. Styrene (Aldrich) and 1,5-cyclooctadiene (Aldrich) were vacuum transferred from di-*n*-butylmagnesium at 40 °C to remove inhibitors and trace water. Cyclohexane was purified by sequential passage through activated alumina followed by Q-5 (Englehard) to remove protic impurities and trace oxygen.[12]

Standard ^{1}H NMR spectra in $CDCl_3$ acquired on a Varian UI-300 spectrometer were referenced to the residual protiated solvent peak. "No-D" ^{1}H NMR spectra[13,14] were acquired on a Varian UI-500 spectrometer in cyclohexane using 1,5-cyclooctadiene as both a chemical shift reference (δ 5.58 ppm, 2.36 ppm) and an internal standard to determine analyte concentrations. The latter experiments employed an acquisition time of 25 s and a pulse repetition delay of 35 s.

Room temperature size-exclusion chromatography (SEC) analyses employing THF as the mobile phase (flow rate 1.0 mL/min) were performed on a Waters 717 GPC

equipped with three Polymer Labs Mixed-C columns and a Waters 410 differential refractometer. A calibration curve constructed using 10 polystyrene standard samples with M_n ranging from 580-377400 g/mol (Polymer Labs) was used to determine the molecular weights and polydispersities of all PS samples.

Triisopropylsilyloxy-1-chloropropane. Triisopropylsilyloxy-1-chloropropane (TIPSOPrCl; b.p. 75 °C/185 mm Hg) was prepared using a modified version of a previously reported procedure.[15] Imidazole and triisopropylchlorosilane were added to anhydrous DMF (~1g imidazole per 5 mL of DMF) under an argon atmosphere in a molar ratio of ~1.2 / 1 and stirred until they formed a clear solution. 3-chloro-1-propanol was added to this solution (equivalent number of moles as imidazole) and since, this reaction is exothermic, the solution quickly warmed. The reaction mixture was stirred overnight at room temperature and molar excesses of 3-chloro-1-propanol and imidazole were used to ensure complete reaction of the triisopropylchlorosilane, the most expensive starting material. Following the overnight stirring, diethyl ether was added to the solution (~6 times as much diethyl ether as DMF by volume) and three successive aqueous extractions were used to (presumably) remove the HCl reaction byproduct, the DMF solvent, and the excess imidazole base from the mixture. The diethyl ether solvent was then evaporated under dynamic vacuum and the TIPSOPrCl product was purified by fractional vacuum distillation, not the silica gel chromatography reported in the literature,[15] to facilitate scalable synthesis. The excess 3-chloro-1-propanol was readily removed from TIPSOPrCl during this distillation process, as indicated by the lack of characteristic peaks of that starting material in the ^{1}H NMR spectra of the purified TIPSOPrCl.

^{1}H NMR (300 MHz, $CDCl_3$, 22 °C): δ (ppm) 3.81 (*t*, 2H, Si-O-CH_2), 3.66 (*t*, 2H, -CH_2Cl), 1.95 (*quintet*, 2H, O-CH_2C$H_2$$CH_2$Cl), 1.04 (br *m*, 21H, Si-CH(CH_2)$_2$).

3-tert-Butyldimethylsilyloxy-1-chloropropane. 3-*tert*-Butyldimethylsilyloxy-1-chloropropane (*t*BDMSOPrCl; b.p. 68 °C/1100 mm Hg) was synthesized using the TIPSOPrCl procedure described above, except 3-*tert*-Butyldimethylchlorosilane was used instead of triisopropylchlorosilane.

^{1}H NMR (300 MHz, $CDCl_3$, 22 °C): δ (ppm) 3.72 (*t*, 2H, Si-O-CH_2), 3.62 (*t*, 2H, -CH_2Cl), 1.93 (*quintet*, 2H, O-CH_2C$H_2$$CH_2$Cl), 0.88 (*s*, 9H, Si-C(CH_3)$_3$), 0.04 (*s*, 6H, Si-(CH_3)$_2$).

In principle it should be possible to prepare other x-1-chloropropane molecules containing protecting groups with even more steric bulk than TIPSOPrCl, such as *tert*-butyldiphenylsilyloxy-1-chloropropane or triphenylsilyloxy-1-chloropropane. These bulkier materials would likely have elevated boiling points that would preclude purification by vacuum distillation and require tedious silica gel chromatography, however, making them less attractive from a practical perspective.

Triisopropylsilyloxy-1-propyllithium. Lithium (2.55 g, 0.37 mol) was placed under an argon atmosphere in a 500 mL 3-neck round-bottom flask equipped with a Telfon-coated stirbar (1½" x 3/8"), a condenser, and a pressure equalizing addition funnel. [NOTE: Argon was employed as the inert gas because lithium reacts with nitrogen.] The surface of the lithium metal was prepared by the following two step procedure to ensure reliable reactivity: (i) the wire was stirred vigorously at a rate of ~1000 min^{-1} for 1 h with cyclohexane (50 mL) to remove the mineral oil, before decanting the solution, (ii) the wire was treated with fresh cyclohexane (50 mL) and

stirred vigorously at a rate of ~1000 min^{-1} overnight at 22 °C to activate the surface by mechanical abrasion. The second cyclohexane wash was decanted and fresh cyclohexane (50 mL) was added to the lithium as the reaction solvent. The pressure equalizing addition funnel was then charged with TIPSOPrCl (6.45 g, 0.026 mol), which was added dropwise to the lithium in cyclohexane at 40 °C over 0.5 h. [NOTE: *Beware of unpredictable initiation period.* The reaction may initiate slowly and the rapid addition of the TIPSOPrCl can lead to uncontrollable exotherms.] Occasionally, a slight exotherm (1-2 °C) in the temperature bath was observed; in such cases, the addition was slowed to maintain a constant reaction temperature. Upon complete addition, the reaction was heated to 60 °C until "No-D" ^{1}H NMR of reaction aliquots indicated complete consumption of the starting material (up to 31 h). The reaction was cooled to 22 °C and Schlenk filtered through a pad of Celite to yield a transparent, faint yellow or orange solution of the organolithium reagent.

^{1}H NMR (500 MHz, C_6H_{12}, 22 °C): δ (ppm) 3.85 (br *m*, 2H, Si-O-CH_2), 2.20 (br *m*, 2H, O-CH_2C$H_2$$CH_2$Li), –0.73 (br *m*, 2H, -CH_2Li). Final concentration: 0.55 M based on the COD internal reference.

3-tert-butyldimethysilyloxy-1-propyllithium. The *t*BDMSOPrLi initiator was synthesized using the TIPSOPrLi procedure, except *t*BDMSOPrCl was used instead of TIPSOPrCl.

^{1}H NMR (500 MHz, C_6H_{12}, 22 °C): δ (ppm) 3.83 (br *m*, 2H, Si-O-CH_2), 2.18 (br *m*, 2H, O-CH_2C$H_2$$CH_2$Li), –0.80 (br *m*, 2H, -CH_2Li). Final concentration: 0.18 M based on the COD internal reference.

α-Hydroxypolystyrene Synthesis. Anionic polymerization of styrene at 40 °C in cyclohexane was initiated by *t*BDMSOPrLi or TIPSOPrLi. In a typical "unseeded" polymerization, TIPSOPrLi (3.5 mL) was added to cyclohexane (500 mL) thermostated at 40 °C. After 15 minutes, styrene monomer (12.8 g) was added and allowed to react for 8 h at 40 °C. Reactions were terminated by the addition of degassed MeOH (10 mL) and the polymer was isolated by precipitation in MeOH (1.5 L), followed by freeze-drying from C_6H_6. In the freeze drying process, the polystyrene was dissolved in 200 mL of C_6H_6 and placed in a stainless steel beaker (500 mL). The beaker was partially submerged in liquid nitrogen to freeze the solution and the polymer was freeze-dried overnight in a vacuum oven until the pressure reached the baseline oven pressure (500 mTorr). In "seeded" reactions, three aliquots of styrene monomer (0.5 g) initially were added at 20 minute intervals before the balance of the monomer was added to the reaction.

The resultant trialkylsilyloxy-polystyrene (10 g) was dissolved in THF (100 mL) and treated with excess TBAF (10 equivalents per Si) for 48 h at 22 °C. The THF was removed using a rotary evaporator. The polymer was re-dissolved in CH_2Cl_2 (200 mL) and aqueous extractions (3 x 200 mL) of the solution were used to remove any residual salts. The washed polymer was recovered by precipitation in MeOH from the CH_2Cl_2 solution, dissolved in C_6H_6, and freeze-dried. ^{1}H NMR data provided evidence that this deprotection reaction was successful; the peak at 0.9 ppm that is associated with the 21 isopropyl protons was absent from the spectrum of the deprotected polymer.

4.3 Results and Discussion

The reaction between a silyloxy-protected alkyl chloride and elemental lithium is very sensitive to the condition of the lithium surface. We found that lithiation of TIPSOPrCl or *t*BDMSOPrCl does not proceed without first preparing the lithium wire by vigorously stirring it in cyclohexane overnight to mechanically abrade the surface and expose fresh metal. Bromobutane, in contrast, lithiates without any special surface preparation. Tong *et al.* previously noted a similar sensitivity in the synthesis of *t*BDMSOPrLi using a mineral oil dispersion of lithium and reported washing the lithium repeatedly to obtain "a silvery metal surface."[6]

The use of "No-D" ^{1}H NMR enabled real-time monitoring of the progress of the lithiation reaction and final determination of the concentration of the initiator solution.[13,14] Previous syntheses of *t*BDMSOPrLi employed a reaction time of 2 h at 60 °C with Gilman double titration assays to confirm the presence of an active organolithium; however, the initiator solution was not analyzed with any other techniques.[1,6] The full ^{1}H NMR spectrum of the TIPSOPrLi solution is presented in Figure 4.1, in which the upfield peak at –0.73 ppm associated with protons bound to the carbanionic center indicates lithiation has occurred.[14] A portion of the ^{1}H NMR spectrum of the TIPSOPrLi solution at five different reaction times is presented in Figure 4.2. The broad initiator multiplet (δ 3.85 ppm, H_a in Figure 4.2) increases in intensity, while the sharp TIPSOPrCl triplets (δ 3.93 ppm, δ 3.68 ppm, H_d and H_e, respectively, in Figure 4.2) concurrently diminish in intensity as the reaction progresses.

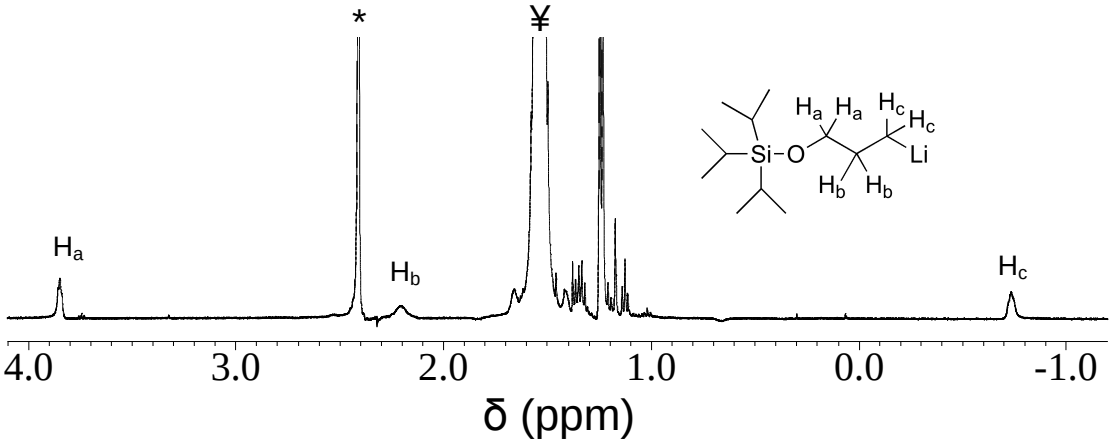

Figure 4.1. Truncated ^{1}H NMR spectrum of the TIPSOPrLi initiator in cyclohexane, with the peaks corresponding to the propyl protons on the initiator labeled H_a, H_b, and H_c. The cyclohexane resonance is marked with a ¥ and the sharp peak labeled * corresponds to the eight protons on the 1,5-cyclooctadiene used to reference the spectrum and determine the concentration of the initiator solution.

It is crucial that all of the TIPSOPrCl is consumed during lithiation since the alkyl halide starting material can serve as a chain termination agent in anionic polymerizations. The reaction time necessary to achieve complete lithiation varied for every batch of initiator prepared. Although the source of this variation was not identified, we speculate that variability in the condition of the lithium surface results in different reaction rates. "No-D" ^{1}H NMR serves as a convenient means of monitoring the extent of reaction and confirming complete consumption of TIPSOPrCl.

The polydispersities and molecular weights of the end-functionalized PS initiated using *t*BDMSOPrLi and TIPSOPrLi in cyclohexane are reported in Table 4.1. Some researchers have suggested that "seeding" the initiator by mixing a small fraction

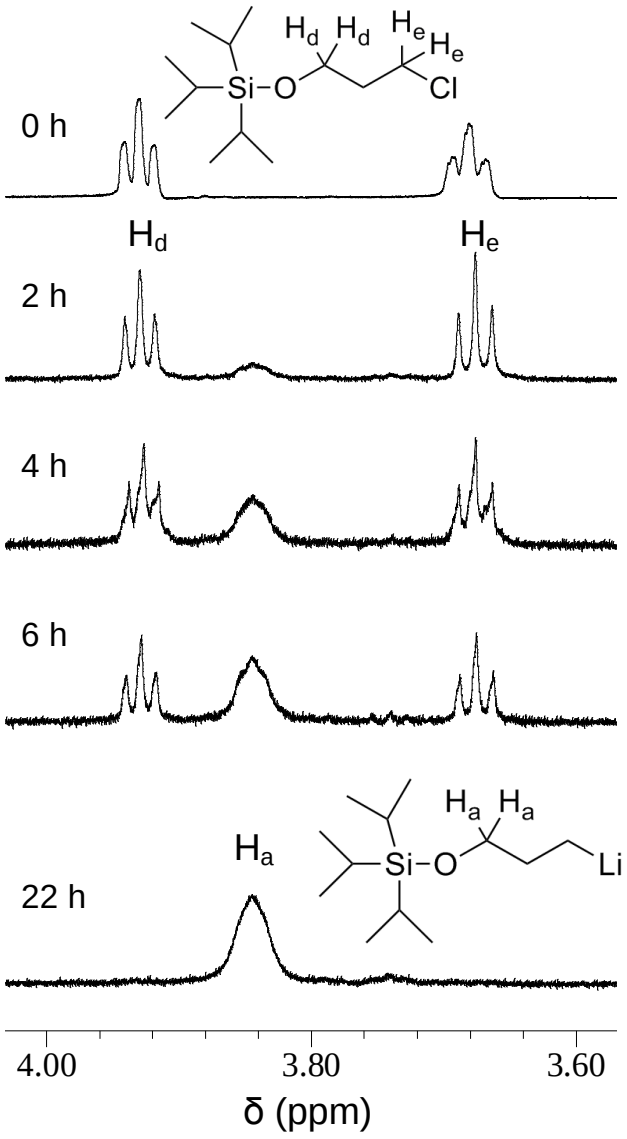

Figure 4.2. ^{1}H NMR spectra of the TIPSOPrLi at five different reaction times. The TIPSOPrCl peaks diminish in intensity as the starting material is consumed, while the TIPSOPrLi peak grows in intensity as the initiator is produced.

Table 4.1. Styrene Polymerizations Using Two Functionalized Initiators

Initiator	Initiation Strategy[a]	M_n (kg/mol)[a]	Expected M_n (kg/mol)[b]	M_w/M_n[c]	F_n[d]
*t*BDMSOPrLi	Unseeded	4.8	5.0	1.40	0.96
*t*BDMSOPrLi	Seeded	6.0	5.0	1.30	1.03
*t*BDMSOPrLi	Seeded	7.1	6.8	1.32	0.99
TIPSOPrLi	Unseeded	7.1	6.9	1.33	0.95
TIPSOPrLi	Seeded	4.0	4.9	1.22	0.87
TIPSOPrLi	Seeded	6.8	6.9	1.11	1.01
TIPSOPrLi	Seeded	8.7	8.5	1.10	1.10
TIPSOPrLi	Seeded	10.2	9.7	1.08	0.98
TIPSOPrLi	Seeded	16.5	unknown[e]	1.07	0.95

[a] See experimental section. [b] Calculated using the initiator concentration and the amount of styrene added. [c] Measured using size exclusion chromatography against PS standards at 22 °C in a tetrahydrofuran mobile phase. [d] Calculated using the M_n values measured using (1) size exclusion chromatography against polystyrene standards and (2) ^{1}H NMR end group analysis. [e] The syringe containing the TIPSOPrLi leaked as the initiator was injected into the reactor, making the added TIPSOPrLi volume unknown.

of monomer with all of the initiator can prevent the broadening of the molecular weight distribution that results from initiation kinetics that are slow relative to the rate of

propagation.[16,17] Although the efficacy of this "seeding" strategy has been questioned,[18] the polydispersities we obtained using both *t*BDMSOPrLi and TIPSOPrLi clearly narrowed with the use of the "seeding" technique. The "seeding" strategy has only a limited effect on reactions initiated with *t*BDMSOPrLi, as the polydispersities remain significantly higher than the values typically obtained for living anionic polymerizations using *sec*-butyllithium ($M_w/M_n < 1.1$).[19] The measured polydispersity index for the 4.0 kg/mol TIPSO-PS ($M_w/M_n = 1.22$) was higher than the measured polydispersity indices for the TIPSO-PS samples with $M_n \geq 6.8$ kg/mol ($M_w/M_n \leq 1.11$). This increase may not reflect a lower molecular weight limit for achieving narrow polydispersity indices using the "seeding" technique given the variations in the concentrations of TIPSOPrLi and styrene for different polymerizations. The relative rates of initiation and propagation of polystyrene in cyclohexane may depend on the concentration of either the initiator or the monomer (or both) when using *t*BDMSOPrLi or TIPSOPrLi.[17]

The SEC traces of functional PS samples synthesized using the "seeding" strategy with *t*BDMSOPrLi ($M_n = 7.1$ kg/mol) and TIPSOPrLi ($M_n = 6.8$ kg/mol) are presented in Figure 4.3. The TIPSO-PS molecular weight distribution is significantly narrower than that of the *t*BDMSO-PS. We attribute the narrower molecular weight distribution of the TIPSO-PS to an increase in the rate of styrene initiation and suggest that this enhanced initiation rate is due to a reduction in intermolecular association that results from coordination of the silyl ether oxygen to lithium. The use of the more sterically hindered TIPSOPrLi, along with the "seeding" technique to initiate polymerizations, facilitates the synthesis of nearly monodisperse protected polystyrene in cyclohexane.

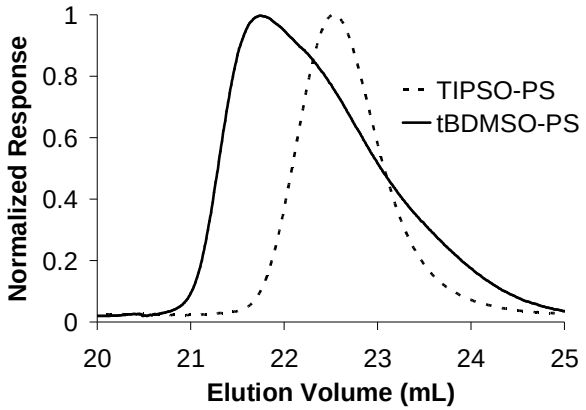

Figure 4.3. SEC traces of the TIPSO-PS (M_n = 6.8 kg/mol) and *t*BDMSO-PS (M_n = 7.1 kg/mol) synthesized using the "seeding" technique.

Functionalized alkyllithium initiators derive their value from the ability to install a protected group that can be readily converted into an α-functionality on every polymer chain. The degree of functionality (F_n) can be assessed by comparing the molecular weight of the polystyrene measured using ^{1}H NMR end-group analysis and that measured by SEC using PS standards. The F_n values for all of the polystyrene samples are presented in Table 4.1. All of the values are within 13% of F_n =1.0, indicating one TIPS group is present on each polystyrene chain. Treatment with TBAF under mild conditions cleaves the silyl ether to unmask an hydroxyl functionality, a common treatment applicable to TIPS and *t*BDMS functionalities.[11] The absence of the ^{1}H NMR resonance at 0.98 ppm corresponding to the isopropyl protons of the TIPS group after TBAF treatment indicates complete deprotection to produce α-hydroxypolystyrene with a narrow molecular weight distribution.

Many well-defined telechelic block copolymers containing 1,4-polydiene blocks can be synthesized from the nearly monodisperse living polystyrene. For example, we

prepared an α,ω-dihydroxypoly(styrene-*b*-isoprene-*b*-styrene) triblock copolymer (M_n = 25.5 kg/mol, M_w/M_n = 1.08) that contained 94% 1,4-polyisoprene linkages in cyclohexane via sequential addition of styrene, isoprene, and styrene followed by ethylene oxide end-capping using the TIPSOPrLi initiator along with the "seeding" technique. An aliquot from the reactor was taken to analyze the initial polystyrene block (M_n = 6.8 kg/mol, M_w/M_n = 1.13, both based on calibration with PS standards) and TBAF was used to cleave the silyl ether and unmask the latent α-hydroxyl group. Ethylene oxide was subsequently polymerized from both terminal hydroxyl groups to yield an OSISO pentablock terpolymer; the structures and properties of a series of these materials is the focus of Chapter 5.

Acknowledgement. I am grateful to Professor Mahesh K. Mahanthappa for initially suggesting the TIPS strategy and for subsequent assistance with the lithiation chemistry. I also thank Professor Thomas R. Hoye and Dr. Ziyad F. Al-Rashid for helpful discussions.

4.4 References

(1) Sutton, D. E.; Schwindeman, J. A. *ACS Symp. Ser.* **1998**, *704*, 58-70.

(2) Shepherd, N.; Stewart, M. J. Pat. Appl. GB 2241239, 1991.

(3) Quirk, R. P.; Jang, S. H.; Han, K.; Yang, H.; Rix, B.; Lee, Y. *ACS Symp. Ser.* **1998**, *704*, 71-84.

(4) Zhang, P.; Moore, J. S. *J. Polym. Sci. Part A* **2000**, *38*, 207-219.

(5) Frick, E. M.; Hillmyer, M. A. *Macromol. Rapid Commun.* **2000**, *21*, 1317-1322.

(6) Tong, J.; Zhou, C.; Ni, S.; Winnik, M. A. *Macromolecules* **2001**, *34*, 696-705.

(7) Wang, X.; Winnik, M. A.; Manners, I. *Macromol. Rapid Commun.* **2002**, *23*, 210-213.

(8) Quirk, R. P.; You, F.; Wesdemiotis, C.; Arnould, M. A. *Macromolecules* **2004**, *37*, 1234-1242.

(9) Brannan, A. K.; Bates, F. S. *Macromolecules* **2004**, *37*, 8816-8819.

(10) Hutchings, L. R.; Roberts-Bleming, S. J. *Macromolecules* **2006**, *39*, 2144-2152.

(11) Greene, T. W.; Wuts, P. G. M. In *Protective Groups in Organic Synthesis*, 2nd ed.; Wiley-Interscience: New York, 1991; p 473.

(12) Pangborn, A. B.; Giardello, M. A.; Grubbs, R. H.; Rosen, R. K.; Timmers, F. J. *Organometallics* **1996**, *15*, 1518-1520.

(13) Hoye, T. R.; Eklov, B. M.; Ryba, T. D.; Voloshin, M.; Yao, L. J. *Org. Lett.* **2004**, *6*, 953-956.

(14) Hoye, T. R.; Eklov, B. M.; Voloshin, M. *Org. Lett.* **2004**, *6*, 2567-2570.

(15) Hill, S. T.; Mokotoff, M. *J. Org. Chem.* **1984**, *49*, 1441-1442.

(16) Morton, M. In *Anionic Polymerization: Principles and Practice;* Academic Press: New York, 1983; p 244.

(17) Lo, G. Y.; Otterbacher, E. W.; Gatzke, A. L.; Tung, L. H. *Macromolecules* **1994**, *27*, 2233-2240.

(18) Szwarc, M.; Van Byelen, M.; Van Hoyweghen, D. *Macromolecules* **1987**, *20*, 445-448.

(19) Lee, W.; Lee, H.; Cha, J.; Chang, T.; Hanley, K. J.; Lodge, T. P. *Macromolecules* **2000**, *33*, 5111-5115.

5

Structure and Mechanical Properties of OSISO Pentablock Terpolymers

* Reproduced in part with permission from Meuler, A. J.; Fleury, G.; Hillmyer, M. A.; Bates, F. S. *Macromolecules* **2008**, *41*, 5809-5817.

5.1 Introduction

Decades of theoretical and experimental investigations have led to an understanding of the physics governing the phase behavior of AB diblock copolymers.[1-5] Diblock copolymer phase behavior is controlled primarily by two parameters: volume fraction f_A and the product $\chi_{AB}N$, where χ_{AB} is the segment-segment interaction parameter and N the overall degree of polymerization (both χ_{AB} and N are measured with respect to a reference volume). Four equilibrium morphologies have been identified in AB diblocks: lamellae, hexagonally packed cylinders, spheres arranged on a BCC lattice, and the gyroid with $Ia\bar{3}d$ symmetry (herein called Q^{230}, where "Q" indicates a cubic unit cell and "230" refers to the number of the space group in the crystallographic tables[6]). (A fifth morphology, the orthorhombic *Fddd* network (herein called O^{70}, where "O" indicates an orthorhombic unit cell and "70" refers to the number of the space group in the crystallographic tables[6]), recently has been identified

over a very narrow range of f_A and $\chi_{AB}N$.[7-10] See Chapter 2 for an extensive discussion of this recent development.) The regions where these morphologies are stable are often presented on a "universal" phase map defined by f_A and $\chi_{AB}N$.[1, 3-5]

The basic physical principles elucidated from diblock copolymers are readily extended to other macromolecular architectures. Many studies comparing the phase behavior of AB diblocks and ABA triblocks have appeared in the literature, and lamellae, hexagonally packed cylinders, BCC spheres, and Q^{230} have been identified as equilibrium morphologies.[11-24] The phase boundaries, domain spacings, and order-disorder transition temperatures (T_{ODT}'s) shift only slightly in changing the architecture from AB diblocks to ABA triblocks, indicating such a change barely alters the free energy of the system. Matsen and Thompson provided a simple explanation for the similarity of the AB and ABA systems.[23] They noted, for the ABA triblock, that while the segments of the B chains near the interface stretch to minimize interfacial area, the middle of the B block adopts a relaxed conformation in the center of the domain. Consequently, the free energy of the melt does not significantly change when the ABA triblocks are snipped in the center of the relaxed B chains to produce a system of AB diblocks. They suggested that similar reasoning can be applied to higher-order multiblock copolymers (e.g., symmetric ABCBA pentablocks should behave like the homologous ABC triblocks).

The addition of a third chemically distinct block to form ABC triblock terpolymers significantly complicates matters, and more than 30 equilibrium mesostructures have been identified in such multiblocks.[25] This higher level of complexity derives from an increased number of molecular variables, including two

independent composition variables, the overall degree of polymerization N, three χ_{ij}'s (χ_{AB}, χ_{AC}, and χ_{BC}), three statistical segment lengths (b_A, b_B, and b_C), and three distinct block sequences (ABC, ACB, BAC). While this large number of variables has prevented development of a "universal" ABC triblock phase map analogous to that created for AB diblocks, the complex phase behavior of ABC triblocks has motivated interest in harnessing these fascinating morphologies in practical applications.

Bates and colleagues have extensively investigated the structures of poly(isoprene-*b*-styrene-*b*-ethylene oxide) (ISO) triblock terpolymers.[8, 26-34] The interaction parameter between the I and O end blocks is the largest in this system ($\chi_{IO} > \chi_{IS} \approx \chi_{SO}$),[35] making formation of the optional (i.e., not required by chain connectivity) I/O interface enthalpically unfavorable; Bailey et al. described block terpolymers with this block sequence as "non-frustrated."[36] The enthalpic free energy associated with formation of the I/O interface drives ISO triblocks to adopt morphologies with two interfaces (the I/S and S/O interfaces required by chain connectivity) and promotes formation of network morphologies. Three network morphologies have been identified experimentally[26, 28, 29] and theoretically[8] in O-lean ($f_O < 0.30$) ISO triblocks: core-shell gyroid (Q^{230}), O^{70}, and an alternating gyroid with $I4_132$ symmetry (also called Q^{214}, where "Q" indicates a cubic unit cell and "214" refers to the number of the space group in the crystallographic tables[6]). These structures were described in detail in Chapter 2. Formation of these ordered networks is sensitive to the polydispersity index ($PDI = M_w/M_n$, where M_w and M_n are the weight-average and number-average molecular weights) of the polystyrene (PS)[33] and poly(ethylene oxide) (PEO)[34] blocks; polydispersity could drive morphological transitions both to[34] and

from[33] network mesostructures, as will be discussed in Chapter 6. Network formation in ISO triblock materials is also sensitive to the overall molecular weight (segregation strength) of the triblocks. Epps and Bates reported that high molecular weight ISO triblocks with $f_I \approx f_S$ formed interpenetrating, triply periodic networks that lacked the translational order of O^{70}. They attributed this lack of order to kinetic limitations and suggested that O^{70} could still be the equilibrium mesostructure for these higher segregation strength ISO compounds,[31] a prediction supported by recent theoretical work.[37]

The percolating interconnected domains of the network morphologies identified in ISO triblocks and other ABC systems (see Chapter 2 for a complete discussion)[36, 38-43] could find utility in a number of applications requiring mechanical toughness, including use as a photonic crystal[44] or as a membrane (e.g., for gas separation[38] or, after degradation and removal of one of the blocks,[45] for water purification[46, 47]). In some separation applications (e.g., water filtration), anisotropic morphologies like hexagonally packed cylinders may require costly and/or time consuming alignment procedures to minimize pore dead ends and maximize flux through the membrane. The percolating domains of network morphologies, in contrast, are not likely to terminate at grain boundaries, rendering expensive alignment procedures unnecessary. Unfortunately, ISO triblocks are brittle materials, limiting their potential efficacy in many applications. Brittleness is common in ABC triblocks and is often the result of a rubbery end block(s); constraining a rubbery domain between glassy end blocks significantly improves mechanical toughness.[17]

In this Chapter, the mechanical properties of ABC block terpolymers are enhanced by exploiting the ABCBA pentablock architecture, a strategy previously pursued by Kopchick et al. in poly(acrylic acid-*b*-styrene-*b*-isobutylene-*b*-styrene-*b*-acrylic acid) pentablock terpolymers.[48] This strategy requires an intrinsically tough BCB triblock, a constraint satisfied by symmetric poly(ethylene oxide-*b*-styrene-*b*-isoprene-*b*-styrene-*b*-ethylene oxide) (OSISO) pentablock terpolymers. Two-domain lamellae (LAM_2), O^{70}, and three-domain lamellae (LAM_3) are identified in the OSISO pentablocks. To the best of our knowledge, no network morphologies have previously been identified in ABCBA pentablocks. The terminal poly(ethylene oxide) (PEO) blocks do not enhance the mechanical properties of the SIS thermoplastic elastomer, but potentially provide added functionality. For instance, PEO has been degraded to yield a nanoporous material[49, 50] and used as a polymer electrolyte.[51-53] The mechanical consequences of adding the brittle PEO blocks to the termini of SIS are probed via tensile testing.

5.2 Experimental Section

OSISO Synthesis. The poly(ethylene oxide-*b*-styrene-*b*-isoprene-*b*-styrene-*b*-ethylene oxide) (OSISO) pentablock terpolymers were prepared by living anionic polymerization using a protected initiation strategy. All polymerizations were performed under an inert argon atmosphere following established techniques.[54] α,ω-Dihydroxypoly(styrene-*b*-isoprene-*b*-styrene) (HO-SIS-OH) triblocks were first prepared using the functional organolithium 3-triisopropylsilyloxy-1-propyllithium

(TIPSOPrLi)[55] that was described in Chapter 4. Ethylene oxide polymerizations were subsequently initiated from both ends of the HO-SIS-OH using potassium naphthalenide to yield the OSISO pentablocks. This reaction scheme is summarized in Figure 5.1 and the specific details of the procedure are described in the following paragraphs.

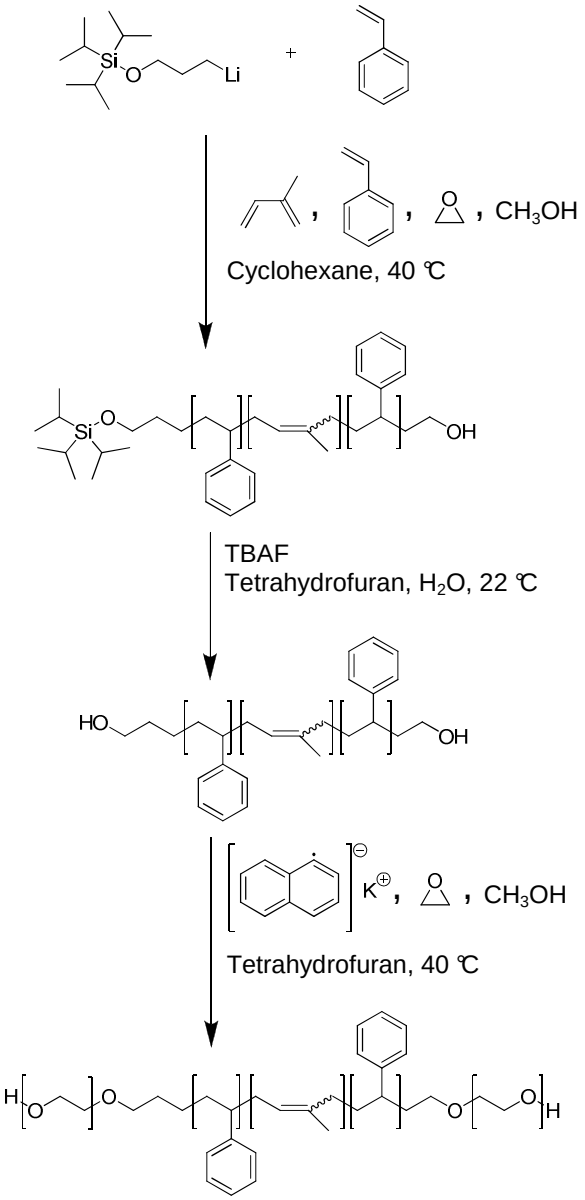

Figure 5.1. Synthetic scheme for the OSISO pentablock terpolymers.

Anionic polymerization of styrene in cyclohexane at 40 °C was initiated by TIPSOPrLi. TIPSOPrLi and cyclohexane (500 mL) were thermostated at 40 °C and the initiator was "seeded" to minimize the breadth of the polystyrene (PS) molecular weight distribution.[55, 56] To "seed" the initiator, three aliquots of styrene monomer (~0.5 g) were added in successive 20 minute intervals before the balance of the styrene (12.7 g including initial aliquots) was added to the reactor. Living polystyryllithium chains (~3 mL of solution) were removed from the reactor, terminated via precipitation in degassed methanol, and analyzed using size exclusion chromatography (SEC) calibrated with PS standards to determine the M_n and M_w/M_n of the first PS block. Isoprene (21.9 g) and styrene (12.7 g) were subsequently sequentially added to the reactor and polymerized (all polymerizations lasted at least 8 hours to ensure essentially complete conversion) before ethylene oxide (~2 g) was added to end-cap the triblocks with an oxanion. Degassed methanol (10 mL) was injected into the reactor to terminate the living chains and create terminal hydroxyl groups; the polymer was recovered via precipitation into methanol (~2 L).

The α-hydroxyl group was unmasked using tetra(*n*-butyl)ammonium fluoride (TBAF) and the HO-SIS-OH was recovered and freeze dried from benzene following the protocol described in Chapter 4.[55] The α,ω-dihydroxy SIS triblock (~4g) was dissolved in tetrahydrofuran (THF) (~300 mL) stirring at 40 °C and ethylene oxide polymerizations were initiated from the terminal hydroxyl groups with potassium naphthalenide and terminated with degassed methanol (~5 mL) after reacting for at least 40 hours.[57] The OSISO pentablocks were subsequently dissolved in dichloromethane

and washed with distilled water to remove excess salts in accordance with reported procedures.[36, 57] The OSISO pentablocks were recovered from the dichloromethane solution by precipitation in isopropanol and were then freeze-dried from benzene. SEC traces of the OSISO pentablocks revealed no evidence of PS homopolymers, IS diblocks, or parent SIS triblocks.

Molecular Characterization. The compositions of the OSISO pentablocks were determined using a 300 MHz Varian NMR instrument operating at room temperature with deuterated chloroform as the solvent. Block mole fractions were calculated using the integrated ^{1}H NMR spectra and converted to volume fractions f_I, f_S, and f_O using published homopolymer densities at 140 °C (ρ_I = 0.830, ρ_S = 0.969, ρ_O = 1.064 g/cm^3).[58]

Room temperature SEC analyses employing THF as the mobile phase (flow rate 1.0 mL/min) were performed on a Waters 717 GPC equipped with three Polymer Labs Mixed-C columns and a Waters 410 differential refractometer. A calibration curve constructed using 10 PS standard samples with M_n ranging from 580-377400 g/mol (Polymer Labs) was used to determine M_w/M_n of all polymers. SEC analysis of the PS in the aliquot removed from the reactor provided M_n of the initiated PS block; M_n values of the SIS triblocks were computed using the M_n of the initiated PS block and the masses of isoprene and styrene subsequently added to the reactor. Actual compositions were verified by ^{1}H NMR spectroscopy and in all cases indicated that complete addition of isoprene and styrene monomers had been achieved. OSISO M_n values were calculated from M_n of the SIS triblocks and the overall compositions measured using ^{1}H NMR spectroscopy.

Synchrotron Small-Angle X-ray Scattering (SAXS). Synchrotron SAXS experiments were conducted at Argonne National Laboratory using the equipment maintained by the DuPont-Northwestern-Dow Collaborative Access Team (DND-CAT). Two equipment setups (yielding equivalent data for our purposes) were employed: (1) an x-ray wavelength (λ) of 1.032 Å with a sample-to-detector distance of 2.01 m and (2) λ = 0.886 Å with a sample-to-detector distance of 5.47 m. Both distances were calibrated with silver behenate and data were acquired on a Mar CCD area detector. Sample temperatures were controlled using a liquid-nitrogen cooled differential scanning calorimetry (DSC) chamber under a helium purge. All samples were heated 10 °C above T_{ODT} (when possible) or to 250 °C for 5 min before data were acquired in an effort to erase effects due to thermal history. Samples were cooled and held at target temperatures for 5 min before data were collected. 2-D diffraction intensities were azimuthally averaged and data are presented in this Chapter as plots of intensity (I) as a function of the scattering wave-vector modulus ($q = |\mathbf{q}| = 4\pi/\lambda \sin(\theta/2)$, where θ is the scattering angle).

Transmission Electron Microscopy (TEM). TEM micrographs were obtained using a JEOL 1210 TEM operating at 120 kV located in the University of Minnesota Institute of Technology Characterization Facility. Samples were compression molded between Teflon sheets into bars 0.5-1 mm thick using a pressure of 500-1000 psi at 100 °C for 5 min. The molds were placed in a vacuum oven and annealed ~10 °C below T_{ODT} for ~ 4 hrs, cooled to 80 °C for ~1 hr, and then cooled to room temperature. Sample slices (50-100 nm thickness) were prepared using a Reichart ultramicrotome fitted with a Microstar diamond knife operated at –120 °C. Slices were placed on

copper grids (Ted Pella) and stained through exposure to the vapor from a 4 % aqueous solution of OsO_4 for 3-5 min (10 min for SIS). The metal oxide selectively reacts with the olefinic groups present in the polyisoprene (PI) and enhances electron mass density contrast.

Dynamic Mechanical Spectroscopy (DMS). DMS experiments were conducted on a Rheometrics Scientific ARES strain-controlled rheometer equipped with 25 mm diameter parallel plates. Polymers were compression molded between Teflon sheets into 1 mm thick discs using a pressure of 500-1000 psi at 100 °C for 5 min. The discs were placed in the rheometer and heated in a nitrogen atmosphere 10 °C above T_{ODT} or to 250 °C for 10 min in an effort to erase effects due to thermal history. Isochronal (ω = 1 rad/s) dynamic elastic (G') and loss (G'') moduli measurements were obtained while heating or cooling at 1 °C/min. Isothermal frequency (ω) sweeps between $\omega = 10^2$ and 10^{-1} rad/s were conducted to probe the viscoelastic behavior at specific temperatures. All data were acquired using a low strain amplitude (1–2 %) that was determined to be within the linear viscoelastic regime.

Tensile Testing. Samples were compression molded between Teflon sheets into 0.5 mm thick bars at 500-1000 psi and 100 °C for 5 min. These master bars had a rectangular cross section measuring 17 mm x 13 mm and were stored at –26 °C. Prior to tensile testing, the master bars were removed from the freezer, allowed to warm to room temperature, and cut into rectangular tensile bars measuring 13 mm x 2.5 mm x 0.5 mm using a fresh razor blade. Uniaxial tensile tests were carried out at room temperature using a Rheometrics Scientific MINIMAT equipped with a 200 N load cell. The MINIMAT operated with a crosshead speed of 8 mm/min and an initial gauge length of

8 mm (length-independent strain rate of 1 min^{-1}) for all samples except ISO-7a; the tensile tests for this brittle material were performed using a crosshead speed of 1 mm/min and an initial gauge length of 8 mm. The force-displacement measurements were converted to engineering stress $\sigma = F/A_o$ vs. nominal strain $\varepsilon = (l - l_o)/l_o$, where l is the length of the sample and A_o and l_o are the initial cross-sectional area and length of the sample, respectively. All reported values are averages from at least four independent trials.

Differential Scanning Calorimetry (DSC). Calorimetry experiments were conducted with a TA Instruments Q1000 DSC. Portions of the master tensile bar that had been stored in the freezer were used for the DSC experiments. 8 ± 1 mg of polymer were placed into aluminum DSC pans and data were acquired while heating the samples from 20 °C to 150 °C at 10 °C/min. Three separate DSC pans were examined for each sample.

5.3 Results and Analysis

Four symmetric polymers with narrow overall molecular weight distributions were synthesized along the $f_I \approx f_S$ isopleth: a parent SIS triblock and three OSISO pentablocks. The molecular characterization data obtained from these samples are provided in Table 5.1. An aliquot of the first PS block was extracted from the reactor during SIS synthesis and analyzed using SEC; this first PS block had M_n = 6.8 kg/mol with M_w/M_n = 1.13. The overall molecular weights were computed using this M_n value and the ^{1}H NMR spectra of the final polymers. The morphology assignments, lattice dimensions, and T_{ODT}*'s* were obtained using a combination of DMS, TEM, and SAXS.

Table 5.1. OSISO and ISO Characterization Data

Polymer	f_I[d]	f_S[d]	f_O[d]	M_n (kDa)	N[e]	M_w/M_n	Lattice Dimensions (nm)[f]	Morphology	T_{ODT}[g] (°C)
SIS[a]	0.50	0.50	0	25.5	399	1.08	15.3 (85 °C)	LAM_2	122
OSISO(.06)[a]	0.47	0.47	0.06	27.3	424	1.10	16.7 (110 °C)	LAM_2	172
OSISO(.13)[a]	0.44	0.43	0.13	29.9	458	1.10	0.293, 0.577, 73.2	O^{70}	237
OSISO(.35)[a]	0.33	0.32	0.35	41.5	612	1.07	25.0	LAM_3	> 250
IS-OH3[b]	0.50	0.50	0	13.6	212	1.05	15.8 (85 °C)	LAM_2	97
ISO2[b]	0.47	0.47	0.06	14.6	226	1.06	16.9 (110 °C)	LAM_2	146
ISO4[b]	0.44	0.44	0.12	15.8	242	1.05	0.294, 0.582, 65.4	O^{70}	194
ISO12[b]	0.33	0.33	0.34	21.8	321	1.06	25.3	LAM_3	> 300
ISO-7a[c]	0.43	0.42	0.15	30.2	460	1.05	0.301, 0.580, 97.4	O^{70}	> 250
ISO-7b[c]	0.41	0.39	0.20	32.4	489	1.06	26.8	Network	> 250

[a] M_w/M_n value for the first PS block is 1.13. [b] Polymers were previously synthesized and characterized[26, 29] and are labeled using the nomenclature of Bailey et al.[26] The M_w/M_n value for the PS block in this series is 1.08.[33] [c] Polymers were previously synthesized and characterized by Epps and Bates and are labeled using their nomenclature.[31] [d] Volume fractions are calculated from published density values at 140 °C (ρ_I = 0.830, ρ_S = 0.969, ρ_O = 1.064 g/cm^3).[58] [e] Based on a segment reference volume of 118 Å^3. [f] Lattice dimensions are obtained from SAXS data and are reported at 160 °C unless otherwise noted in parentheses (°C). The lattice dimensions listed for O^{70} correspond to *a/c*, *b/c*, and *c* and the value listed for ISO-7b corresponds to the length scale associated with the primary scattering vector. [g] Measured using DMS.

The characterization data from two previously studied[26, 28, 29, 31] series of ISO triblocks are also reproduced in Table 5.1. The lower segregation strength ISO triblocks have approximately half the overall molecular weight of the OSISO pentablocks and the phase behavior of these two series is expected to be similar.[23] The higher segregation strength ISO polymers have overall molecular weights comparable to the OSISO pentablocks, allowing us to isolate the influence of chain architecture on the mechanical tensile properties.

SAXS. Synchrotron SAXS powder patterns for the OSISO pentablocks and the ISO-7a triblock are presented in Figure 5.2. Data for SIS were collected at 85 °C, data for OSISO(.06) were obtained at 100 °C, and data for OSISO(.13), OSISO(.35), and ISO-7a were acquired at 160 °C; these temperatures were targeted to facilitate comparison of lattice dimensions between the OSISO pentablocks and the previously reported[26, 29] ISO triblocks. The SAXS peaks for SIS, OSISO(.06), and OSISO(.35) are indexed to a lamellar morphology. The absences of the 002 peak for SIS and OSISO(.06) and of the 003 peak for OSISO(.35) are consistent with structure factor extinctions for symmetric LAM_2 and symmetric LAM_3, respectively.[29] The rich assortment of diffraction peaks for OSISO(.13) and ISO-7a are indexed to O^{70}. The allowed reflections for the orthorhombic lattice of O^{70} are not simple multiples of the primary peak q^*, as they are for a cubic lattice such as Q^{230}. Rather, the orthorhombic peak positions change with the lattice dimensions a, b, and c according to $q_{hkl} = 2\pi [h^2/a^2 + k^2/b^2 + l^2/c^2]^{1/2}$, where h, k, and l are the associated Miller indices. Specific orthorhombic space groups are associated with different sets of allowed reflections, as identified in the crystallographic tables.[6] The a, b, and c parameters were varied to obtain the optimal least–squares fits of the allowed reflections for O^{70} to the recorded SAXS peaks that are provided in Figure 5.2 (see Section 8.2 for details).

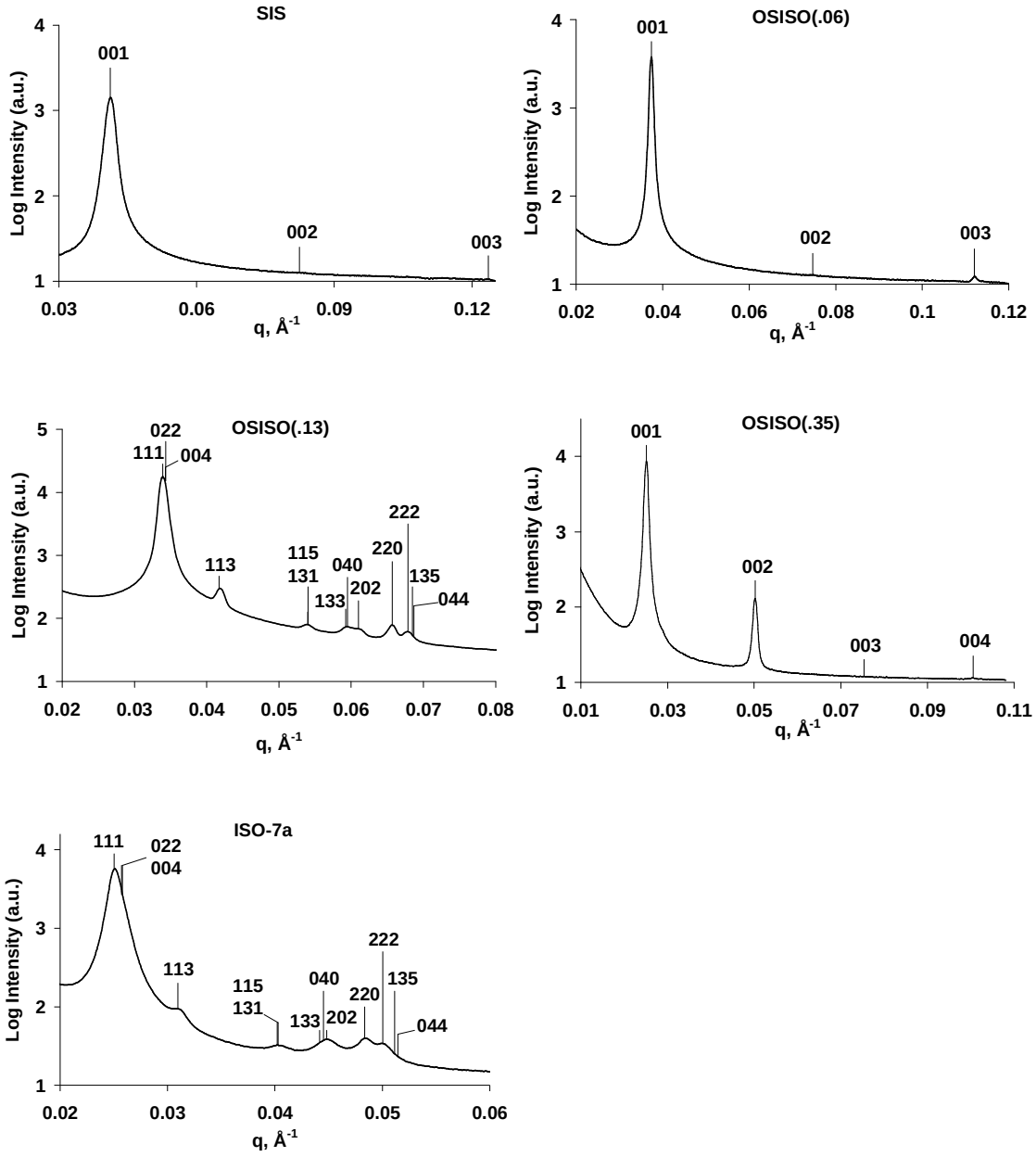

Figure 5.2. Synchrotron SAXS data acquired at 85 °C (SIS), 100 °C (OSISO(.06)), or 160 °C (OSISO(.13), OSISO(.35), and ISO-7a). All samples were annealed 10 °C above T_{ODT} for 5 min (at 250 °C for OSISO(.35) and ISO-7a) before data were collected. The data for SIS, OSISO(.06), and OSISO(.35) are indexed to a lamellar morphology, while the diffraction patterns for OSISO(.13) and ISO-7a are indexed to O^{70}. The absences of the 002 peak in SIS and OSISO(.06) and the 003 peak in OSISO(.35) are consistent with structure factor extinctions for symmetric LAM_2 and symmetric LAM_3, respectively.[29]

TEM. Selected TEM micrographs of the SIS triblock and the OSISO pentablocks are presented in Figure 5.3. Dark sections correspond to OsO_4-stained PI domains while the white areas are unstained PS and/or PEO regions. The alternating white and dark stripes in the SIS, OSISO(.06), and OSISO(.35) images are domains of the lamellar mesostructures; the white stripes are thicker than the black ones for OSISO(.35) as they account for both the PS and PEO domains in this LAM_3 morphology. The TEM micrograph of OSISO(.13) does not contain the alternating stripes of lamellae, but consists of rows of slightly ellipsoidal white separated by gray connections. This micrograph is consistent with the 101 projection of the O^{70} space group.[29] All of the TEM images are consistent with the morphology assignments made using the SAXS data.

DMS. Isochronal dynamic elastic moduli (*G'*) measurements obtained while heating a specimen (not shown) were used to identify the order-disorder transition temperatures (T_{ODT}) of SIS and the OSISO pentablocks; T_{ODT} is associated with the temperature at which *G'* discontinuously decreases upon heating a polymer.[59] No discontinuous increases or decreases in *G'* or *G"* were observed while heating the polymers from 100 °C to just below T_{ODT}, which we interpret as an absence of order-order transitions prior to disordering. T_{ODT} values are listed in Table 5.1 for samples SIS, OSISO(.06), and OSISO(.13). Samples OSISO(.35), ISO-7a, and ISO-7b remained ordered up to 250 °C, the highest temperature accessed during these measurements. Both the T_{ODT} values and the lack of order-order transitions are consistent with the SAXS results.

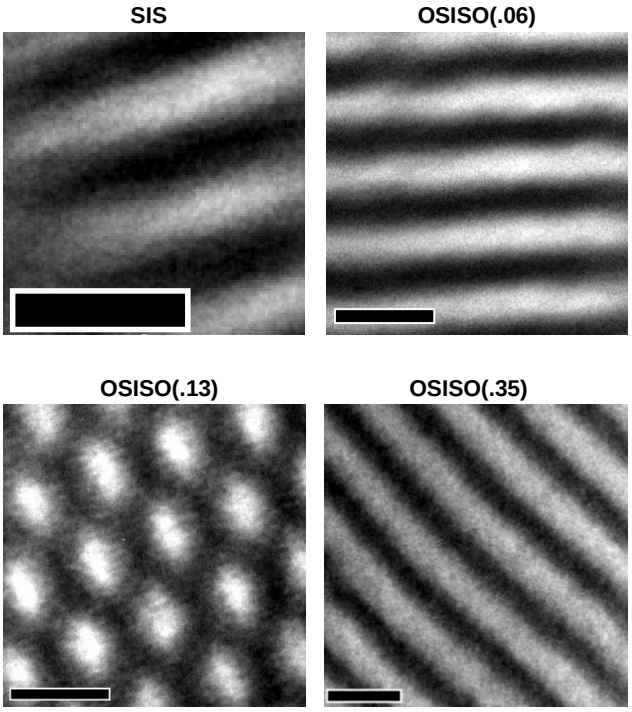

Figure 5.3. TEM micrographs of SIS and the OSISO pentablocks. Dark regions in the TEM micrographs result from OsO_4 staining of the PI domains. The unstained PS and PEO appear much lighter. Scale bars correspond to 20 nm. These images were acquired by Dr. Guillaume Fleury.

The linear viscoelastic behavior of the polymers was investigated using isothermal frequency sweeps. The time-temperature superimposed (TTS) responses of SIS and the OSISO pentablocks are provided in Figure 5.4. Kossuth and coworkers have demonstrated that the low-frequency *G'* response is sensitive to the nature of the periodic order.[60] A plateau in *G'* ($G' \sim \omega^0$) indicates solidlike behavior that is characteristic of triply periodic morphologies such as Q^{230}, O^{70}, or BCC spheres. The plateau in *G'* for OSISO(.13) is consistent with the triply periodic O^{70} network.[29] *G'* of

singly and doubly periodic morphologies such as lamellae or cylinders decreases with decreasing ω; the SIS, OSISO(.06), and OSISO(.35) responses are all consistent with a lamellar morphology.

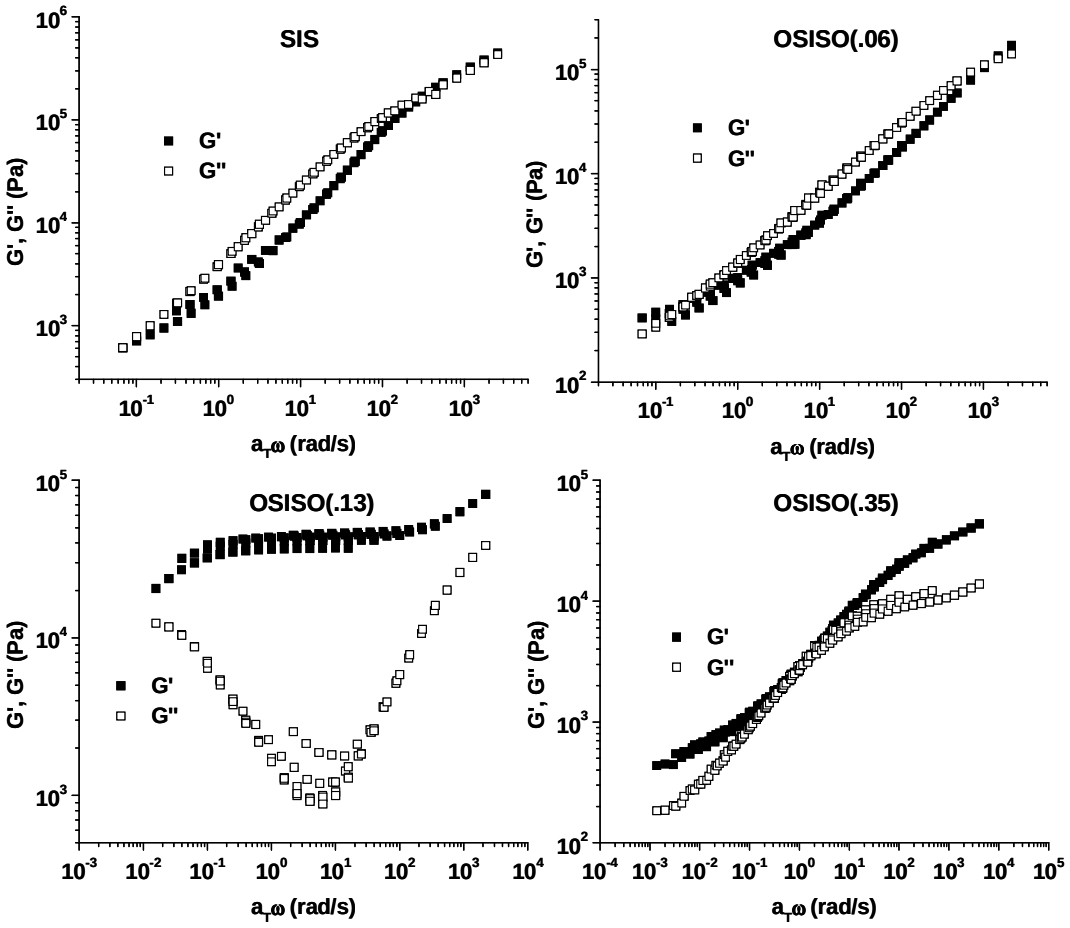

Figure 5.4. Superposition of isothermal frequency responses at 100 °C, 110 °C, and 120 °C (SIS, T_{ref} = 120 °C), 100 °C, 115 °C, 130 °C, 145 °C and 160 °C (OSISO(.06), T_{ref} = 130 °C), 120 °C, 145 °C, 170 °C, 195 °C, and 220 °C (OSISO(.13), T_{ref} = 170 °C), and 100 °C, 125 °C, 150 °C, 175 °C, 200 °C, 225 °C, and 250 °C (OSISO(.35), T_{ref} = 150 °C).

DSC. The fractional crystallinity of the PEO block (X_c) was calculated for each sample from the heat of melting (ΔH_m) measured by DSC, based on:

$$X_c = \Delta H_m / w_{PEO} \Delta H°_{m,\,PEO}$$

where w_{PEO} is the weight fraction of PEO in the block terpolymer and $\Delta H°_{m,\,PEO}$ is the heat of fusion of bulk PEO (213 J/g).[61] The X_c's were calculated from data obtained during the first heating of a specimen with the same thermal history (compression molded, stored at –26 °C, and warmed to room temperature) as the samples that underwent tensile testing; the values are listed in Table 5.2.

Table 5.2. PEO Crystallinities and Tensile Properties of SIS, the OSISO Pentablocks, and Triblock ISO-7a

Sample	Morphology	X_c, PEO	σ_{yield} (MPa)	ε_{fail}	σ_{fail} (MPa)
ISO-7a (f_O = .15)	O^{70}	0.57	-	0.02 ± 0.01	0.8 ± 0.1
OSISO(.35)	LAM_3	0.76	-	0.06 ± 0.01	4.2 ± 0.6
OSISO(.13)	O^{70}	0.29	4.2 ± 0.5	1.3 ± 0.2	4.2 ± 0.3
OSISO(.06)	LAM_2	0.06	3.1 ± 0.2	2.2 ± 0.5	2.7 ± 0.3
SIS	LAM_2	-	3.8 ± 0.4	3.7 ± 0.6	6.2 ± 0.7

Tensile Testing. The tensile properties of block copolymers depend on composition, block architecture, and morphology. Representative engineering stress (σ) versus nominal strain (ε) curves are presented in groups in Figure 5.5 to facilitate discussion of the effects induced by varying these parameters. A summary of the tensile properties is provided in Table 5.2. Here we note that in all cases failure of the specimens occurred in close proximity to the grips, suggesting the reported values for

the stress at break (σ_{fail}) and the strain at break (ε_{fail}) represent lower bounds for these materials. Values of Young's modulus (E) are not included in Table 5.2. While Young's modulus values are readily obtained from the slope of the σ versus ε plot at low strains, the instrument and test specimens were not configured to produce optimal linear results at low strains. As a result, the values obtained from multiple MINIMAT experiments were not statistically meaningful (± 50%), although the magnitudes were consistent with previously reported Young's moduli for SIS triblocks ($E \approx 25$ - 150 MPa).[62-64] Since this study focuses on fracture, additional measurements of Young's moduli were not pursued.

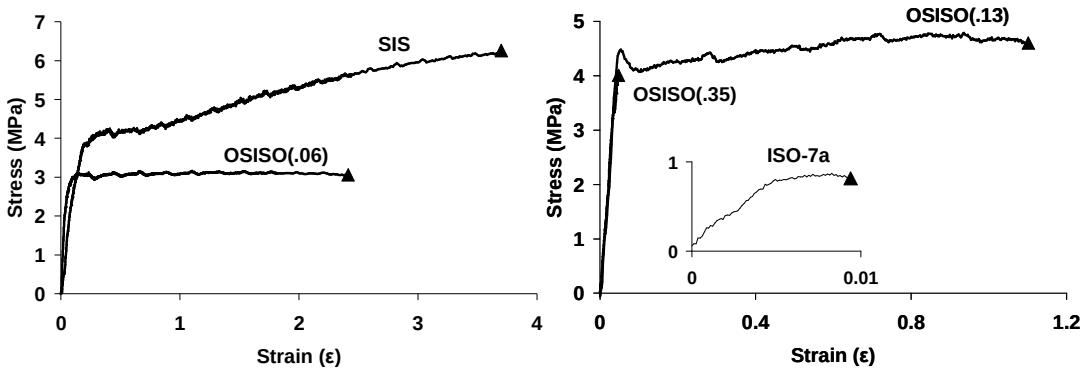

Figure 5.5. Representative engineering stress (σ) versus nominal strain (ε) curves for SIS, the OSISO pentablocks, and ISO-7a. Sample failures are marked by ▲.

5.4 Discussion

Synthetic Strategy. A synthetic route for preparing symmetric OSISO pentablock terpolymers with narrow molecular weight distributions in all blocks was described in the Experimental section. The combination of the TIPSOPrLi protected

initiator and ethylene oxide end-capping can be used to synthesize a variety of α,ω-dihydroxy block copolymers (or homopolymers) by anionic polymerization. Subsequent polymerizations can be initiated from these hydroxyl groups and these reactions could proceed via an anionic, atom transfer radical (ATRP),[65] or ring-opening[66] mechanisms.

Morphology. Epps and Bates previously described the morphology of both ISO-7a (f_O = 0.15) and ISO-7b (f_O = 0.20) as a triply periodic "network" that lacked long-range translational order.[31] While the morphology assignment for ISO-7b is the same in this report, the O^{70} mesostructure is now assigned to ISO-7a. This assignment was made using the synchrotron SAXS data presented in Figure 5.2; the reflections in this figure are indexed to O^{70}. Epps and Bates annealed both ISO-7a and ISO-7b at 200 °C and only observed two broad reflections in the SAXS data. These broad peaks were consistent with a lack of translational order and Epps and Bates attributed this feature to kinetic limitations associated with the relatively high segregation strengths of the polymers. They hypothesized that, absent kinetic limitations, well-formed grains of O^{70} could form. We annealed the samples at 250 °C for 5 minutes and obtained the well-defined Bragg peaks characteristic of O^{70} for sample ISO-7a. Heating ISO-7a to 250 °C decreased the segregation strength and increased the chain mobility, enabling the sample to adopt the (presumably equilibrium) O^{70} microstructure. The 250 °C heat treatment did not alter the state of order of sample ISO-7b, leading us to keep Epps and Bates' original "network" assignment.

Relatively few investigations of symmetric ABCBA pentablock terpolymers have appeared in the literature.[48, 65, 67-79] Previous reports have focused on synthetic methodology,[67-70, 72] hydrogel[75, 79] or ion gel[78] formation, and micellization in

solvents.[65, 71, 73, 74] Only a few reports have interrogated ABCBA pentablock terpolymers in the bulk.

Kopchick and coworkers have, to the best of the author's knowledge, published the only previous investigation of bulk ABCBA pentablock terpolymers containing non-lamellar morphologies.[48, 80] These researchers examined poly(acrylic acid-*b*-styrene-*b*-isobutylene-*b*-styrene-*b*-acrylic acid) pentablock terpolymers that reportedly adopted a mesostructure containing hexagonally packed cylinders.[80] Poly(acrylic acid-*b*-styrene-*b*-isobutylene) triblocks were not extensively characterized, preventing Kopchick et al. from comparing the phase behavior of ABC triblock and ABCBA pentablock terpolymers. The OSISO system, in contrast, is an extension of well-characterized ISO triblocks, facilitating comparison of the phase behavior of the respective architectures.

Mahanthappa and coworkers prepared poly(cyclohexylethylene-*b*-(ethylene-*alt*-propylene)-*b*-ethylene-*b*-(ethylene-*alt*-propylene)-*b*-cyclohexylethylene) (CPEPC) pentablock and CPE triblock terpolymers.[76, 77] All of these block terpolymers contained lamellar mesostructures, including a CPEPC pentablock and its homologous CPE triblock. Pentablock CPEPC-50 (M_n = 30.9 kg/mol and T_{ODT} = 208 °C) and its homologous CPE-50 triblock (M_n = 16.2 kg/mol and T_{ODT} = 168 °C) both adopted lamellar morphologies, with CPEPC-50 having a higher T_{ODT} (208 °C) and larger domain spacing (20.0 nm) than CPE-50 (168 °C, 17.9 nm).[76]

The ISO system exhibits rich phase behavior[26, 28, 29] and the ability of OSISO pentablocks to adopt the same complex network morphologies was previously unknown. The identification of the O^{70} network for sample OSISO(.13) proves that pentablock terpolymers can form network microstructures. SIS, OSISO(.06), and

OSISO(.35) also adopt the same lamellar mesostructures as the homologous ISO counterparts (i.e., the lower molecular weight ISO triblocks summarized in Table 5.1). These results, along with those of Mahanthappa et al.,[76] support Matsen and Thompson's hypothesis that symmetric ABCBA pentablocks adopt the same morphologies as the homologous ABC counterparts.[23]

In addition to the identity of the ordered equilibrium mesostructure, the T_{ODT} and domain spacing are important parameters describing phase behavior. In the analogous AB and ABA systems, the ABA triblocks have higher T_{ODT}*'s* than their homologous AB diblocks,[14, 24]a result in agreement with self-consistent field theory calculations.[23] AB diblocks disorder at lower temperatures because the dangling B chain ends of the AB diblock can more readily penetrate A domains than the middle B segment of the ABA triblock.[23] OSISO(.06) and OSISO(.13) both have higher T_{ODT}*'s* than the homologous ISO triblocks (see Table 5.1); these results are consistent with the CPE/CPEPC data reported by Mahanthappa et al.[76] T_{ODT}*'s* for OSISO(.35) and ISO12 (f_O = .34) were not accessed because thermal degradation occurs at the elevated temperatures required to disorder both polymers. The rationale for the higher T_{ODT}*'s* of the ABCBA pentablocks is presumably the same as that presented by Matsen and Thompson for AB diblocks and ABA triblocks;[23] the ABCBA pentablocks remain ordered to higher temperatures than the homologous ABC triblocks because a longer C chain must be dragged into the A and B domains to disorder the polymer in the pentablock case.

Only slight variations (± 10%) in domain periodicity have been reported[16, 24] for ABA triblocks and the homologous AB diblocks, a result in agreement with self-consistent field theory calculations.[23] The comparison in domain spacing can be

extended into ABCBA pentablocks and ABC triblocks. Both Mahanthappa et al.'s reported CPEPC/CPE domain periodicities[76] and our OSISO/ISO values are relatively constant (± 12%), a result generally expected based upon the AB/ABA precedent.

PEO Crystallinity. Bailey et al. measured the fractional crystallinity (X_c) of a series of ISO triblocks along the $f_I \approx f_S$ isopleth (including the lower molecular weight ISO triblocks listed in Table 5.1); X_c increased from 0 to ~0.55 as f_O changed from 0.05 to 0.12 and then remained constant at ~0.55 as f_O increased to 0.35.[26] The fractional crystallinity of 0.57 measured for the O^{70}-forming ISO-7a specimen is consistent with Bailey et al.'s results. The crystallinity of O^{70}-forming OSISO(.13) is ~40% below the value measured by Bailey et al. for an ISO with a comparable f_O. This composition, however, is very close to the ISO phase boundary between LAM_2 and O^{70} and the associated rapid increase in X_c that occurs as PEO forms a relatively pure domain in the O^{70} mesostructure. We attribute the decrease in X_c for OSISO(.13) to some mixing of the PS and PEO domains. X_c for LAM_3-forming OSISO(.35) exceeds Bailey et al.'s previously reported values for ISO triblocks and is near the value for bulk PEO.[81]

Mechanical Properties. We can probe the consequences of attaching varying amounts of PEO to intrinsically tough SIS triblock by examining the tensile data of the OSISO series. The first comparison can be made between SIS and OSISO(.06). Representative data are provided in Figure 5.5. Both polymers contain lamellae, but SIS has a 24% higher σ_{yield} and 72% larger ε_{fail} than OSISO(.06). We suggest the differences in both values can be attributed to plasticization of the PS domain via mixing with the terminal PEO blocks. Several pieces of experimental data suggest the PS and PEO domains are mixed. First, the fractional PEO crystallinity of 0.06 in OSISO(.06) is

minimal, suggesting the PEO does not form pure domains. Second, the 002 reflection in the OSISO(.06) SAXS data is extinct (see Figure 5.2), a result consistent with a LAM_2 microstructure comprised of alternating layers of PI and a PS/PEO mixture.[29] Furthermore, $\chi N_{SO} = 8.6$ for OSISO(.06) and a neat SO diblock of this composition ($f_O = 0.11$) would not be expected to microphase-separate for χN_{SO} below ~50.[5] Both polymers yield and plastically deform, and SIS strain hardens, prior to failure.

Another relevant comparison can be made between OSISO(.13) and OSISO(.35). Sample OSISO(.13) contains O^{70} while specimen OSISO(.35) forms LAM_3; representative stress-strain curves for these two materials are provided in Figure 5.5. OSISO(.13) yields and plastically deforms prior to failure, and the reduction in σ in the stress-strain curve at $\varepsilon \approx 0.06$ is indicative of necking. Necking has been reported in thermoplastic elastomers when a glassy domain is continuous in the loading direction. Dair et al., for instance, observed necking in SIS triblocks containing the Q^{230} (gyroid) morphology.[62, 63] Necking in OSISO(.13) is consistent with a continuous glassy PS domain created by the O^{70} morphology. In contrast to OSISO(.13), OSISO(.35) exhibits brittle failure at very low strains. We suggest that this drastically different behavior is the result of the different morphologies of the two samples; schematics of the LAM_3 and O^{70} mesostructures are depicted in Figure 5.6. In the LAM_3 morphology of sample OSISO(.35), cracks can readily propagate across the two-dimensionally continuous PEO domains without encountering the SIS core material. As the cracks in the PEO fracture plane spread throughout the sample, there are no continuous glassy and rubbery domains to provide mechanical support and the sample fails. The OSISO(.13) network, in contrast, has percolating PI, PS, and PEO domains; the [311]

projection of the O^{70} unit cell is provided in Figure 5.6. Clearly, there is no fragile PEO bilayer in the O^{70} morphology of sample OSISO(.13). As a result, a crack initiated in the PEO domain would have to split the tough SIS subdomains at every unit cell in order to traverse the material. Eliminating the fragile PEO bilayers by wrapping them into a three-dimensional network prevents failure at very low strains.

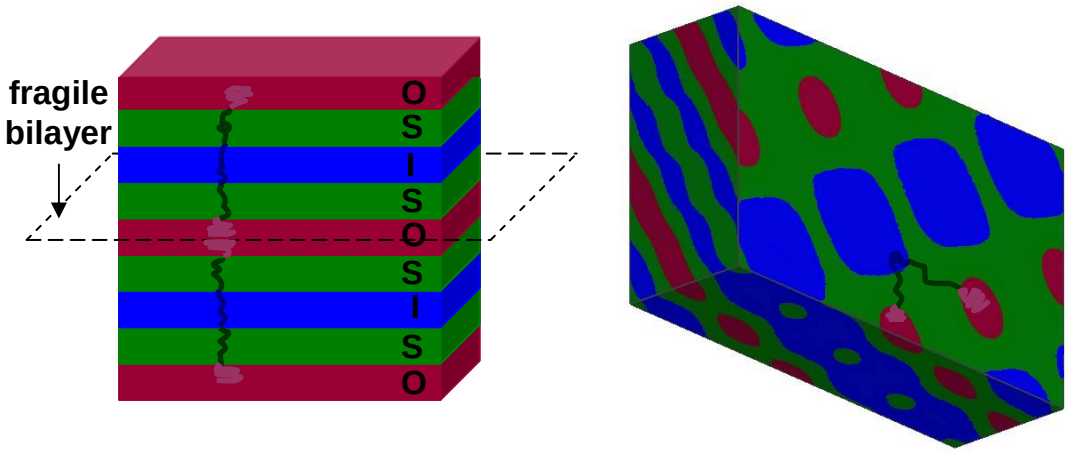

Figure 5.6. Schematics of the LAM_3 (left) and O^{70} (right) morphologies of samples OSISO(.35) and OSISO(.13). The LAM_3 mesostructure is a cartoon representation while the [311] projection of the O^{70} unit cell was generated using level-set modeling with $f_I \approx f_S$ and $f_O = 0.13$.[29] A crack can readily propagate through the fragile PEO bilayer in the LAM_3 microstructure. The [311] projection clearly shows that there are no fragile PEO bilayers in the O^{70} unit cell. As a result, the tough SIS subdomain that surrounds the PEO would have to be broken in order for a crack to traverse the O^{70} morphology.

Here we note that samples OSISO(.13) and OSISO(.35) have different compositions and levels of PEO crystallinity (see Table 5.2). We suspect, based upon a previous report, that the increased PEO crystallinity of OSISO(.35) compared to OSISO(.13) does not cause the sharp decrease in toughness. Phatak and coworkers published a related study on the fracture properties of poly(ethylene-*b*-cyclohexylethylene-*b*-ethylene-*b*-cyclohexylethylene) (ECEC) tetrablock and ECECE pentablock copolymers.[82] All of the block copolymers examined by Phatak et al. contained an isotropic LAM_2 morphology. These materials, like the OSISO pentablocks, are comprised of an intrinsically tough ABA triblock with terminal semicrystalline blocks attached. The level of polyethylene (PE) crystallinity in the ECEC and ECECE samples ranged from 0.21-0.27, values below the PEO fractional crystallinity of 0.29 measured in sample OSISO(.13). Even with these lower crystallinities, the isotropic lamellar ECEC and ECECE materials exhibited brittle behavior, effectively establishing a "threshold" of crystallinity at or above which brittle failure can result. The X_c of 0.29 in OSISO(.13) is above this threshold, yet OSISO(.13) does not fail in a brittle manner; we attribute the material's toughness to its network mesostructure. A more definitive conclusion would require a study of samples of the same polymer containing different morphologies. It might be possible to capture different morphologies by solvent casting OSISO pentablocks from solvents of varying quality. This strategy has been successfully used in block copolymers,[64, 83] but has not yet been pursued for the ISO block terpolymers.

Comparison of the tensile data in Figure 5.5 for ISO-7a (f_O = .15) and OSISO(.13) shows that the network morphology does not, by itself, prevent brittle

failure. These samples have comparable compositions, overall molecular weights, and PEO crystallinities, but differ in chain architecture. Clearly, chain architecture has a significant impact on the mechanical behavior of the materials. Cracks initiated in the PEO domain of ISO-7a can easily propagate because they can readily break the brittle IS subdomain. Sample OSISO(.13), in contrast, contains a tough SIS thermoplastic elastomer that limits crack propagation and increases the toughness dramatically compared to the ISO triblock, with sharp increases in both the stress (σ_{fail}) and strain (ε_{fail}) at break. OSISO(.13) yielded and plastically deformed prior to failure while ISO-7a fractured in a brittle fashion at very low strains. An intrinsically tough material with a brittle bilayer can be toughened by wrapping it into a network mesostructure; intrinsically brittle materials with a network microstructure are still brittle.

5.5 Conclusion

A synthetic strategy to prepare OSISO pentablock terpolymers with narrow molecular weight distributions in all blocks was presented. The morphologies of a symmetric SIS triblock and three OSISO pentablocks were characterized using SAXS, TEM, DMS, and DSC. The OSISO pentablocks are higher-order extensions of previously well-characterized ISO triblocks,[26, 28, 29] enabling us to experimentally compare the phase behavior of ABCBA pentablocks and the homologous ABC triblocks. The O^{70} network was identified in the OSISO pentablocks between LAM_2 and LAM_3, a morphology sequence identical to that reported in ISO triblocks. The identification of O^{70} in OSISO(.13) demonstrates that the network mesostructures

observed in ABC triblocks can be obtained in the higher-order symmetric ABCBA pentablocks.

Tensile testing was used to probe the mechanical consequences of adding various lengths of PEO chains to the ends of an intrinsically tough SIS thermoplastic elastomer. Sample OSISO(.35) contained the LAM_3 microstructure and had semicrystalline terminal PEO blocks; the PEO bilayer led to fracture in a brittle fashion at very low strains, a result consistent with the work of Phatak and coworkers.[82] OSISO(.13), in contrast, contained the O^{70} network and had a strain at failure of 1.3, even though the crystallinity of the terminal PEO blocks was above the brittle threshold established by Phatak et al. This improved toughness is attributed to the triply continuous nature of the O^{70} morphology and demonstrates than an intrinsically robust material with a fragile bilayer can be toughened by wrapping it into a three-dimensional network. The OSISO network is much tougher than the ISO counterpart, suggesting that pentablock terpolymers could prove useful in applications requiring tough, multiply continuous morphologies (e.g., use as a separation membrane).

Acknowledgement. I am indebted to Dr. Guillaume for acquiring the TEM micrographs provided in Figure 5.3. I thank Dr. Steven Weigand and Dr. Denis Keane for setting up the equipment at the Advanced Photon Source that was used to acquire the SAXS data presented in this Chapter. I also thank Professor Eric W. Cochran for letting me use his level-set software and thank Michael J. Bluemle for his help in running the software and generating the level-set projection provided in Figure 5.6.

5.6 References

(1) Leibler, L. *Macromolecules* **1980**, *13*, 1602-1617.

(2) Bates, F. S.; Fredrickson, G. H. *Annu. Rev. Phys. Chem.* **1990**, *41*, 525-557.

(3) Khandpur, A. K.; Förster, S.; Bates, F. S.; Hamley, I. W.; Ryan, A. J.; Bras, W.; Almdal, K.; Mortensen, K. *Macromolecules* **1995**, *28*, 8796-8806.

(4) Matsen, M. W.; Bates, F. S. *Macromolecules* **1996**, *29*, 1091-1098.

(5) Cochran, E. W.; Garcia-Cervera, C. J.; Fredrickson, G. H. *Macromolecules* **2006**, *39*, 2449-2451.

(6) Hahn, T., Ed. *International Tables for Crystallography*, 4th revised ed.; 1994; Vol. A.

(7) Tyler, C. A.; Morse, D. C. *Phys. Rev. Lett.* **2005**, *94*, 208302.

(8) Tyler, C. A.; Qin, J.; Bates, F. S.; Morse, D. C. *Macromolecules* **2007**, *40*, 4654-4668.

(9) Takenaka, M.; Wakada, T.; Akasaka, S.; Nishitsuji, S.; Saijo, K.; Shimizu, H.; Kim, M. I.; Hasegawa, H. *Macromolecules* **2007**, *40*, 4399-4402.

(10) Kim, M. I.; Wakada, T.; Akasaka, S.; Nishitsuji, S.; Saijo, K.; Hasegawa, H.; Ito, K.; Takenaka, M. *Macromolecules* **2008**, *41*, 7667-7670.

(11) Helfand, E.; Wasserman, Z. R. *Macromolecules* **1976**, *9*, 879-888.

(12) Mayes, A. M.; Olvera de la Cruz, M. *J. Chem. Phys.* **1989**, *91*, 7228-7235.

(13) Mayes, A. M.; Olvera de la Cruz, M. *J. Chem. Phys.* **1991**, *95*, 4670-4677.

(14) Gehlsen, M. D.; Almdal, K.; Bates, F. S. *Macromolecules* **1992**, *25*, 939-943.

(15) Adams, J. L.; Graessley, W. W.; Register, R. A. *Macromolecules* **1994**, *27*, 6026-6032.

(16) Matsushita, Y.; Nomura, M.; Watanabe, J.; Mogi, Y.; Noda, I.; Imai, M. *Macromolecules* **1995**, *28*, 6007-6013.

(17) McKay, K. W.; Gros, W. A.; Diehl, C. F. *J. Appl. Polym. Sci.* **1995**, *56*, 947-958.

(18) Ryu, C. Y.; Lee, M. S.; Hajduk, D. A.; Lodge, T. P. *J. Polym. Sci. Part B* **1997**, *35*, 2811-2823.

(19) Avgeropoulos, A.; Dair, B. J.; Hadjichristidis, N.; Thomas, E. L. *Macromolecules* **1997**, *30*, 5634-5642.

(20) Avgeropoulos, A.; Chan, V. Z.; Lee, V. Y.; Ngo, D.; Miller, R. D.; Hadjichristidis, N.; Thomas, E. L. *Chem. Mater.* **1998**, *10*, 2109-2115.

(21) Laurer, J. H.; Hajduk, D. A.; Fung, J. C.; Sedat, J. W.; Smith, S. D.; Gruner, S. M.; Agard, D. A.; Spontak, R. J. *Macromolecules* **1997**, *30*, 3938-3941.

(22) Mani, S.; Weiss, R. A.; Cantino, M. E.; Khairallah, L. H.; Hahn, S. F.; Williams, C. E. *Eur. Polym. J.* **1999**, *36*, 215-219.

(23) Matsen, M. W.; Thompson, R. B. *J. Chem. Phys.* **1999**, *111*, 7139-7146.

(24) Mai, S.; Mingvanish, W.; Turner, S. C.; Chaibundit, C.; Fairclough, J. P. A.; Heatley, F.; Matsen, M. W.; Ryan, A. J.; Booth, C. *Macromolecules* **2000**, *33*, 5124-5130.

(25) Bates, F. S.; Fredrickson, G. H. *Phys. Today* **1999**, *52*, 32-38.

(26) Bailey, T. S.; Hardy, C. M.; Epps, T. H., III; Bates, F. S. *Macromolecules* **2002**, *35*, 7007-7017.

(27) Epps, T. H., III; Bailey, T. S.; Waletzko, R.; Bates, F. S. *Macromolecules* **2003**, *36*, 2873-2881.

(28) Epps, T. H., III; Cochran, E. W.; Hardy, C. M.; Bailey, T. S.; Waletzko, R. S.; Bates, F. S. *Macromolecules* **2004**, *37*, 7085-7088.

(29) Epps, T. H., III; Cochran, E. W.; Bailey, T. S.; Waletzko, R. S.; Hardy, C. M.; Bates, F. S. *Macromolecules* **2004**, *37*, 8325-8341.

(30) Epps, T. H., III; Chatterjee, J.; Bates, F. S. *Macromolecules* **2005**, *38*, 8775-8784.

(31) Epps, T. H., III; Bates, F. S. *Macromolecules* **2006**, *39*, 2676-2682.

(32) Chatterjee, J.; Jain, S.; Bates, F. S. *Macromolecules* **2007**, *40*, 2882-2896.

(33) Meuler, A. J.; Ellison, C. J.; Evans, C. M.; Hillmyer, M. A.; Bates, F. S. *Macromolecules* **2007**, *40*, 7072-7074.

(34) Meuler, A. J.; Ellison, C. J.; Hillmyer, M. A.; Bates, F. S. *Macromolecules* **2008**, *41*, 6272-6275.

(35) Frielinghaus, H.; Hermsdorf, N.; Almdal, K.; Mortensen, K.; Messe, L.; Corvazier, L.; Fairclough, J. P. A.; Ryan, A. J.; Olmsted, P. D.; Hamley, I. W. *Europhys. Lett.* **2001**, *53*, 680-686.

(36) Bailey, T. S.; Pham, H. D.; Bates, F. S. *Macromolecules* **2001**, *34*, 6994-7008.

(37) Qin, J. *Private Communication*.

(38) Shefelbine, T. A.; Vigild, M. E.; Matsen, M. W.; Hajduk, D. A.; Hillmyer, M. A.; Cussler, E. L.; Bates, F. S. *J. Am. Chem. Soc.* **1999**, *121*, 8457-8465.

(39) Goldacker, T.; Abetz, V. *Macromolecules* **1999**, *32*, 5165-5167.

(40) Suzuki, J.; Seki, M.; Matsushita, Y. *J. Chem. Phys.* **2000**, *112*, 4862-4868.

(41) Hückstädt, H.; Goldacker, T.; Goepfert, A.; Abetz, V. *Macromolecules* **2000**, *33*, 3757-3761.

(42) Hardy, C. M.; Bates, F. S.; Kim, M.; Wignall, G. D. *Macromolecules* **2002**, *35*, 3189-3197.

(43) Cochran, E. W.; Bates, F. S. *Phys. Rev. Lett.* **2004**, *93*, 087802.

(44) Urbas, A. M.; Maldovan, M.; DeRege, P.; Thomas, E. L. *Adv. Mater.* **2002**, *14*, 1850-1853.

(45) Hillmyer, M. A. *Adv. Polym. Sci.* **2005**, *190*, 137-181.

(46) Yang, S. Y.; Ryu, I.; Kim, H. Y.; Kim, J. K.; Jang, S. K.; Russell, T. P. *Adv. Mater.* **2006**, *18*, 709-712.

(47) Phillip, W. A.; Rzayev, J.; Hillmyer, M. A.; Cussler, E. L. *J. Membr. Sci.* **2006**, *286*, 144-152.

(48) Kopchick, J. G.; Storey, R. F.; Beyer, F. L.; Mauritz, K. A. *Polymer* **2007**, *48*, 3739-3748.

(49) Mao, H.; Hillmyer, M. A. *Macromolecules* **2005**, *38*, 4038-4039.

(50) Mao, H.; Hillmyer, M. A. *Soft Matter* **2006**, *2*, 57-59.

(51) Ruzette, A. G.; Soo, P. P.; Sadoway, D. R.; Mayes, A. M. *J. Electrochem. Soc.* **2001**, *148*, A537-A543.

(52) Vorrey, S.; Teeters, D. *Electrochim. Acta* **2003**, *48*, 2137-2141.

(53) Singh, M.; Odusanya, O.; Wilmes, G. M.; Eitouni, H. B.; Gomez, E. D.; Patel, A. J.; Chen, V. L.; Park, M. J.; Fragouli, P.; Iatrou, H.; Hadjichristidis, N.; Cookson, D.; Balsara, N. P. *Macromolecules* **2007**, *40*, 4578-4585.

(54) Ndoni, S.; Papadakis, C. M.; Bates, F. S.; Almdal, K. *Rev. Sci. Instrum.* **1995**, *66*, 1090-1095.

(55) Meuler, A. J.; Mahanthappa, M. K.; Hillmyer, M. A.; Bates, F. S. *Macromolecules* **2007**, *40*, 760-762.

(56) Lo, G. Y.; Otterbacher, E. W.; Gatzke, A. L.; Tung, L. H. *Macromolecules* **1994**, *27*, 2233-2240.

(57) Hillmyer, M. A.; Bates, F. S. *Macromolecules* **1996**, *29*, 6994-7002.

(58) Fetters, L. J.; Lohse, D. J.; Richter, D.; Witten, T. A.; Zirkel, A. *Macromolecules* **1994**, *27*, 4639-4647.

(59) Rosedale, J. H.; Bates, F. S. *Macromolecules* **1990**, *23*, 2329-2338.

(60) Kossuth, M. B.; Morse, D. C.; Bates, F. S. *Journal of Rheology* **1999**, *43*, 167-196.

(61) Wunderlich, B. *Macromolecular Physics*; Academic Press: New York, 1980; Vol. 3.

(62) Dair, B. J.; Honeker, C. C.; Alward, D. B.; Avgeropoulos, A.; Hadjichristidis, N.; Fetters, L. J.; Capel, M.; Thomas, E. L. *Macromolecules* **1999**, *32*, 8145-8152.

(63) Dair, B. J.; Avgeropoulos, A.; Hadjichristidis, N.; Thomas, E. L. *J. Mater. Sci.* **2000**, *35*, 5207-5213.

(64) Qiao, L.; Leibig, C.; Hahn, S. F.; Winey, K. I. *Ind. Eng. Chem. Res.* **2006**, *45*, 5598-5602.

(65) Sha, K.; Li, D.; Li, Y.; Zhang, B.; Wang, J. *Macromolecules* **2008**, *41*, 361-371.

(66) Bailey, T. S.; Rzayev, J.; Hillmyer, M. A. *Macromolecules* **2006**, *39*, 8772-8781.

(67) Vazaios, A.; Pitsikalis, M.; Hadjichristidis, N. *J. Polym. Sci., Part A: Polym. Chem.* **2003**, *41*, 3094-3102.

(68) Toman, L.; Janata, M.; Spevacek, J.; Vlcek, P.; Latalova, P.; Masar, B.; Sikora, A. *J. Polym. Sci., Part A: Polym. Chem.* **2004**, *42*, 6098-6108.

(69) Toman, L.; Janata, M.; Spevacek, J.; Vlcek, P.; Latalova, P.; Sikora, A.; Masar, B. *J. Polym. Sci., Part A: Polym. Chem.* **2005**, *43*, 3823-3830.

(70) Ling, J.; Chen, W.; Shen, Z. *J. Polym. Sci., Part A: Polym. Chem.* **2005**, *43*, 1787-1796.

(71) Determan, M. D.; Cox, J. P.; Seifert, S.; Thiyagarajan, P.; Mallapragada, S. K. *Polymer* **2005**, *46*, 6933-6946.

(72) Storey, R. F.; Scheuer, A. D.; Achord, B. C. *J. Macromol. Sci., Part A: Pure Appl. Chem.* **2006**, *43*, 1493-1512.

(73) Thunemann, A. F.; Kubowicz, S.; von, B. H.; Mohwald, H. *Langmuir* **2006**, *22*, 2506-2510.

(74) Peleshanko, S.; Anderson, K. D.; Goodman, M.; Determan, M. D.; Mallapragada, S. K.; Tsukruk, V. V. *Langmuir* **2007**, *23*, 25-30.

(75) Triftaridou, A. I.; Vamvakaki, M.; Patrickios, C. S. *Biomacromolecules* **2007**, *8*, 1615-1623.

(76) Mahanthappa, M. K.; Lim, L. S.; Hillmyer, M. A.; Bates, F. S. *Macromolecules* **2007**, *40*, 1585-1593.

(77) Mahanthappa, M. K.; Hillmyer, M. A.; Bates, F. S. *Macromolecules* **2008**, *41*, 1341-1351.

(78) He, Y.; Lodge, T. P. *Macromolecules* **2008**, *41*, 167-174.

(79) Stavrouli, N.; Katsampas, I.; Aggelopoulos, S.; Tsitsilianis, C. *Macromol. Rapid Commun.* **2008**, *29*, 130-135.

(80) Kopchick, J. G.; Storey, R. F.; Jarrett, W. L.; Mauritz, K. A. *Polymer* **2008**, *49*, 5045-5052.

(81) Li, X.; Hsu, S. L. *J. Polym. Sci., Polym. Phys.* **1984**, *22*, 1331-1342.

(82) Phatak, A.; Lim, L. S.; Reaves, C. K.; Bates, F. S. *Macromolecules* **2006**, *39*, 6221-6228.

(83) Sakurai, S.; Sakamoto, J.; Shibayama, M.; Nomura, S. *Macromolecules* **1993**, *26*, 3351-3356.

6

Polydispersity Effects in ISO Triblock Terpolymers

6.1 Introduction

Most research on block copolymers has focused on "model" macromolecules that contain nearly monodisperse ($M_w/M_n < 1.1$) blocks. These materials are typically prepared using living anionic polymerization, a methodology that has seen commercial success.[1] However, only a limited number of monomers and reaction sequences are amenable to living anionic polymerization, which may be prohibitively expensive.[2] To overcome these limitations, researchers have developed a variety of alternative synthetic strategies, such as ring–opening metathesis polymerizations (ROMP)[3] and controlled radical polymerizations (CRP).[4-7] While these methods increase the number of monomers that can be incorporated into block copolymers, and possibly lower costs, polydispersity indices greater than 1.2 often result.[8, 9] Since many block copolymer properties are derived from the underlying morphology, understanding the effects of

polydispersity on block copolymer phase behavior should hasten the implementation of polydisperse block copolymers in advanced materials applications.

Although the potential significance of polydispersity effects was pointed out more than 25 years ago by Leibler,[10] few reports appeared in the literature prior to 2002,[11-20] when Bendejacq et al. showed that poly(styrene–*b*–acrylic acid) diblock copolymers with overall polydispersities near 2 formed ordered mesostructures.[8] A flurry of theoretical[21-27] and experimental[9, 22, 28-35] studies of polydispersity effects in AB block copolymers followed Bendejacq et al.'s report. This topic recently has been reviewed,[36] and only a brief summary is provided below.

Polydisperse AB diblock and ABA triblock materials generally adopt the familiar block copolymer mesostructures of lamellae (LAM), hexagonally packed cylinders (HEX), spheres packed on a body–centered cubic lattice (BCC), and gyroid (Q^{230}).[21-23, 25, 26] Polydispersity does influence block copolymer phase behavior, however, as it affects the order–disorder transition temperatures (T_{ODT}'s)[33] and can drive morphological transitions; the locations of the boundaries on the phase portrait depend on the polydispersities of the constituent A and B blocks.[21-23, 25, 26] Such morphological transitions have been attributed to changes in the average stretching energy that accompany the introduction of domain polydispersity.[23, 25] The ensemble of chains in a polydisperse block does not have to stretch as much as its monodisperse counterpart to fill space, effectively lowering the stretching free energy of the block.[23, 25] As a result, there is a tendency for the "softer" (polydisperse) block to stretch so that chains in the opposing monodisperse domain may relax; this process may drive morphological transitions in which the interfaces curve towards the polydisperse domain.[21-23, 25]

Morphologies with smaller mean interfacial curvatures are stabilized when the polydisperse block is the major component while microstructures with larger mean interfacial curvatures are preferred when the minority block is polydisperse. The reduction in elastic free energy is also accompanied by an increase in the height of end–grafted polymer brushes[37] and an increase in the domain period in the melt.[22-24, 26, 28-30] Furthermore, the distribution of chain lengths present in polydisperse materials may stabilize additional ordered mesostructures. Listak et al. recently reported that polydispersity stabilized a hexagonally–perforated lamellar (HPL) mesostructure in poly(styrene–*b*–methyl acrylate) diblock copolymers;[35] this structure is considered metastable in nearly monodisperse materials.[38, 39] Polydispersity may also induce macrophase separation into multiple coexisting grains containing different morphologies,[25] as reported in homopolymer/polydisperse diblock[8] and multicomponent diblock/diblock blends,[28-30] and as predicted for some polydisperse materials with continuous molecular weight distributions (MWD's).[25]

While AB systems have received significant research attention, only one previous report that we know of discusses polydispersity effects in ABC triblock terpolymers. Jiang and coworkers used 2–D real space self–consistent field theory (SCFT) to study melt–phase ABC triblock terpolymers with equal interaction energies between the blocks (i.e., $\chi_{AB} = \chi_{BC} = \chi_{AC}$).[40] Polydispersity was introduced into either the middle or terminal block using a continuous Schulz–Zimm distribution and 2–D equilibrium mesostructures were identified. Although, as noted by the authors, the 2–D model makes comparison of structures with 3–D systems difficult, several phenomena were described. For systems with terminal block polydispersity, domain periodicities

increased monotonically with the polydispersity of the terminal block. Polydispersity in the middle block, meanwhile, promoted the formation of A/C domain interfaces.[40]

This Chapter provides a comprehensive presentation and discussion of polydispersity effects in poly(isoprene-*b*-styrene-*b*-ethylene oxide) (ISO) triblock terpolymers with equivalent volume fractions of polyisoprene (PI) and polystyrene (PS) ($f_I \approx f_S$) and poly(ethylene oxide) (PEO) volume fractions (f_O) below 0.35. Nearly monodisperse ISO materials in this composition range have been thoroughly investigated by Bates and colleagues,[41-44] as was discussed in Chapter 2. These previous studies identified a network "window" ($0.13 < f_O < 0.24$) along the $f_I \approx f_S$ isopleth, with a stable region of the multiply continuous O^{70} (the orthorhombic *Fddd* network, space group number 70[45]) lying between two- and three-domain LAM phases, referred to as LAM_2 and LAM_3.[41-44] (Here we note that the distinction between LAM_2 and LAM_3, which share a common symmetry, is somewhat arbitrary. We only make the distinction when a network mesostructure is identified along the $f_I \approx f_S$ isopleth.) As was mentioned in Chapter 2, multiply continuous network mesostructures such as O^{70} are of interest because they can have superior mechanical properties (compared to their 1–D and 2–D counterparts)[46, 47] and could be employed in, for example, catalysis,[48] photonic materials,[49] or separation[50] applications. The research described in this Chapter assessed the stability of the network mesostructures in ISO triblock materials with respect to polydispersity in both the PS and PEO blocks, and provides some guidance for utilizing polydispersity as a tool to tune block terpolymer phase behavior.[51, 52]

To interrogate the effects of polydispersity in the middle PS block, four hydroxy–terminated poly(isoprene–*b*–styrene) (IS–OH) diblocks with comparable

number–average molecular weights and compositions ($f_I \approx f_S$) but different PS molecular weight distributions (M_w/M_n = 1.06, 1.16 1.31, 1.44) were synthesized by anionic polymerization. A total of 38 ethylene oxide polymerizations were initiated from these four IS–OH diblocks, yielding four series of ISO triblocks spanning the network "window" ($0.13 < f_O < 0.24$) established in the nearly monodisperse materials.[41-43] Furthermore, thirteen multicomponent blends of ISO materials (PS M_w/M_n = 1.06) were prepared at four different compositions (f_O = 0.20, 0.27, 0.30, 0.33) to systematically explore the effects of varying the PEO molecular weight distribution. The phase behavior of these 51 polydisperse samples is characterized using small angle X–ray scattering (SAXS) and dynamic mechanical spectroscopy (DMS). Numerous polydispersity–driven morphological transitions are reported, including transitions from LAM to the core-shell gyroid (Q^{230}), from Q^{230} to HEX, and from network morphologies (either Q^{230} or O^{70}) to LAM. SCFT calculations augment the experimental analysis and enable us to provide insight into the statistical mechanical phenomena underlying the polydispersity effects.

6.2 Experimental Section

Polymer Synthesis. All polymers were synthesized under an inert argon atmosphere using established Schlenk techniques.[53] Cyclohexane was purified by sequential passage through activated alumina followed by Q–5 (Englehard) while tetrahydrofuran (THF) was purified by passage through activated alumina.[54] Four

IS–OH diblock copolymers were prepared using two different living anionic polymerization strategies; all isoprene and styrene polymerizations were allowed to proceed for at least eight hours to ensure essentially complete monomer conversion. Diblock IS(1.06)–OH (PS M_w/M_n = 1.06) was prepared using a method designed to minimize the PI and PS block polydispersities. In this procedure, *sec*–butyllithium was used to initiate an isoprene polymerization in cyclohexane at 40 °C (~ 94 % 1,4-addition). An aliquot (~3 mL of solution) was extracted from the reactor and terminated via precipitation in degassed methanol; the PI chains therein were analyzed using size exclusion chromatography (SEC) calibrated with PI standards to provide M_n and M_w/M_n of the PI block. Styrene was then added to the reactor and polymerized before ethylene oxide was added to end–cap the IS diblock with an oxanion.[55] Degassed methanol was injected into the reactor to terminate the living chains and create terminal hydroxyl groups; the polymer was recovered via precipitation into methanol. The PI chains in the IS–OH diblock were degraded by ozonolysis (see below) and the PS block was recovered; subsequent SEC analyses using PS standards yielded M_n and M_w/M_n of this block.

Three other IS–OH diblock copolymers were prepared using a protocol designed to yield broader PS block molecular weight distributions. Three styrene polymerizations were initiated by the functional organolithium 3–triisopropylsilyloxy–1–propyllithium (TIPSOPrLi).[56] Cyclohexane and TIPSOPrLi were thermostated at 40 °C and styrene monomer was added to the reactor at different rates to vary the PS polydispersity. Living polystyryllithium chains (~3 mL of solution) were removed from the reactor, terminated via precipitation in degassed methanol, and analyzed using SEC calibrated

with PS standards to determine M_n and M_w/M_n of the three PS blocks. PS M_w/M_n values of 1.31 and 1.44 are generally expected when styrene is rapidly added to a TIPSOPrLi solution over a short time interval (< 2 sec).[56] The PS M_w/M_n value of 1.16 is typically expected when the TIPSOPrLi is "seeded" with styrene by adding three aliquots of styrene monomer (~0.5 g) to the reactor in successive 20 minute intervals before adding the balance of the styrene.[56] Isoprene was then added to the reactors and polymerized before degassed methanol was injected to terminate the living chains. The SI diblock copolymers were recovered via precipitation in methanol, dissolved in THF, and reacted with tetra(*n*–butyl)ammonium fluoride (TBAF) to unmask the α–hydroxyl group following an established protocol[56] that was described in Chapter 4.

Four parent IS–OH diblocks were freeze–dried from benzene before PEO chains were grown to yield ISO triblocks. IS–OH powder was dissolved in THF stirring at 40 °C and the ethylene oxide polymerizations were initiated with potassium naphthalenide following an established protocol.[57] These reactions were allowed to proceed for at least 40 hours before the living chains were terminated with degassed methanol. ISO triblocks were subsequently dissolved in dichloromethane and washed with distilled water to remove excess salts in accordance with reported procedures.[55, 57] ISO triblock terpolymers were recovered from the dichloromethane solution by precipitation in isopropanol and were then freeze–dried from benzene. Multicomponent ISO blends were prepared by dissolving ISO triblocks in benzene, stirring the polymers at room temperature for at least one hour, and freeze drying the samples from benzene.

Ozonolysis. The IS(1.06)–OH diblock (~0.5 g) was dissolved in toluene (~30 mL) and the solution was cooled to –78 °C using a dry ice bath. Ozone was generated using an OREC Ozone Systems V Series instrument operating with 1.5 Amps of current and the gas was bubbled through the stirring toluene solution at a rate of 1 mL/min for 5 minutes to degrade the PI. The PS block was recovered by precipitation in methanol and analyzed; ^{1}H NMR analysis confirmed PI degradation was complete and SEC analyses provided M_w/M_n for the PS block.

Molecular Characterization. The compositions of the neat ISO triblock terpolymers and the ISO blends were determined using a 300 MHz Varian NMR. The instrument operated at room temperature and deuterated chloroform was employed as the solvent. Block mole fractions were computed using the integrated ^{1}H NMR spectra and converted to volume fractions f_I, f_S, and f_O using published homopolymer densities at 140 °C (ρ_I = 0.830, ρ_S = 0.969, ρ_O = 1.064 g/cm^3).[58]

SEC experiments were performed at 30 °C on a Waters 717 GPC equipped with three Polymer Labs Mixed–C columns and a Waters 410 differential refractometer. THF was used as the mobile phase, with a flow rate of 1.0 mL/min. Calibration curves were constructed using either 6 PI standard samples (1000 < M_n < 27000 g/mol, Scientific Polymer Products) or 10 PS standard samples (580 < M_n < 377400 g/mol, Polymer Labs). The PI calibration was used to measure M_n and M_w/M_n of the PI aliquot while the PS calibration was employed to determine M_n and M_w/M_n of the PS aliquot and M_w/M_n of all other polymers. M_n values of the IS–OH diblocks were computed using the M_n's of the initiated PI (PS) blocks and the masses of styrene (isoprene) subsequently added to the reactor. The actual compositions were verified by ^{1}H NMR

spectroscopy and indicated that essentially complete addition of isoprene and styrene monomers had been achieved. ISO M_n values were calculated from M_n's of the IS diblocks and the overall compositions measured using ^{1}H NMR spectroscopy. SEC traces indicated that less than 5% of terminated PI or PS homopolymers and IS diblocks were present in the ISO triblock samples.

Synchrotron Small–Angle X–ray Scattering (SAXS). Synchrotron SAXS experiments were conducted at the Advanced Photon Source at Argonne National Laboratory using the equipment maintained by the DuPont–Northwestern–Dow Collaborative Access Team (DND–CAT). Two different sample–to–detector distances (providing equivalent data for our purposes) were employed with an X–ray wavelength (λ) of 0.8856 Å: (1) 5.47 m and (2) 8.56 m. Distances in both cases were calibrated using silver behenate. Sample temperatures were controlled with a liquid nitrogen-cooled DSC chamber operating under a helium purge. All samples were heated 10 °C above T_{ODT} (when possible) or to 250 °C for 5 min before data were collected in an effort to erase effects due to thermal history. Samples were held at target temperatures for 5 min before data were collected on a Mar CCD area detector. The 2–D diffraction intensities measured by the detector were azimuthally averaged and the data are presented in this Chapter as plots of intensity (I) versus the scattering wave–vector modulus ($q = |\mathbf{q}| = 4\pi/\lambda \sin(\theta/2)$, where θ is the scattering angle).

Dynamic Mechanical Spectroscopy (DMS). DMS experiments were conducted on a Rheometrics Scientific ARES strain–controlled rheometer equipped with 25 mm diameter parallel plates. All experiments were performed in an inert nitrogen atmosphere. Polymer powders were placed on the parallel plates, melted at

100 °C, and heated 10 °C above T_{ODT} (when possible) or to 250 °C for 10 min in an effort to erase effects due to thermal history. Isochronal (ω = 1 rad/s) dynamic elastic (G') and loss (G'') moduli measurements were obtained while heating and cooling the samples at 1–2 °C/min. All data were acquired using a low strain amplitude (1–2 %) that was determined to be within the linear viscoelastic regime.

6.3 Results and Analysis

A total of 38 ISO triblock terpolymers with nearly equivalent volume fractions of PS and PI ($f_I \approx f_S$) were synthesized from four separate parent IS–OH diblock copolymers. The parent diblocks have narrow molecular weight distributions in the PI blocks but different PS polydispersities. These polymers are labeled using the notation IS(PDI_S)O(f_O), where PDI_S is the PDI of the PS block and f_O is the volume fraction of the PEO. The molecular characterization data for all of the neat ISO triblock terpolymers are presented in Table 6.1 and summarized in Figure 6.1. A series of previously characterized[41-43] higher molecular weight ISO samples is also included in Table 6.1. These samples are labeled using the original ISOi notation of Bailey et al.[41] and the characterization data are reproduced from Epps and Cochran et al.'s report.[43]

The morphology assignments and lattice dimensions listed in Table 6.1 are determined using SAXS data. Order–disorder transition temperatures (T_{ODT}'s) were measured using DMS; T_{ODT} is associated with the temperature at which the dynamic elastic modulus (G') discontinuously decreases while heating a sample.[59] In all cases the T_{ODT} determined from DMS is consistent with the SAXS data. T_{ODT}'s above 250 °C

were not accessed because thermal degradation of the materials may occur at these elevated temperatures. We have identified order–order phase transitions (OOT's) from Q^{230} to PEO cylinders packed hexagonally in an IS matrix (HEX_O) in samples IS(1.06)O(0.13) and IS(1.06)O(0.20) and from LAM_3 to O^{70} in triblock IS(1.16)O(0.25). Morphological coexistence is reported in samples IS(1.06)O(0.28) and IS(1.44)O(0.24), as Bragg peaks consistent with both Q^{230} and O^{70} are present in the SAXS data obtained from these polymers. For these materials, the reported lattice parameters correspond to the morphology with the higher peak intensities that is listed on the left in the "Phase" column in Table 6.1. While it is possible coexistence represents the equilibrium states of these specimens,[25] an accurate assessment of thermodynamic stability would require lengthy annealing times at a synchrotron facility and is beyond the scope of the current discussion.

Thirteen blends of nominally monodisperse ISO triblock terpolymers were prepared at four different compositions. Eleven of the blends contain ISO samples prepared from IS(1.06)–OH; the other two blends are comprised of higher molecular weight ISO materials synthesized by Bailey et al.[41] The blends are labeled using the notation ISO(PDI_O, f_O), where f_O is the overall PEO volume fraction in the blend and PDI_O is the PDI of the PEO block calculated by assuming that all of the neat triblocks have perfectly monodisperse PEO chains. The characterization data obtained for these blends are listed in Table 6.2 and summarized in Figure 6.1, and the relative mass fractions of the ISO triblocks in each blend are provided in Table 8.2 in Section 8.4.

Table 6.1. Neat ISO Characterization Data

Polymer	N_I[c]	N_S[c]	N_O[c]	f_O[d]	M_n (kDa)	M_w/M_n	Lattice Dimensions (nm)[e]	Phase[f]	T_{ODT} (°C)[g]
IS(1.06)–OH[a]	81	84	0	0	10.6	1.08	12.5 (80 °C)	DIS	
IS(1.06)O(0.05)[a]	81	84	9	0.05	11.3	1.10	13.9 (80 °C)	LAM_2	88
IS(1.06)O(0.10)[a]	81	84	19	0.10	12.0	1.13	37.0	Q^{230}	127
IS(1.06)O(0.13)[a]	81	84	25	0.13	12.5	1.13	38.6	$Q^{230}\rightarrow HEX_O$[h]	155
IS(1.06)O(0.20)[a]	81	84	41	0.20	13.7	1.11	42.3	$Q^{230}\rightarrow HEX_O$[h]	230
IS(1.06)O(0.21)[a]	81	84	44	0.21	13.9	1.10	44.0	Q^{230}	242
IS(1.06)O(0.23)[a]	81	84	49	0.23	14.3	1.14	45.1	Q^{230}	> 250
IS(1.06)O(0.26)[a]	81	84	58	0.26	15.0	1.11	46.3	Q^{230}	> 250
IS(1.06)O(0.27)[a]	81	84	61	0.27	15.2	1.13	0.280, 0.577, 76.9	O^{70}	> 250
IS(1.06)O(0.28)[a]	81	84	64	0.28	15.4	1.12	0.280, 0.578, 77.3	O^{70}/ Q^{230} [i]	> 250
IS(1.06)O(0.33)[a]	81	84	81	0.33	16.7	1.14	20.2	LAM_3	> 250
IS(1.06)O(0.35)[a]	81	84	89	0.35	17.3	1.16	20.7	LAM_3	> 250
IS(1.06)O(0.44)[a]	81	84	130	0.44	20.4	1.19	23.0	LAM_3	> 250
IS(1.16)–OH	80	84	0	0	10.5	1.12	12.6 (80 °C)	DIS	
IS(1.16)O(0.11)	80	84	20	0.11	12.0	1.14	0.294, 0.584, 62.9	O^{70}	139
IS(1.16)O(0.13)	80	84	25	0.13	12.4	1.10	0.294, 0.578, 64.2	O^{70} [j]	160
IS(1.16)O(0.15)	80	84	29	0.15	12.7	1.11	0.295, 0.578, 65.9	O^{70} [j]	174
IS(1.16)O(0.20)	80	84	41	0.20	13.6	1.11	0.292, 0.578, 69.1	O^{70}	221
IS(1.16)O(0.21)	80	84	44	0.21	13.8	1.12	0.292, 0.578, 72.3	O^{70}	229
IS(1.16)O(0.25)	80	84	55	0.25	14.7	1.14	19.4	$LAM_3\rightarrow O^{70}$ [k]	> 250
IS(1.16)O(0.31)	80	84	75	0.31	16.2	1.13	20.4	LAM_3	> 250
IS(1.16)O(0.34)	80	84	85	0.34	16.9	1.15	20.9	LAM_3	> 250

Polymer	N_I[c]	N_S[c]	N_O[c]	f_O[d]	M_n (kDa)	M_w/M_n	Lattice Dimensions (nm)[e]	Phase[f]	T_{ODT}[g] (°C)
IS(1.31)–OH	88	91	0	0	11.5	1.17	13.6 (80 °C)	DIS	
IS(1.31)O(0.04)	88	91	7	0.04	12.1	1.20	14.7 (90 °C)	LAM	93
IS(1.31)O(0.09)	88	91	18	0.09	12.8	1.21	15.8 (100 °C)	LAM	112
IS(1.31)O(0.11)	88	91	22	0.11	13.2	1.16	15.9	LAM	140
IS(1.31)O(0.14)	88	91	29	0.14	13.7	1.13	16.5	LAM	147
IS(1.31)O(0.17)	88	91	37	0.17	14.3	1.18	17.1	LAM	157
IS(1.31)O(0.24)	88	91	57	0.24	15.8	1.15	18.0	LAM	190
IS(1.31)O(0.30)	88	91	77	0.30	17.3	1.11	19.0	LAM	195
IS(1.44)–OH	86	89	0	0	11.2	1.15	13.5 (80 °C)	LAM	
IS(1.44)O(0.04)	86	89	7	0.04	11.8	1.13	14.8 (100 °C)	LAM	103
IS(1.44)O(0.05)	86	89	9	0.05	11.9	1.16	15.1 (100 °C)	LAM	121
IS(1.44)O(0.09)	86	89	17	0.09	12.5	1.14	15.4	LAM	146
IS(1.44)O(0.10)	86	89	19	0.10	12.7	1.13	15.9	LAM	151
IS(1.44)O(0.12)	86	89	24	0.12	13.0	1.14	16.2	LAM	165
IS(1.44)O(0.14)	86	89	29	0.14	13.4	1.14	16.7	LAM	180
IS(1.44)O(0.16)	86	89	33	0.16	13.7	1.13	16.9	LAM	184
IS(1.44)O(0.17)	86	89	36	0.17	13.9	1.13	0.290, 0.578, 69.5	O^{70}	201
IS(1.44)O(0.21)	86	89	47	0.21	14.7	1.11	18.0	LAM [l]	216
IS(1.44)O(0.22)	86	89	50	0.22	15.0	1.12	0.291, 0.578, 72.8	O^{70}	> 250
IS(1.44)O(0.24)	86	89	55	0.24	15.4	1.15	48.6	Q^{230}/O^{70} [m]	> 250
IS–OH3[b]	106	106	0	0	13.6	1.05	15.8 (85 °C)	LAM_2	97
ISO1[b]	106	106	3	0.02	13.8	1.05	16.1 (105 °C)	LAM_2	111
ISO5[b]	106	106	10	0.05	14.3	1.05	16.4 (100 °C)	LAM_2	134
ISO2[b]	106	106	14	0.06	14.6	1.06	16.9 (110 °C)	LAM_2	146
ISO10[b]	106	106	77	0.27	19.4	1.06	23.0 (160 °C)	LAM_3	> 250
ISO11[b]	106	106	90	0.30	20.4	1.05	24.1 (160 °C)	LAM_3	> 250
ISO12[b]	106	106	109	0.34	21.8	1.06	25.3 (160 °C)	LAM_3	> 250

[a] M_w/M_n value for the PI block measured using SEC is 1.10. [b] Polymers were previously characterized[41-43] and are labeled using the notation of Bailey et al.[41] [c] Number–average degrees of polymerization (N_i) based on a segment reference volume of 118 Å^3 and calculated using published density values at 140 °C (ρ_I = 0.830, ρ_S = 0.969, ρ_O = 1.064 g/cm^3).[58] [d] Volume fractions calculated from the provided N_i values. [e] Lattice dimensions are obtained from SAXS data and are reported at 120 °C unless otherwise noted in parentheses (°C). The lattice dimensions listed for O^{70} correspond to *a/c*, *b/c*, and *c* and the values listed for disordered samples correspond to the length scales associated with the principal scattering vectors. [f] Morphologies identified using SAXS data. [g] Measured using DMS. [h] Samples IS(1.06)O(0.13) and IS(1.06)O(0.20) undergo OOT's from Q^{230} to HEX$_O$ at 148 °C and 217 °C, respectively. [i] Bragg peaks characteristic of both O^{70} and Q^{230} are identified at 120 ºC; the intensities of the O^{70} peaks are higher and the listed lattice parameters are for O^{70}. [j] Some low intensity peaks in these SAXS data are not consistent with O^{70}, suggesting a small fraction of these materials (< 5%) form a different, undetermined mesostructure. [k] Specimen IS(1.16)O(0.25) undergoes an OOT from LAM$_3$ to O^{70} at 160 °C. [l] A transient O^{70} mesostructure was identified above 185 °C.[60] [m] One small Bragg peak consistent with O^{70} is present in the SAXS data obtained at 120 °C; the remaining peaks are indexed to Q^{230} and the listed domain periodicity is for Q^{230}.

Table 6.2. ISO Blend Characterization Data

Blend	N^a	M_n (kDa)	$f_O{}^b$	$PDI_O{}^c$	Lattice Dimensions (nm)[d]	Phase[e]	T_{OOT} (°C)[f]	T_{ODT} (°C)
ISO(1.17, 0.20)	206	13.7	0.20	1.17	43.6	$Q^{230} \rightarrow HEX_O$	195	> 250
ISO(1.33, 0.20)	206	13.7	0.20	1.33	44.1	$Q^{230} \rightarrow HEX_O$	165	> 250
ISO(1.46, 0.20)	206	13.7	0.20	1.46	44.3	$Q^{230} \rightarrow HEX_O$	150	> 250
ISO(1.53, 0.20)	206	13.7	0.20	1.53	44.8	$Q^{230} \rightarrow HEX_O$	142	> 250
ISO(1.16, 0.30)	236	16.0	0.30	1.16	50.5	Q^{230}	–	> 250
ISO(1.28, 0.30)	236	16.0	0.30	1.28	51.4	Q^{230}	–	> 250
ISO(1.40, 0.30)	236	16.0	0.30	1.40	52.4	Q^{230}	–	> 250
ISO(1.73, 0.30)	236	16.0	0.30	1.73	22.9	HEX_O	–	> 250
ISO(1.27, 0.33)	246	16.7	0.33	1.27	53.6 [g]	$LAM_3 \rightarrow Q^{230}$	210	> 250
ISO(1.30, 0.33)	246	16.7	0.33	1.30	53.6	Q^{230}	–	> 250
ISO(1.45, 0.33)	246	16.7	0.33	1.45	55.5	Q^{230}	–	> 250
ISO(1.17, 0.27)	289	19.4	0.27	1.17	55.1 (160 °C)	Q^{230}	–	> 250
ISO(1.30, 0.27)	289	19.4	0.27	1.30	56.8 (160 °C)	Q^{230}	–	> 250

[a] Number–average degrees of polymerization based on a segment reference volume of 118 $Å^3$ and calculated using published density values at 140 °C (ρ_I = 0.830, ρ_S = 0.969, ρ_O = 1.064 g/cm^3).[58]. [b] PEO volume fractions computed from the N_i values. [c] Calculated for the PEO block by assuming the PEO chains in the component ISO triblocks are perfectly monodisperse. [d] Lattice dimensions are obtained from SAXS data and are reported at 120 °C unless otherwise noted in parentheses (°C). [e] Morphologies identified using SAXS data. When two morphologies are listed, the one on the left is the low temperature structure and the one on the right is the high temperature phase. [f] Measured using DMS; the T_{OOT} listed is the temperature at which the slope in *G'* sharply changes upon heating. [g] Domain periodicity of the long-lived metastable Q^{230} at 120 °C.

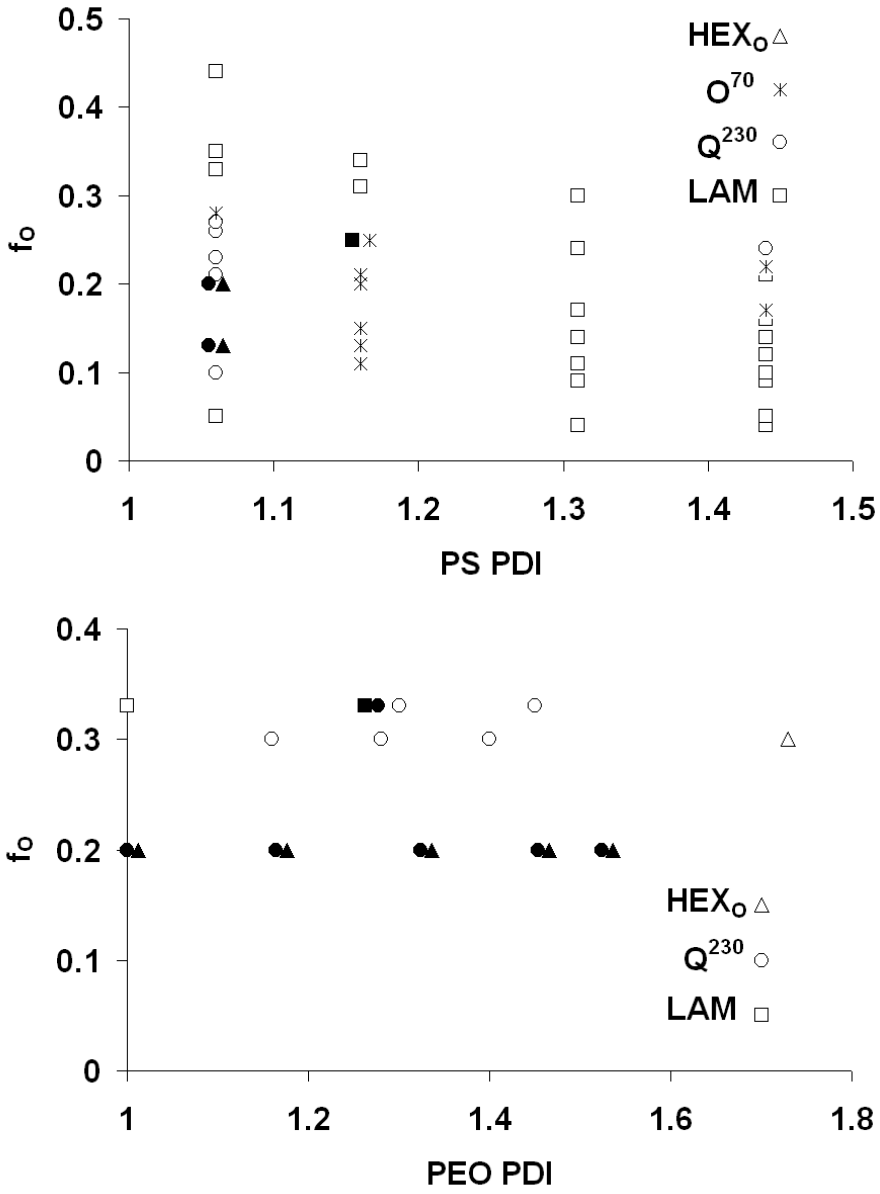

Figure 6.1. Plots summarizing the morphologies identified in ISO triblock terpolymers as a function of composition and either the PS (top plot) or PEO (bottom plot) PDI. All of the materials have comparable PI and PS molecular weights and have compositions that lie on the $f_I \approx f_S$ isopleth (see Tables 6.1 and 6.2). The pairs of adjacent solid symbols indicate an OOT is identified in a sample upon heating.

IS(1.06)O Triblock Terpolymers. Twelve IS(1.06)O triblocks were synthesized from the parent IS(1.06)–OH diblock material. The morphologies of all of the IS(1.06)O samples are identified using SAXS and, in all cases, the SAXS data are consistent with the DMS analysis. Representative synchrotron SAXS powder patterns for IS(1.06)O(0.05), IS(1.06)O(0.26), IS(1.06)O(0.27), and IS(1.06)O(0.33) are provided in Figure 6.2. The SAXS data for IS(1.06)O(0.26), IS(1.06)O(0.27), and IS(1.06)O(0.33) were acquired at 120 °C while the data for IS(1.06)O(0.05) were collected at 80 °C. The Bragg patterns for IS(1.06)O(0.05) and IS(1.06)O(0.33) are indexed to lamellae; the absence of the 002 peak in the IS(1.06)O(0.05) data is consistent with a structure factor extinction for symmetric LAM_2.[43] The rich assortments of peaks in the IS(1.06)O(0.26) and IS(1.06)O(0.27) data are indexed to Q^{230} and O^{70}, respectively. The allowed reflections for the orthorhombic lattice of O^{70} are not simple multiples of the primary peak q^*, as they are for a cubic lattice such as Q^{230}. Rather, the orthorhombic peak positions change with the lattice dimensions *a*, *b*, and *c* according to $q_{hkl} = 2\pi\,[h^2/a^2 + k^2/b^2 + l^2/c^2]^{1/2}$, where *h*, *k*, and *l* are the associated Miller indices. Specific orthorhombic space groups are associated with different sets of allowed reflections, as identified in the crystallographic tables.[45] The *a*, *b*, and *c* parameters were varied to obtain the optimal least–squares fit of the allowed reflections for O^{70} to the recorded SAXS peaks (see Section 8.2 for details); an example of this indexing scheme is provided in Figure 6.2.

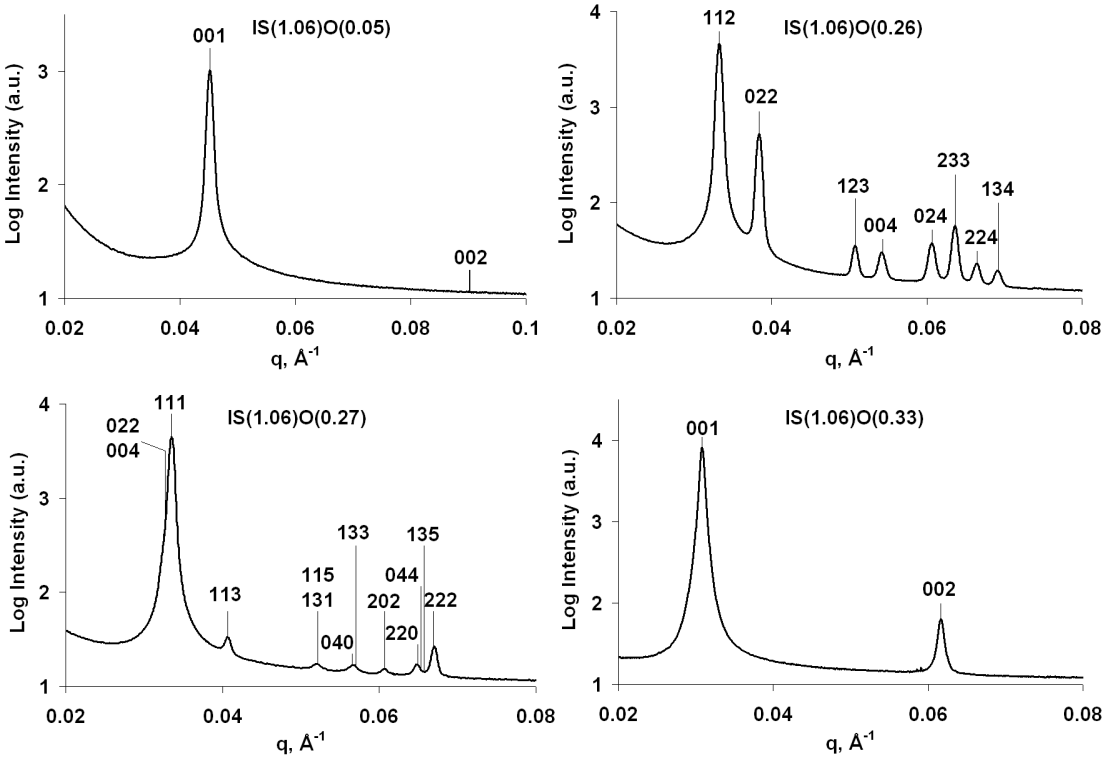

Figure 6.2. Synchrotron SAXS data acquired at 120 ºC (80 ºC for IS(1.06)O(0.05)). All samples were annealed at 250 ºC for 5 min (at 100 °C for IS(1.06)O(0.05)) before data were collected. The data for IS(1.06)O(0.05) and IS(1.06)O(0.33) are indexed to a lamellar morphology; the absence of the 002 peak in the IS(1.06)O(0.05) data is consistent with a structure factor extinction for symmetric LAM_2.[43] The Bragg peaks for IS(1.06)O(0.26) are indexed to Q^{230} and the diffraction pattern for IS(1.06)O(0.27) is indexed to O^{70}.

Four multicomponent blends of IS(1.06)O triblocks were prepared with an overall f_O = 0.20. Isochronal (ω = 1 rad/sec) *G'* measurements were employed to interrogate the viscoelastic response of these materials; all samples were annealed 10 °C above T_{ODT} (or at 250 °C) for 10 min prior to data collection in an effort to erase effects

associated with thermal history. These four blends, along with neat triblocks IS(1.06)O(0.13) and IS(1.06)O(0.20), exhibited similar viscoelastic responses; representative data for specimen IS(1.06)O(0.20) are provided in Figure 6.3. The initial discontinuous decrease in *G'* upon heating at 217 °C is consistent with an order-order transition (OOT), and T_{OOT} is assigned to this onset temperature. While heating/cooling hysteresis was present in all *G'* traces, the eventual recovery of *G'* on cooling suggests that the OOT is reversible. SAXS experiments were utilized to probe the mesostructures of these materials as a function of temperature. Representative SAXS data obtained from blend ISO(1.46, 0.20) at 120 °C and 250 °C are provided in Figure 6.4. The Bragg peaks obtained at 120 °C are indexed to Q^{230} and those acquired at 250 °C are indexed to a hexagonal morphology. Assuming this hexagonal mesostructure is hexagonally packed cylinders, two possible configurations are possible: PEO cylinders packed hexagonally in an IS matrix (HEX_O), and PI cylinders packed hexagonally in an SO matrix (HEX_I).[44] As will be discussed in the SCFT Analysis and Results Section, HEX_O has a lower calculated free energy than HEX_I for all of the samples in this study. This result leads us to identify the hexagonal morphology as HEX_O. Similar SAXS data were obtained for the other blends with f_O = 0.20 and for the neat triblocks IS(1.06)O(0.13) and IS(1.06)O(0.20); all of these samples undergo an OOT from Q^{230} to HEX_O upon heating.

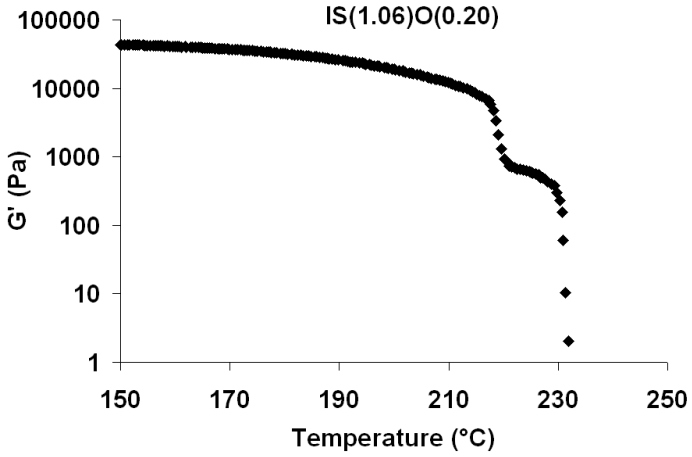

Figure 6.3. Representative isochronal (ω = 1 rad/sec) *G'* measurements acquired while heating specimen IS(1.06)O(0.20) at 2 °C/min. The sample was first annealed at 250 °C for 10 min in an effort to erase effects associated with thermal history and then cooled to 100 °C prior to data collection. These data were acquired by Professor Christopher J. Ellison.

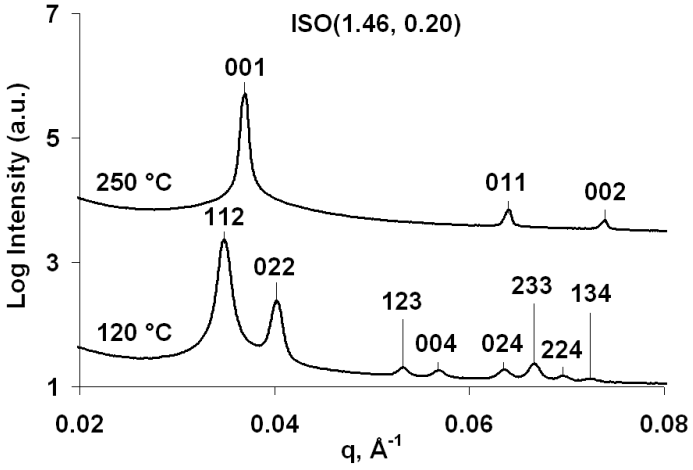

Figure 6.4. SAXS data acquired at 120 °C and 250 °C for ISO(1.46, 0.20). The sample was annealed for five minutes at each target temperature prior to data collection (250 °C anneal preceded 120 °C anneal). The Bragg pattern at 120 °C is indexed to Q^{230} while the peaks at 250 °C are indexed to a hexagonal mesostructure (here identified as HEX_O).

Four IS(1.06)O blends were prepared with an overall f_O = 0.30. There were no discontinuities in the isochronal *G'* measurements (data not shown) for any of these samples, which we interpret as an indication that none of the materials undergo OOT's between 100 °C and 250 °C. SAXS data were consistent with these DMS measurements, as the relative peak positions varied only slightly with temperature for each blend. SAXS data acquired at 120 °C for samples ISO(1.40, 0.30) and ISO(1.73, 0.30) are presented in Figure 6.5. The Bragg pattern for ISO(1.40, 0.30) is indexed to Q^{230}; similar data were acquired for samples ISO(1.16, 0.30) and ISO(1.28, 0.30). The peaks for specimen ISO(1.73, 0.30) are indexed to a hexagonal morphology (HEX_O).

Three IS(1.06)O blends were prepared with an overall f_O = 0.33. There are no discontinuities in the *G'* data acquired for blends ISO(1.30, 0.33) and ISO(1.45, 0.33), suggesting these samples do not undergo OOT's. SAXS data (not shown) are consistent with this DMS analysis and are used to identify the mesostructure of these samples as Q^{230} over temperatures ranging from 100 °C to 250 °C. The isochronal *G'* data for blend ISO(1.27, 0.33) increases sharply at 210 °C upon heating, consistent with an OOT; recovery of *G'* during cooling suggests the transition is reversible. SAXS data obtained at 120 °C and 250 °C for sample ISO(1.27, 0.33) are presented in Figure 6.6. The material was heated to 120 °C and then to 250 °C, with four minute anneals prior to data collection at each temperature. The Bragg pattern acquired at 120 °C is indexed to LAM_3 while the 250 °C peaks are indexed to Q^{230}; these morphology assignments are consistent with the *G'* measurements. The blend was subsequently cooled

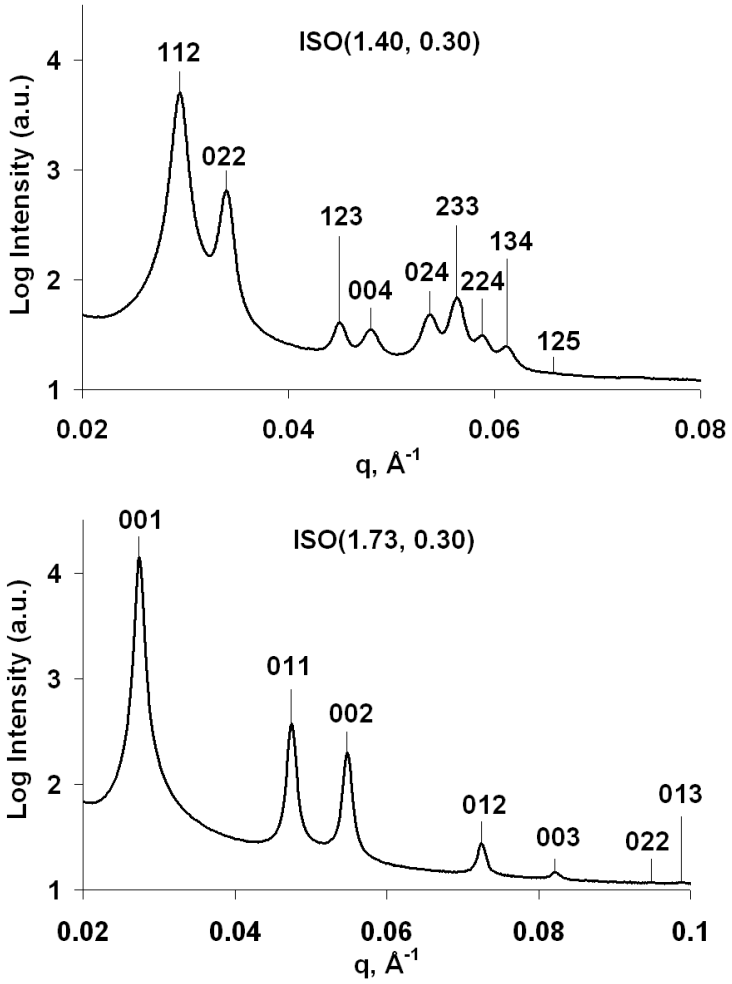

Figure 6.5. Synchrotron SAXS data acquired at 120 °C for two IS(1.06)O blends with overall f_O = 0.30. The polymers were annealed at 250 ºC for five minutes prior to a five minute anneal and data collection at 120 ºC. ISO(1.40, 0.30) SAXS data are indexed to Q^{230} and the ISO(1.73, 0.30) Bragg peaks are indexed to a hexagonal morphology (here identified as HEX_O).

(at ~ 50 °C / minute) to 120 °C and annealed for four minutes. Interestingly, the SAXS data collected at 120 °C upon cooling did not index to LAM_3, but were consistent with Q^{230}. Since an OOT was evident (by a discontinuous decrease in *G'*) in the DMS measurements with a slower 1 °C / minute cooling rate, the Q^{230} present at 120 °C upon cooling in the SAXS experiment is likely a long–lived metastable mesostructure. This result is consistent with reports of gyroid persisting as a long–lived metastable morphology in several AB diblock copolymer systems.[38, 61]

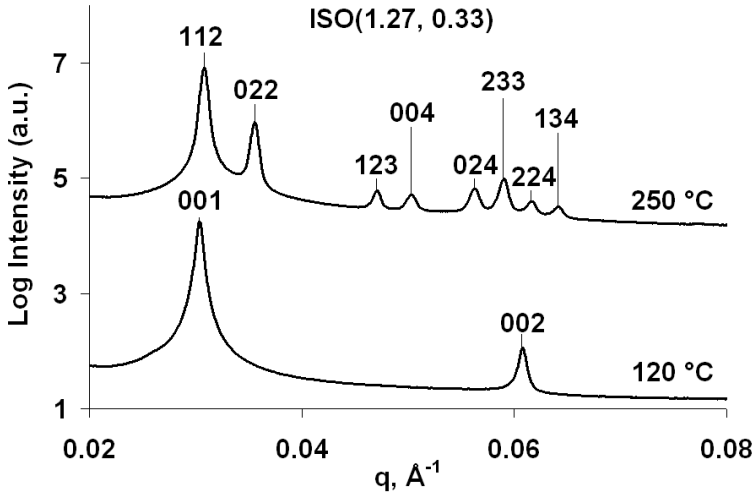

Figure 6.6. SAXS data acquired at 120 °C and 250 °C for blend ISO(1.27, 0.33). The sample was annealed for five minutes at each target temperature prior to data collection (120 °C anneal preceded 250 °C anneal). The Bragg pattern at 120 °C is indexed to LAM_3 while the peaks at 250 °C are indexed to Q^{230}.

Two ISO blends with an overall $f_O = 0.27$ were prepared using the higher molecular weight ISO triblock terpolymers that were previously synthesized and

characterized by Bates and colleagues.[41-43] The neat ISO10 triblock (f_O = 0.27) forms LAM_3 at temperatures ranging from 100 °C to 250 °C. SAXS and DMS data (not shown) indicate that the ISO(1.17, 0.27) and ISO(1.30, 0.27) blends with the same overall M_n and composition as ISO10 adopt a Q^{230} mesostructure over an identical temperature range. These results demonstrate that polydispersity can be employed to drive morphological transitions at higher molecular weights and is not limited as a tool to the molecular weights of the IS(1.06)O series of polymers.

These f_O = 0.27, 0.30, and 0.33 data demonstrate that polydispersity can be employed to drive morphological transitions and stabilize technologically useful (see Chapter 2) network morphologies. A few other groups had previously hypothesized that polydispersity could be used as a tool to stabilize an ordered network mesostructure. Hasegawa et al. speculated that a distribution of block lengths would help stabilize bicontinuous AB block copolymer mesostructures.[62] Martínez-Veracoechea and Escobedo tested this hypothesis by employing lattice Monte Carlo (MC) simulations to examine bimodal blends of AB diblock copolymers.[63] They found that introducing bidispersity widens the temperature range at which the gyroid is stable in the simulations because the distribution of chain lengths relieves packing frustration, with the longer chains occupying domain centers. They noted that their MC results support the idea that bidispersity could be used to stabilize the gyroid mesostructure. Lynd and Hillmyer reported experimental data that support Martínez-Veracoechea and Escobedo's hypothesis.[22] They identified polydispersity-driven morphological transitions to gyroid at two different compositions in poly((ethylene-*alt*-propylene)-*b*-lactide) diblock copolymers. Schröder-Turk et al. also suggested polydispersity could be

used to relieve the packing frustration of complex multiply continuous morphologies.[64] These authors used geometric arguments to suggest that a complex triply continuous phase (called I-WP) could be stabilized in certain multicomponent blends of ABC triblock terpolymers that have varying chain lengths in the C domain and monodisperse A and B domains. None of these previous reports provided experimental evidence that polydispersity could stabilize a network mesostructure in ABC triblock terpolymers, however. The generic multicomponent blending strategy we employed is particularly appealing because it facilitates an effective widening of the network "window" without the use of any new synthetic methodologies. Network morphologies can be accessed in the $0.10 < f_O < 0.27$ range (for the IS(1.06)O materials) by preparing nearly monodisperse ISO samples. The upper bound on the network window can effectively be extended to at least $f_O = 0.33$ by multicomponent blending, a process whose only "cost" is the preparation of additional ISO samples with different compositions. (Note that it is not clear precisely which composition in the $0.27 < f_O < 0.33$ range marks the upper bound on the network "window" for the nearly monodisperse ISO materials. However, we have definitively established that polydispersity extended the upper bound of the network "window," as a broadening of the molecular weight distribution drove a morphological transition from LAM_3 to Q^{230} for $f_O = 0.33$.)

IS(1.16)O Triblock Terpolymers. Eight IS(1.16)O triblocks were synthesized from the IS(1.16)–OH parent diblock. SAXS patterns (not shown) that are indexed to O^{70} were acquired at all temperatures below T_{ODT} for samples IS(1.16)O(0.11), IS(1.16)O(0.20), and IS(1.16)O(0.21). The SAXS data obtained for samples IS(1.16)O(0.13) and IS(1.16)O(0.15) contain a few low intensity peaks that are not

consistent with O^{70} (see Figure 8.9). The low intensities of these extra peaks make identification of potential coexisting morphologies difficult. However, since > 95% of these materials form O^{70}, that network mesostructure is assigned as the morphology in Table 6.1. SAXS data (not shown) consistent with LAM_3 were acquired at temperatures ranging from 100 °C to 250 °C for specimens IS(1.16)O(0.31) and IS(1.16)O(0.34). Only specimen IS(1.16)O(0.25) undergoes an OOT. The *G'* data obtained while heating this sample exhibit a sharp increase at 160 °C; recovery of *G'* during cooling suggests the transition is reversible. Synchrotron SAXS data collected above and below 160 °C are provided in Figure 6.7. The Bragg peaks at 120 °C are indexed to LAM_3 and those at 200 °C are indexed to O^{70}; these DMS and SAXS data are consistent with an OOT from LAM_3 to O^{70} at 160 °C. There is a low intensity peak in the 120 °C data (marked with ♦) that is consistent with the 113 reflection for O^{70}; a small portion of the material is likely (given the short five minute annealing time) trapped in a metastable O^{70} configuration.

IS(1.31)O Triblock Terpolymers. Seven IS(1.31)O triblocks were prepared from the IS(1.31)–OH parent diblock. None of these materials have discontinuous changes in *G'* that are characteristic of OOT's and SAXS data for all of these samples index to a lamellar morphology, termed LAM. LAM_2 and LAM_3 are not differentiated in this series of IS(1.31)O triblocks because no other mesostructure was identified along the $f_I \approx f_S$ isopleth. The lack of an intermediate morphology suggests the composition profiles continuously vary as f_O increases and renders arbitrary a morphological assignment of LAM_2 or LAM_3.

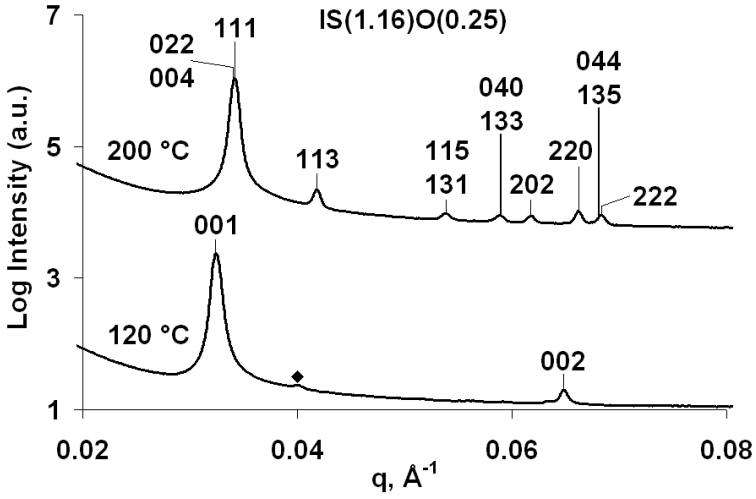

Figure 6.7. SAXS data acquired at 120 °C and 200 °C for sample IS(1.16)O(0.25). The sample was annealed for five minutes at 250 °C and then annealed for five minutes at each target temperature prior to data collection (200 °C anneal preceded 120 °C anneal). The Bragg pattern at 120 °C is indexed to LAM_3 while the peaks at 200 °C are indexed to O^{70}. The low intensity peak in the 120 °C data (marked with ♦) corresponds to the 113 reflection from O^{70} and is consistent with a small fraction of the material being trapped in a metastable O^{70} mesostructure.

IS(1.44)O Triblock Terpolymers. Eight IS(1.44)O triblocks were initially synthesized from the IS(1.44)–OH parent diblock. SAXS and DMS data obtained from seven of these polymers (those with $f_O \leq 0.16$) are consistent with a LAM mesostructure.[60] The isochronal DMS data from the eighth sample, triblock IS(1.44)O(0.21), contain a sharp increase in *G'* at 185 °C upon heating (see Figure 8.10). As has been discussed in previous sections, this type of increase is often associated with an OOT. The SAXS data indicate the IS(1.44)O(0.21) sample formed a

LAM morphology at low temperatures and then briefly transitioned to an O^{70} network above 185 °C upon heating (see SAXS data in Figure 8.10). This O^{70} structure always transitioned back to LAM during thermal annealing at temperatures above 185 °C (< 15 min anneal time required for the transition), however, indicating the network morphology was a transient, metastable phase. Triblocks IS(1.44)O(0.17), IS(1.44)O(0.22), and IS(1.44)O(0.24) were prepared to probe the stability of the O^{70} network at compositions close to that of sample IS(1.44)O(0.21). SAXS data acquired at 120 °C for these four samples are provided in Figure 6.8. The Bragg peaks for IS(1.44)O(0.17) and IS(1.44)O(0.22) are indexed to O^{70}, the data for IS(1.44)O(0.21) are indexed to LAM, and the powder pattern for IS(1.44)O(0.24) is indexed to Q^{230}. These results clearly indicate that PS polydispersity does not always destroy network morphologies. The SAXS pattern for specimen IS(1.44)O(0.24) contains a low intensity peak that does not index to Q^{230}. This peak is marked with a ♦ in Figure 6.8 and its location is consistent with the 113 reflection from the O^{70} mesostructure (this peak is not present in SAXS data acquired at 250 °C or 200 °C). The IS(1.44)O(0.24) material was subsequently annealed for three minutes at 250 °C and then for two hours at 120 °C to probe the relative stability of the Q^{230} and O^{70} morphologies. Peaks consistent with both mesostructures were still present in the SAXS data following this thermal treatment, with the O^{70} peaks growing in relative intensity (i.e., the O^{70} peaks are more prominent than they are in the data provided in Figure 6.8). It is possible that coexistence of the Q^{230} and O^{70} networks is the equilibrium state for sample IS(1.44)O(0.24) at 120 °C,[25] although more extended annealing times would be required

to determine if Q^{230} is a long–lived metastable morphology or part of the equilibrium configuration.

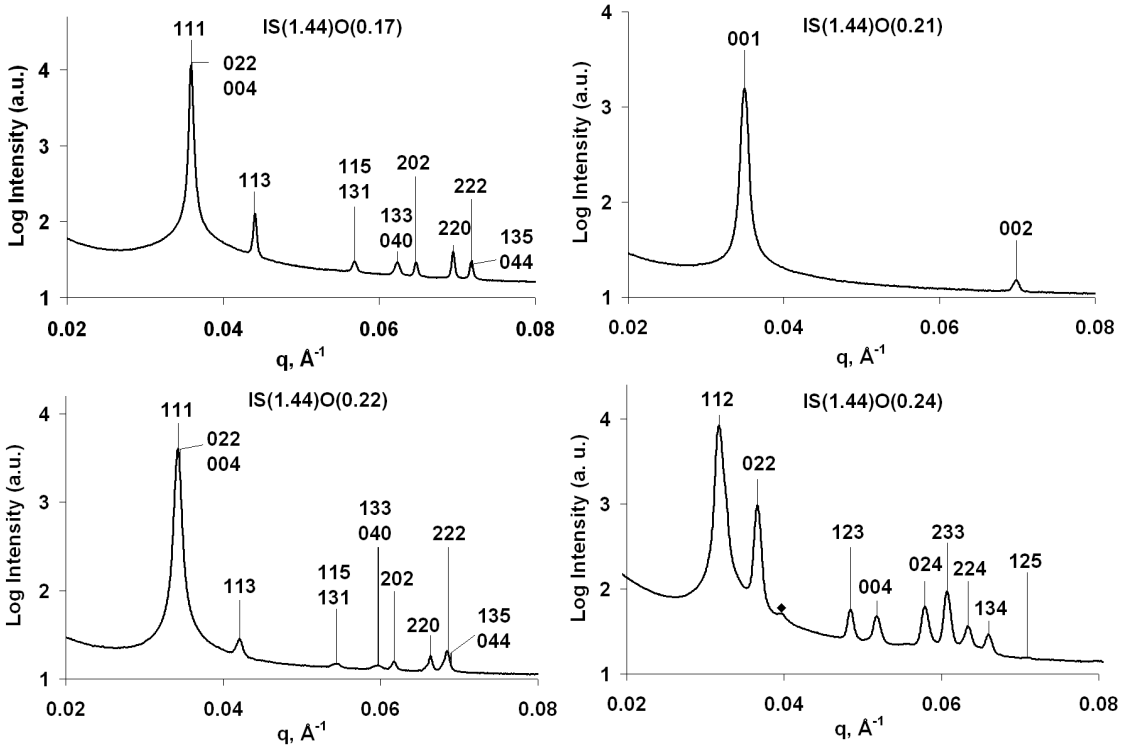

Figure 6.8. SAXS data acquired at 120 °C for samples IS(1.44)O(0.17), IS(1.44)O(0.21), IS(1.44)O(0.22), and IS(1.44)O(0.24). All of the materials were annealed at 250 °C for five minutes before they were held at 120 °C for five minutes. The peaks for IS(1.44)O(0.17) and IS(1.44)O(0.22) are indexed to O^{70}, those for IS(1.44)O(0.21) are indexed to LAM, and those for IS(1.44)O(0.24) are indexed to Q^{230}. The low intensity peak in the IS(1.44)O(0.24) data (marked with a ♦) is consistent with the 113 reflection for O^{70}; a small portion of the material apparently has formed O^{70} that coexists with the Q^{230} network.

6.4 SCFT Analysis and Results

SCFT Methodology. Comprehensive details of SCFT are available in a recently published review[65] and book;[66] only a brief synopsis of the theory is provided here. SCFT represents the molecular interactions experienced by a segment of a polymer chain as a chemical potential field. In the calculations process, an initial chemical potential field is guessed and the modified diffusion equation for a single chain placed in this field is solved to yield a segment density profile. A new chemical potential field is then calculated from the density profile solution and the process begins anew with this new potential field; the procedure continues until the calculated potential fields and densities are self–consistent.[65, 67] The same general framework applies to multicomponent systems, although the procedural details of computing overall segment density profiles and chemical potential fields are somewhat different. In a multicomponent system, a single potential field interacts with all of the chains and the modified diffusion equation is independently solved for each chain in this field. The overall segment density profile is generated by summing the individual chain segment density profiles (weighted by their respective number fractions). The chemical potential field used in subsequent iterations is computed from this overall segment density profile.

Our SCFT calculations were performed using the code developed by Tyler et al.[44, 68] This approach involves calculating the free energies of selected mesostructural candidates; the morphology with the lowest free energy is considered the equilibrium structure. In Tyler et al.'s implementation, the modified diffusion equation is solved using a pseudo–spectral method and the symmetry–adapted basis functions.

The free energy of each candidate is then minimized with respect to the unit cell parameters using the variable–unit–cell algorithm described by Tyler and Morse.[69] Additional details of this SCFT methodology are described in the literature.[44, 70]

In this research, we do not attempt to consider all possible space group symmetries for every sample but are striving to understand the physics underlying the phase behavior of the experimental materials described earlier. Therefore the experimental data are used to select five possible ordered morphologies: LAM, O^{70}, Q^{230}, PEO cylinders packed hexagonally in an IS matrix (HEX_O), and PI cylinders packed hexagonally in an SO matrix (HEX_I). SAXS data consistent with LAM, O^{70}, Q^{230}, and a phase with hexagonal symmetry are reported for samples in this study. We assume the hexagonal mesostructure contains hexagonally packed cylinders; HEX_O and HEX_I are the two possible configurations of hexagonally packed cylinders in the ISO system.[44] The monomer reference volume for these calculations is 118 $Å^3$ and Flory–Huggins interaction parameters (χ), statistical segment lengths (b), and degrees of polymerization (N) are all scaled to this quantity. The χ (here taken at 100 °C)[71] and b[58, 72] values are adapted from the literature: $\chi_{IS} = 0.044$, $\chi_{SO} = 0.057$, $\chi_{IO} = 0.183$, $b_I = 6.07$, $b_S = 5.47$, and $b_O = 7.80$. These values were previously used by Tyler et al.[44, 68]

SCFT calculations are performed on hypothetical sets of ISO triblocks that mimic those prepared experimentally. N of each IS diblock is kept constant at our experimental values and the lengths of the PEO chains are varied. The PI and PEO block length distributions are approximated as monodisperse while the PS chain distributions are either i) approximated as monodisperse (calculations for ISO blends)

or ii) approximated using 12–14 different PS chain lengths (calculations for materials with polydisperse PS blocks). Including significantly more than 12-14 chain lengths is not feasible because of the large amount of computational memory required for the SCFT calculations (the required memory increases roughly linearly with the number of chains). The PS chain lengths are input into the SCFT calculations in relative quantities that match their values measured experimentally using SEC (i.e., all input values lie on the SEC trace, as illustrated in Figure 8.11) and the individual PS chains were selected to make the PDI's and number–average N values of the input PS distributions equal those measured experimentally (within 0.01 and 0.5, respectively). This chain discretization strategy captures both the shape and PDI of the experimentally measured distributions; the PDI alone is not sufficient to describe polydispersity effects in block copolymers.[26]

IS(1.06)O Free Energy Calculations. The computed free energy curves of the LAM, Q^{230}, O^{70}, HEX_O, and HEX_I morphologies for perfectly monodisperse ISO triblocks ($N_I = 81$, $N_S = 84$, $0.10 < f_O < 0.40$) are provided in Figure 6.9.[73] The molecular weights of this theoretical series match those of the IS(1.06)O triblocks and the predicted sequence of morphologies is LAM→O^{70}→LAM. This LAM→O^{70}→LAM sequence was previously reported experimentally[41-43] and theoretically[44, 68] in higher segregation strength ISO materials, although there were quantitative discrepancies in the locations of the phase boundaries. As discussed earlier, the experimentally–determined sequence of morphologies in the IS(1.06)O series is LAM→Q^{230}→O^{70}→LAM, not the LAM→O^{70}→LAM predicted using SCFT. The calculated free energy differences between Q^{230}, LAM, and O^{70} are, however, less than

0.01 k_BT for 0.20 < f_O < 0.25 (the compositions where O^{70} is the predicted equilibrium structure).[73] Given the comparable free energies of Q^{230} and O^{70}, the uncertainty in composition measurements, the uncertainty in χ values, and the approximation of perfectly monodisperse blocks, it is not surprising that we experimentally identified Q^{230} as the (presumably) equilibrium mesostructure at compositions where O^{70} is the predicted morphology.

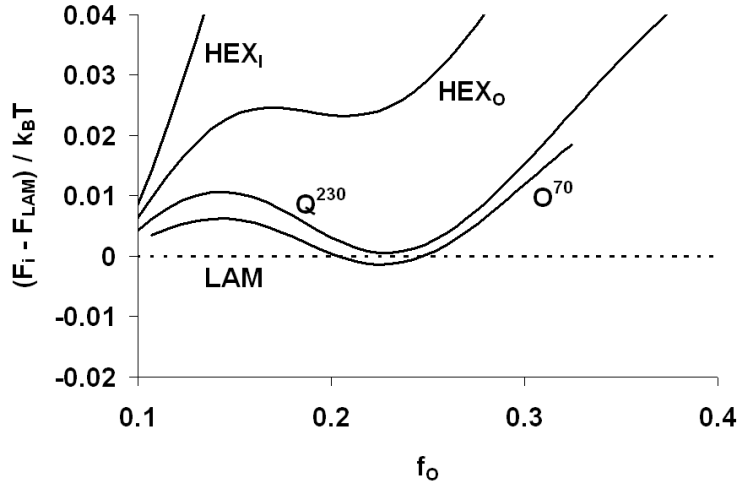

Figure 6.9. SCFT free energies of four mesostructural candidates, relative to LAM and normalized by k_BT, along the f_I = 0.49, f_S = 0.51 isopleth (N_I = 81, N_S = 84). The predicted stable morphologies are, from left to right, LAM, O^{70}, and LAM. The free energy curve for O^{70} terminates at f_O = 0.11 and f_O = 0.32 due to a previously reported technical issue that prevents the identification of SCFT solutions (see Reference 44 for more details).

The experimental IS(1.06)O blends contain between two and nine neat IS(1.06)O triblock terpolymers. SCFT calculations are performed on model mixtures that mimic these IS(1.06)O blends to compare the predicted and experimental phase behavior and elucidate the molecular factors driving the block copolymer self–assembly. The SCFT inputs contain monodisperse ISO triblocks with the N_i values listed in Table 6.1. The relative quantities of the chains in the model mixtures are equivalent to the relative masses added to the experimental IS(1.06)O blends (values provided in Table 8.2). Accounting for individual PI or PS block polydispersities is not feasible because of the large quantity of computer memory that would be required for SCFT calculations with that many discrete chain lengths. However, as the blends only differ in the PEO MWD's, approximating the PI and PS blocks as monodisperse should not seriously detract from our efforts to model self–assembly in these materials.

SCFT results obtained for the eleven ISO blends are summarized in Table 6.3. In Table 6.3, the mesostructure with the lowest computed free energy is listed as the "predicted phase" and all of the component free energies are reported as differences (Δ) between the values associated with two mesostructural candidates. The overall Helmholtz free energy for each microstructure can be expressed as the sum of the component free energies according to:

$$F_{ordered} = F_{IS} + F_{SO} + F_{IO} + F_I + F_O + F_{excess} \quad (6\text{-}1)$$

where F_{IS}, F_{SO}, and F_{IO} are the free energies associated with PI/PS, PS/PEO, and PI/PEO segment interactions, F_I and F_O are the free energies associated with the conformational entropies of the PI and PEO blocks, and F_{excess} encompasses all other free energy contributions, including the free energies associated with PS chain

Table 6.3. Differences in Free Energy Components and Relative Domain Spacings of the Morphologies with Comparable Free Energies for the Multicomponent ISO Blends

f_O	PEO PDI	predicted phase	$F_{Q230} - F_{LAM}$ [a]	ΔF_I [b]	ΔF_O [b]	ΔF_{IS} [c]	ΔF_{SO} [c]	ΔF_{IO} [c]	ΔF_{excess} [d]	d^*_{Q230} / d^*_{LAM} [e]
0.20	1.00	LAM	0.003	–0.063	0.052	0.060	–0.070	0.018	0.006	1.016
0.20	1.17	Q^{230}	–0.025	–0.067	0.057	0.061	–0.093	0.004	0.013	1.028
0.30	1.00	LAM	0.015	–0.040	0.076	0.045	–0.052	0.031	–0.045	1.028
0.30	1.16	Q^{230}	–0.009	–0.040	0.062	0.040	–0.058	0.027	–0.040	1.040
0.30	1.28	Q^{230}	–0.027	–0.039	0.054	0.032	–0.058	0.017	–0.034	1.042
0.30	1.40	Q^{230}	–0.045	–0.036	0.048	0.022	–0.057	0.006	–0.028	1.041
0.33	1.00	LAM	0.026	–0.033	0.079	0.040	–0.040	0.030	–0.050	1.039
0.33	1.27	Q^{230}	–0.012	–0.033	0.053	0.031	–0.045	0.023	–0.041	1.060
0.33	1.30	Q^{230}	–0.017	–0.033	0.051	0.029	–0.045	0.020	–0.039	1.060
0.33	1.45	Q^{230}	–0.043	–0.034	0.036	0.026	–0.051	0.018	–0.038	1.067

f_O	PEO PDI	predicted phase	$F_{HEXo} - F_{Q230}$ [a]	ΔF_I [b]	ΔF_O [b]	ΔF_{IS} [c]	ΔF_{SO} [c]	ΔF_{IO} [c]	ΔF_{excess} [d]	d^*_{HEXo} / d^*_{Q230} [e]
0.20	1.17	Q^{230}	0.007	–0.031	0.020	0.039	–0.030	0.030	–0.021	1.151
0.20	1.33	HEX_O	–0.003	–0.031	0.017	0.037	–0.033	0.025	–0.018	1.157
0.20	1.46	HEX_O	–0.007	–0.030	0.015	0.035	–0.033	0.023	–0.017	1.159
0.20	1.53	HEX_O	–0.011	–0.030	0.014	0.034	–0.034	0.020	–0.015	1.161
0.30	1.40	Q^{230}	0.002	–0.023	0.032	0.030	–0.026	0.010	–0.021	1.173
0.30	1.73	HEX_O	–0.019	–0.020	0.020	0.016	–0.025	–0.001	–0.009	1.184

All free energies are computed with respect to a reference volume of 118 $Å^3$ and are normalized by k_BT. In the top half of this Table, all differences (Δ) are listed as the value for Q^{230} minus the value for LAM. In the bottom half of this Table, all differences (Δ) are listed as the value for HEX_O minus the value for Q^{230}. [a] Differences in the overall Helmholtz free energy. [b] Differences in the free energies associated with the conformational entropies of the PI and PEO blocks. [c] Differences in the interaction energies of IS, SO, and IO monomer pairs. [d] Differences in the excess free energy, a quantity that includes the entropic free energy associated with stretching the PS block and the entropic free energy associated with the localization of chain junction points. [e] Ratio of the length scales associated with the principal scattering vector ($d^* = 2\pi / q^*$).

stretching and the localization of chain junction points. In the top half of Table 6.3, the Δ symbol identifies the quantity associated with Q^{230} minus the quantity associated with LAM. In the lower half of Table 6.3, the Δ symbol indicates the value associated with HEX_O minus the value associated with Q^{230}. Presenting the data in this manner will facilitate the discussion of the thermodynamics underlying the polydispersity-driven morphological transitions.

OOT's from Q^{230} to HEX_O upon heating were identified earlier using experimental data in all of the IS(1.06)O blends with $f_O = 0.20$. T_{OOT} depends on the PEO molecular weight distribution, with increases in PDI_O accompanied by decreases in T_{OOT}. These experimental results intimate that HEX_O becomes more stable as PDI_O is increased. The SCFT results also suggest that HEX_O is stabilized by increasing PDI_O; the equilibrium mesostructure is predicted to change from Q^{230} to HEX_O as PDI_O is increased from 1.17 to 1.33. Furthermore, the differences in the computed free energies of the Q^{230} and HEX_O morphologies are less than 0.012 k_BT for all of the ISO blends with $f_O = 0.20$, making it unsurprising that OOT's were identified in the experiments.

We believe the thermodynamic driving force for these polydispersity effects is related to the magnitudes of chain stretching summed over the distribution of chain lengths. In all cases the exact contributions to the system free energies depend on the length distribution function of the PEO (and PI and PS) chains.[26] Q^{230} becomes preferred over LAM as the PDI_O is increased from 1.00 to 1.17. According to SCFT, changes in enthalpic interactions are largely responsible for this LAM-to-Q^{230} transition, as both ΔF_{SO} and ΔF_{IO} decrease significantly upon increasing PDI_O. We suggest that these decreases result from a disproportionate increase in the purity of the

PEO domain in the Q^{230} morphology, relative to LAM, when PDI_O is raised from 1.00 to 1.17. The composition profiles obtained from SCFT support this reasoning; the purity of the PEO domain in the LAM mesostructure is relatively invariant over this PDI_O range, while the purity of the PEO domain in the Q^{230} morphology increases as PDI_O is increased from 1.00 to 1.17. Presumably the longer PEO chains present in the blend more readily segregate from the PI and PS chains than the shorter chains of the monodisperse material.[21] As the PEO molecular weight distribution is further broadened to PDI_O = 1.33, HEX_O is predicted to have a lower free energy than Q^{230}. The enthalpic interactions also favor this transition, although in a different manner than the LAM-to-Q^{230} transition described above. As PDI_O is increased from 1.17 to 1.33, ΔF_{IS}, ΔF_{SO}, and ΔF_{IO} all decline by a comparable amount (see bottom half of Table 6.3). We suggest these differences are related to the increase in the d^*_{HEXo} / d^*_{Q230} (where $d^* = 2\pi/q^*$) ratio as PDI_O is elevated. The greater increase in d^*_{HEXo} relative to the increase in d^*_{Q230} (as evidenced by the increased d^*_{HEXo} / d^*_{Q230} ratios provided in Table 6.3) means the interfacial area per chain is lower for HEX_O (relative to Q^{230}) at the higher PDI_O value. Consequently, there are fewer segment-segment contacts and lower values of ΔF_{IS}, ΔF_{SO}, and ΔF_{IO}. In addition to enthalpic considerations, the broadening of the PEO molecular weight distribution relieves the entropic penalty (ΔF_O) incurred by the PEO chains as they stretch to accommodate the HEX_O mesostructure. Presumably the longer chains fill space in the center of the PEO domain while the shorter chains adopt relaxed conformations near the interface or mix with the PI or PS domains.[21, 23, 24, 31, 32]

The Q^{230} and HEX_O morphologies were also identified earlier in the IS(1.06)O blends with f_O = 0.30 and f_O = 0.33. The SCFT calculations are in good agreement with this experimental analysis and correctly predict the equilibrium mesostructure (either Q^{230} or HEX_O) for each PEO molecular weight distribution (Blend ISO(1.27, 0.33) undergoes an OOT from LAM_3 to Q^{230}upon heating at 210 °C; SCFT predicts Q^{230} as the equilibrium morphology, with a free energy only 0.026 k_BT lower than LAM). Similar arguments to those employed above can be used to describe the thermodynamics driving the phase behavior of these ISO blends with f_O = 0.30 and f_O = 0.33. As PDI_O increases above 1, Q^{230} becomes preferred over LAM at both compositions mainly due to i) a reduction in the entropic penalty (ΔF_O) incurred by the PEO chains as they stretch to accommodate the Q^{230} morphology and ii) a reduction in the enthalpic interactions (lower ΔF_{IS}, ΔF_{SO}, and ΔF_{IO}) resulting from a decrease in the interfacial area per chain (increased d^*_{Q230} / d^*_{LAM}). Once the PEO molecular weight distribution reaches a certain breadth, HEX_O becomes more stable than Q^{230}, as evidenced by the SCFT results (and experimental data) for a blend with f_O = 0.30 and PDI_O = 1.73. This Q^{230}-to-HEX_O transition is also largely explained by a combination of i) and ii). For all of these blends, when polydispersity drives a morphological transition, the interfaces curve toward the polydisperse terminal PEO blocks, a result consistent with previous AB diblock reports.[21-23, 25]

In addition to the identity of the ordered mesostructure, the T_{ODT} and domain periodicity are important parameters describing block copolymer phase behavior. Our experimental analysis of the effects of PEO block polydispersity on the order-disorder transition is limited by the fact that most of our samples do not disorder below 250 °C

(and higher temperatures lead to polymer degradation). Our data do allow for some qualitative analysis of the PEO polydispersity effects on T_{ODT} for ISO materials with f_O = 0.20. Triblock IS(1.06)O(0.20), which contains a narrower PEO molecular weight distribution than the ISO blends with f_O = 0.20, disorders at 230 °C. In contrast, none of the ISO blends with this composition disorder below 250 °C, meaning an increase in the PDI of the minority PEO block was accompanied by an increase (of unknown magnitude) in T_{ODT}. This result is consistent with Lynd and Hillmyer's AB diblock report that T_{ODT} increases monotonically with the PDI of a constituent minority block.[33] Our SCFT results also indicate T_{ODT} increases monotonically with the PDI of the PEO block at the compositions probed in this work (as $F_{ordered} - F_{homogeneous}$ decreases as PDI_O increases). We caution against drawing too strong a set of conclusions from our SCFT analysis of T_{ODT}, however, as SCFT fails to qualitatively predict changes in T_{ODT} for all compositions of polydisperse AB diblock copolymers.[23, 25, 33, 36] While our SCFT analysis qualitatively agrees with our experimental data over the composition range interrogated here, it likely offers limited predictive capability for other compositions.

Polydispersity effects on lattice spacings have been widely studied and, unlike the order-disorder transition, there is good general agreement between experiment and theory. Polydispersity has reportedly led to increases in the heights of end–grafted polymer brushes[37] and in the domain periodicities of block copolymers[22-24, 26, 28-30] and block terpolymers[40] in the melt. These increases have been attributed to a reduction in the elastic free energy associated with stretching a polydisperse ensemble of chains compared to its monodisperse counterpart.[23, 25, 26] The effects of PEO polydispersity on ISO domain periodicities are summarized in Figure 6.10, where the measured and

predicted normalized principal scattering lengths ($d^* = 2\pi/q^*$) are plotted as a function of PDI_O for the ISO materials with f_O = 0.20, 0.30, and 0.33. The data are presented in this normalized manner to facilitate quantitative comparison of the experiment and theory; SCFT does not typically accurately predict absolute domain periodicities using χ values measured at phase transitions.[74] The normalized SCFT predictions are in good qualitative agreement with the experimental data, with the normalized d^* values increasing monotonically with the polydispersity of the terminal PEO block. This result generally agrees with previous block copolymer[22-24, 26, 28-30] and block terpolymer[40] reports; presumably the polydispersity relieves the entropic free energy penalty associated with stretching the PEO chains and leads to larger lattice spacings. Interestingly, our SCFT predictions corroborate the experimental conclusion that the sensitivity of the lattice spacing to changes in PDI is higher at increased segregation strengths (i.e., an increase in PDI_O for the materials with f_O = 0.33 leads to a bigger relative increase in domain periodicity than an equivalent increase in PDI_O does for the samples with f_O = 0.20). This trend was not predicted by several SCFT analyses of polydisperse AB diblock copolymers,[23, 24, 26] although it was identified experimentally by Lynd and Hillmyer for polydisperse poly[(ethylene-*alt*-propylene)-*b*-lactide] diblock copolymers.[22] There are, however, some quantitative differences between our ISO experimental data and SCFT results. Namely, the SCFT consistently overestimates the relative increase in d^*. There are numerous potential sources of this discrepancy between experiment and theory, including uncertainties in measurements of χ and N, the approximation of the PI and PS blocks as monodisperse, and non-equilibrium effects (our experimental materials may not be fully equilibrated following the relatively short

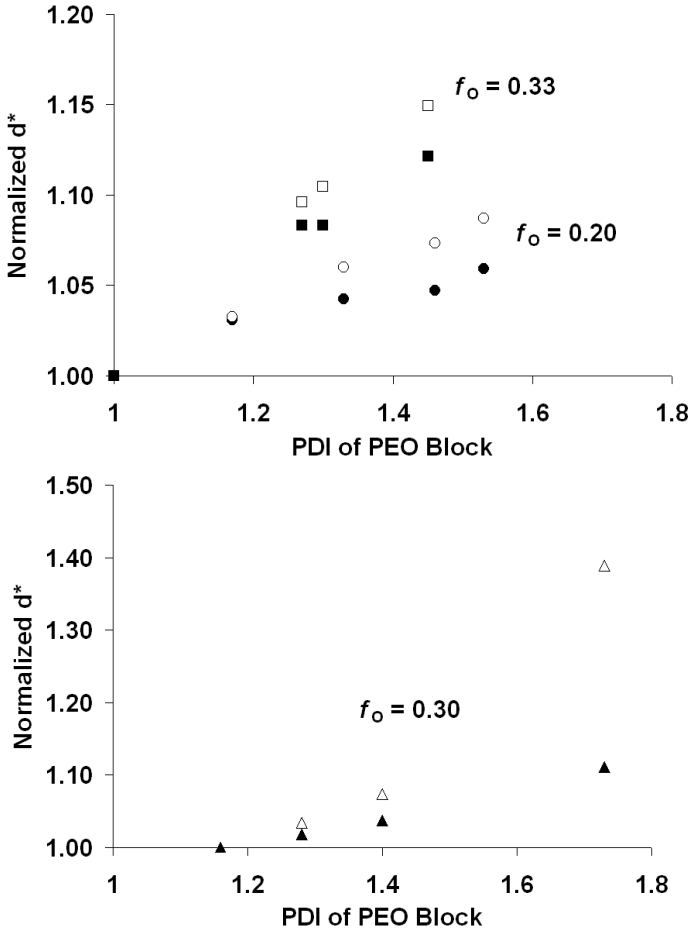

Figure 6.10. Measured (by SAXS, solid points) and predicted (by SCFT, open points) normalized d^* values ($d^* = 2\pi/q^*$) for the ISO samples with f_O = 0.20, 0.30, and 0.33. The experimentally measured principal scattering lengths are normalized by dividing them by d^* measured for triblock IS(1.06)O(0.20) (data for f_O = 0.20), triblock IS(1.06)O(0.33) (data for f_O = 0.33), or blend ISO(1.16, 0.30) (data for f_O = 0.30). Here PDI_O is approximated as 1 for samples IS(1.06)O(0.20) and IS(1.06)O(0.33). The predicted d^* values are normalized by dividing them by either d^* computed for monodisperse ISO triblocks with the same composition (f_O = 0.20, 0.33) or by d^* calculated for blend ISO(1.16, 0.30) (f_O = 0.30). In all cases d^* was computed for the morphology identified using experimental data, even if it was not the mesostructure with the lowest calculated free energy (e.g., the predicted d^* for blend ISO(1.46, 0.20) was computed for the Q^{230} morphology, not HEX_O).

annealing times). Further experimental and theoretical investigations are required to fully understand polydispersity effects on lattice spacings.

IS(1.16, 1.31, 1.44)O Free Energy Calculations. The computed free energies (relative to LAM and normalized by k_BT) of the morphological candidates in the model systems designed to mimic the IS(1.16)O, IS(1.31)O, and IS(1.44)O materials are provided in Figure 6.11. The solid curves represent the free energies of the morphologies in the model polydisperse systems, while the dashed lines, for comparison, correspond to the free energies of the mesostructures in monodisperse systems with the same molecular weights and compositions. The free energy curves for the HEX_I, HEX_O, Q^{230}, O^{70}, and LAM morphologies are provided for the model IS(1.16)O system in the upper left plot. The HEX_I and HEX_O mesostructures do not closely compete for the lowest free energy in this, or either other, system. As a result, the other three plots only include the Q^{230}, O^{70}, and LAM free energies to facilitate analysis of these closely competing mesostructural candidates.

The monodisperse and polydisperse free energy curves provided in the IS(1.16)O plots in the upper half of Figure 6.11 correspond to model monodisperse and polydisperse systems that approximate the experimental IS(1.06)O and IS(1.16)O materials, respectively. As discussed above, SCFT predicts a morphology sequence of LAM→O^{70}→LAM upon increasing f_O for the monodisperse materials, while the LAM→Q^{230}→O^{70}→LAM sequence was identified in the IS(1.06)O polymers. As the PS molecular weight distribution is broadened to a PS PDI = 1.16, SCFT predicts that both the O^{70} and Q^{230} mesostructures increase in free energy relative to the LAM

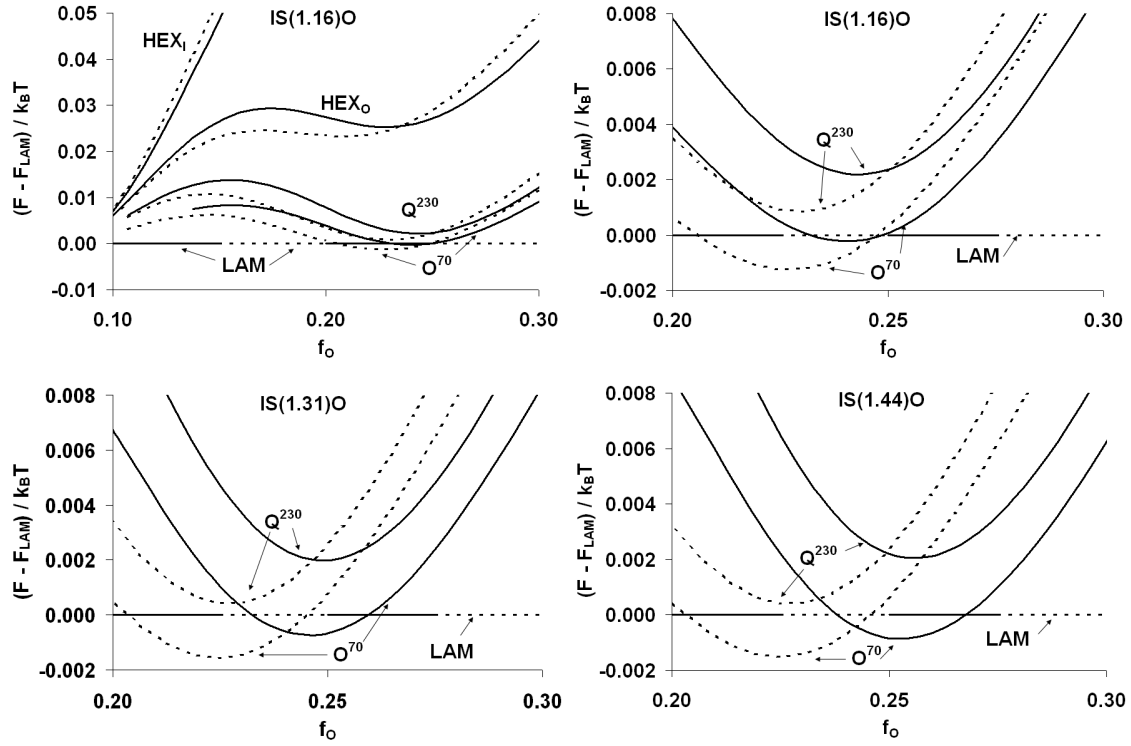

Figure 6.11. Calculated SCFT free energies (relative to LAM and normalized by k_BT) of competing mesostructural candidates for model systems that approximate the experimental IS(1.16)O, IS(1.31)O, and IS(1.44)O systems. All of the free energy curves were computed at the molecular weights and along the isopleths defined by the number-averaged N_I and N_S values that are listed in Table 6.11. The HEX_I and HEX_O morphologies have higher computed free energies for all of the systems and, for clarity, their free energy curves are not provided on the IS(1.31)O and IS(1.44)O plots. The solid lines are the curves computed for the polydisperse materials while the dashed lines are calculated for monodisperse systems with the same compositions and molecular weights.

morphology. O^{70} is still, however, predicted as the equilibrium structure over a narrow composition range ($0.23 < f_O < 0.25$). This predicted LAM→O^{70}→LAM sequence was identified using the experimental data obtained for the IS(1.16)O samples, although the experimental "network" window ($0.11 < f_O < 0.25$) is significantly wider than predicted. The IS(1.06) and IS(1.16)O characterization data indicate that increasing the PS PDI from 1.06 to 1.16 changes the identity of the predominant network structure from Q^{230} to O^{70}. This result intimates that O^{70} becomes relatively lower in free energy than Q^{230} in this composition range ($0.10 < f_O < 0.25$) as the PS PDI increases from 1.06 to 1.16. The SCFT calculations agree with this deduction, as the calculated free energy of O^{70} (relative to Q^{230}) is lower in the model IS(1.16)O system than in the monodisperse system when $0.15 < f_O < 0.27$ (see Figure 8.12 for details).

The SCFT analysis for the model IS(1.31)O system predicts that O^{70} should be the equilibrium mesostructure at a higher f_O and over a narrower composition range ($0.24 < f_O < 0.26$ versus $0.21 < f_O < 0.25$) in the IS(1.31)O polymers than it is in monodisperse materials with the same molecular weights and compositions. We did not identify O^{70} (or Q^{230}) in the experimental materials. It is possible that the network window occupies compositions not investigated experimentally; network structures could form in either the $0.11 < f_O < 0.14$ or $0.17 < f_O < 0.24$ composition ranges. It should also be noted that the calculated free energy differences between LAM, Q^{230}, and O^{70} are small ($< 0.006\ k_BT$) over the computed network window. Uncertainties in composition measurements, molecular weights, and χ values, or the block polydispersity approximations (monodisperse PI and PEO blocks, a PS chain

distribution comprised of only 13 different chain lengths) could cause SCFT to erroneously identify the equilibrium morphology.

SCFT analysis also suggests that the O^{70} window will narrow and shift to higher PEO volume fractions (from $0.21 < f_O < 0.25$ to $0.24 < f_O < 0.27$) as the PS PDI is increased from 1 to 1.44 (as shown in the IS(1.44)O plot in Figure 6.11). Unlike the IS(1.31)O experimental data, the IS(1.44)O data are in qualitative agreement with the prediction that the network window shifts to higher PEO volume fractions. A network window was identified in the IS(1.44)O materials beginning at $f_O = 0.17$, while it begins in the $0.10 < f_O < 0.13$ range in comparable monodisperse materials (e.g., the IS(1.06) series or the ISO polymers characterized in References 41, 42, and 43). The experimental data are also consistent with the SCFT calculations that indicate the LAM, Q^{230}, and O^{70} mesostructures have comparable free energies (they differ by $< 0.006\ k_BT$ in the network window); all three of these morphologies were identified in the experimental materials. We did not prepare any LAM-forming IS(1.44)O materials on the PEO-rich side of the network window and are thus unable to evaluate the SCFT prediction that the window would narrow.

To understand the thermodynamics underlying these polydispersity effects, we can examine the components of the free energies computed using SCFT. In our three systems, the trends in the component free energy differences between either O^{70} and LAM or Q^{230} and LAM are qualitatively similar. We provide representative SCFT results comparing the LAM and O^{70} morphologies for the IS(1.44)O system in Figure 6.12. The data are plotted such that curves below the horizontal zero line represent free energy components that favor network formation at PS PDI = 1.44, while

the curves above the horizontal zero line indicate the components prefer formation of LAM at the elevated PS PDI. The thermodynamic factors that favor network formation at the higher f_O values as PS PDI increases are the decreases in the free energies associated with the segment-segment interactions between the PS and PEO chains (ΔF_{SO}), the PI/PEO interactions (ΔF_{IO}), and the conformational entropy of the PI block (ΔF_I). The free energies that favor LAM at these compositions are those associated with the PI/PS segment-segment interactions (ΔF_{IS}), the conformational entropy of the PEO chains (ΔF_O), and the excess entropy (ΔF_{excess}), which includes the conformational entropy of the PS and the localization of chain junctions. We suggest that these thermodynamic changes are driven by changes in the segment density distributions within the unit cells. The composition profiles computed by SCFT indicate that increases in the PS polydispersity are accompanied by additional chain mixing and an increase in the number of segment-segment contacts. While the broadening of the PS molecular weight distribution decreases chain segregation in both the LAM and O^{70} mesostructures, the relative changes are mesostructure-dependent. The changes in the PEO chain segregation are more pronounced in the LAM morphology (making ΔF_{SO} and ΔF_{IO} negative in Figure 6.12) while the changes in the PI/PS contacts are more significant in O^{70} (making ΔF_{IS} positive in Figure 6.12). The net effect of the increased PS PDI is not a preference for morphologies with domain interfaces curved toward the polydisperse domain. These results are qualitatively different than the effects associated with an increase in the PEO polydispersity and are not consistent with previous studies[22, 23, 25, 26] of AB block copolymer systems.

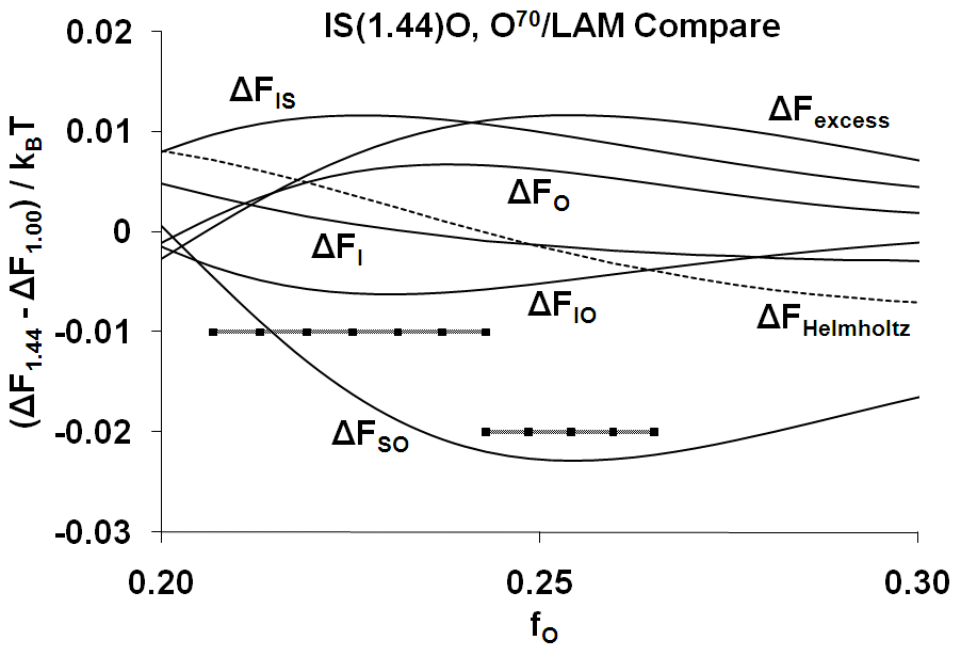

Figure 6.12. Differences in computed free energy components (normalized by k_BT) of the O^{70} and LAM morphologies between the model IS(1.44)O system and its monodisperse counterpart. The values plotted on the ordinate are obtained by

i) subtracting the value of each free energy component calculated for LAM from the value of each component computed for O^{70} (i.e., $\Delta F_i = F_{i,\,O70} - F_{i,\,LAM}$) and

ii) subtracting these component differences for a PS PDI = 1.00 from these component differences for a PS PDI = 1.44. The solid curves represent the components of the free energies and are labeled using the nomenclature described in Table 6.3. The dashed curve represents the overall Helmholtz free energy. The horizontal lines (marked with ■) denote the compositions at which SCFT predicts O^{70} to be the equilibrium mesostructure for the monodisperse ($0.21 < f_O < 0.25$) and polydisperse ($0.24 < f_O < 0.27$) systems.

Changing PS polydispersity also alters T_{ODT} and domain periodicity.

Unfortunately, no firm conclusions regarding the effects of PS polydispersity on T_{ODT} can be drawn from the experimental data. A plot of the measured T_{ODT} values versus f_O (values from Table 6.1, plot not shown) for each PS PDI value yields a scatter of points that generally lie on the same line, with the exception of the IS(1.31)O values, which are slightly below those of the other materials. Given the lack of clear trends and the molecular weight and composition variations across the parent IS diblocks (and thus the ISO triblocks), it is not possible to say whether the differences in the T_{ODT} values are driven by changes in the PS molecular weight distribution. Unlike with the PEO polydispersity, SCFT does not predict T_{ODT} to increase monotonically with PS polydispersity. A plot describing the relative stability of LAM in the polydisperse ISO systems and their monodisperse analogs is provided in Figure 6.13. For the low f_O values, the PS polydispersity stabilizes the ordered LAM mesostructure relative to the homogeneous, disordered state (ordinate values below 0), a result qualitatively similar to the SCFT analysis of the PEO polydispersity. However, as f_O increases, F_{LAM} becomes closer to $F_{homogeneous}$ (ordinate values above 0) for the polydisperse systems, representing a polydispersity-induced destabilization of the ordered mesostructure (i.e., a decrease in T_{ODT}). Note that while LAM SCFT results are plotted in Figure 6.13, the same trend is present in the calculations for the other morphological candidates. While the scatter in the experimental data prevent us from evaluating the validity of these predictions, this analysis does provide a rationale for polydispersity-driven decreases in T_{ODT} within the SCFT framework; only Matsen's calculations considering the close-

packed spherical morphology have provided for this possibility in polydisperse AB diblock copolymers.[25]

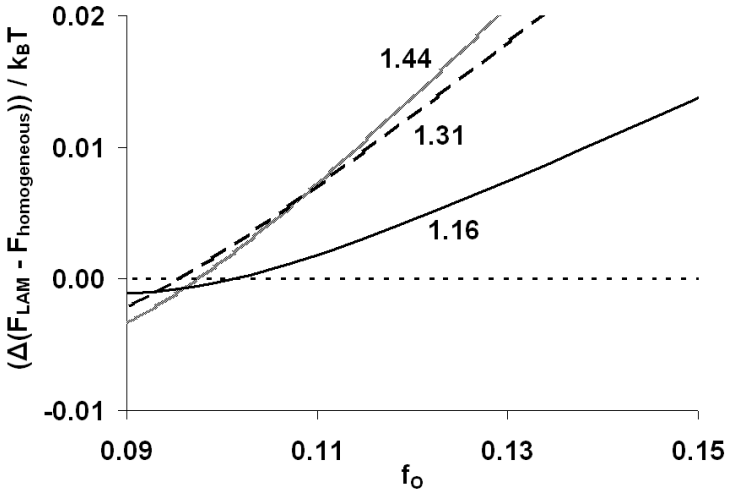

Figure 6.13. Curves representing the relative stability of the LAM mesostructure relative to a nearly homogeneous, disordered state for the polydisperse ISO systems and their monodisperse analogs. The values plotted on the ordinate were obtained by i) computing F_{LAM} - $F_{homogeneous}$ for both the monodisperse and polydisperse systems and ii) subtracting this difference for the monodisperse system from this difference for the polydisperse system (e.g., $\Delta F_{1.44} - \Delta F_{1.00}$). When the ordinate value is negative, LAM is relatively more stable for the polydisperse material (i.e., higher T_{ODT} for the polydisperse systems). When the ordinate value is positive, LAM is more stable for the monodisperse material (i.e., lower T_{ODT} for the polydisperse systems).

The domain periodicities measured using SAXS, like the experimental T_{ODT} data, do not follow any clear tends with PS polydispersity. We can, however, compute

the predicted polydispersity-driven changes in lattice spacings using SCFT. These results are provided in Figure 6.14 for compositions where LAM is predicted to be the equilibrium mesostructure of both the polydisperse and monodisperse materials. (Presenting the results in this manner eliminates discontinuities in the curves resulting from morphological transitions. Domain periodicities computed when O^{70} is the predicted mesostructure follow the same general trends illustrated in Figure 6.14.) In this plot the calculated domain periodicities of the polydisperse series are normalized by

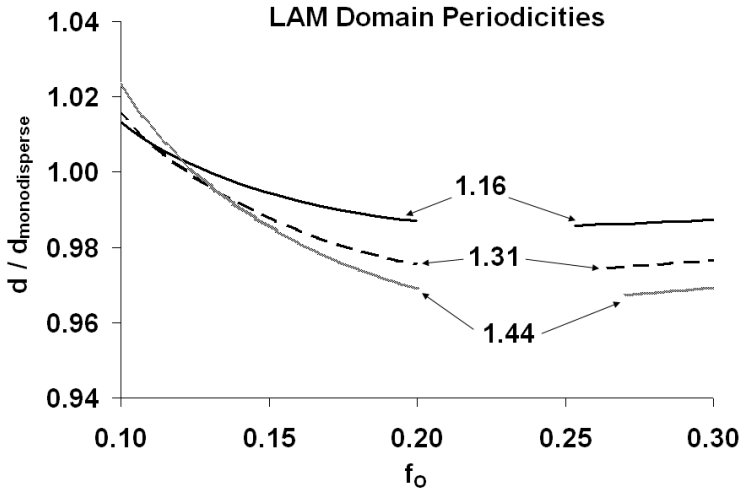

Figure 6.14. Normalized LAM domain periodicities computed using SCFT for the three polydisperse ISO systems. The values are normalized by dividing them by the lattice spacings calculated for the monodisperse analogs to the polydisperse series. Results are only plotted when SCFT predicts LAM to be the equilibrium mesostructure for both the monodisperse and polydisperse systems; the gaps represent compositions at which O^{70} is predicted to be the equilibrium morphology for the polydisperse and/or monodisperse materials.

dividing them by the values computed for the monodisperse analogs. SCFT predicts that, for low values of f_O (f_O < ~0.12 in Figure 6.14), the LAM domain periodicity increases slightly with the PS PDI, while for higher values of f_O, the LAM lattice spacing decreases with increasing PS PDI. The predicted variations in domain spacing are small, making it unsurprising that no trends were identified in the experimental data.

Increasing the polydispersity of the middle PS block does not lead to the same qualitative morphological changes as increasing the polydispersity of the terminal PEO block. Broadening the PEO molecular weight distribution results in changes that generally mirror those reported in polydisperse AB diblock copolymers- namely, morphologies with interfaces that are curved toward the polydisperse block are preferred at higher polydispersities and domain periodicity increases monotonically with block polydispersity.[36] Increases in the PS block polydispersity do not lead to these same trends, as the morphological changes depend on the block copolymer composition. We attribute these differences to the fact that the middle PS block does not have any dangling chain ends, but is covalently bonded to both PI and PEO chains. The enthalpic incompatibility between these terminal PI and PEO blocks (χ_{IO} = 0.183 at 100 °C)[71] prevents the polydisperse PS chains from behaving like the polydisperse chains in AB diblock or ABA triblock copolymers. Namely, the short PS chains do not simply adopt relaxed conformations near the domain interface and the long chains do not always occupy space in the center of the domain. Generally, the effects of polydispersity in blocks without free chain ends will depend not only on the chain distribution functions, but also the sequence of χ values in a given system. The research

described in this Chapter provides some foundation for analyzing these complicated polydisperse systems.

6.5 Conclusion

The effects of middle PS or terminal PEO block polydispersity on the phase behavior of ISO triblock terpolymers with $f_I \approx f_S$ have been probed both experimentally and theoretically. The different block polydispersities drive different changes in ISO phase behavior. The terminal PEO block polydispersity effects generally mimic polydispersity effects reported in AB diblock or ABA triblock copolymers,[36] and there is broad agreement between our experimental and SCFT results for the ISO system. Namely, lattice periodicities increase monotonically with block polydispersity and morphologies with interfaces curved toward the polydisperse PEO block are preferred. Broadening the PS molecular weight distribution does not lead to the same general trends in ISO triblock terpolymers as an increase in PEO polydispersity. Increases in PS polydispersity do not always lead to increases in domain periodicity and do not always drive interfaces to curve toward the polydisperse block. These differences are attributed to the fact that, unlike the polydisperse PEO chains and the polydisperse blocks in AB block copolymers, the polydisperse PS chains are covalently connected to two enthalpically incompatible blocks. The exact effects of middle block polydispersity will depend on both the chain distribution functions and the sequence of χ parameters.

Notably, in the ISO system, neither PS nor PEO block polydispersities prevent the formation of the multiply continuous Q^{230} and/or O^{70} network mesostructures,

although the compositions at which both are stable are sensitive to the individual block molecular weight distributions. In fact, we have used terminal PEO block polydispersity (introduced by multicomponent blending) to drive a morphological transition from LAM_3 to the Q^{230} network mesostructure, effectively widening the network "window." These results highlight the utility of polydispersity as a tool to tune block terpolymer phase behavior.[51, 52]

Acknowledgement. The work described in Chapter 6 would not have been possible without the contributions of numerous other people. While all flaws in the work are my own, many of the virtues are due to their contributions. Dr. Nathaniel A. Lynd was a particularly valuable resource when I was contemplating undertaking an investigation of polydispersity effects in the ISO system. We had many stimulating conversations about polydispersity effects, and without his encouragement the research described in this Chapter would not have happened. Professor Christopher J. Ellison was a terrific collaborator in polydispersity research. I learned a great deal from him and his focus, hard work, and patience preparing blends were invaluable drivers of this work. Christopher M. Evans contributed significantly to the experimental effort, particularly in blend preparation and rheological measurements. None of the SCFT calculations would have happened without the efforts of Jian Qin. He taught me how to complete SCFT calculations and very patiently answered many of my questions. These discussions contributed significantly to my understanding of block copolymers in general and SCFT in particular. I am also grateful to Professor David C. Morse for providing his group's SCFT code and for encouraging me to use it to augment my experimental work. Finally, I thank Dr. Steven Weigand and Dr. Denis Keane for

setting up the equipment at the Advanced Photon Source (APS) that was used to acquire the SAXS data presented in this Chapter.

6.6 References

(1) Holden, G., Legge, N. R., Quirk, R. P., Schroeder, H. E. *Thermoplastic Elastomers*, 2nd ed.; Hansen Publishers: New York, NY, 1996.

(2) Perrier, S.; Wang, X. *Nature* **2007**, *445*, 271-272.

(3) Bielawski, C. W.; Grubbs, R. H. *Prog. Polym. Sci.* **2007**, *32*, 1-29.

(4) Hawker, C. J.; Bosman, A. W.; Harth, E. *Chem. Rev.* **2001**, *101*, 3661-3688.

(5) Kamigaito, M.; Ando, T.; Sawamoto, M. *Chem. Rev.* **2001**, *101*, 3689-3746.

(6) Matyjaszewski, K.; Xia, J. *Chem. Rev.* **2001**, *101*, 2921-2990.

(7) Braunecker, W. A.; Matyjaszewski, K. *Prog. Polym. Sci.* **2007**, *32*, 93-146.

(8) Bendejacq, D.; Ponsinet, V.; Joanicot, M.; Loo, Y.-L.; Register, R. A. *Macromolecules* **2002**, *35*, 6645-6649.

(9) Ruzette, A.; Tence-Girault, S.; Leibler, L.; Chauvin, F.; Bertin, D.; Guerret, O.; Gerard, P. *Macromolecules* **2006**, *39*, 5804-5814.

(10) Leibler, L. *Macromolecules* **1980**, *13*, 1602-1617.

(11) Leibler, L.; Benoit, H. *Polymer* **1981**, *22*, 195-201.

(12) Hadziioannou, G.; Skoulios, A. *Macromolecules* **1982**, *15*, 267-271.

(13) Hong, K. M.; Noolandi, J. *Polym. Commun.* **1984**, *25*, 265-268.

(14) Milner, S. T.; Witten, T. A.; Cates, M. E. *Macromolecules* **1989**, *22*, 853-861.

(15) Burger, C.; Ruland, W.; Semenov, A. N. *Macromolecules* **1990**, *23*, 3339-3346.

(16) Almdal, K.; Rosedale, J. H.; Bates, F. S. *Macromolecules* **1990**, *23*, 4336-4338.

(17) Spontak, R. J.; Williams, M. C. *J. Polym. Sci., Part B* **1990**, *28*, 1379-1407.

(18) Nguyen, D.; Zhong, X.; Williams, C. E.; Eisenberg, A. *Macromolecules* **1994**, *27*, 5173-5181.

(19) Erukhimovich, I.; Dobrynin, A. V. *Macromol. Symp.* **1994**, *81*, 253-315.

(20) Dobrynin, A. V.; Leibler, L. *Macromolecules* **1997**, *30*, 4756-4765.

(21) Sides, S. W.; Fredrickson, G. H. *J. Chem. Phys.* **2004**, *121*, 4974-4986.

(22) Lynd, N. A.; Hillmyer, M. A. *Macromolecules* **2005**, *38*, 8803-8810.

(23) Cooke, D. M.; Shi, A. *Macromolecules* **2006**, *39*, 6661-6671.

(24) Matsen, M. W. *Eur. Phys. J. E* **2007**, *21*, 199-207.

(25) Matsen, M. W. *Phys. Rev. Lett.* **2007**, *99*, 148304.

(26) Lynd, N. A.; Hillmyer, M. A.; Matsen, M. W. *Macromolecules* **2008**, *41*, 4531-4533.

(27) Han, Y.; Cui, J.; Jiang, W. *Macromolecules* **2008**, *41*, 6239-6245.

(28) Matsushita, Y.; Noro, A.; Iinuma, M.; Suzuki, J.; Ohtani, H.; Takano, A. *Macromolecules* **2003**, *36*, 8074-8077.

(29) Noro, A.; Iinuma, M.; Suzuki, J.; Takano, A.; Matsushita, Y. *Macromolecules* **2004**, *37*, 3804-3808.

(30) Noro, A.; Cho, D.; Takano, A.; Matsushita, Y. *Macromolecules* **2005**, *38*, 4371-4376.

(31) Noro, A.; Okuda, M.; Odamaki, F.; Kawaguchi, D.; Torikai, N.; Takano, A.; Matsushita, Y. *Macromolecules* **2006**, *39*, 7654-7661.

(32) Torikai, N.; Noro, A.; Okuda, M.; Odamaki, F.; Kawaguchi, D.; Takano, A.; Matsushita, Y. *Phys. B* **2006**, *385-386*, 709-712.

(33) Lynd, N. A.; Hillmyer, M. A. *Macromolecules* **2007**, *40*, 8050-8055.

(34) Lynd, N. A.; Hamilton, B. D.; Hillmyer, M. A. *J. Polym. Sci., Part B* **2007**, *45*, 3386-3393.

(35) Listak, J.; Jakubowski, W.; Mueller, L.; Plichta, A.; Matyjaszewski, K.; Bockstaller, M. R. *Macromolecules* **2008**, *41*, 5919-5927.

(36) Lynd, N. A.; Meuler, A. J.; Hillmyer, M. A. *Prog. Polym. Sci.* **2008**, *33*, 875-893.

(37) Milner, S. T.; Witten, T. A.; Cates, M. E. *Macromolecules* **1989**, *22*, 853-861.

(38) Hajduk, D. A.; Takenouchi, H.; Hillmyer, M. A.; Bates, F. S.; Vigild, M. E.; Almdal, K. *Macromolecules* **1997**, *30*, 3788-3795.

(39) Cochran, E. W.; Garcia-Cervera, C. J.; Fredrickson, G. H. *Macromolecules* **2006**, *39*, 2449-2451.

(40) Jiang, Y.; Yan, X.; Liang, H.; Shi, A. *J. Phys. Chem. B* **2005**, *109*, 21047-21055.

(41) Bailey, T. S.; Hardy, C. M.; Epps III, T. H.; Bates, F. S. *Macromolecules* **2002**, *35*, 7007-7017.

(42) Epps, T. H., III; Cochran, E. W.; Hardy, C. M.; Bailey, T. S.; Waletzko, R. S.; Bates, F. S. *Macromolecules* **2004**, *37*, 7085-7088.

(43) Epps, T. H., III; Cochran, E. W.; Bailey, T. S.; Waletzko, R. S.; Hardy, C. M.; Bates, F. S. *Macromolecules* **2004**, *37*, 8325-8341.

(44) Tyler, C. A.; Qin, J.; Bates, F. S.; Morse, D. C. *Macromolecules* **2007**, *40*, 4654-4668.

(45) Hahn, T. *International Tables for Crystallography*, 4th ed., 1994; Vol. A.

(46) Dair, B. J.; Honeker, C. C.; Alward, D. B.; Avgeropoulos, A.; Hadjichristidis, N.; Fetters, L. J.; Capel, M.; Thomas, E. L. *Macromolecules* **1999**, *32*, 8145-8152.

(47) Meuler, A. J.; Fleury, G.; Hillmyer, M. A.; Bates, F. S. *Macromolecules* **2008**, *41*, 5809-5817.

(48) Hashimoto, T.; Tsutsumi, K.; Funaki, Y. *Langmuir* **1997**, *13*, 6869-6872.

(49) Urbas, A. M.; Maldovan, M.; DeRege, P.; Thomas, E. L. *Adv. Mater.* **2002**, *14*, 1850-1853.

(50) Chan, V. Z. –H.; Hoffman, J.; Lee, V. Y.; Latrou, H.; Avgeropoulos, A.; Hadjichristidis, N.; Miller, R. D; Thomas, E. L. *Science* **1999**, *286*, 1716-1719.

(51) Leibler, L. *Prog. Polym. Sci.* **2005**, *30*, 898-914.

(52) Hillmyer, M. A. *J. Polym. Sci., Part B* **2007**, *45*, 3249-3251.

(53) Ndoni, S.; Papadakis, C. M.; Bates, F. S.; Almdal, K. *Rev. Sci. Instrum.* **1995**, *66*, 1090-1095.

(54) Pangborn, A. B.; Giardello, M. A.; Grubbs, R. H.; Rosen, R. K.; Timmers, F. J. *Organometallics* **1996**, *15*, 1518-1520.

(55) Bailey, T. S.; Pham, H. D.; Bates, F. S. *Macromolecules* **2001**, *34*, 6994-7008.

(56) Meuler, A. J.; Mahanthappa, M. K.; Hillmyer, M. A.; Bates, F. S. *Macromolecules* **2007**, *40*, 760-762.

(57) Hillmyer, M. A.; Bates, F. S. *Macromolecules* **1996**, *29*, 6994-7002.

(58) Fetters, L. J.; Lohse, D. J.; Richter, D.; Witten, T. A.; Zirkel, A. *Macromolecules* **1994**, *27*, 4639-4647.

(59) Rosedale, J. H.; Bates, F. S. *Macromolecules* **1990**, *23*, 2329-2338.

(60) Meuler, A. J.; Ellison, C. J.; Evans, C. M.; Hillmyer, M. A.; Bates, F. S. *Macromolecules* **2007**, *40*, 7072-7074.

(61) Mao, H.; Hillmyer, M. A. *Soft Matter* **2006**, *2*, 57-59.

(62) Hasegawa, H.; Hashimoto, T.; Hyde, S. T. *Polymer* **1996**, *37*, 3825-3833.

(63) Martínez-Veracoechea, F. J.; Escobedo, F. A. *Macromolecules* **2005**, *38*, 8522-8531.

(64) Schröder-Turk, G. E.; Fogden, A.; Hyde, S. T. *Eur. Phys. J. B* **2007**, *59*, 115-126.

(65) Matsen, M. W. *J. Phys.: Condens. Matter* **2002**, *14*, R21-R47.

(66) Fredrickson, G. H. *The Equilibrium Theory of Inhomogeneous Polymers*; Clarendon Press: Oxford, 2006.

(67) Matsen, M. W. *J. Chem. Phys.* **1998**, *108*, 785-796.

(68) Tyler, C. A.; Morse, D. C. *Phys. Rev. Lett.* **2005**, *94*, 208302.

(69) Tyler, C. A.; Morse, D. C. *Macromolecules* **2003**, *36*, 8184-8188.

(70) The SCFT code is available on the internet at: http://www.cems.umn.edu/research/morse/code/pscf/home.php.

(71) Frielinghaus, H.; Hermsdorf, N.; Almdal, K.; Mortensen, K.; Messe, L.; Corvazier, L.; Fairclough, J. P. A.; Ryan, A. J.; Olmsted, P. D.; Hamley, I. W. *Europhys. Lett.* **2001**, *53*, 680-686.

(72) Cochran, E. W.; Morse, D. C.; Bates, F. S. *Macromolecules* **2003**, *36*, 782-792.

(73) Meuler, A. J.; Ellison, C. J.; Hillmyer, M. A.; Bates, F. S. *Macromolecules* **2008**, *41*, 6272-6275.

(74) Ellison, C. J.; Meuler, A. J.; Qin, J.; Evans, C. M.; Wolf, L. M.; Bates, F. S. *J. Phys. Chem. B In Press*

7

Potential Future Directions

7.1 Thesis Recap

The research described in this Thesis centered around multiply continuous network morphologies in multiblock terpolymers comprised of polystyrene (PS), polyisoprene (PI), and poly(ethylene oxide) (PEO) chains. The advances broadly fell under two categories. The first involved a strategy for improving the mechanical toughness of network morphologies. This strategy relied on preparing higher order multiblock terpolymers that contain an intrinsically tough multiblock core. The poly(ethylene oxide-*b*-styrene-*b*-isoprene-*b*-styrene-*b*-ethylene oxide) (OSISO) pentablock materials we described in Chapter 5 satisfied this requirement, as they contained a tough poly(styrene-*b*-isoprene-*b*-styrene) (SIS) triblock core. We demonstrated that the O^{70} network morphology previously reported[1-3] in poly(isoprene-*b*-styrene-*b*-ethylene oxide) (ISO) triblock terpolymers is also formed by OSISO pentablock specimens, and that these network-forming pentablock terpolymers were significantly tougher than their ISO counterparts.

The second research thrust focused on the stability of network morphologies in ISO materials with respect to polydispersity in both the PS and PEO blocks. Understanding polydispersity effects should prove to be important as the use of

controlled radical polymerization strategies, which often yield broader molecular weight distributions than living anionic techniques,[4] proliferates. We demonstrated that polydispersity in general does not prevent the formation of network structures in ISO samples, and that judicious broadening of the PEO molecular weight distribution could be used to drive morphological transitions from lamellae to Q^{230} (the core-shell gyroid) and broaden the network "window." These results highlight the utility of polydispersity as a tool to tune block copolymer phase behavior.[5, 6]

There are many other potential studies of ISO block terpolymer materials that could be used to further understand the structures and properties of the network morphologies formed by block copolymers. The physical understanding derived from investigations of the model ISO system should also aid in the design of other block copolymer materials. A few possible future research directions are described in the following sections.

7.2 Revisiting OSISO Mechanical Properties

In Chapter 5, we reported that a network-forming OSISO(0.13) pentablock sample was mechanically tough, with a stress at break of 4.2 MPa and a strain at break of 1.3. We attributed this toughness to a combination of the tough SIS core and the triply continuous network structure. We surmised that the SIS core by itself would not impart toughness, as the lamellae-forming OSISO(0.35) fractured in a brittle fashion at a strain of 0.06, presumably due to the presence of fragile bilayers in the lamellar material. This hypothesis was consistent with Phatak et al.'s investigation of poly(ethylene-*b*-cyclohexylethylene-*b*-ethylene-*b*-cyclohexylethylene) (ECEC)

tetrablock and ECECE pentablock copolymers.[7] These EC-containing block copolymers formed an isotropic two-domain lamellae morphology, had polyethylene (PE) crystallinities ranging from 0.21-0.27, and exhibited brittle behavior, even though they contained an intrinsically tough CEC core. We suggested that Phatak et al.'s investigation had effectively established a "threshold" of terminal block crystallinity at or above which brittle failure can result, and we posited that the O^{70} network structure toughed the OSISO materials by wrapping the fragile bilayers into triply periodic networks.

As we noted in Chapter 5, however, samples OSISO(0.13) and OSISO(0.35) not only contain different mesostructures, but they have different compositions and levels of PEO crystallinity. We reasoned that the different morphologies, and not the compositions or PEO crystallinities, were responsible for the differences in mechanical behavior. Definitive proof of this hypothesis would require the preparation of tensile specimens with the same composition and molecular weight, but different morphologies. This task is not trivial, given that the equilibrium morphology is a function of the sample composition. Qiao et al. used solvent casting with solvents of varying selectivity to produce test samples with three different morphologies from the same block copolymers.[8] This type of solvent casting strategy may be feasible in the ISO system, although there is an additional solvent-block interaction to consider. Here we propose an alternative, polydispersity-driven methodology to produce samples with different morphologies but the same composition and (presumably) the same PEO crystallinity. We demonstrated in Chapter 6 that ISO triblock terpolymer phase behavior can be tuned by blending ISO samples comprised of identical IS segments, but different

lengths of PEO chains. This same general strategy can, in principle, be applied to OSISO pentablock materials. A series of OSISO pentablock terpolymers could be prepared from the same parent HO-SIS-OH triblock. One of these OSISO samples should have a PEO volume fraction of ~0.30 that places it just above the network "window" and within the lamellar region. A network structure could then be prepared at this same composition by blending some of the other OSISO samples to broaden the PEO molecular weight distribution and drive a lamellae-to-network morphological transition. These samples could be subjected to uniaxial tensile testing and the results would be used to test our hypothesis that morphology differences, and not composition and crystallinity variations, were responsible for the different mechanical properties of samples OSISO(0.13) and OSISO(0.35).

7.3 ISO Triblocks with Polydispersity in Two Blocks

The investigations of polydispersities described in Chapter 6, along with nearly all of those reported in the literature,[9] focused on the effects of polydispersity in only one of the blocks. Only a small amount of research has focused on materials with broad molecular weight distributions in multiple blocks.[10] In the ISO system, polydispersity could readily be introduced into both the PS and PEO blocks using a combination of the techniques discussed in Chapter 6. A hydroxy-terminated poly(isoprene-*b*-styrene) diblock copolymer (IS-OH) with a broad, continuous PS molecular weight distribution could first be synthesized using either 3-*tert*-butyldimethylsilyloxy-1-propyllithium (*t*BDMSOPrLi) or 3-triisopropylsilyloxy-1-propyllithium (TIPSOPrLi) (see Chapter 6). This diblock could have any desired composition and molecular weight. A series of ISO

triblocks with varying lengths of PEO chains could then be prepared from this parent IS-OH diblock following established protocols. These ISO specimens would be blended to create a multimodal PEO molecular weight distribution and produce ISO samples with polydisperse PS and PEO blocks. In principle this study could be completed using the materials described in Chapter 6. However, none of these ISO samples with polydisperse PS blocks have PEO volume fractions above 0.34, limiting the potential range of compositions and PEO block polydispersities that could be interrogated.

These multiple-block polydispersity studies would be of interest for at least several reasons. First, polydispersity may stabilize morphologies that are not formed by the monodisperse materials. For instance, Listak et al. recently reported that polydispersity stabilized the typically metastable[11, 12] hexagonally–perforated lamellar mesostructure in poly(styrene–*b*–methyl acrylate) diblock copolymers.[13] It is possible that multiple-block polydispersity could drive the formation of new, technologically useful morphologies in ISO materials. Second, these materials would have an increased amount of molecular-level disorder. It would be interesting to see if this increased disorder would be accommodated by a single well-ordered mesostructure, or if the specimens would macrophase-separate[14] into coexisting domains.

7.4 Alternative Pentablock Terpolymer Systems

Nanoporous materials have been prepared from a wide variety of ordered block copolymer mesostructures by the chemical degradation and removal of one of the domains.[15] These nanoporous morphologies could find utility in membrane applications. For instance, plastic matrices with cylindrical nanopores have been

employed as ultrafiltration membranes for water purification.[16, 17] These anisotropic hexagonally packed cylindrical mesostructures may, however, require costly and/or time consuming alignment procedures to minimize pore dead ends and maximize flux through the membrane. Multiply continuous network morphologies, in contrast, have percolating domains that are not likely to terminate at grain boundaries, making them particularly attractive candidates for membrane applications. Mechanical strength is another important attribute for membranes, as macroscopic cracks would decrease membrane selectivity and separation performance.

The O^{70}-forming OSISO(0.13) sample has both percolating domains and mechanical strength. In principle, the PEO domains can be degraded and removed using strong acid to yield a nanoporous material,[18] making OSISO(0.13) a potential candidate for membrane applications. We attempted to degrade and remove the PEO from sample OSISO(0.13) by submerging a compression molded piece of the material in concentrated hydroiodic acid (HI) at 50 °C for two days. This sample turned dark purple or black and did not readily dissolve in chloroform for ^{1}H NMR analysis, suggesting some of the PI chains had crosslinked. An extensive amount of crosslinking could adversely impact mechanical toughness by transforming the rubbery PI domains into brittle material. Some of the HI-treated OSISO(0.13) specimen did dissolve in chloroform following an overnight soak. ^{1}H NMR analysis of this material revealed that the PEO chains had not degraded, possibly because the PEO domains were not actually continuous in the OSISO(0.13) material. The hydrophobicity of the PI chains may have also played a role by limiting the wetting of the potential channels by the HI solution.[19] The ^{1}H NMR experiments were also consistent with some of the PI segments having

crosslinked, as the relative intensity of the characteristic PI peaks in the ^{1}H NMR spectrum decreased following the HI treatment. In any event, nanoporous SIS would not be an ideal membrane material, even if the PEO domains were removed, because the unsaturated PI domains can degrade over time in the presence of oxygen. In the following sections, we describe two alternative block terpolymer systems that could form precursors to mechanically robust nanoporous networks that do not contain unsaturated polydiene domains and thus should offer enhanced chemical stability.

Poly(isoprene-*b*-styrene-*b*-ethylene oxide-*b*-styrene-*b*-isoprene) (ISOSI) Pentablock Terpolymers. ISOSI pentablock terpolymers contain the same block sequence as the ISO and OSISO samples, and would be expected to form the same multiply continuous network morphologies as those previously investigated materials. The glassy-crystalline-glassy poly(styrene-*b*-ethylene oxide-*b*-styrene) (SOS) core would impart mechanical toughness, and the terminal PI chains can in principle be degraded using ozonolysis. ISOSI pentablocks can be prepared by coupling living ISO triblocks through the oxanion using α,α'-dibromo-*p*-xylene; this reaction is summarized schematically in Figure 7.1. We used this scheme to prepare three ISOSI pentablock samples, and the characterization data obtained from these specimens are provided in Table 7.1. Prior to the addition of the α,α'-dibromo-*p*-xylene during these syntheses, some of the reaction solution was cannulated out of the reactor and into a flask containing degassed methanol; this ISO triblock was subsequently used to evaluate the coupling efficiency. The α,α'-dibromo-*p*-xylene was dissolved in tetrahydrofuran (THF) that had been purified by passage through activated alumina columns and subsequent

stirring with *n*-butyllithium overnight. This coupling solution was poured into a burette and slowly added dropwise to the reactor (through an airlock) over the course of ~2 hours to maintain a high ratio of living oxanions to α,α'-dibromo-*p*-xylene and maximize coupling. (Slower addition times may lead to even higher coupling efficiencies than those reported in Table 7.1.) Size exclusion chromatography (SEC) analyses revealed that this protocol yielded ISOSI materials that were approximately 50-60% coupled; the chromatograms are provided in Figure 7.2.

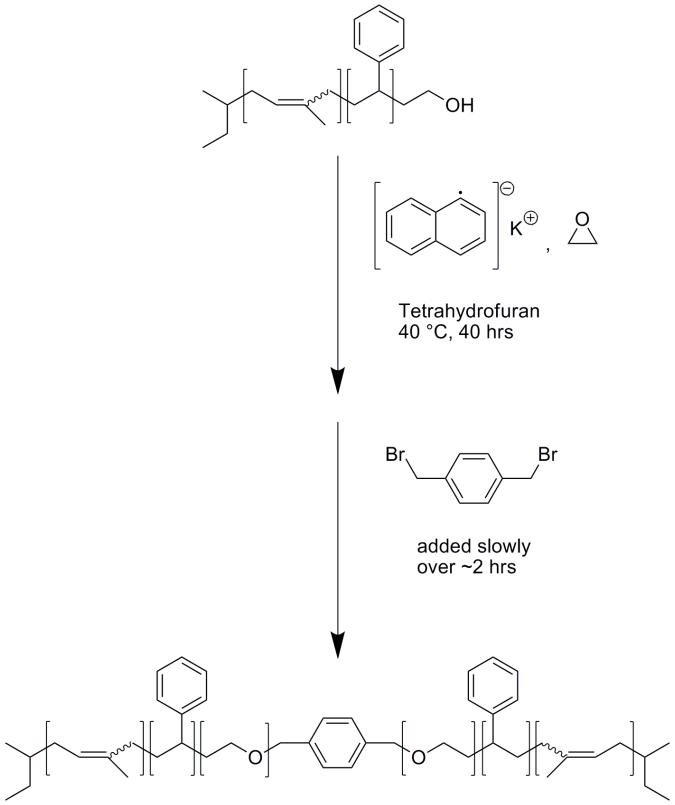

Figure 7.1. Reaction scheme for coupling ISO triblocks to make ISOSI pentablocks.

Table 7.1. ISOSI Characterization Data

Polymer	f_I[a]	f_S[a]	f_O[a]	M_n (kDa)	N[b]	M_w/M_n[c]	Fraction Coupled[d]	Lattice Dimensions (nm)[e]	Morphology[f]
ISOSI(0.16)	0.41	0.43	0.16	25.2	383	1.25	0.6	15.9	Q^{230} / O^{70} [g]
ISOSI(0.20)	0.39	0.41	0.20	26.7	402	1.26	0.6	16.6	Q^{230} / O^{70} [g]
ISOSI(0.27)	0.35	0.38	0.27	29.6	440	1.25	0.5	0.258, 0.578, 73.4	O^{70}

[a] Volume fractions are calculated from published density values at 140 °C (ρ_I = 0.830, ρ_S = 0.969, ρ_O = 1.064 g/cm^3).[20] [b] Based on a segment reference volume of 118 Å^3. [c] Measured using SEC at 30 °C with THF as the eluent. The peak that was measured included both the coupled ISOSI pentablock and unreacted ISO triblock. [d] Computed by taking the ratio of the amplitude of the ISOSI SEC response to the sum of the amplitudes of the ISOSI and ISO SEC responses. [e] Lattice dimensions are obtained from SAXS data and are reported at 120 °C. The lattice dimensions listed for O^{70} correspond to *a/c*, *b/c*, and *c*. [f] Determined using SAXS. [g] Bragg peaks characteristic of both Q^{230} and O^{70} are identified at 120 ºC; the intensities of the Q^{230} peaks are higher and the listed lattice parameters are for Q^{230}.

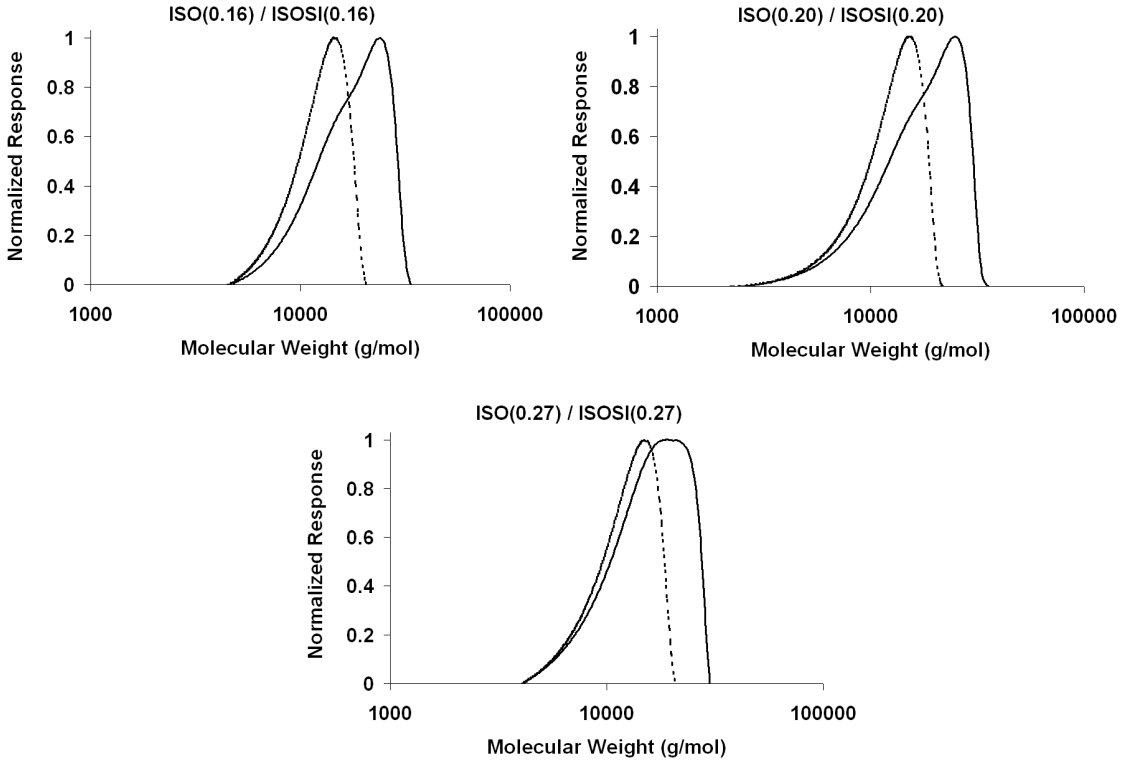

Figure 7.2. SEC chromatograms of the ISOSI(0.16), ISOSI(0.20), and ISOSI(0.27) pentablock terpolymers (solid curves) and the respective uncoupled ISO triblock terpolymers (dashed curves). The experiments were performed at 30 °C using THF as the eluent, and the abscissa values are calibrated to PS.

The melt-phase morphologies of the ISOSI pentablock samples were interrogated using synchrotron SAXS. The samples were first annealed at 250 °C for five minutes in an effort to erase effects associated with thermal history and were then annealed for five minutes at 120 °C before data were acquired; these data are provided in Figure 7.3. The Bragg pattern for ISOSI(0.27) is indexed to O^{70}. The Bragg patterns for specimens ISOSI(0.16) and ISOSI(0.20), meanwhile, contain reflections that are consistent with

multiple coexisting morphologies. Many of the peaks are consistent with Q^{230}, and these reflections are marked in both Bragg patterns with vertical lines. The remaining low intensity peaks appear to be consistent with the O^{70} network, and these peaks are marked with ♦. The coexistence in these specimens is likely metastable, given the short five minute annealing times. A film of the ISOSI(0.20) material was also prepared by solvent casting. The polymer was dissolved in dichloromethane (10 wt% polymer), the solution was poured into the bottom of a glass petri dish, and the dish was placed in a fume hood overnight to allow the solvent to evaporate. The polymer film was floated off of the glass surface by submerging the petri dish in a mixture of water and methanol and subsequently dried under dynamic vacuum. The film was then placed in the X-ray beam at room temperature with the film surface oriented normal to the beam; the SAXS data from this experiment are provided in Figure 7.3. This Bragg pattern is clearly different from that obtained from the melt-phase ISOSI(0.20) sample, and the first three peaks in Figure 7.3 are indexed to a lamellar mesostructure. The broad first peak is consistent with some distortions in the lamellar morphology.

The mechanical properties of these polymer samples were not quantified using uniaxial tensile testing. Qualitatively, however, these ISOSI materials are tougher than comparable ISO materials (such as the ISO specimen investigated in Chapter 5). We were able to bend and twist films of these materials without fracturing them. This qualitative analysis suggests that the SOS core in the ISOSI architecture may provide mechanical strength. We attempted to degrade the terminal PI chains using ozonolysis. The solvent cast ISOSI(0.20) film was sandwiched between two Teflon sheets. This sandwich was tied to a metal disc using copper wire and the entire apparatus was

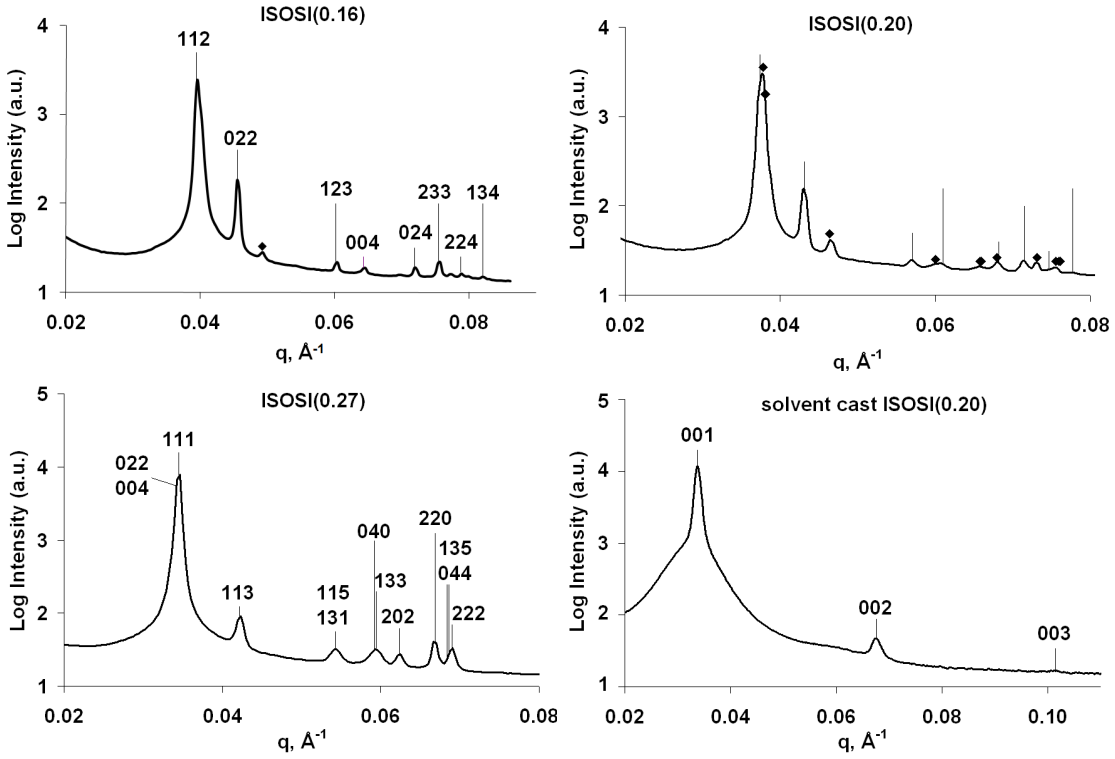

Figure 7.3. Synchrotron SAXS data acquired at 120 °C from melt-phase samples of ISOSI(0.16), ISOSI(0.20), and ISOSI(0.27) and at room temperature from a film of OSISO(0.20) that was solvent cast from a 10 wt% dichloromethane solution. The melt-phase samples were first annealed for five minutes at 250 °C and then annealed for five minutes at 120 °C before data were acquired. The vertical lines in the ISOSI(0.16) and ISOSI(0.20) data mark the allowed reflections for Q^{230}, while the peaks marked with ♦ are the allowed reflections for O^{70}. These two samples apparently contain both of the Q^{230} and O^{70} mesostructures, a configuration that is likely metastable, given the short five minute annealing times. The ISOSI(0.20) film was cast from a 10 wt % dichloromethane solution overnight and then dried under dynamic vacuum prior to X-ray exposure. The allowed peaks for the lamellar morphology are marked in this Bragg pattern.

submerged in methanol. The methanol was cooled to -78 °C using dry ice and ozone was bubbled through the solvent at a rate of 1 mL/min for ~20 hours. The film was then soaked in fresh methanol and dried overnight under dynamic vacuum. The mass loss was consistent with a loss of ~30% of the PI chains, providing some evidence that this strategy may yield nanoporous materials.

Poly(ethylene oxide-*b*-cyclohexylethylene-*b*-(ethylene-*alt*-propylene)-*b*-cyclohexylethylene-*b*-ethylene oxide) (OCPCO) Pentablock Terpolymers. OCPCO pentablock terpolymers, like OSISO materials, are comprised of a tough, glassy-rubbery-glassy core (CPC)[21] and potentially degradable[18] PEO termini. These materials can be made using a synthetic protocol analogous to that used for OSISO pentablock terpolymers. The process would begin with the preparation of a HO-SIS-OH triblock copolymer by living anionic polymerization initiated with TIPSOPrLi. These materials could then be hydrogenated to yield HO-CPC-OH, and PEO could be polymerized from each hydroxyl group using the established protocol[22] described in Chapters 5 and 6. (Note that other degradable blocks, such as polylactide, could be grown from the terminal hydroxyl groups in place of the PEO.) Preservation of the hydroxyl groups requires the careful selection of a hydrogenation catalyst. The widely used Dow Hydrogenation Catalyst (DHC) consists of Pt and Re supported on silica. The Re is reportedly present because it reacts with methanol that would otherwise poison the catalyst, and it may react with hydroxyl groups by a similar mechanism.[23] While DHC without Re may catalyze hydrogenation of the HO-SIS-OH and preserve hydroxyl groups, we pursued an alternative procedure using Pd on $CaCO_3$ as the catalyst.

Initial efforts focused on minimizing the amount of Pd catalyst required to hydrogenate a symmetric HO-SIS-OH triblock. The Pd catalyst was loaded into the high pressure reactor and the reactor was evacuated using a vacuum pump. The catalyst was baked at 100 °C under vacuum for ~1 hour and then exposed to ~100 psi of hydrogen for ~1 hour to activate the Pd. *NOTE: The reactor was then flushed with argon prior to transfer of the polymer, as exposing the activated catalyst and hydrogen to oxygen could result in an explosion.* The HO-SIS-OH polymer was dissolved in cyclohexane (~8 g in 150 mL of cyclohexane) and the solution was sparged by bubbling argon through it for 15 minutes. This polymer solution was then transferred to the reactor through a tube without exposing it to oxygen, and the reactor was pressurized with hydrogen (500 psi). The solution was heated to 120 °C, stirred, and allowed to react with the hydrogen for ~24 hours. The reactor was then cooled to 60 °C and vented, and the reaction solution was filtered to remove the Pd catalyst. The hydrogenated polymer was recovered by precipitation in methanol.

The efficacies of several Pd on $CaCO_3$ to polymer weight ratios (w_{Pd} / w_{SIS}) were investigated. When w_{Pd} / w_{SIS} = 0.2, essentially all of the PI chains hydrogenated, but a significant fraction of the PS (~50%) had not reacted. A ratio of 1, meanwhile, catalyzed the hydrogenation of nearly all of the PI and PS segments, with more than 95% of the PS converted into poly(cyclohexylethylene). The ^{1}H NMR spectra of the resulting polymer contained a peak at 3.6 ppm, consistent with a preservation of the terminal hydroxyl groups. This Pd-catalyzed hydrogenation procedure could be used to prepare various hydroxy-functionalized block copolymer containing poly(cyclohexylethylene) chains.

7.5 References

(1) Bailey, T. S.; Hardy, C. M.; Epps, T. H., III; Bates, F. S. *Macromolecules* **2002**, *35*, 7007-7017.

(2) Epps, T. H., III; Cochran, E. W.; Hardy, C. M.; Bailey, T. S.; Waletzko, R. S.; Bates, F. S. *Macromolecules* **2004**, *37*, 7085-7088.

(3) Epps, T. H., III; Cochran, E. W.; Bailey, T. S.; Waletzko, R. S.; Hardy, C. M.; Bates, F. S. *Macromolecules* **2004**, *37*, 8325-8341.

(4) Braunecker, W. A.; Matyjaszewski, K. *Prog. Polym. Sci.* **2007**, *32*, 93-146.

(5) Leibler, L. *Prog. Polym. Sci.* **2005**, *30*, 898-914.

(6) Hillmyer, M. A. *J. Polym. Sci., Part B* **2007**, *45*, 3249-3251.

(7) Phatak, A.; Lim, L. S.; Reaves, C. K.; Bates, F. S. *Macromolecules* **2006**, *39*, 6221-6228.

(8) Qiao, L.; Leibig, C.; Hahn, S. F.; Winey, K. I. *Ind. Eng. Chem. Res.* **2006**, *45*, 5598-5602.

(9) Lynd, N. A.; Meuler, A. J.; Hillmyer, M. A. *Prog. Polym. Sci.* **2008**, *33*, 875-893.

(10) Ruzette, A.; Tence-Girault, S.; Leibler, L.; Chauvin, F.; Bertin, D.; Guerret, O.; Gerard, P. *Macromolecules* **2006**, *39*, 5804-5814.

(11) Hajduk, D. A.; Takenouchi, H.; Hillmyer, M. A.; Bates, F. S.; Vigild, M. E.; Almdal, K. *Macromolecules* **1997**, *30*, 3788-3795.

(12) Cochran, E. W.; Garcia-Cervera, C. J.; Fredrickson, G. H. *Macromolecules* **2006**, *39*, 2449-2451.

(13) Listak, J.; Jakubowski, W.; Mueller, L.; Plichta, A.; Matyjaszewski, K.; Bockstaller, M. R. *Macromolecules* **2008**, *41*, 5919-5927.

(14) Matsen, M. W. *Phys. Rev. Lett.* **2007**, *99*, 148304.

(15) Hillmyer, M. A. *Adv. Polym. Sci.* **2005**, *190*, 137-181.

(16) Yang, S. Y.; Ryu, I.; Kim, H. Y.; Kim, J. K.; Jang, S. K.; Russell, T. P. *Adv. Mater.* **2006**, *18*, 709-712.

(17) Phillip, W. A.; Rzayev, J.; Hillmyer, M. A.; Cussler, E. L. *J. Membr. Sci.* **2006**, *286*, 144-152.

(18) Mao, H.; Hillmyer, M. A. *Macromolecules* **2005**, *38*, 4038-4039.

(19) Bailey, T. S.; Rzayev, J.; Hillmyer, M. A. *Macromolecules* **2006**, *39*, 8772-8781.

(20) Fetters, L. J.; Lohse, D. J.; Richter, D.; Witten, T. A.; Zirkel, A. *Macromolecules* **1994**, *27*, 4639-4647.

(21) Lim, L. S.; Harada, T.; Hillmyer, M. A.; Bates, F. S. *Macromolecules* **2004**, *37*, 5847-5850.

(22) Hillmyer, M. A.; Bates, F. S. *Macromolecules* **1996**, *29*, 6994-7002.

(23) Hahn, S. F. ACS Spring 2008 Conference. “Heterogeneous catalytic process for the hydrogenation of styrene-butadiene block copolymers.”

8

Appendices

8.1 Performing a "No-D" ^{1}H NMR Experiment

The TIPSOPrLi reagent is both air and moisture sensitive, and reactive towards chlorinated species such as chloroform. This reactivity hinders the interrogation of the chemical structure using the standard ^{1}H NMR spectroscopy methods that include dissolution in a deuterated solvent. Fortunately, a deuterated solvent is not required for ^{1}H NMR experiments and the TIPSOPrLi could be analyzed in its native hydrogenated cyclohexane solvent.[1, 2] This section will describe this "No-Deuterium (No-D)" ^{1}H NMR methodology. The sample preparation is relatively straightforward. The TIPSOPrLi initiator is stored in the glovebox under an argon atmosphere. The NMR tube (with the glass quality required for use in the "hands-on" instruments) is transferred into the glovebox and a small volume of TIPSOPrLi solution is transferred into the tube using a syringe. A known mass of 1,5-cyclooctadiene (COD, 4H at δ = 5.58 ppm, 8H at δ = 2.36 ppm) may be added to the NMR tube as an internal standard for determination of the analyte concentration. The NMR tube is then sealed with a standard rubber cap and agitated to homogenize the solution. The tube should not be removed from the glovebox until immediately prior to ^{1}HMR analysis in order to limit reaction of the TIPSOPrLi with ambient oxygen and/or water.

The “No-D” experiment must be run on the “hands-on” spectrometers because it requires operating the machine in the unlocked mode. Modern spectrometers do not suffer from significant magnet drift, and narrow lines may be obtained even in the unlocked mode.[1] (The instrument magnet should always be locked onto a standard following completion of the “No-D” experiment.) There are numerous strategies for shimming the proton probe to a “No-D” sample.[1] We preferred shimming the sample using the free-induction decay (FID). The details of this procedure are as follows. First, turn off the lock on the spectrometer and spin the sample. Acquire a single scan spectrum and then enter the interactive acquisition display process (<acqi>) to allow real-time observation of the FID. Select the FID button and change the gain until the FID level is between 500 and 1000, a magnitude that facilitates the observation of small changes in the FID level. Now adjust the shims and allow the FID level to stabilize following each adjustment. The two shims should be iteratively tuned to maximize the FID level. Depending on the initial quality of the shims, the gain may have to be lowered during the shimming process to keep the FID level within the 500-1000 range. Once the shims are optimized, exit the <acqi> mode and acquire the desired spectrum. It is advisable to first collect a spectrum using short acquisition times to verify that the shim settings yield spectra with symmetric peaks. We typically acquired the final desired spectra using 8-16 scans, an acquisition time of 25 s, and a pulse repetition delay of 35 s. This protocol always led to the expected relative COD peak integrals of 1.00:2.00 ± 0.04 and was therefore deemed sufficient (i.e., it provided enough time for the magnetic moments to relax).[2] Several examples of “No-D” ^{1}H NMR spectra were provided in Figures 4.1 and 4.2.

References

(1) Hoye, T. R.; Eklov, B. M.; Ryba, T. D.; Voloshin, M.; Yao, L. J. *Org. Lett.* **2004**, *6*, 953-956.

(2) Hoye, T. R.; Eklov, B. M.; Voloshin, M. *Org. Lett.* **2004**, *6*, 2567-2570.

8.2 Indexing O^{70} SAXS Data

As was discussed earlier, the Bragg reflections for a mesostructure with an orthorhombic unit cell are given by:

$$q_{hkl} = 2\pi\sqrt{\frac{h^2}{a^2}+\frac{k^2}{b^2}+\frac{l^2}{c^2}} \tag{8-1}$$

Since these q_{hkl} values are a function of the *a*, *b*, and *c* lattice parameters, the allowed peaks are not located at constant relative positions (i.e., the allowed q_{hkl} / q_{001} ratios are not constant). This feature makes the identification of morphologies with orthorhombic symmetries difficult, as a given orthorhombic lattice may accommodate many combinations of relative Bragg positions in scattering data. All of the O^{70} morphologies that have been described in the literature[1-13] have lattice dimensions with relative magnitudes of approximately $1:2:2\sqrt{3}$; these exact ratios yield coincident 111, 022, and 004 reflections and a specific set of allowed q_{hkl} / q_{001} ratios. Even small deviations from these precise values, however, as are common in experimental materials,[2-10] can result in significant changes in the allowed q_{hkl} / q_{001} ratios, particularly for the higher *q* values detected in experiments.

The SAXS data obtained from specimen OSISO(0.13) are reproduced in Figure 8.1. A least-squares fit of the O^{70} lattice to this scattering data is obtained using the following procedure:

1) The first, second, and third peaks are assigned to the 111, 113, and 131/115 reflections (i.e., q_{111} = 0.0339 $Å^{-1}$, q_{113} = 0.0418 $Å^{-1}$, and $q_{115} = q_{131}$ = 0.0540 $Å^{-1}$).

2) These four *hkl* scattering vectors are computed for arbitrary values of *a*, *b*, and *c* using Equation 8-1.
3) The differences between the assigned experimental peaks and the computed q_{hkl} values are squared and then summed.
4) This sum of squares is minimized by varying the *a*, *b*, and *c* values, and thus the computed allowed q_{hkl} reflections. This minimization can be done using, for example, the Solver function in Microsoft Excel.
5) These new *a*, *b*, and *c* values are used to compute additional *hkl* scattering vectors. The *a*, *b*, and *c* parameters are then refined by fitting these higher q_{hkl} values to the remaining experimental SAXS peaks using the above steps. The first three peaks are fit before the higher *q* reflections because it is not possible to know, *a priori*, which allowed q_{hkl} values correspond to which experimental peaks; the *a*, *b*, and *c* values obtained from the fits to the first three peaks provide some guidance.

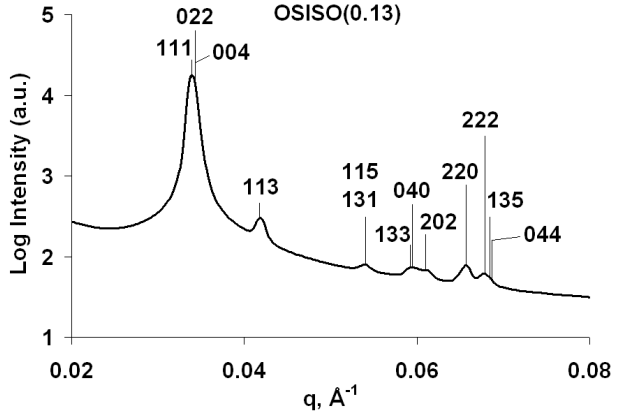

Figure 8.1. Synchrotron SAXS data acquired from sample OSISO(0.13) at 160 °C. The allowed reflections for O^{70} are marked.

References

(1) Bailey, T. S.; Hardy, C. M.; Epps, T. H., III; Bates, F. S. *Macromolecules* **2002**, *35*, 7007-7017.

(2) Epps, T. H., III; Cochran, E. W.; Hardy, C. M.; Bailey, T. S.; Waletzko, R. S.; Bates, F. S. *Macromolecules* **2004**, *37*, 7085-7088.

(3) Epps, T. H., III; Cochran, E. W.; Bailey, T. S.; Waletzko, R. S.; Hardy, C. M.; Bates, F. S. *Macromolecules* **2004**, *37*, 8325-8341.

(4) Epps, T. H., III; Chatterjee, J.; Bates, F. S. *Macromolecules* **2005**, *38*, 8775-8784.

(5) Epps, T. H., III; Bates, F. S. *Macromolecules* **2006**, *39*, 2676-2682.

(6) Chatterjee, J.; Jain, S.; Bates, F. S. *Macromolecules* **2007**, *40*, 2882-2896.

(7) Meuler, A. J.; Fleury, G.; Hillmyer, M. A.; Bates, F. S. *Macromolecules* **2008**, *41*, 5809-5817.

(8) Meuler, A. J.; Ellison, C. J.; Hillmyer, M. A.; Bates, F. S. *Macromolecules* **2008**, *41*, 6272-6275.

(9) Takenaka, M.; Wakada, T.; Akasaka, S.; Nishitsuji, S.; Saijo, K.; Shimizu, H.; Kim, M. I.; Hasegawa, H. *Macromolecules* **2007**, *40*, 4399-4402.

(10) Kim, M. I.; Wakada, T.; Akasaka, S.; Nishitsuji, S.; Saijo, K.; Hasegawa, H.; Ito, K.; Takenaka, M. *Macromolecules* **2008**, *41*, 7667-7670.

(11) Ranjan, A.; Morse, D. C. *Phys. Rev. E* **2006**, *74*, 011803.

(12) Tyler, C. A.; Morse, D. C. *Phys. Rev. Lett.* **2005**, *94*, 208302.

(13) Tyler, C. A.; Qin, J.; Bates, F. S.; Morse, D. C. *Macromolecules* **2007**, *40*, 4654-4668.

8.3 Additional OSISO Samples

Fifteen OSISO pentablock terpolymers that are not summarized in Table 5.1 were prepared during the course of this research program from seven different HO-SIS-OH triblock copolymers: three synthesized using 3-*tert*-butyldimethylsilyloxy-1-propyllithium (*t*BDMSOPrLi) and four prepared using 3-triisopropylsilyloxy-1-propyllithium (TIPSOPrLi). The molecular characterization data obtained from these 15 OSISO samples are provided in Table 8.1. The first letter in each polymer name is either "*t*" or "T"; a "*t*-" indicates the HO-SIS-OH triblock precursor was prepared using *t*BDMSOPrLi and a "T-" denotes HO-SIS-OH triblock precursors synthesized using TIPSOPrLi. The number in the OSISO nomenclature identifies a specific parent HO-SIS-OH triblock. When multiple OSISO samples were prepared from the same HO-SIS-OH triblock, they are labeled using letters. For instance, samples T-OSISO8A and T-OSISO8B were both prepared from the same HO-SIS-OH parent. Four of the OSISO specimens were prepared in pairs using a single reaction vessel. Two reactors were set up following the standard procedure described in Section 5.2 and one burette of ethylene oxide was added to each reactor and polymerized. About half of each reaction solution was then cannulated out of the reaction vessels and into sparged and stirring acidic methanol; these terminated polymers are samples *t*-OSISO4A and *t*-OSISO6A. A second burette of ethylene oxide was added to each reactor and polymerized before the reactions were terminated; these polymers are samples *t*-OSISO4B and *t*-OSISO6B.

Table 8.1. Additional OSISO Characterization Data

Polymer	f_I [a]	f_S [a]	f_O [a]	M_n (kDa)	N [b]	1st PS Block M_w/M_n [c]	SIS M_w/M_n [c]	M_w/M_n [c]	Lattice Dimensions (nm) [d]	Morphology [e]	T_{ODT} [f] (°C)
t-OSISO1	0.46	0.46	0.08	49.2	758	1.33	1.07	1.06	26.4	LAM	> 250
t-OSISO4A	0.43	0.43	0.14	23.3	356	1.33	1.24	1.28	16.1	LAM	147
t-OSISO4B	0.35	0.37	0.28	28.4	423	1.33	1.24	1.47	17.5	LAM	221
t-OSISO6A	0.46	0.47	0.07	35.7	551	1.29	1.09	1.34	20.5	LAM	233
t-OSISO6B	0.39	0.40	0.21	42.9	646	1.29	1.09	1.45	23.4	LAM	> 250
T-OSISO1B	0.49	0.49	0.02	26.1	408	1.13	1.05	1.14	15.9	LAM	< 150
T-OSISO1C	0.47	0.48	0.05	27.0	419	1.13	1.05	1.13	16.7	LAM	< 175
T-OSISO1F	0.46	0.47	0.07	27.6	428	1.13	1.05	1.06	17.2	LAM	180
T-OSISO5A	0.47	0.46	0.07	66.0	1020	1.07	1.04		31.0 (120 °C)	LAM	> 250
T-OSISO5B	0.45	0.44	0.11	69.7	1069	1.07	1.04		33.5	?	> 250
T-OSISO5D	0.31	0.31	0.38	103.7	1519	1.07	1.04		47.3	?	> 250
T-OSISO7A	0.34	0.34	0.32	57.3	847	1.08	1.06		30.9	LAM	> 250
T-OSISO7B	0.38	0.37	0.25	50.6	759	1.08	1.06		28.6	LAM	> 250
T-OSISO8A	0.30	0.45	0.25	36.9	546	1.10	1.05		22.6	LAM_3	> 250
T-OSISO8B	0.31	0.47	0.22	35.6	529	1.10	1.05		20.2	Q[214]	> 250

[a] Volume fractions are calculated from published density values at 140 °C (ρ_I = 0.830, ρ_S = 0.969, ρ_O = 1.064 g/cm^3).[1] [b] Based on a segment reference volume of 118 Å^3. [c] Measured using a room temperature, THF-eluting SEC calibrated with PS standards. The "1st PS Block" refers to the first PS block prepared during SIS triblock synthesis; some of the reaction solution was extracted from the reactor prior to isoprene addition and the PS polymer therein was characterized. [d] Lattice dimensions are obtained from SAXS data and are reported at 100 °C unless otherwise noted in parentheses. The lattice dimensions listed for samples T-OSISO5B and T-OSISO5D correspond to the length scales associated with the principal scattering vectors. [e] Assigned using SAXS data. [f] Precise temperatures measured using DMS and temperature ranges obtained from SAXS data.

The mesostructures of all 15 of these OSISO specimens were interrogated using SAXS, and some were also probed using DMS. Representative SAXS and DMS data are provided on the following pages. A discussion of some notable features of these OSISO materials follows the presentation of the SAXS and DMS data.

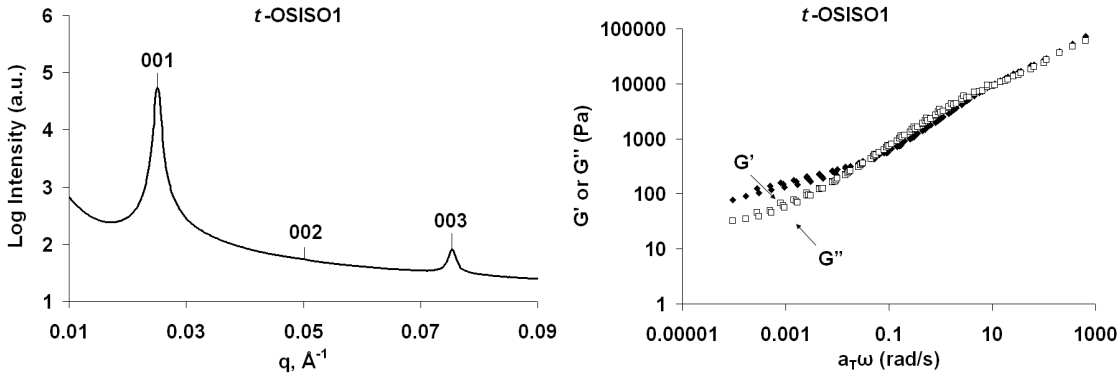

Figure 8.2. Synchrotron SAXS (left) and DMS (right) data obtained from sample *t*-OSISO1. The SAXS data were acquired at 200 °C following five minute anneals at 250 °C and 200 °C. Samples for DMS analysis were first annealed for ten minutes at 250 °C and then sequentially at target temperatures for ten minutes. The plotted DMS data contain isothermal frequency responses that were obtained at 125 °C, 150 °C, 175 °C, 200 °C, 225 °C, and 250 °C and shifted to a reference temperature of 150 °C using time-temperature superposition. The Bragg pattern is indexed to a lamellar morphology and the decrease in *G'* with decreasing ω is consistent with this mesostructural assignment.

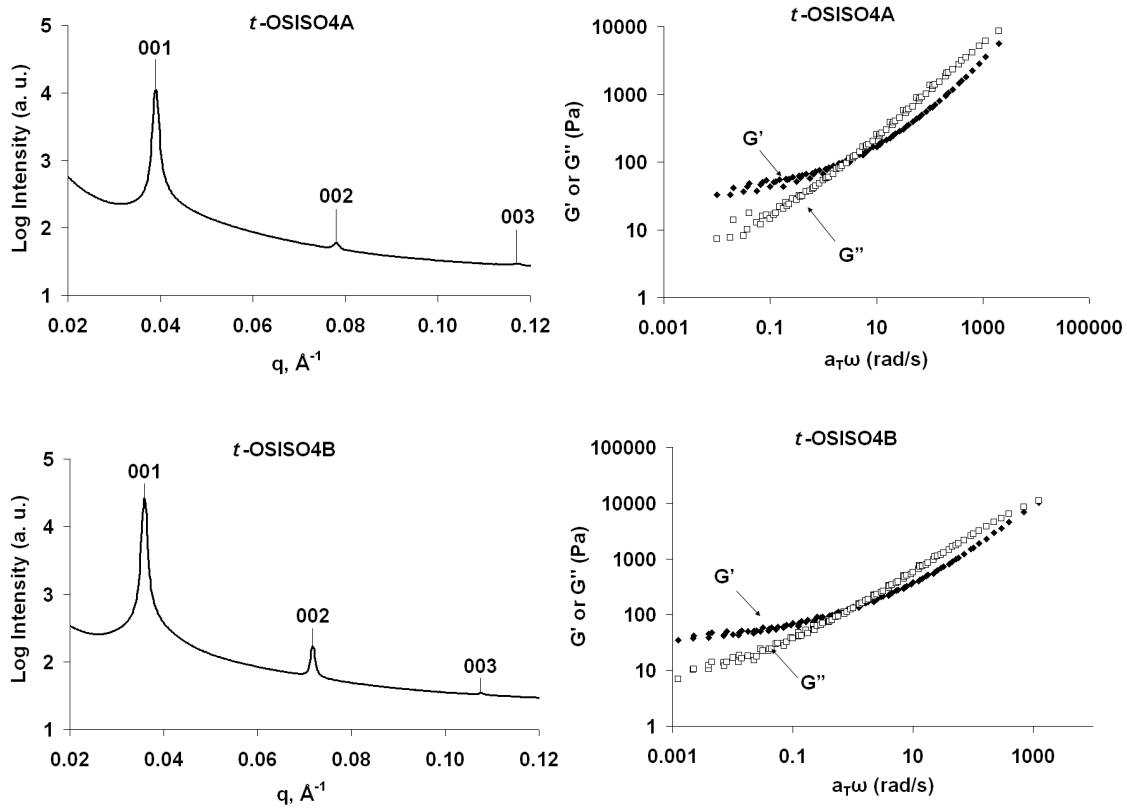

Figure 8.3. Synchrotron SAXS (left) and DMS (right) data obtained from samples *t*-OSISO4A and *t*-OSISO4B. The SAXS data were acquired at 100 °C following five minute anneals at 160 °C (250 °C for *t*-OSISO4B) and 100 °C. Samples for DMS analysis were first annealed for ten minutes at 160 °C (250 °C for *t*-OSISO4B) and then sequentially at target temperatures for ten minutes. The plotted DMS data contain isothermal frequency responses that were obtained at multiple temperatures and shifted to a reference temperature of 140 °C using time-temperature superposition. *t*-OSISO4A data were acquired at 100 °C, 110 °C, 120 °C, 130 °C, and 140 °C and *t*-OSISO4B data were obtained at 100 °C, 120 °C, 140 °C, 160 °C, 180 °C, and 200 °C. Both Bragg patterns are indexed to lamellar morphologies and the decreases in *G'* with decreasing ω are consistent with these mesostructural assignments.

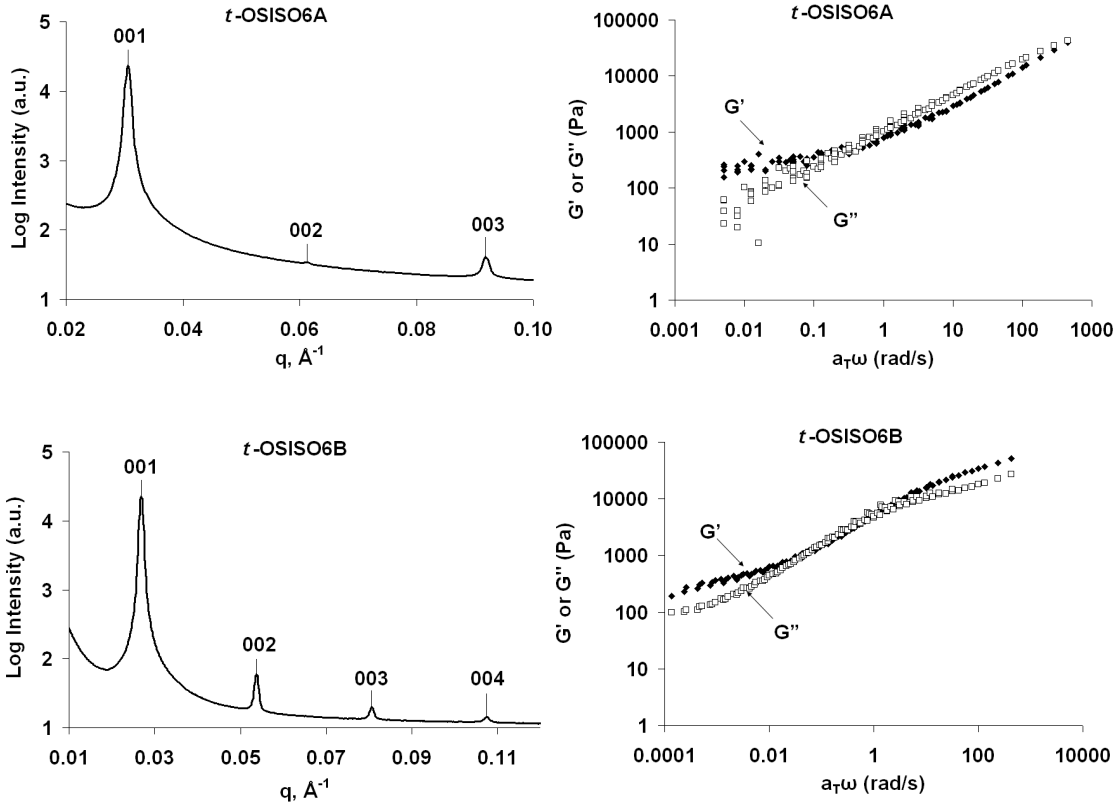

Figure 8.4. Synchrotron SAXS (left) and DMS (right) data obtained from samples *t*-OSISO6A and *t*-OSISO6B. The SAXS data were acquired at 100 °C following five minute anneals at 250 °C and 100 °C. Samples for DMS analysis were first annealed for ten minutes at 250 °C and then sequentially at target temperatures for ten minutes. The plotted DMS data contain isothermal frequency responses that were obtained at multiple temperatures and shifted to a reference temperature of 140 °C using time-temperature superposition. *t*-OSISO6A data were acquired at 120 °C, 140 °C, 160 °C, 180 °C, 200 °C, and 220 °C and *t*-OSISO6B data were obtained at 120 °C, 140 °C, 160 °C, 180 °C, 200 °C, 220 °C, and 240 °C. Both Bragg patterns are indexed to lamellar morphologies and the decreases in *G'* with decreasing ω are consistent with these mesostructural assignments.

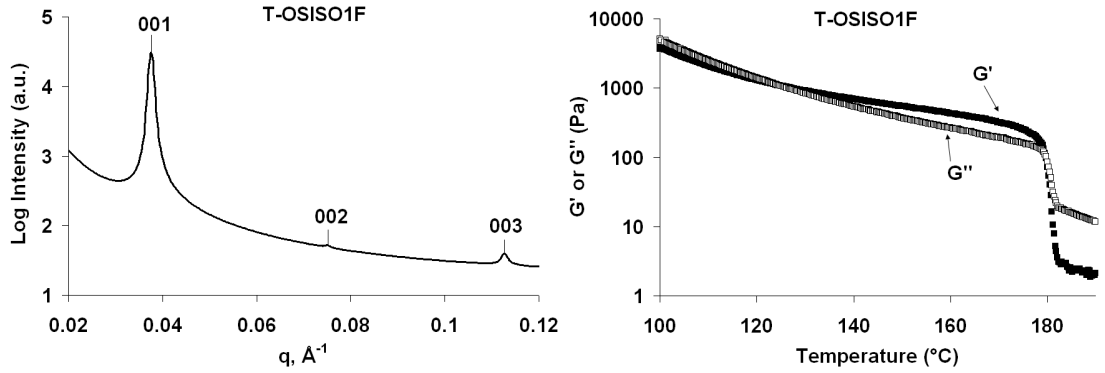

Figure 8.5. Synchrotron SAXS (left) and DMS (right) data obtained from sample T-OSISO1F. The SAXS data were acquired at 120 °C following five minute anneals at 200 °C and 120 °C and the Bragg pattern is indexed to a lamellar morphology. Similar SAXS data were acquired from samples T-OSISO1B and T-OSISO1C. The isochronal (ω = 1 rad/s) DMS data were obtained while heating the specimen at 1 °C/min following ten minute thermal anneals at 200 °C and 100 °C. These data are representative of the viscoelastic response associated with a single ordered morphology and disorder.

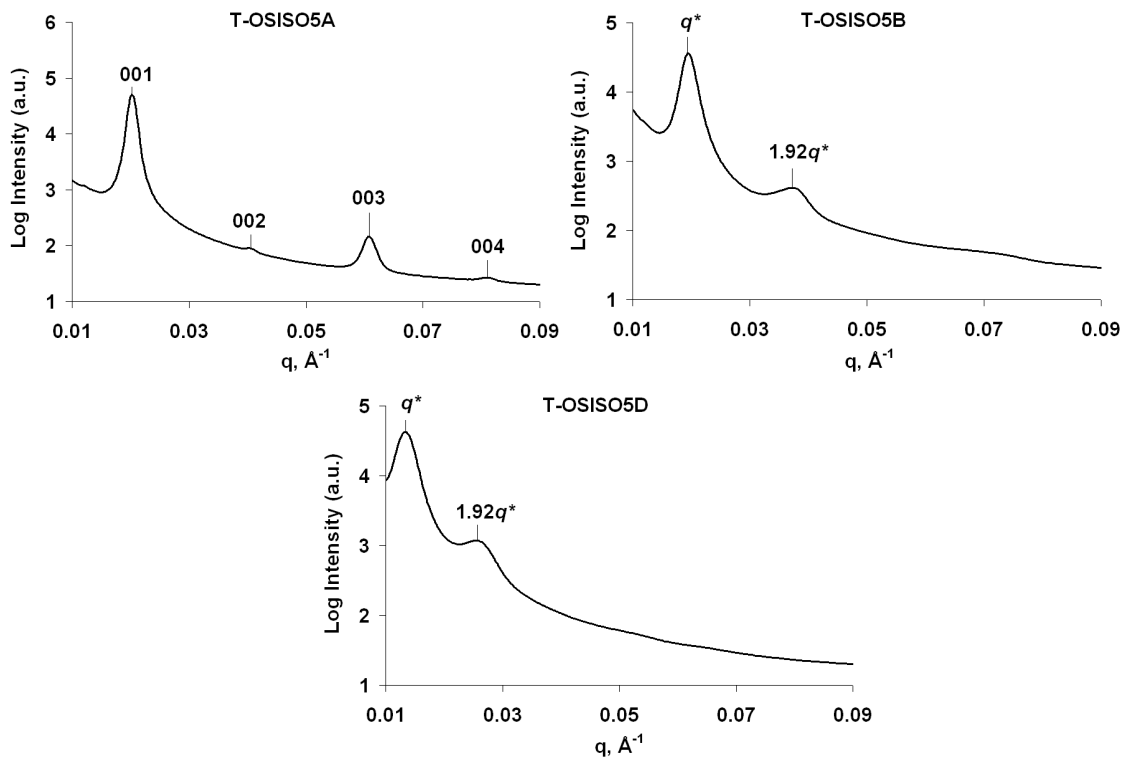

Figure 8.6. Synchrotron SAXS data acquired at 120 °C (T-OSISO5A) and 250 °C (T-OSISO5B and T-OSISO5D). All of the samples were first annealed for five minutes at 250 °C, and sample T-OSISO5A subsequently for five minutes at 120 °C, before data were acquired. The Bragg pattern from specimen T-OSISO5A is indexed to lamellae, while q^* and $1.92q^*$ are marked in the T-OSISO5B and T-OSISO5D data. Reflections at q^* and $1.92q^*$ were previously reported by Epps and Bates for a poorly ordered network morphology.[2]

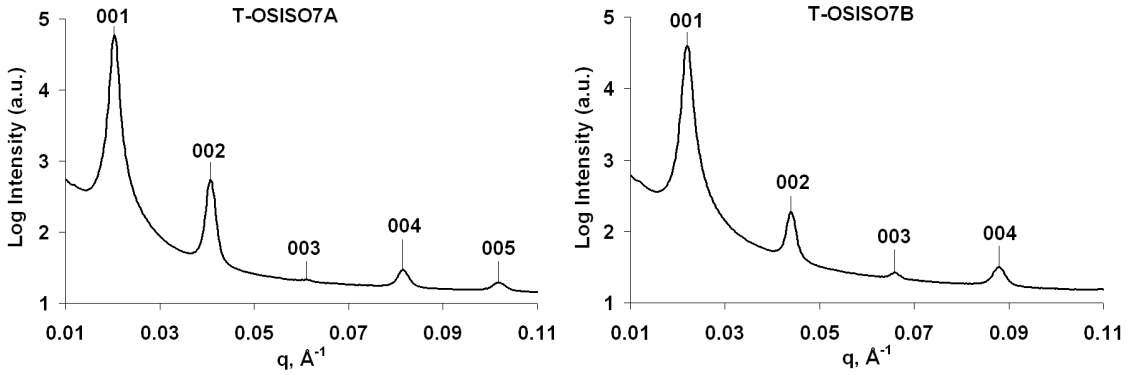

Figure 8.7. Synchrotron SAXS data acquired at 100 °C from samples T-OSISO7A and T-OSISO7B. Both specimens were annealed for five minutes at 250 °C and for five minutes at 100 °C prior to data acquisition. The allowed Bragg reflections for the lamellar mesostructure are marked in both plots.

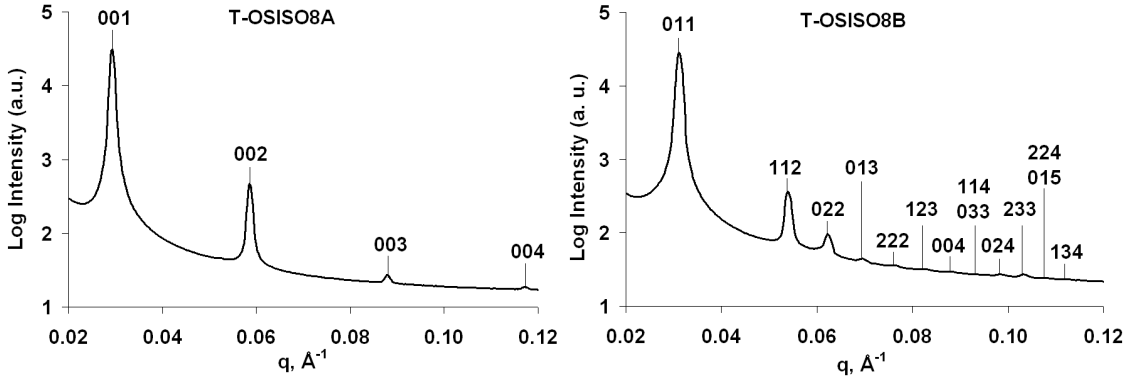

Figure 8.8. Synchrotron SAXS data acquired at 175 °C from samples T-OSISO8A and T-OSISO8B. Both specimens were annealed for 15 minutes at 250 °C and for 15 minutes at 175 °C prior to data acquisition. The peaks in the T-OSISO8A data are indexed to a lamellar morphology while the allowed Bragg reflections for the Q^{214} (alternating gyroid) mesostructure are labeled in the T-OSISO8B plot.

Samples *t*-OSISO4A and *t*-OSISO6B both have compositions within the O^{70} window ($f_I \approx f_S$ isopleth, $0.13 < f_O < 0.24$) that was previously established[3-5] for ISO triblock terpolymers. Neither of these materials adopt a network morphology, however. The *t*-OSISO4A and *t*-OSISO6B specimens were prepared before the OSISO pentablocks summarized in Table 5.1, and, at the time, we posited that at least two factors could account for the lack of network morphologies: (i) the higher order pentablock architecture and (ii) the polydispersity of the PS chains. The subsequent identification of O^{70} in specimen OSISO(.13) proved that the pentablock materials could form network mesostructures, and we undertook investigations of ISO triblock terpolymers that sought to validate or refute our hypothesis that the PS polydispersity was responsible for the formation of lamellae, and not a network morphology. These investigations are described in Chapter 6, and we demonstrate that network formation is sensitive to PS (and PEO) block polydispersity.

The highest molecular weight OSISO materials that we investigated were the T-OSISO5 samples. The decreased molecular diffusion that accompanies the increased molecular weight and segregation strength does not appear to significantly inhibit ordering in sample T-OSISO5A, as that specimen formed a well-ordered lamellar morphology (as indicated by four sharp, visible reflections in the SAXS data) with less than 10 minutes of thermal annealing. SAXS analysis indicates that polymers T-OSISO5B and T-OSISO5D did not form well-ordered mesostructures following thermal treatments as long as 20 minutes. These Bragg patterns are provided in Figure 8.6 and contain two broad peaks that are consistent with a lack of translational order. As was discussed in Section 5.4, Epps and Bates reported similar SAXS data

from strongly segregated ISO triblock terpolymers with compositions within the network window.[2] Their Bragg patterns, like those shown in Figure 8.6, contain two broad reflections with relative positions of q^* and $1.92q^*$. Additional TEM and SAXS analyses led Epps and Bates to conclude that their ISO samples had adopted a network mesostructure that lacked translational order. The lack of translational order was attributed to limited chain diffusion in triply periodic morphologies, as the strongly segregated ISO materials did form well-ordered lamellae.[2] It is possible that our T-OSISO5 materials also contain poorly ordered network morphologies, although DMS and TEM characterization would be required to make a more definitive statement. Formation of a poorly ordered network by specimen T-OSISO5B would be consistent with Epps and Bates' report,[2] as this sample has a composition within the established network window.[3-5] Sample T-OSISO5D, in contrast, would be expected to adopt lamellae. Given that Epps and Bates reported that the strongly segregated ISO materials formed well-ordered lamellae, it is not clear why specimen T-OSISO5D contained a structure that lacked translational order. There are several possible explanations. First, the T-OSISO5D sample had a higher molecular weight than the ISO materials investigated by Epps and Bates,[2] and kinetic limitations may be present in lamellae-forming ISO materials at these elevated molecular weights. Next, it is possible that segregation strength impacts the lamellar ordering kinetics in OSISO, but not ISO, materials, as additional constraints are placed on the chains by the pentablock architecture (e.g., the PI chains do not have dangling chain ends). Finally, it is possible that the location of the network window is a function of molecular weight and, although

unlikely, the equilibrium state of sample T-OSISO5D may not be a lamellar morphology.

Sample T-OSISO8B is the only one of the 15 OSISO pentablock terpolymers described in this Section that did not form lamellae. The Bragg pattern obtained from this specimen is provided Figure 8.8 and is indexed to the Q^{214} (alternating gyroid) network morphology. Epps and Cochran et al. previously identified Q^{214} in ISO materials with comparable compositions and segregation strengths,[4, 5] and the identification of Q^{214} in specimen T-OSISO8B provides additional evidence that the phase behaviors of ISO triblock and OSISO pentablock terpolymers are comparable.

References

(1) Fetters, L. J.; Lohse, D. J.; Richter, D.; Witten, T. A.; Zirkel, A. *Macromolecules* **1994**, *27*, 4639-4647.

(2) Epps, T. H., III; Bates, F. S. *Macromolecules* **2006**, *39*, 2676-2682.

(3) Bailey, T. S.; Hardy, C. M.; Epps, T. H., III; Bates, F. S. *Macromolecules* **2002**, *35*, 7007-7017.

(4) Epps, T. H., III; Cochran, E. W.; Hardy, C. M.; Bailey, T. S.; Waletzko, R. S.; Bates, F. S. *Macromolecules* **2004**, *37*, 7085-7088.

(5) Epps, T. H., III; Cochran, E. W.; Bailey, T. S.; Waletzko, R. S.; Hardy, C. M.; Bates, F. S. *Macromolecules* **2004**, *37*, 8325-8341.

8.4 Supporting Information for Chapter 6

Table 8.2. Relative Mass Fractions of the Neat IS(1.06)O Triblocks in Each IS(1.06)O Blend

Blend	f_O	M_w/M_n	Lattice Dimensions (nm)	d^* (nm)	Phase	T_{OOT} (°C)	T_{ODT} (°C)	Component	Mass Fraction
ISO(1.17, 0.20)	0.20	1.17	43.6	17.8	Q^{230} / HEX_O	195	>250	IS(1.06)O(0.05)	0.026
								IS(1.06)O(0.10)	0.088
								IS(1.06)O(0.13)	0.158
								IS(1.06)O(0.20)	0.288
								IS(1.06)O(0.23)	0.239
								IS(1.06)O(0.28)	0.162
								IS(1.06)O(0.35)	0.039
ISO(1.33, 0.20)	0.20	1.33	44.1	18.0	Q^{230} / HEX_O	165	>250	IS(1.06)O(0.05)	0.063
								IS(1.06)O(0.10)	0.138
								IS(1.06)O(0.13)	0.177
								IS(1.06)O(0.20)	0.262
								IS(1.06)O(0.28)	0.224
								IS(1.06)O(0.35)	0.136
ISO(1.46, 0.20)	0.20	1.46	44.3	18.1	Q^{230} / HEX_O	150	>250	IS(1.06)O(0.05)	0.085
								IS(1.06)O(0.10)	0.144
								IS(1.06)O(0.13)	0.186
								IS(1.06)O(0.20)	0.255
								IS(1.06)O(0.28)	0.170
								IS(1.06)O(0.35)	0.111
								IS(1.06)O(0.44)	0.049

Blend	f_O	M_w/M_n	Lattice Dimensions (nm)	d^* (nm)	Phase	T_{OOT} (°C)	T_{ODT} (°C)	Component	Mass Fraction
ISO(1.53, 0.20)	0.20	1.53	44.8	18.3	Q^{230}/ HEX_O	142	>250	IS(1.06)O(0.05)	0.114
								IS(1.06)O(0.10)	0.154
								IS(1.06)O(0.13)	0.169
								IS(1.06)O(0.20)	0.200
								IS(1.06)O(0.28)	0.172
								IS(1.06)O(0.35)	0.131
								IS(1.06)O(0.44)	0.060
ISO(1.16, 0.30)	0.30	1.16	50.5	20.6	Q^{230}		>250	IS(1.06)O(0.05)	0.018
								IS(1.06)O(0.10)	0.030
								IS(1.06)O(0.13)	0.037
								IS(1.06)O(0.20)	0.066
								IS(1.06)O(0.26)	0.133
								IS(1.06)O(0.28)	0.163
								IS(1.06)O(0.33)	0.233
								IS(1.06)O(0.35)	0.218
								IS(1.06)O(0.44)	0.102
ISO(1.28, 0.30)	0.30	1.28	51.4	21.0	Q^{230}		>250	IS(1.06)O(0.05)	0.122
								IS(1.06)O(0.26)	0.271
								IS(1.06)O(0.33)	0.365
								IS(1.06)O(0.44)	0.242
ISO(1.40, 0.30)	0.30	1.40	52.4	21.4	Q^{230}		>250	IS(1.06)O(0.05)	0.209
								IS(1.06)O(0.33)	0.500
								IS(1.06)O(0.44)	0.291
ISO(1.73, 0.30)	0.30	1.73	22.9	22.9	HEX_O		>250	IS(1.06)O(0.05)	0.343
								IS(1.06)O(0.44)	0.657

Blend	f_O	M_w/M_n	Lattice Dimensions (nm)	d^* (nm)	Phase	T_{OOT} (°C)	T_{ODT} (°C)	Component	Mass Fraction
ISO(1.27, 0.33)	0.33	1.27	53.6	21.9	LAM_3 / Q^{230}	210	>250	IS(1.06)O(0.05)	0.057
								IS(1.06)O(0.21)	0.177
								IS(1.06)O(0.28)	0.274
								IS(1.06)O(0.44)	0.492
ISO(1.30, 0.33)	0.33	1.30	53.6	21.9	Q^{230}		>250	IS(1.06)O(0.05)	0.079
								IS(1.06)O(0.21)	0.161
								IS(1.06)O(0.28)	0.247
								IS(1.06)O(0.44)	0.513
ISO(1.45, 0.33)	0.33	1.46	55.5	22.7	Q^{230}		>250	IS(1.06)O(0.05)	0.059
								IS(1.06)O(0.10)	0.106
								IS(1.06)O(0.13)	0.153
								IS(1.06)O(0.44)	0.682
ISO(1.17, 0.27)	0.27	1.17	55.1 (160 °C)	22.5	Q^{230}		>250	ISO5	0.109
								ISO10	0.450
								ISO12	0.441
ISO(1.30, 0.27)	0.27	1.30	56.8 (160 °C)	23.2	Q^{230}		>250	ISO1	0.146
								ISO2	0.031
								ISO11	0.129
								ISO12	0.694

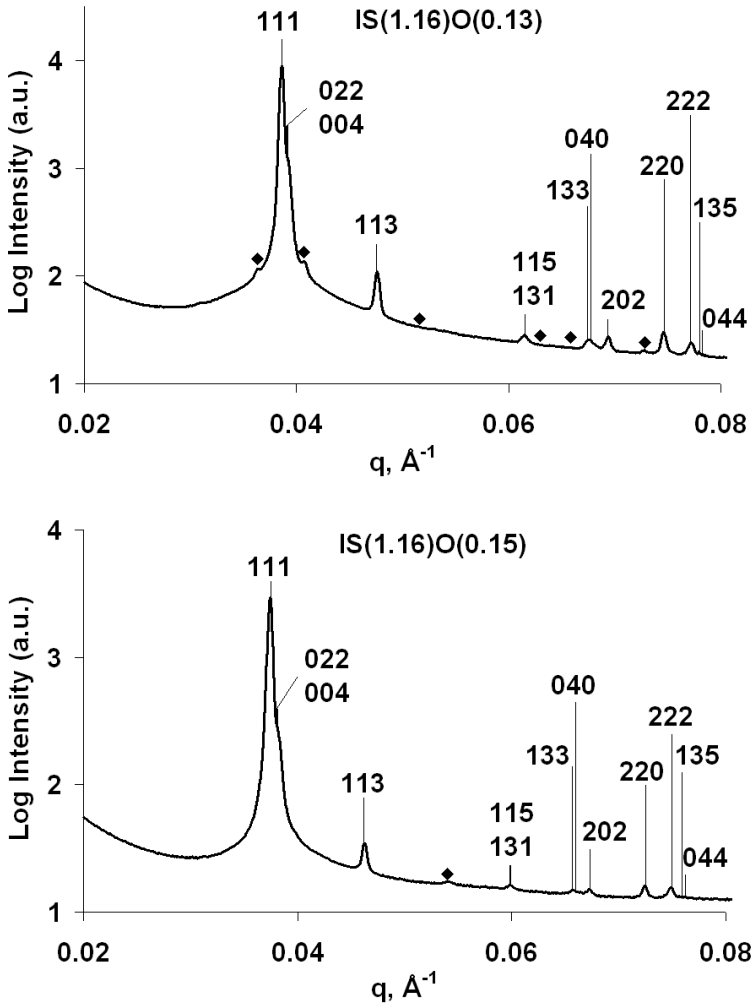

Figure 8.9. SAXS data acquired at 120 °C for samples IS(1.16)O(0.13) and IS(1.16)O(0.15). The first thirteen reflections consistent with the majority O^{70} morphology in both samples are labeled using the *hkl* notation. Specimen IS(1.16)O(0.13) contains several low intensity peaks that do not fit within the O^{70} indexing scheme. We tentatively suggest these reflections may be from a small amount of coexisting *ab*–stacked perforated lamellae with $P6_3mmc$ symmetry (PL_{ab}). The first nine reflections allowed by the PL_{ab} symmetry are marked with ♦'s. From low to high q, these reflections are 100 and 002 (both on first ♦), 101, 102, 110, 103, and 200, 112, 004 (all three on last ♦). The SAXS pattern for sample IS(1.16)O(0.15) contains one low intensity peak (marked with ♦) that is not consistent with O^{70}. We hesitate to offer even a speculative rationale for the presence of this additional solitary peak.

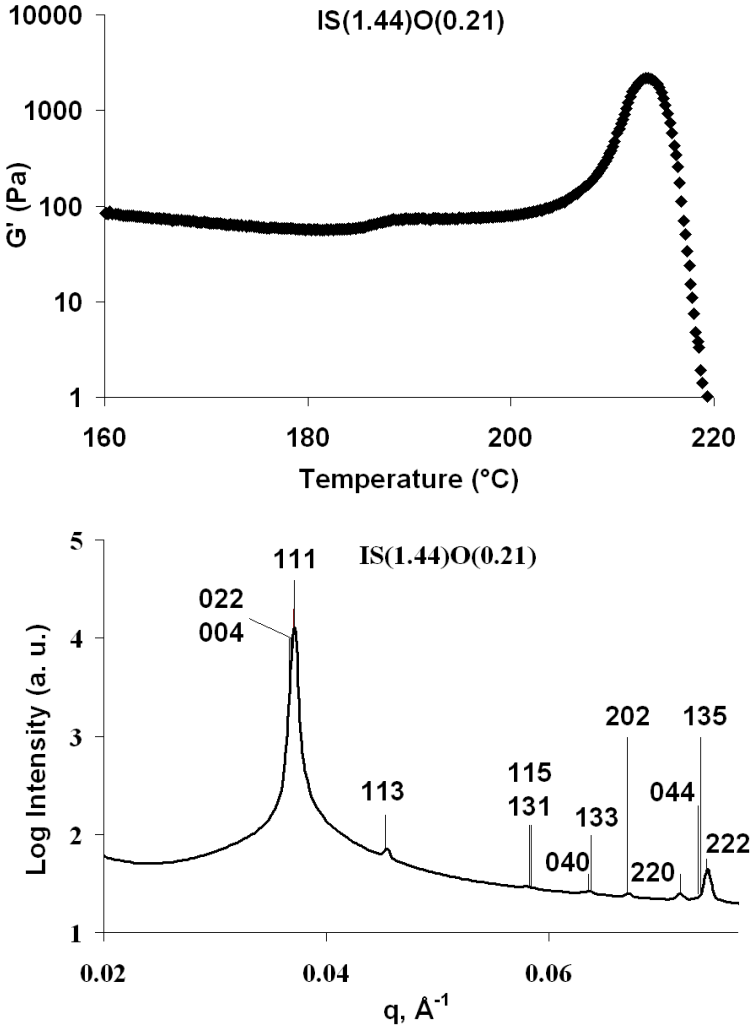

Figure 8.10. Top) Isochronal (ω = 1 rad/sec) *G'* measurements acquired while heating specimen IS(1.44)O(0.21) at 1 °C/min. The sample was first annealed at 250 °C for 10 min in an effort to erase effects associated with thermal history and then cooled to 100 °C prior to data collection. These data were acquired by Professor Christopher J. Ellison. **Bottom)** Synchrotron SAXS data acquired at 200 °C. The sample was first annealed at 250 °C in an effort to erase effects associated with thermal history and was then annealed at 200 °C for 2 min before being exposed to X-rays.

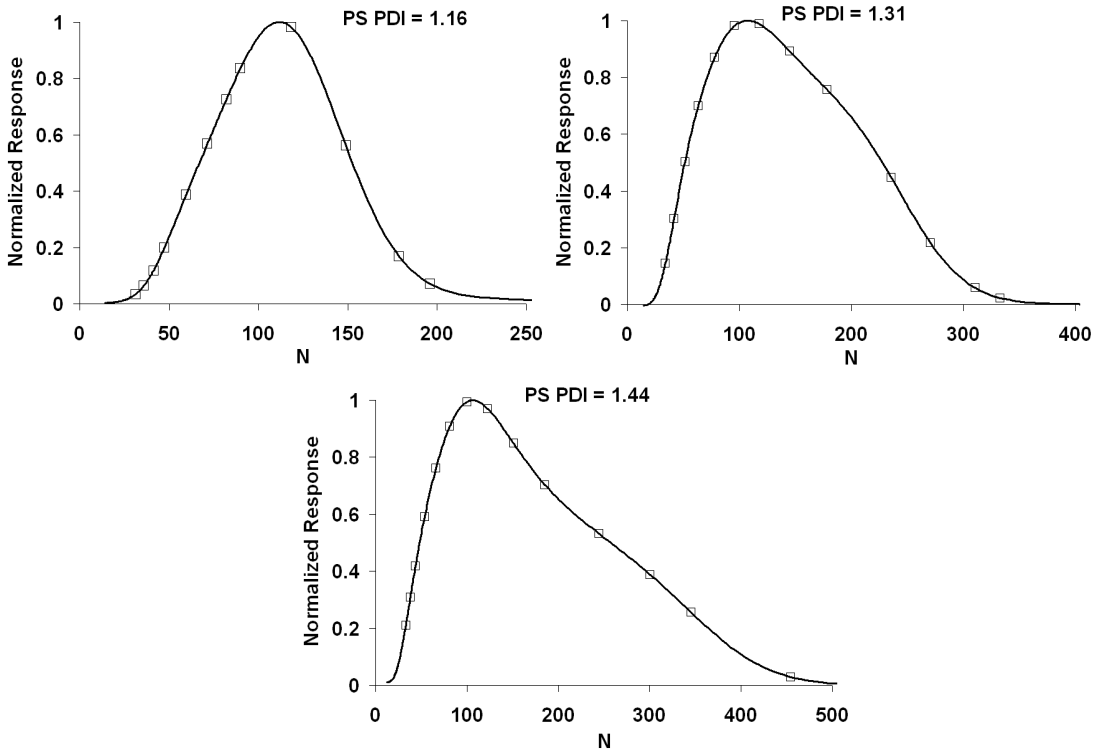

Figure 8.11. Comparisons between the PS block molecular weight distributions measured using SEC (solid curves) and the multimodal blends used as inputs for the SCFT calculations (open squares) for the model IS(1.16)O, IS(1.31)O, and IS(1.44)O systems. The values on the ordinate are proportional to the mass concentrations, while the "N" on the abscissa represents the degree of polymerization (with respect to a reference volume of 118 $Å^3$).

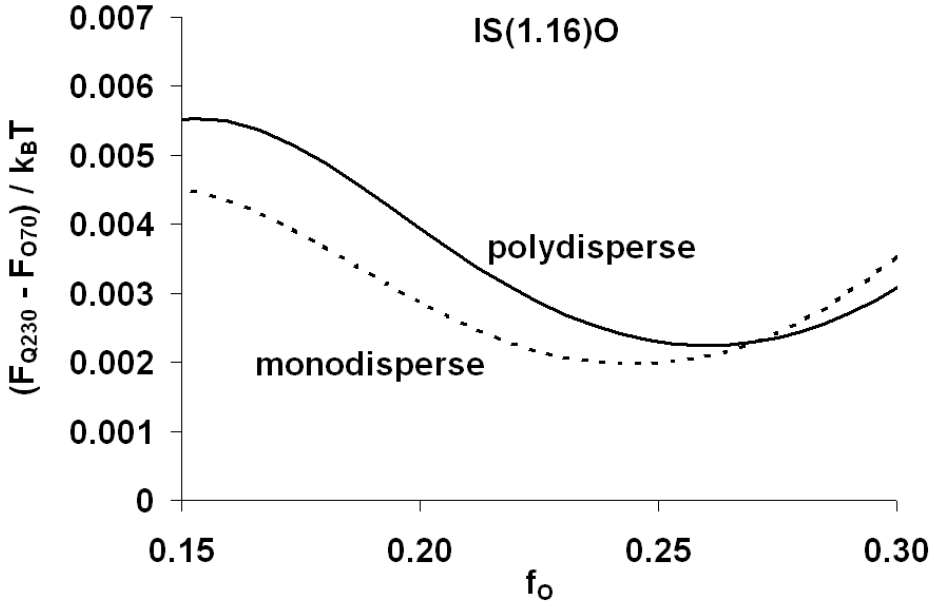

Figure 8.12. Curves representing the differences in the SCFT free energies (normalized by k_BT) of the Q^{230} and O^{70} mesostructures at the molecular weights and along the isopleth defined by the N_I and N_S values listed in Table 6.1 for the IS(1.16)O system. The dashed line portrays the free energy difference for a monodisperse system while the solid line represents the free energy difference in the model polydisperse IS(1.16)O system. O^{70} becomes more stable, relative to Q^{230}, when $0.15 < f_O < 0.27$ as the PS PDI is increased from 1 to 1.16.

8.5 Effects of Statistical Segment Length Variation

The effects of conformational asymmetry (i.e., changes in block statistical segment lengths (b_i))[1-5] and variations in block polydispersities (PDI)[6-10] on AB diblock copolymer phase behavior have been described in the literature. Some of the changes that result from an increase in either of these parameters are qualitatively the same. Namely, increases in b_i (block PDI) lead to larger domain periodicities and may drive morphological transitions to mesostructures in which the domain interfaces curve towards the high b (PDI) chains. The rationales for the conformational asymmetry and polydispersity effects are related. When b_A increases, the free energy penalty associated with stretching A chains decreases, and AB diblock copolymers can lower their free energy by having the A chains stretch further to avoid unfavorable segment-segment interactions (increased domain periodicities) and allow chains in the opposing domain to relax (morphological transitions in which the interfaces curve towards the A domains).[4] When PDI_A increases, the ensemble of A chains does not have to stretch as much to fill space because the longer chains can occupy the centers of domains without significantly deviating from their Gaussian conformations while the shorter chains can adopt relaxed configurations near domain interfaces. These chain packing considerations effectively increase the elasticity of a polydisperse ensemble of A chains relative to its monodisperse counterpart and drive morphological changes that are comparable to those associated with an increase in b_A.[7, 9] There is at least one significant difference between increases in b_A and increases in PDI_A, however. A monodisperse AB diblock copolymer only contains a single component and will always adopt a single

equilibrium configuration. An AB diblock copolymer with a polydisperse A block, in contrast, contains many components with different lengths of A. These chains may segregate according to their length (i.e., macrophase separate) and form multiple, coexisting mesostructures at equilibrium.[9]

No previous reports that we are aware of have compared the effects of increases in block PDI and b_i in ABC triblock terpolymers. The middle B block is of particular interest, as the chain packing considerations for that block may be fundamentally different than those associated with terminal blocks (e.g., those in AB diblock copolymers). Terminal chains have one free, dangling end that is not constrained to a domain interface by chain connectivity. This feature allows the short chains in a polydisperse ensemble to adopt relaxed configurations near the interfaces, as they are not required to stretch across a domain. The B segments in ABC triblock terpolymers do not have free chain ends, as both ends are covalently attached to either A or C blocks. When the A and C blocks are not miscible, as is the case in the ISO system, all of the B chains must stretch across the domain. This forced bridging makes polydispersity effects in the B block fundamentally different than polydispersity effects in blocks with free chain ends, as the short B chains are not able to adopt relaxed conformations near the domain interfaces. Our SCFT results from model ISO triblock terpolymers that were discussed in Section 6.4 illustrated this point; changes in the terminal PEO and middle PS block molecular weight distributions led to qualitatively different morphological effects.

Here we use the SCFT methodology described in Section 6.4 to investigate the effects of variations in b_I, b_S, and b_O. (Note that here the value of χ_{IS} is 1.8% higher than

it was in the SCFT calculations discussed in Section 6.4.) Only lamellae (LAM) and O^{70} are considered as mesostructural candidates in this preliminary investigation. The free energies of these morphologies are computed using SCFT for three series of model ISO molecules with $N_I = N_S = 90$ and various lengths of N_O. In each ISO series, the statistical segment length values reported in the literature (b_I = 6.07 Å, b_S = 5.47 Å, b_O = 7.80 Å)[11] are used for two of the blocks while b_i of the third block is varied. (Note that the b_i values, like χ_{ij} and N, are defined with respect to a segment reference volume of 118 $Å^3$.) The differences in the free energies (relative to k_BT) of LAM and O^{70} are plotted for various values of b_I, b_S, and b_O in Figure 8.13. Increases in b_O and decreases in b_I or b_S stabilize O^{70} relative to LAM along this $f_I = f_S$ isopleth. The effects of an increase in b_O are qualitatively similar to those associated with an increase in the PDI of the terminal PEO block (see Section 6.4); increases in either quantity lead to higher domain periodicities and lower the free energy of a network morphology relative to LAM. Changes in b_S and the PDI of the bridged PS block, in contrast, are not qualitatively similar. Our SCFT analysis predicted (see Figure 6.11) that broadening the PS molecular weight distribution would stabilize O^{70} relative to LAM for f_O values above the network window, and would destabilize O^{70} relative to LAM for compositions below the network window. The opposite trend is predicted for increases in b_S; O^{70} has a higher relative free energy for f_O > ~0.2 and a lower relative free energy for f_O < ~0.2. Furthermore, the equilibrium domain periodicity monotonically increases along with b_S, but not with PDI of the PS block (see Figure 6.13).

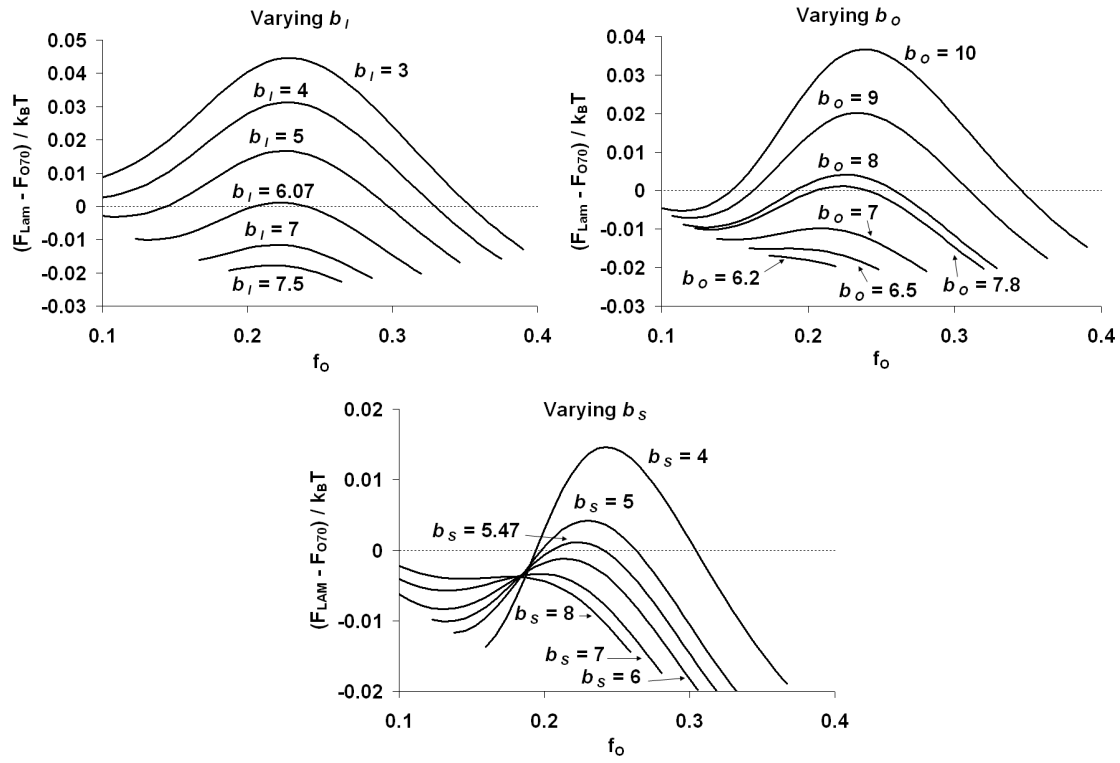

Figure 8.13. Differences in the computed free energies (normalized by k_BT) of LAM and O^{70} for model ISO triblock terpolymers ($N_I = N_S = 90$) with various b_i values. The three series of free energy curves are obtained by using the statistical segment lengths reported in the literature (b_I = 6.07 Å, b_S = 5.47 Å, b_O = 7.80 Å)[11] for two of the blocks, and varying b_i of the third block. Note that the b_i values, like χ_{ij} and N, are defined with respect to a segment reference volume of 118 $Å^3$. Some of these free energy curves terminate due to a previously reported technical issue that prevents the identification of SCFT solutions for O^{70} (see Reference 12 for more details).

The results provided in Figure 8.13 clearly demonstrate that the relative free energies of LAM and O^{70} are sensitive to the b_i values, and not just the χ_{ij} parameters. We believe that conformational asymmetry between the terminal blocks (i.e., $b_A \neq b_C$)

may play an integral role in stabilizing both the O^{70} and Q^{230} morphologies in nonfrustrated ABC triblock terpolymers, including ISO materials. Our argument can be rationalized in the context of previous conformational asymmetry studies of AB diblock copolymers[1-5] as well as our SCFT results provided in Figure 8.13. An increase in b_A reportedly[4] stabilizes mesostructures with domain interfaces curved towards the A chains, while a decrease in b_A stabilizes mesostructures with domain interfaces curved away from the A chains. The terminal domain interfaces in the O^{70} and Q^{230} mesostructures curve in opposite directions with respect to the terminal blocks; the interfaces possess a net mean curvature towards the core and away from the matrix. Using the AB diblock rationale, an increase in b_i of the core block and/or a decrease in b_i of the terminal matrix block should stabilize the O^{70} and Q^{230} morphologies. Our SCFT calculations summarized in Figure 8.13 corroborate this reasoning, as an increase in b_O of the core PEO chains and a decrease in b_I of the matrix PI segments both lead to a widening of the O^{70} window. Tyler et al.'s investigation of nonfrustrated ABC triblock terpolymer melts is also consistent with our reasoning.[12] These researchers used SCFT to calculate ternary phase portraits for several ABC triblock terpolymers. A model ABC system had both segment-segment interaction and conformational symmetry (i.e., $\chi_{AB} = \chi_{BC}$ and $b_A = b_B = b_C$) while a second "realistic" system approximated ISO triblock terpolymers ($\chi_{SO} = 1.291\ \chi_{IS}$ and $b_O = 1.285\ b_I$). While the O^{70} and Q^{230} morphologies were predicted to be stable in both of these systems, the stability windows were significantly larger for the realistic, asymmetric molecules. Tyler et al. analyzed the sensitivity of the phase behavior with respect to χ asymmetry and reported that increases in the asymmetry of the χ_{AB} and χ_{BC} parameters generally

were accompanied by expanded network windows.[12] Our SCFT results intimate that increases in conformational asymmetry would similarly expand the O^{70} and Q^{230} network windows. More definitive conclusions would require SCFT analysis of additional mesostructural candidates and wider ranges of compositions. This additional SCFT analysis could prove impactful because it would further refine the design criteria for the stabilization of potentially useful multiply continuous network morphologies.

References

(1) Vavasour, J. D.; Whitmore, M. D. *Macromolecules* **1993**, *26*, 7070-7075.

(2) Vavasour, J. D.; Whitmore, M. D. *Macromolecules* **1996**, *29*, 5244.

(3) Matsen, M. W.; Schick, M. *Macromolecules* **1994**, *27*, 4014-4015.

(4) Matsen, M. W.; Bates, F. S. *J. Polym. Sci. Part B* **1997**, *35*, 945-952.

(5) Pochan, D. J.; Gido, S. P.; Zhou, J.; Mays, J. W.; Whitmore, M.; Ryan, A. J. *J. Polym. Sci. Part B* **1997**, *35*, 2629-2643.

(6) Sides, S. W.; Fredrickson, G. H. *J. Chem. Phys.* **2004**, *121*, 4974-4986.

(7) Cooke, D. M.; Shi, A. *Macromolecules* **2006**, *39*, 6661-6671.

(8) Matsen, M. W. *Eur. Phys. J. E* **2007**, *21*, 199-207.

(9) Matsen, M. W. *Phys. Rev. Lett.* **2007**, *99*, 148304.

(10) Lynd, N. A.; Hillmyer, M. A.; Matsen, M. W. *Macromolecules* **2008**, *41*, 4531-4533.

(11) Fetters, L. J.; Lohse, D. J.; Richter, D.; Witten, T. A.; Zirkel, A. *Macromolecules* **1994**, *27*, 4639-4647.

(12) Tyler, C. A.; Qin, J.; Bates, F. S.; Morse, D. C. *Macromolecules* **2007**, *40*, 4654-4668.

Bibliography

Abetz, V.; Goldacker, T. *Macromol. Rapid Commun.* **2000**, *21*, 16-34.

Abu-Sharkh, B.; Al Sunaidi, A. *Macromol. Theory Simul.* **2006**, *15*, 507-515.

Adams, J. L.; Graessley, W. W.; Register, R. A. *Macromolecules* **1994**, *27*, 6026-6032.

Aggarwal, S. L. *Polymer* **1976**, *17*, 938-956.

Ahn, J.; Zin, W. *Macromol. Res.* **2003**, *11*, 152-156.

Alexandridis, P.; Olsson, U.; Lindman, B. *Macromolecules* **1995**, *28*, 7700-7710.

Alexandridis, P.; Olsson, U.; Lindman, B. *J. Phys. Chem.* **1996**, *100*, 280-288.

Alexandridis, P.; Olsson, U.; Lindman, B. *Langmuir* **1997**, *13*, 23-34.

Alexandridis, P. *Macromolecules* **1998**, *31*, 6935-6942.

Alexandridis, P.; Olsson, U.; Lindman, B. *Langmuir* **1998**, *14*, 2627-2638.

Almdal, K.; Rosedale, J. H.; Bates, F. S. *Macromolecules* **1990**, *23*, 4336-4338.

Almdal, K.; Koppi, K. A.; Bates, F. S.; Mortensen, K. *Macromolecules* **1992**, *25*, 1743-1751.

Almdal, K.; Mortensen, K.; Ryan, A. J.; Bates, F. S. *Macromolecules* **1996**, *29*, 5940-5947.

Alward, D. B.; Kinning, D. J.; Thomas, E. L.; Fetters, L. J. *Macromolecules* **1986**, *19*, 215-224.

Anderson, D. M.; Thomas, E. L. *Macromolecules* **1988**, *21*, 3221-3230.

Anderson, D. M.; Davis, H. T.; Scriven, L. E.; Nitsche, J. C. C. *Adv. Chem. Phys.* **1990**, *77*, 337-396.

Avgeropoulos, A.; Dair, B. J.; Hadjichristidis, N.; Thomas, E. L. *Macromolecules* **1997**, *30*, 5634-5642.

Avgeropoulos, A.; Chan, V. Z.; Lee, V. Y.; Ngo, D.; Miller, R. D.; Hadjichristidis, N.; Thomas, E. L. *Chem. Mater.* **1998**, *10*, 2109-2115.

Bailey, T. S.; Pham, H. D.; Bates, F. S. *Macromolecules* **2001**, *34*, 6994-7008.

Bailey, T. S.; Hardy, C. M.; Epps, T. H., III; Bates, F. S. *Macromolecules* **2002**, *35*, 7007-7017.

Bailey, T. S.; Rzayev, J.; Hillmyer, M. A. *Macromolecules* **2006**, *39*, 8772-8781.

Bates, F. S. *Macromolecules* **1984**, *17*, 2607-2613.

Bates, F. S.; Fredrickson, G. H. *Annu. Rev. Phys. Chem.* **1990**, *41*, 525-557.

Bates, F. S. *Science* **1991**, *251*, 898-905.

Bates, F. S.; Schulz, M. F.; Khandpur, A. K.; Förster, S.; Rosedale, J. H.; Almdal, K.; Mortensen, K. *Faraday Discuss.* **1994**, 7-18.

Bates, F. S.; Schulz, M. F.; Khandpur, A. K.; Förster, S.; Rosedale, J. H. *Faraday Discuss.* **1995**, *98*, 7-18.

Bates, F. S.; Maurer, W. W.; Lipic, P. M.; Hillmyer, M. A.; Almdal, K.; Mortensen, K.; Fredrickson, G. H.; Lodge, T. P. *Phys. Rev. Lett.* **1997**, *79*, 849-852.

Bates, F. S.; Fredrickson, G. H. *Phys. Today* **1999**, *52*, 32-38.

Bates, F. S. *MRS Bull.* **2005**, *30*, 525-532.

Bendejacq, D.; Ponsinet, V.; Joanicot, M.; Loo, Y.-L.; Register, R. A. *Macromolecules* **2002**, *35*, 6645-6649.

Bielawski, C. W.; Grubbs, R. H. *Prog. Polym. Sci.* **2007**, *32*, 1-29.

Bluemle, M. J.; Fleury, G; Lodge, T. P.; Bates, F. S. *Manuscript in Preparation.*

Bodycomb, J.; Yamaguchi, D.; Hashimoto, T. *Macromolecules* **2000**, *33*, 5187-5197.

Bohbot-Raviv, Y.; Wang, Z. *Phys. Rev. Lett.* **2000**, *85*, 3428-3431.

Brannan, A. K.; Bates, F. S. *Macromolecules* **2004**, *37*, 8816-8819.

Braunecker, W. A.; Matyjaszewski, K. *Prog. Polym. Sci.* **2007**, *32*, 93-146.

Brazovskii, S. A. *Sov. Phys. JETP* **1975**, *41*, 85.

Burger, C.; Ruland, W.; Semenov, A. N. *Macromolecules* **1990**, *23*, 3339-3346.

Callister, W. D., Jr. *Materials Science and Engineering: An Introduction*, 7th ed.; John Wiley & Sons, Inc.: New York, NY, 2007.

Campbell, M.; Sharp, D. N.; Harrison, M. T.; Denning, R. G.; Turberfield, A. J. *Nature* **2000**, *404*, 53-56.

Cavicchi, K. A.; Lodge, T. P. *Macromolecules* **2003**, *36*, 7158-7164.

Cavicchi, K. A.; Lodge, T. P. *Macromolecules* **2004**, *37*, 6004-6012.

Chan, V. Z. -H.; Hoffman, J.; Lee, V. Y.; Latrou, H.; Avgeropoulos, A.; Hadjichristidis, N.; Miller, R. D; Thomas, E. L. *Science* **1999**, *286*, 1716-1719.

Chandrasekhar, V. *Adv. Polym. Sci.* **1998**, *135*, 139-205.

Chastek, T. Q.; Lodge, T. P. *Macromolecules* **2003**, *36*, 7672-7680.

Chatterjee, J.; Jain, S.; Bates, F. S. *Macromolecules* **2007**, *40*, 2882-2896.

Chen, F.; Kondo, Y.; Hashimoto, T. *Macromolecules* **2007**, *40*, 3714-3723.

Cho, B. -K.; Jain, A.; Gruner, S. M.; Wiesner, U. *Science* **2004**, *305*, 1598-1601.

Cochran, E. W.; Morse, D. C.; Bates, F. S. *Macromolecules* **2003**, *36*, 782-792.

Cochran, E. W.; Bates, F. S. *Phys. Rev. Lett.* **2004**, *93*, 087802-1.

Cochran, E. W.; Garcia-Cervera, C. J.; Fredrickson, G. H. *Macromolecules* **2006**, *39*, 2449-2451.

Cohen, Y.; Albalak, R. J.; Dair, B. J.; Capel, M. S.; Thomas, E. L. *Macromolecules* **2000**, *33*, 6502-6516.

Cooke, D. M.; Shi, A. *Macromolecules* **2006**, *39*, 6661-6671.

Court, F.; Yamaguchi, D.; Hashimoto, T. *Macromolecules* **2006**, *39*, 2596-2605.

Crews, P.; Rodríguez, J.; Jaspars, M. *Organic Structure Analysis*; Oxford University Press: New York, NY, 1998.

Crossland, E. J. W.; Kamperman, M.; Nedelcu, M.; Ducati, C.; Wiesner, U.; Smilgies, D.; Toombes, G. E. S.; Hillmyer, M. A.; Ludwigs, S.; Steiner, U.; Snaith, H. J. *Nano Lett.* In Press.

Crossland, E. J. W.; Nedelcu, M.; Ducati, C.; Ludwigs, S.; Hillmyer, M. A.; Steiner, U.; Snaith, H. J. *Nano Lett.* In Press.

Cullity, B. D. *Elements of X-ray Diffraction*; Addison-Wesley Pub. Co.: Reading, Mass., 1978.

Dair, B. J.; Honeker, C. C.; Alward, D. B.; Avgeropoulos, A.; Hadjichristidis, N.; Fetters, L. J.; Capel, M.; Thomas, E. L. *Macromolecules* **1999**, *32*, 8145-8152.

Dair, B. J.; Avgeropoulos, A.; Hadjichristidis, N.; Capel, M.; Thomas, E. L. *Polymer* **2000**, *41*, 6231-6236.

Dair, B. J.; Avgeropoulos, A.; Hadjichristidis, N.; Thomas, E. L. *J. Mater. Sci.* **2000**, *35*, 5207-5213.

Daoulas, K. C.; Muller, M.; Stoykovich, M. P.; Park, S.; Papakonstantopoulos, Y. J.; de Pablo, J. J.; Nealey, P. F.; Solak, H. H. *Phys. Rev. Lett.* **2006**, *96*, 036104/1-036104/4.

Davidock, D. A.; Hillmyer, M. A.; Lodge, T. P. *Macromolecules* **2003**, *36*, 4682-4685.

Davidock, D. A.; Hillmyer, M. A.; Lodge, T. P. *Macromolecules* **2004**, *37*, 397-407.

Determan, M. D.; Cox, J. P.; Seifert, S.; Thiyagarajan, P.; Mallapragada, S. K. *Polymer* **2005**, *46*, 6933-6946.

Dobrynin, A. V.; Leibler, L. *Macromolecules* **1997**, *30*, 4756-4765.

Dotera, T.; Hatano, A. *J. Chem. Phys.* **1996**, *105*, 8413-8427.

Dotera, T. *Phys. Rev. Lett.* **2002**, *89*, 205502/1-205502/4.

Drolet, F.; Fredrickson, G. H. *Phys. Rev. Lett.* **1999**, *83*, 4317-4320.

Ellison, C. J.; Meuler, A. J.; Qin, J.; Evans, C. M.; Wolf, L. M.; Bates, F. S. *J. Phys. Chem. B* In Press.

Epps, T. H.,III; Bailey, T. S.; Pham, H. D.; Bates, F. S. *Chem. Mater.* **2002**, *14*, 1706-1714.

Epps, T. H., III; Bailey, T. S.; Waletzko, R.; Bates, F. S. *Macromolecules* **2003**, *36*, 2873-2881.

Epps, T. H., III; Cochran, E. W.; Hardy, C. M.; Bailey, T. S.; Waletzko, R. S.; Bates, F. S. *Macromolecules* **2004**, *37*, 7085-7088.

Epps, T. H., III; Cochran, E. W.; Bailey, T. S.; Waletzko, R. S.; Hardy, C. M.; Bates, F. S. *Macromolecules* **2004**, *37*, 8325-8341.

Epps, T. H., III; University of Minnesota: Doctoral Thesis, 2004.

Epps, T. H., III; Chatterjee, J.; Bates, F. S. *Macromolecules* **2005**, *38*, 8775-8784.

Epps, T. H., III; Bates, F. S. *Macromolecules* **2006**, *39*, 2676-2682.

Epps, T. H., III; DeLongchamp, D. M.; Fasolka, M. J.; Fischer, D. A.; Jablonski, E. L. *Langmuir* **2007**, *23*, 3355-3362.

Erukhimovich, I.; Dobrynin, A. V. *Macromol. Symp.* **1994**, *81*, 253-315.

Erukhimovich, I.; Abetz, V.; Stadler, R. *Macromolecules* **1997**, *30*, 7435-7443.

Erukhimovich, I. Y. *Eur. Phys. J. E Soft Matter* **2005**, *18*, 383-406.

Fasolka, M. J.; Mayes, A. M. *Annu. Rev. Mater. Res.* **2001**, *31*, 323-355.

Fetters, L. J.; Lohse, D. J.; Richter, D.; Witten, T. A.; Zirkel, A. *Macromolecules* **1994**, *27*, 4639-4647.

Fetters, L. J.; Huang, J. S.; Young, R. N. *J. Polym. Sci. Part A* **1996**, *34*, 1517-1527.

Finnefrock, A. C.; Ulrich, R.; Du Chesne, A.; Honeker, C. C.; Schumacher, K.; Unger, K. K.; Gruner, S. M.; Wiesner, U. *Angew. Chem., Int. Ed.* **2001**, *40*, 1208-1211.

Finnefrock, A. C.; Ulrich, R.; Toombes, G. E. S.; Gruner, S. M.; Wiesner, U. *J. Am. Chem. Soc.* **2003**, *125*, 13084-13093.

Floudas, G.; Ulrich, R.; Wiesner, U. *J. Chem. Phys.* **1999**, *110*, 652-663.

Floudas, G.; Ulrich, R.; Wiesner, U.; Chu, B. *Europhys. Lett.* **2000**, *50*, 182-188.

Floudas, G.; Vazaiou, B.; Schipper, F.; Ulrich, R.; Wiesner, U.; Iatrou, H.; Hadjichristidis, N. *Macromolecules* **2001**, *34*, 2947-2957.

Fontell, K. *Colloid Polym. Sci.* **1990**, *268*, 264-285.

Förster, S.; Khandpur, A. K.; Zhao, J.; Bates, F. S.; Hamley, I. W.; Ryan, A. J.; Bras, W. *Macromolecules* **1994**, *27*, 6922-6935.

Fredrickson, G. H.; Helfand, E. *J. Chem. Phys.* **1987**, *87*, 697-705.

Fredrickson, G. H.; Bates, F. S. *Ann. Rev. Mater. Sci.* **1996**, *26*, 501-550.

Fredrickson, G. H. *The Equilibrium Theory of Inhomogeneous Polymers*; Clarendon Press: Oxford, 2006.

Frick, E. M.; Hillmyer, M. A. *Macromol. Rapid Commun.* **2000**, *21*, 1317-1322.

Frielinghaus, H.; Hermsdorf, N.; Almdal, K.; Mortensen, K.; Messe, L.; Corvazier, L.; Fairclough, J. P. A.; Ryan, A. J.; Olmsted, P. D.; Hamley, I. W. *Europhys. Lett.* **2001**, *53*, 680-686.

Gehlsen, M. D.; Almdal, K.; Bates, F. S. *Macromolecules* **1992**, *25*, 939-943.

Goldacker, T.; Abetz, V. *Macromolecules* **1999**, *32*, 5165-5167.

Goldacker, T.; Abetz, V.; Stadler, R.; Erukhimovich, I.; Leibler, L. *Nature* **1999**, *398*, 137-139.

Gervais, M.; Gallot, B. *Makromol. Chem.* **1973**, *171*, 157-178.

Greene, T. W.; Wuts, P. G. M. *Protective Groups in Organic Synthesis*, 2nd ed.; Wiley-Interscience: New York, 1991; p 473.

Gruner, S. M. *J. Phys. Chem.* **1989**, *93*, 7562-7570.

Guo, Z.; Zhang, G.; Qiu, F.; Zhang, H.; Yang, Y.; Shi, A. *Phys. Rev. Lett.* **2008**, *101*, 028301/1-028301/4.

Hadziioannou, G.; Skoulios, A. *Macromolecules* **1982**, *15*, 267-271.

Hahn, T., Ed. *International Tables for Crystallography*, 4th revised ed.; 1994; Vol. A.

Hahn, S. F. ACS Spring 2008 Conference. "Heterogeneous catalytic process for the hydrogenation of styrene-butadiene block copolymers."

Hajduk, D. A.; Harper, P. E.; Gruner, S. M.; Honeker, C. C.; Kim, G.; Thomas, E. L.; Fetters, L. J. *Macromolecules* **1994**, *27*, 4063-4075.

Hajduk, D. A.; Harper, P. E.; Gruner, S. M.; Honeker, C. C.; Thomas, E. L.; Fetters, L. J. *Macromolecules* **1995**, *28*, 2570-2573.

Hajduk, D. A.; Takenouchi, H.; Hillmyer, M. A.; Bates, F. S.; Vigild, M. E.; Almdal, K. *Macromolecules* **1997**, *30*, 3788-3795.

Hajduk, D. A.; Kossuth, M. B.; Hillmyer, M. A.; Bates, F. S. *J. Phys. Chem. B* **1998**, *102*, 4269-4276.

Hamley, I. W.; Fairclough, J. P. A.; Ryan, A. J.; Mai, S. -M.; Booth, C. *Phys. Chem. Chem. Phys.* **1999**, *1*, 2097-2101.

Han, C. D.; Kim, J. K. *Polymer* **1993**, *34*, 2533-2539.

Han, Y.; Cui, J.; Jiang, W. *Macromolecules* **2008**, *41*, 6239-6245.

Hanley, K. J.; Lodge, T. P.; Huang, C. *Macromolecules* **2000**, *33*, 5918-5931.

Hardy, C. M.; Bates, F. S.; Kim, M.; Wignall, G. D. *Macromolecules* **2002**, *35*, 3189-3197.

Hasegawa, H.; Tanaka, H.; Yamasaki, K.; Hashimoto, T. *Macromolecules* **1987**, *20*, 1651-1662.

Hasegawa, H.; Hashimoto, T.; Hyde, S. T. *Polymer* **1996**, *37*, 3825-3833.

Hashimoto, T.; Nagatoshi, K.; Todo, A.; Hasegawa, H.; Kawai, H. *Macromolecules* **1974**, *7*, 364-373.

Hashimoto, T.; Tsutsumi, K.; Funaki, Y. *Langmuir* **1997**, *13*, 6869-6872.

Hashimoto, T.; Nishikawa, Y.; Tsutsumi, K. *Macromolecules* **2007**, *40*, 1066-1072.

Hawker, C. J.; Bosman, A. W.; Harth, E. *Chem. Rev.* **2001**, *101*, 3661-3688.

He, Y.; Lodge, T. P. *Macromolecules* **2008**, *41*, 167-174.

Helfand, E. *Macromolecules* **1975**, *8*, 552-556.

Helfand, E.; Wasserman, Z. R. *Macromolecules* **1976**, *9*, 879-888.

Herman, D. S.; Kinning, D. J.; Thomas, E. L.; Fetters, L. J. *Macromolecules* **1987**, *20*, 2940-2942.

Hiemenz, P. C.; Lodge, T. P. *Polymer Chemistry*, 2nd ed.; CRC Press: Boca Raton, FL, 2004.

Hill, S. T.; Mokotoff, M. *J. Org. Chem.* **1984**, *49*, 1441-1442.

Hillmyer, M. A.; Bates, F. S.; Almdal, K.; Mortensen, K.; Ryan, A. J.; Fairclough, J. P. A. *Science* **1996**, *271*, 976-978.

Hillmyer, M. A.; Bates, F. S. *Macromolecules* **1996**, *29*, 6994-7002.

Hillmyer, M. A. *Adv. Polym. Sci.* **2005**, *190*, 137-181.

Hillmyer, M. A. *J. Polym. Sci., Part B* **2007**, *45*, 3249-3251.

Holden, G., Legge, N. R., Quirk, R. P., Schroeder, H. E. *Thermoplastic Elastomers*, 2nd ed.; Hansen Publishers: New York, NY, 1996.

Hong, K. M.; Noolandi, J. *Polym. Commun.* **1984**, *25*, 265-268.

Hong, K.; Uhrig, D.; Mays, J. W. *Curr. Opin. Solid State Mater. Sci.* **2000**, *4*, 531-538.

Hoye, T. R.; Eklov, B. M.; Ryba, T. D.; Voloshin, M.; Yao, L. J. *Org. Lett.* **2004**, *6*, 953-956.

Hoye, T. R.; Eklov, B. M.; Voloshin, M. *Org. Lett.* **2004**, *6*, 2567-2570.

Hsieh, H. L.; Quirk, R. P. *Anionic Polymerization: Principles and Practical Applications*, 1997; Vol. 70.

Hückstädt, H.; Goldacker, T.; Goepfert, A.; Abetz, V. *Macromolecules* **2000**, *33*, 3757-3761.

Hutchings, L. R.; Roberts-Bleming, S. J. *Macromolecules* **2006**, *39*, 2144-2152.

Hwang, J.; Huh, J.; Jung, B.; Hong, J.; Park, M.; Park, C. *Polymer* **2005**, *46*, 9133-9143.

Inoue, T.; Soen, T.; Hashimoto, T.; Kawai, H. *J. Polym. Sci., Polym. Phys. Ed.* **1969**, *7*, 1283-1301.

Jain, S.; Bates, F. S. *Science* **2003**, *300*, 460-464.

Jain, S.; Gong, X.; Scriven, L. E.; Bates, F. S. *Phys. Rev. Lett.* **2006**, *96*, 138304/1-138304/4.

Jiang, Y.; Yan, X.; Liang, H.; Shi, A. *J. Phys. Chem. B* **2005**, *109*, 21047-21055.

Jin, S.; Yoon, J.; Heo, K.; Park, H. W.; Kim, J.; Kim, K. W.; Shin, T. J.; Chang, T.; Ree, M. *J. Appl. Crystallogr.* **2007**, *40*, 950-958.

Jinnai, H.; Nishikawa, Y.; Spontak, R. J.; Smith, S. D.; Agard, D. A.; Hashimoto, T. *Phys. Rev. Lett.* **2000**, *84*, 518-521.

Kamigaito, M.; Ando, T.; Sawamoto, M. *Chem. Rev.* **2001**, *101*, 3689-3746.

Kawasaki, K.; Onuki, A. *Phys. Rev. A: At. Mol. Opt. Phys.* **1990**, *42*, 3664-3666.

Kelly, A.; Groves, G. W.; Kidd, P. *Crystallography and Crystal Defects*; Wiley: New York, NY 2000.

Khandpur, A. K.; Förster, S.; Bates, F. S.; Hamley, I. W.; Ryan, A. J.; Bras, W.; Almdal, K.; Mortensen, K. *Macromolecules* **1995**, *28*, 8796-8806.

Kim, M. I.; Wakada, T.; Akasaka, S.; Nishitsuji, S.; Saijo, K.; Hasegawa, H.; Ito, K.; Takenaka, M. *Macromolecules* **2008**, *41*, 7667-7670.

Kinning, D. J.; Thomas, E. L.; Alward, D. B.; Fetters, L. J.; Handlin, D. L.,Jr *Macromolecules* **1986**, *19*, 1288-1290.

Kloninger, C.; Rehahn, M. *Macromolecules* **2004**, *37*, 8319-8324.

Kopchick, J. G.; Storey, R. F.; Beyer, F. L.; Mauritz, K. A. *Polymer* **2007**, *48*, 3739-3748.

Kopchick, J. G.; Storey, R. F.; Jarrett, W. L.; Mauritz, K. A. *Polymer* **2008**, *49*, 5045-5052.

Koppi, K. A.; Tirrell, M.; Bates, F. S.; Almdal, K.; Colby, R. H. *J. Phys. II* **1992**, *2*, 1941-1959.

Koppi, K. A.; Tirrell, M.; Bates, F. S. *Phys. Rev. Lett.* **1993**, *70*, 1449-1452.

Kossuth, M. B.; Morse, D. C.; Bates, F. S. *J. Rheol.* **1999**, *43*, 167-196.

Kuo, S.; Huang, W.; Huang, C.; Chan, S.; Chang, F. *Macromolecules* **2004**, *37*, 4164-4173.

Laurer, J. H.; Hajduk, D. A.; Fung, J. C.; Sedat, J. W.; Smith, S. D.; Gruner, S. M.; Agard, D. A.; Spontak, R. J. *Macromolecules* **1997**, *30*, 3938-3941.

Laurer, J. H.; Hajduk, D. A.; Dreckoetter, S.; Smith, S. D.; Spontak, R. J. *Macromolecules* **1998**, *31*, 7546-7549.

Lee, W.; Lee, H.; Cha, J.; Chang, T.; Hanley, K. J.; Lodge, T. P. *Macromolecules* **2000**, *33*, 5111-5115.

Lee, B.; Park, I.; Yoon, J.; Park, S.; Kim, J.; Kim, K.; Chang, T.; Ree, M. *Macromolecules* **2005**, *38*, 4311-4323.

Leibler, L. *Macromolecules* **1980**, *13*, 1602-1617.

Leibler, L.; Benoit, H. *Polymer* **1981**, *22*, 195-201.

Leibler, L. *Prog. Polym. Sci.* **2005**, *30*, 898-914.

Li, X.; Hsu, S. L. *J. Polym. Sci., Polym. Phys.* **1984**, *22*, 1331-1342.

Likhtman, A. E.; Semenov, A. N. *Macromolecules* **1994**, *27*, 3103-3106.

Likhtman, A. E.; Semenov, A. N. *Macromolecules* **1997**, *30*, 7273-7278.

Lim, L. S.; Harada, T.; Hillmyer, M. A.; Bates, F. S. *Macromolecules* **2004**, *37*, 5847-5850.

Lin, S. Y.; Fleming, J. G.; Hetherington, D. L.; Smith, B. K.; Biswas, R.; Ho, K. M.; Sigalas, M. M.; Zubrzycki, W.; Kurtz, S. R.; Bur, J. *Nature* **1998**, *394*, 251-253.

Ling, J.; Chen, W.; Shen, Z. *J. Polym. Sci., Part A: Polym. Chem.* **2005**, *43*, 1787-1796.

Lipic, P. M.; Bates, F. S.; Matsen, M. W. *J. Polym. Sci. Part B* **1999**, *37*, 2229-2238.

Listak, J.; Jakubowski, W.; Mueller, L.; Plichta, A.; Matyjaszewski, K.; Bockstaller, M. R. *Macromolecules* **2008**, *41*, 5919-5927.

Lo, G. Y.; Otterbacher, E. W.; Gatzke, A. L.; Tung, L. H. *Macromolecules* **1994**, *27*, 2233-2240.

Lodge, T. P.; Pudil, B.; Hanley, K. J. *Macromolecules* **2002**, *35*, 4707-4717.

Lodge, T. P.; Hanley, K. J.; Pudil, B.; Alahapperuma, V. *Macromolecules* **2003**, *36*, 816-822.

Lodge, T. P. *Macromol. Chem. Phys.* **2003**, *204*, 265-273.

Luzzati, V.; Spegt, P. A. *Nature* **1967**, *215*, 701-704.

Lynd, N. A.; Hillmyer, M. A. *Macromolecules* **2005**, *38*, 8803-8810.

Lynd, N. A.; Hillmyer, M. A. *Macromolecules* **2007**, *40*, 8050-8055.

Lynd, N. A.; Hamilton, B. D.; Hillmyer, M. A. *J. Polym. Sci., Part B* **2007**, *45*, 3386-3393.

Lynd, N. A.; Hillmyer, M. A.; Matsen, M. W. *Macromolecules* **2008**, *41*, 4531-4533.

Lynd, N. A.; Meuler, A. J.; Hillmyer, M. A. *Prog. Polym. Sci.* **2008**, *33*, 875-893.

Mahanthappa, M. K.; Lim, L. S.; Hillmyer, M. A.; Bates, F. S. *Macromolecules* **2007**, *40*, 1585-1593.

Mahanthappa, M. K.; Hillmyer, M. A.; Bates, F. S. *Macromolecules* **2008**, *41*, 1341-1351.

Mai, S.; Mingvanish, W.; Turner, S. C.; Chaibundit, C.; Fairclough, J. P. A.; Heatley, F.; Matsen, M. W.; Ryan, A. J.; Booth, C. *Macromolecules* **2000**, *33*, 5124-5130.

Maldovan, M.; Urbas, A. M.; Yufa, N.; Carter, W. C.; Thomas, E. L. *Phys. Rev. B: Condens. Matter* **2002**, *65*, 165123/1-165123/5.

Maldovan, M.; Carter, W. C.; Thomas, E. L. *Appl. Phys. Lett.* **2003**, *83*, 5172-5174.

Maldovan, M.; Ullal, C. K.; Carter, W. C.; Thomas, E. L. *Nat. Mater.* **2003**, *2*, 664-667.

Malenfant, P. R. L.; Wan, J.; Taylor, S. T.; Manoharan, M. *Nat. Nanotechnol.* **2007**, *2*, 43-46.

Mani, S.; Weiss, R. A.; Cantino, M. E.; Khairallah, L. H.; Hahn, S. F.; Williams, C. E. *Eur. Polym. J.* **1999**, *36*, 215-219.

Mao, H.; Hillmyer, M. A. *Macromolecules* **2005**, *38*, 4038-4039.

Mao, H.; Hillmyer, M. A. *Soft Matter* **2006**, *2*, 57-59.

Mareau, V. H.; Matsushita, T.; Nakamura, E.; Hasegawa, H. *Macromolecules* **2007**, *40*, 6916-6921.

Mariani, P.; Luzzati, V.; Delacroix, H. *J. Mol. Biol.* **1988**, *204*, 165-189.

Martínez-Veracoechea, F. J.; Escobedo, F. A. *Macromolecules* **2005**, *38*, 8522-8531.

Martínez-Veracoechea, F. J.; Escobedo, F. A. *J. Chem. Phys.* **2006**, *125*, 104907/1-104907/12.

Martínez-Veracoechea, F. J.; Escobedo, F. A. *Macromolecules* **2007**, *40*, 7354-7365.

Matsen, M. W.; Schick, M. *Phys. Rev. Lett.* **1994**, *72*, 2660-2663.

Matsen, M. W.; Schick, M. *Macromolecules* **1994**, *27*, 4014-4015.

Matsen, M. W.; Schick, M. *Macromolecules* **1994**, *27*, 6761-6767.

Matsen, M. W.; Schick, M. *Macromolecules* **1994**, *27*, 7157-7163.

Matsen, M. W. *Phys. Rev. Lett.* **1995**, *74*, 4225-4228.

Matsen, M. W. *Macromolecules* **1995**, *28*, 5765-5773.

Matsen, M. W.; Bates, F. S. *Macromolecules* **1996**, *29*, 1091-1098.

Matsen, M. W.; Bates, F. S. *Macromolecules* **1996**, *29*, 7641-7644.

Matsen, M. W.; Bates, F. S. *J. Chem. Phys.* **1997**, *106*, 2436-2448.

Matsen, M. W.; Bates, F. S. *J. Polym. Sci. Part B* **1997**, *35*, 945-952.

Matsen, M. W. *Phys. Rev. Lett.* **1998**, *80*, 4470-4473.

Matsen, M. W. *J. Chem. Phys.* **1998**, *108*, 785-796.

Matsen, M. W.; Thompson, R. B. *J. Chem. Phys.* **1999**, *111*, 7139-7146.

Matsen, M. W. *J. Chem. Phys.* **2000**, *113*, 5539-5544.

Matsen, M. W. *J. Phys.: Condens. Matter* **2002**, *14*, R21-R47.

Matsen, M. W. *Eur. Phys. J. E* **2007**, *21*, 199-207.

Matsen, M. W. *Phys. Rev. Lett.* **2007**, *99*, 148304/1-148304/4.

Matsushita, Y.; Tamura, M.; Noda, I. *Macromolecules* **1994**, *27*, 3680-3682.

Matsushita, Y.; Nomura, M.; Watanabe, J.; Mogi, Y.; Noda, I.; Imai, M. *Macromolecules* **1995**, *28*, 6007-6013.

Matsushita, Y.; Suzuki, J.; Seki, M. *Physica B* **1998**, *248*, 238-242.

Matsushita, Y.; Torikai, N.; Suzuki, J.; Seki, M. *J. Phys. Chem. Solids* **1999**, *60*, 1279-1284.

Matsushita, Y.; Noro, A.; Iinuma, M.; Suzuki, J.; Ohtani, H.; Takano, A. *Macromolecules* **2003**, *36*, 8074-8077.

Matyjaszewski, K.; Xia, J. *Chem. Rev.* **2001**, *101*, 2921-2990.

Mayes, A. M.; Olvera de la Cruz, M. *J. Chem. Phys.* **1989**, *91*, 7228-7235.

Mayes, A. M.; Olvera de la Cruz, M. *J. Chem. Phys.* **1991**, *95*, 4670-4677.

Meuler, A. J.; Mahanthappa, M. K.; Hillmyer, M. A.; Bates, F. S. *Macromolecules* **2007**, *40*, 760-762.

Meuler, A. J.; Ellison, C. J.; Evans, C. M.; Hillmyer, M. A.; Bates, F. S. *Macromolecules* **2007**, *40*, 7072-7074.

Meuler, A. J.; Fleury, G.; Hillmyer, M. A.; Bates, F. S. *Macromolecules* **2008**, *41*, 5809-5817.

Meuler, A. J.; Ellison, C. J.; Hillmyer, M. A.; Bates, F. S. *Macromolecules* **2008**, *41*, 6272-6275.

Meuler, A. J.; Ellison, C. J.; Qin, J.; Evans, C. M.; Hillmyer, M. A.; Bates, F. S. *Manuscript in Preparation.*

McKay, K. W.; Gros, W. A.; Diehl, C. F. *J. Appl. Polym. Sci.* **1995**, *56*, 947-958.

Miao, B.; Wickham, R. A. *J. Chem. Phys.* **2008**, *128*, 054902/1-054902/5.

Milner, S. T.; Witten, T. A.; Cates, M. E. *Macromolecules* **1989**, *22*, 853-861.

Mogi, Y.; Kotsuji, H.; Kaneko, Y.; Mori, K.; Matsushita, Y.; Noda, I. *Macromolecules* **1992**, *25*, 5408-5411.

Mogi, Y.; Mori, K.; Matsushita, Y.; Noda, I. *Macromolecules* **1992**, *25*, 5412-5415.

Mogi, Y.; Nomura, M.; Kotsuji, H.; Ohnishi, K.; Matsushita, Y.; Noda, I. *Macromolecules* **1994**, *27*, 6755-6760.

Morton, M. *Anionic Polymerization: Principles and Practice*; Academic Press: New York, NY, 1983.

Ndoni, S.; Papadakis, C. M.; Bates, F. S.; Almdal, K. *Rev. Sci. Instrum.* **1995**, *66*, 1090-1095.

Ndoni, S.; Vigild, M. E.; Berg, R. H. *J. Am. Chem. Soc.* **2003**, *125*, 13366-13367.

Nguyen, D.; Zhong, X.; Williams, C. E.; Eisenberg, A. *Macromolecules* **1994**, *27*, 5173-5181.

Nonomura, M.; Yamada, K.; Ohta, T. *J. Phys.: Condens. Matter* **2003**, *15*, L423-L430.

Noro, A.; Iinuma, M.; Suzuki, J.; Takano, A.; Matsushita, Y. *Macromolecules* **2004**, *37*, 3804-3808.

Noro, A.; Cho, D.; Takano, A.; Matsushita, Y. *Macromolecules* **2005**, *38*, 4371-4376.

Noro, A.; Okuda, M.; Odamaki, F.; Kawaguchi, D.; Torikai, N.; Takano, A.; Matsushita, Y. *Macromolecules* **2006**, *39*, 7654-7661.

Nykaenen, A.; Nuopponen, M.; Laukkanen, A.; Hirvonen, S.; Rytelae, M.; Turunen, O.; Tenhu, H.; Mezzenga, R.; Ikkala, O.; Ruokolainen, J. *Macromolecules* **2007**, *40*, 5827-5834.

Odian, G. *Principles of Polymerization*, 4th ed.; John Wiley & Sons, Inc.: New York, NY, 2004.

Okumura, A.; Nishikawa, Y.; Hashimoto, T. *Polymer* **2006**, *47*, 7805-7812.

Olmsted, P. D.; Milner, S. T. *Phys. Rev. Lett.* **1994**, *72*, 936-939.

Olmsted, P. D.; Milner, S. T. *Phys. Rev. Lett.* **1995**, *74*, 829.

Olmsted, P. D.; Milner, S. T. *Macromolecules* **1998**, *31*, 4011-4022.

Pangborn, A. B.; Giardello, M. A.; Grubbs, R. H.; Rosen, R. K.; Timmers, F. J. *Organometallics* **1996**, *15*, 1518-1520.

Park, S.; Cho, D.; Ryu, J.; Kwon, K.; Lee, W.; Chang, T. *Macromolecules* **2002**, *35*, 5974-5979.

Park, S.; Sul, W. *Polymer* **2008**, *49*, 3327-3334.

Park, C.; Yoon, J.; Thomas, E. L. *Polymer* **2003**, *44*, 6725-6760.

Park, I.; Lee, B.; Ryu, J.; Im, K.; Yoon, J.; Ree, M.; Chang, T. *Macromolecules* **2005**, *38*, 10532-10536.

Park, H.; Im, K.; Chung, B.; Ree, M.; Chang, T.; Sawa, K.; Jinnai, H. *Macromolecules* **2007**, *40*, 2603-2605.

Park, M. J.; Downing, K. H.; Jackson, A.; Gomez, E. D.; Minor, A. M.; Cookson, D.; Weber, A. Z.; Balsara, N. P. *Nano Lett.* **2007***, 7*, 3547-3552.

Park, M. J.; Nedoma, A. J.; Geissler, P. L.; Balsara, N. P.; Jackson, A.; Cookson, D. *Macromolecules* **2008***, 41*, 2271-2277.

Park, M. J.; Balsara, N. P. *Macromolecules* **2008**, *41*, 3678-3687.

Park, H.; Jung, J.; Chang, T.; Matsunaga, K.; Jinnai, H. *J. Am. Chem. Soc.* **2009**, *131*, 46-47.

Peleshanko, S.; Anderson, K. D.; Goodman, M.; Determan, M. D.; Mallapragada, S. K.; Tsukruk, V. V. *Langmuir* **2007***, 23*, 25-30.

Pernot, H.; Baumert, M.; Court, F.; Leibler, L. *Nat. Mater.* **2002**, *1*, 54-58.

Perrier, S.; Wang, X. *Nature* **2007**, *445*, 271-272.

Phan, S.; Fredrickson, G. H. *Macromolecules* **1998**, *31*, 59-63.

Phatak, A.; Lim, L. S.; Reaves, C. K.; Bates, F. S. *Macromolecules* **2006**, *39*, 6221-6228.

Phillip, W. A.; Rzayev, J.; Hillmyer, M. A.; Cussler, E. L. *J. Membr. Sci.* **2006**, *286*, 144-152.

Pochan, D. J.; Gido, S. P.; Zhou, J.; Mays, J. W.; Whitmore, M.; Ryan, A. J. *J. Polym. Sci. Part B* **1997**, *35*, 2629-2643.

Podariu, I.; Chakrabarti, A. *J. Chem. Phys.* **2003**, *118*, 11249-11257.

Potschke, P.; Paul, D. R. *J. Macromol. Sci., Polym. Rev.* **2003**, *C43*, 87-141.

Qiao, L.; Leibig, C.; Hahn, S. F.; Winey, K. I. *Ind. Eng. Chem. Res.* **2006**, *45*, 5598-5602.

Qin, J. *Private Communication*.

Quirk, R. P.; Ma, J. J. *J. Polym. Sci. Part A* **1988**, *26*, 2031-2037.

Quirk, R. P.; Jang, S. H.; Han, K.; Yang, H.; Rix, B.; Lee, Y. *ACS Symp. Ser.* **1998**, *704*, 71-84.

Quirk, R. P.; You, F.; Wesdemiotis, C.; Arnould, M. A. *Macromolecules* **2004**, *37*, 1234-1242.

Ranjan, A.; Morse, D. C. *Phys. Rev. E: Stat., Nonlinear, and Soft Matter Phys.* **2006**, *74*, 011803/1-011803/6.

Ranjan, A.; Qin, J.; Morse, D. C. *Macromolecules* **2008**, *41*, 942-954.

Rempp, P.; Merrill, E. W. *Polymer Synthesis*, 2nd ed.; Huethig & Wepf: New York, NY, 1991.

Robitaille, C. D.; Fauteux, D. *J. Electrochem. Soc.* **1986**, *133*, 315-325.

Rosedale, J. H.; Bates, F. S. *Macromolecules* **1990**, *23*, 2329-2338.

Russell, T. P. *Curr. Opin. Colloid Interface Sci.* **1996**, *1*, 107.

Ruzette, A. G.; Soo, P. P.; Sadoway, D. R.; Mayes, A. M. *J. Electrochem. Soc.* **2001**, *148*, A537-A543.

Ruzette, A.; Tence-Girault, S.; Leibler, L.; Chauvin, F.; Bertin, D.; Guerret, O.; Gerard, P. *Macromolecules* **2006**, *39*, 5804-5814.

Ryu, C. Y.; Lee, M. S.; Haiduk, D. A.; Lodge, T. P. *J. Polym. Sci. Part B* **1997**, *35*, 2811-2823.

Sakurai, S.; Sakamoto, J.; Shibayama, M.; Nomura, S. *Macromolecules* **1993**, *26*, 3351-3356.

Sakurai, S.; Umeda, H.; Furukawa, C.; Irie, H.; Nomura, S.; Hyun Lee, H.; Kon Kim, J. *J. Chem. Phys.* **1998**, *108*, 4333-4339.

Sakurai, S.; Irie, H.; Umeda, H.; Nomura, S.; Lee, H. H.; Kim, J. K. *Macromolecules* **1998**, *31*, 336-343.

Sakurai, S.; Isobe, D.; Okamoto, S.; Yao, T.; Nomura, S. *Phys. Rev. E: Stat., Nonlinear, Soft Matter Phys.* **2001**, *63*, 061803/1-061803/5.

Sakurai, S.; Isobe, D.; Okamoto, S.; Nomura, S. *Mater. Sci. Res. Int.* **2001**, *7*, 225-228.

Sakurai, S.; Isobe, D.; Okamoto, S.; Nomura, S. *J. Macromol. Sci., Phys.* **2002**, *B41*, 387-395.

Scriven, L. E. *Nature* **1976**, *263*, 123-125.

Schoen, A. H. *NASA TN D-5541* **1970**.

Schröder-Turk, G. E.; Fogden, A.; Hyde, S. T. *Eur. Phys. J. B* **2007**, *59*, 115-126.

Schulz, M. F.; Bates, F. S.; Almdal, K.; Mortensen, K. *Phys. Rev. Lett.* **1994**, *73*, 86-89.

Schulz, M. F.; Khandpur, A. K.; Bates, F. S.; Almdal, K.; Mortensen, K.; Hajduk, D. A.; Gruner, S. M. *Macromolecules* **1996**, *29*, 2857-2867.

Seddon, J. M. *Biochim. Biophys. Acta* **1990**, *1031*, 1-69.

Seki, M.; Suzuki, J.; Matsushita, Y. *J. Appl. Crystallogr.* **2000**, *33*, 285-290.

Semenov, A. N. *Sov. Phys. JETP* **1985**, *61*, 733-742.

Sha, K.; Li, D.; Li, Y.; Zhang, B.; Wang, J. *Macromolecules* **2008**, *41*, 361-371.

Shefelbine, T. A.; Vigild, M. E.; Matsen, M. W.; Hajduk, D. A.; Hillmyer, M. A.; Cussler, E. L.; Bates, F. S. *J. Am. Chem. Soc.* **1999**, *121*, 8457-8465.

Shepherd, N.; Stewart, M. J. Pat. Appl. GB 2241239, 1991.

Sides, S. W.; Fredrickson, G. H. *J. Chem. Phys.* **2004**, *121*, 4974-4986.

Singh, M.; Odusanya, O.; Wilmes, G. M.; Eitouni, H. B.; Gomez, E. D.; Patel, A. J.; Chen, V. L.; Park, M. J.; Fragouli, P.; Iatrou, H.; Hadjichristidis, N.; Cookson, D.; Balsara, N. P. *Macromolecules* **2007**, *40*, 4578-4585.

Snaith, H. J.; Schmidt-Mende, L. *Adv. Mater.* **2007**, *19*, 3187-3200.

Spontak, R. J.; Williams, M. C. *J. Polym. Sci., Part B* **1990**, *28*, 1379-1407.

Spontak, R. J.; Smith, S. D.; Ashraf, A. *Macromolecules* **1993**, *26*, 956-962.

Spontak, R. J.; Smith, S. D.; Ashraf, A. *Microsc. Res. Tech.* **1994**, *27*, 412-419.

Spontak, R. J.; Fung, J. C.; Braunfeld, M. B.; Sedat, J. W.; Agard, D. A.; Kane, L.; Smith, S. D.; Satkowski, M. M.; Ashraf, A.; et al *Macromolecules* **1996**, *29*, 4494-4507.

Stavrouli, N.; Katsampas, I.; Aggelopoulos, S.; Tsitsilianis, C. *Macromol. Rapid Commun.* **2008**, *29*, 130-135.

Storey, R. F.; Scheuer, A. D.; Achord, B. C. *J. Macromol. Sci., Part A: Pure Appl. Chem.* **2006**, *43*, 1493-1512.

Sugiyama, M.; Shefelbine, T. A.; Vigild, M. E.; Bates, F. S. *J. Phys. Chem. B* **2001**, *105*, 12448-12460.

Sun, P.; Yin, Y.; Li, B.; Chen, T.; Jin, Q.; Ding, D.; Shi, A. *Phys. Rev. E: Stat., Nonlinear, Soft Matter Phys.* **2005**, *72*, 061408/1-061408/6.

Sutton, D. E.; Schwindeman, J. A. *ACS Symp. Ser.* **1998**, *704*, 58-70.

Suzuki, J.; Seki, M.; Matsushita, Y. *J. Chem. Phys.* **2000**, *112*, 4862-4868.

Suzuki, J.; Nakane, K.; Takano, A.; Matsushita, Y. *Polymer* **2004**, *45*, 8989-8997.

Svensson, B.; Alexandridis, P.; Olsson, U. *J. Phys. Chem. B* **1998**, *102*, 7541-7548.

Szwarc, M. *Nature* **1956**, *178*, 1168-1169.

Szwarc, M.; Van Byelen, M.; Van Hoyweghen, D. *Macromolecules* **1987**, *20*, 445-448.

Takenaka, M.; Wakada, T.; Akasaka, S.; Nishitsuji, S.; Saijo, K.; Shimizu, H.; Kim, M. I.; Hasegawa, H. *Macromolecules* **2007**, *40*, 4399-4402.

Tamate, R.; Yamada, K.; Vinals, J.; Ohta, T. *J. Phys. Soc. Jpn.* **2008**, *77*, 034802/1-034802/6.

Thomas, E. L.; Alward, D. B.; Kinning, D. J.; Martin, D. C.; Handlin, D. L., Jr.; Fetters, L. J. *Macromolecules* **1986**, *19*, 2197-2202.

Thomas, E. L.; Anderson, D. M.; Henkee, C. S.; Hoffman, D. *Nature* **1988**, *334*, 598-601.

Thunemann, A. F.; Kubowicz, S.; von, B. H.; Mohwald, H. *Langmuir* **2006**, *22*, 2506-2510.

Toman, L.; Janata, M.; Spevacek, J.; Vlcek, P.; Latalova, P.; Masar, B.; Sikora, A. *J. Polym. Sci., Part A: Polym. Chem.* **2004**, *42*, 6098-6108.

Toman, L.; Janata, M.; Spevacek, J.; Vlcek, P.; Latalova, P.; Sikora, A.; Masar, B. *J. Polym. Sci., Part A: Polym. Chem.* **2005**, *43*, 3823-3830.

Tong, J.; Zhou, C.; Ni, S.; Winnik, M. A. *Macromolecules* **2001**, *34*, 696-705.

Toombes, G. E. S.; Finnefrock, A. C.; Tate, M. W.; Ulrich, R.; Wiesner, U.; Gruner, S. M. *Macromolecules* **2007**, *40*, 8974-8982.

Torikai, N.; Noro, A.; Okuda, M.; Odamaki, F.; Kawaguchi, D.; Takano, A.; Matsushita, Y. *Phys. B* **2006**, *385-386*, 709-712.

Triftaridou, A. I.; Vamvakaki, M.; Patrickios, C. S. *Biomacromolecules* **2007**, *8*, 1615-1623.

Tselikas, Y.; Hadjichristidis, N.; Lescanec, R. L.; Honeker, C. C.; Wohlgemuth, M.; Thomas, E. L. *Macromolecules* **1996**, *29*, 3390-3396.

Tyler, C. A.; Morse, D. C. *Macromolecules* **2003**, *36*, 3764-3774.

Tyler, C. A.; Morse, D. C. *Phys. Rev. Lett.* **2005**, *94*, 208302/1-208302/4.

Tyler, C. A.; Qin, J.; Bates, F. S.; Morse, D. C. *Macromolecules* **2007**, *40*, 4654-4668.

Urbas, A. M.; Maldovan, M.; DeRege, P.; Thomas, E. L. *Adv. Mater* **2002**, *14*, 1850-1853.

Valkama, S.; Ruotsalainen, T.; Nykaenen, A.; Laiho, A.; Kosonen, H.; ten Brinke, G.; Ikkala, O.; Ruokolainen, J. *Macromolecules* **2006**, *39*, 9327-9336.

Vavasour, J. D.; Whitmore, M. D. *Macromolecules* **1993**, *26*, 7070-7075.

Vavasour, J. D.; Whitmore, M. D. *Macromolecules* **1996**, *29*, 5244.

Vazaios, A.; Pitsikalis, M.; Hadjichristidis, N. *J. Polym. Sci., Part A: Polym. Chem.* **2003**, *41*, 3094-3102.

Verdier, P. H.; Stockmayer, W. H. *J. Chem. Phys.* **1962**, *36*, 227-235.

Vigild, M. E.; Almdal, K.; Mortensen, K.; Hamley, I. W.; Fairclough, J. P. A.; Ryan, A. J. *Macromolecules* **1998**, *31*, 5702-5716.

Vorrey, S.; Teeters, D. *Electrochim. Acta* **2003**, *48*, 2137-2141.

Wang, Z. G.; Safran, S. A. *Europhys. Lett.* **1990**, *11*, 425-430.

Wang, C.; Lodge, T. P. *Macromol. Rapid Commun.* **2002**, *23*, 49-54.

Wang, C.; Lodge, T. P. *Macromolecules* **2002**, *35*, 6997-7006.

Wang, X.; Winnik, M. A.; Manners, I. *Macromol. Rapid Commun.* **2002**, *23*, 210-213.

Wells, A. F. *Three-Dimensional Nets and Polyhedra;* John Wiley & Sons: New York, NY 1977.

Williams, D. B.; Carter, C. B. *Transmission Electron Microscopy*; Plenum Press: New York, NY, 1996.

Winey, K. I.; Thomas, E. L.; Fetters, L. J. *Macromolecules* **1992**, *25*, 422-428.

Wunderlich, B. *Macromolecular Physics*; Academic Press: New York, 1980; Vol. 3.

Xi, H.; Milner, S. T. *Macromolecules* **1996**, *29*, 2404-2411.

Xie, R.; Yang, B.; Jiang, B. *Macromolecules* **1993**, *26*, 7097-7099.

Xu, J.; Turner, S. C.; Fairclough, J. P. A.; Mai, S.; Ryan, A. J.; Chaibundit, C.; Booth, C. *Macromolecules* **2002**, *35*, 3614-3621.

Yamada, K.; Nonomura, M.; Ohta, T. *J. Phys: Condens. Matter* **2006**, *18*, L421-L427.

Yamada, K.; Ohta, T. *Europhys. Lett.* **2006**, *73*, 614-620.

Yang, S. Y.; Ryu, I.; Kim, H. Y.; Kim, J. K.; Jang, S. K.; Russell, T. P. *Adv. Mater.* **2006**, *18*, 709-712.

Yang, X.; Loos, J. *Macromolecules* **2007**, *40*, 1353-1362.

Yin, Y.; Sun, P.; Jiang, R.; Li, B.; Chen, T.; Jin, Q.; Ding, D.; Shi, A. *J. Chem. Phys.* **2006**, *124*, 184708/1-184708/8.

Young, R. J.; Lovell, P. A. *Introduction to Polymers*, 2nd ed.; Chapman & Hall: London, 1991.

Yu, Y. S.; Jerome, R.; Fayt, R.; Teyssie, P. *Macromolecules* **1994**, *27*, 5957-5963.

Zhang, P.; Moore, J. S. *J. Polym. Sci. Part A* **2000**, *38*, 207-219.

Zhao, J.; Majumdar, B.; Schulz, M. F.; Bates, F. S.; Almdal, K.; Mortensen, K.; Hajduk, D. A.; Gruner, S. M. *Macromolecules* **1996**, *29*, 1204-1215.

Zheng, W.; Wang, Z. *Macromolecules* **1995**, *28*, 7215-7223.